Universidad Rey Juan Carlos

CSIC
CONSEJO SUPERIOR DE INVESTIGACIONES CIENTÍFICAS

Madrid, 19 de diciembre de 2014

El Dr. Miguel Ángel López Manchado y la Dra. Raquel Verdejo Márquez, investigadores titulares del Instituto de Ciencia y Tecnología de Polímeros (ICTP) perteneciente al Consejo Superior de Investigaciones Científicas (CSIC),

DECLARAN:

Que autorizan la defensa del presente trabajo de investigación, titulado "*Development of epoxy nanocomposites based on carbon nanostructures*" y realizado por D. Mario Martín Gallego para la obtención del título de Doctor en Ingeniería de Materiales por la Universidad Rey Juan Carlos.

Firmado: Firmado:

Miguel Ángel López Manchado Raquel Verdejo Márquez

UNIVERSIDAD REY JUAN CARLOS

ESCUELA SUPERIOR DE CIENCIAS EXPERIMENTALES Y TECNOLOGÍA

CONSEJO SUPERIOR DE INVESTIGACIONES CIENTÍFICAS

INSTITUTO DE CIENCIA Y TECNOLOGÍA DE POLÍMEROS

DEVELOPMENT OF EPOXY NANOCOMPOSITES BASED ON CARBON NANOSTRUCTURES

MARIO MARTÍN GALLEGO

Supervised by:

Dr. MIGUEL ÁNGEL LÓPEZ MANCHADO

Dr. RAQUEL VERDEJO MÁRQUEZ

"Happiness is only true when shared."

Christopher McCandless

A mi familia

AGRADECIMIENTOS

Muchas han sido las personas que me han ayudado y apoyado de manera directa o indirecta durante este viaje de más de cuatro años. El primero de la lista al que me gustaría mencionar es a mi tutor Miguel Ángel. Él fue la persona que confió en mí, cuando era un recién y desubicado ingeniero, para otorgarme una beca financiada por él mismo hasta que obtuve financiación externa al grupo. Siempre te estaré agradecido por este hecho. Sigo por mi cotutora Raquel, a quien agradezco su actitud positiva y su disponibilidad para ayudarme en todo aquello que necesitaba, tanto desde un punto de vista científico-técnico como personal. La combinación de ambos, como tutores de tesis, ha sido el motor de mi aprendizaje científico y crecimiento personal.

Me gustaría agradecer al profesor Kenny por la beca italiana que me ofreció para iniciar mi tesis. A pesar de que no fue posible disfrutarla, agradezco de igual manera su buena intención.

Por otro lado tengo a mis compañeros de laboratorio en Madrid, mis compañeros de batalla. Siempre han estado a mi lado y sin ellos no hubiera sido lo mismo. La convivencia en viajes, su alegría, apoyo, y alguna que otra comilona/desayuno han hecho que estos años se me pasaran volando. Lean, Laura Jiménez, Natacha, Marianella, Laura Peponi, Nico, Ivan, Justo, Jose Maria, Chema, Ali, Valentina. ¡Muchas gracias de todo corazón! A Mar, además de por todo lo mencionado anteriormente me gustaría darle las gracias de manera especial por su ayuda con la reología y demás colaboraciones que hemos tenido, ¡eres una crack! A mis compañeros del máster: Vanessa, Marta Palacios, Marta Alonso, Nacho, Alberto Mejía por ser grandes compañeros. Al servicio de caracterización y de taller del ICTP, en especial a Isabel Raman por su alegría contagiosa.

Del grupo de elastómeros del ICTP me gustaría mencionar a Juanito y a Antonio por su esfuerzo y colaboración con el RMN. Y a todos los demás por los buenos ratos que hemos pasado juntos, en especial a Alberto.

Agradezco la amabilidad del profesor Mohamed Khayet de la Universidad Complutense de Madrid por dejarme usar sus instalaciones y a su equipo de personas por recibirme con los brazos abiertos cada vez que necesitaba usar sus laboratorios.

Ringrazio a Marco Sangermano per diversi motivi. Perchè con lui mi sono iniziato nel mondo dei polimeri quando ero ancora uno studente del Politecnico di Torino. Poi sono tornato da lui durante il dottorato per fare produttive collaborazioni, progetti internazionali... Solamente mi vengono buone parole su te. I miei colleghi italiani dal laboratorio anche facevano la mia adattazione molto facile. Sophie, Ignazio, Giovanna, Annalisa, Davide, grazie mile!

I acknowledge Qipeng for receiving me in his Australian group at Deakin University, where I spent one of the happiest periods of my life. I would like to thank my labmates for their help: Anbu, Marion and Tao. Finally, I thank the French connection (Oliver, Erwan Nico and Thomas), David, James, Lukas and Steve. You guys are the reason why I felt like at home, you were my family!

I would like to thank Marta Cerruti for her invitation to Montreal as well as Jilani and Gul for their support.

A Miguel Ángel y Belén de la Universidad de Valladolid por su ayuda con los ensayos de las espumas.

Gracias también a la Universidad Rey Juan Carlos y al departamento de ciencia e ingeniería de materiales por dejarme defender la tesis en dicho departamento.

A mi gente de Madrid, mis amigos de toda la vida del bloque, de la uni, de Turín y del colegio, quienes hacen que los problemas sean más llevaderos y las alegrías más intensas.

Finalmente, solo me queda dar las gracias a los más importantes, mis padres y hermanos. Ellos son las personas que siempre han estado y estarán conmigo tanto en lo bueno como en lo malo y gracias a ellos soy como soy. ¡Sois los mejores!

¡GRACIAS DE TODO CORAZÓN!

INDEX

Page

LIST OF FIGURES i

LIST OF TABLES ix

SYMBOLS AND ABBREVIATIONS xi

RESUMEN (ESPAÑOL) 1

Antecedentes y objetivos 3

Estructura de la tesis y metodología 5

Conclusiones 6

PREFACE: MOTIVATION, GOALS AND STRUCTURE OF THE THESIS 11

Chapter I. INTRODUCTION TO EPOXY RESIN SYSTEMS 17

I 1. Thermal curing of epoxy resins 19

I 2. UV curing epoxy resins 23

I 3. Nanostructuration by block copolymers 29

I 4. Epoxy resin foams 33

Chapter II. EPOXY NANOCOMPOSITES: STATE OF THE ART 37

II 1. Dispersing methods 40

II 2. Rheology of the epoxy/nanoparticle dispersions 43

II 3. Effect of the nanoparticles on the curing reaction 47

II 4. Mechanical properties 52

II 5. Toughness 60

II 6. Electrical properties 63

II 7. Thermal conductivity 68

II 8. Glass transition temperature 72

II 9. Thermal stability and fireproof properties 76

II 10. Summary 77

Chapter III. CARBON NANOPARTICLES 81

III 1. Introduction 83

III 2. Synthesis, functionalization and characterization of carbon nanotubes 87

III 3. Synthesis and characterization of thermally reduced graphene 98

III 4. Summary 105

Chapter IV. THERMALLY CURED EPOXY NANOCOMPOSITES 107
IV 1. Introduction 109
IV 2. Experimental 110
IV 3. Rheological filler percolation 113
IV 4. Curing kinetics 119
IV 5. Thermal conductivity 132
IV 6. Mechanical properties 138
IV 7. Summary 141
Chapter V. UV CURED EPOXY NANOCOMPOSITES 143
V 1. Introduction 145
V 2. Experimental 145
V 3. Photopolymerization process 149
V 4. Dielectric properties 153
V 5. Morphology 157
V 6. Dynamic mechanical and thermal analyses 159
V 7. Surface hardness 163
V 8. Summary 165
Chapter VI. EPOXY NANOSTRUCTURATION BY BLOCK COPOLYMERS 167
VI 1. Introduction 169
VI 2. Experimental 170
VI 3. Miscibility and crystallization 173
VI 4. Dynamic mechanical analysis 176
VI 5. Morphology 177
VI 6. Toughness 182
VI 7. Summary 184
Chapter VII. EPOXY NANOCOMPOSITE FOAMS 187
VII 1. Introduction 189
VII 2. Experimental 190
VII 3. Characterization of the blowing agent and determination of the processing conditions 193
VII 4. Morphology 195
VII 5. Dynamic mechanical analysis 199
VII 6. Flammability 201
VII 7. Thermal conductivity 204

VII 8. Electrical properties 205
VII 9. Summary 207
Chapter VIII. CONCLUSIONS 209
ANNEX. Low field NMR for polymer networks 215
REFERENCES 223
LIST OF PUBLICATIONS AND PATENTS 263

LIST OF FIGURES

Page

Figure I.1: Curing reaction with tertiary amines as catalysts 20

Figure I.2: Curing reaction with primary amines (DETA)..... 21

Figure I.3: Curing reaction with acid agents 21

Figure I.4: Applications of thermally cured epoxy resins, a) dual-cartridge dispenser for adhesives and b) carbon fiber composite 23

Figure I.5: Scheme of the UV induced photopolymerization 24

Figure I.6: Photoinitiated free radical polymerization mechanism 25

Figure I.7: Structure of an onium salt 26

Figure I.8: Cationic photopolymerization mechanism via UV light 27

Figure I.9: Applications of the UV curing in graphic arts, protective coatings, microelectronics and dentistry sectors.....29

Figure I.10: PEO-PEP phase diagram in an epoxy matrix 30

Figure I.11: TEM image of a self-assembled nanostructure of PEE-PEO in a cured epoxy resin.....31

Figure I.12: AFM image of a nanostructure produced by RIMS of a 30 wt. % of PS-b-PCL-b-PBA in an epoxy matrix 32

Figure I.13: SEM image of a syntactic epoxy foam with a 60 vol. % of glass microballoons 34

Figure I.14: Expancel microspheres. 35

Figure I.15: Marine applications of epoxy foams a) human-operated vehicle and b) flotation modules, c) epoxy panel and d) plug assists 36

Figure II.1: Rotating stirrer for the manufacturing of nanocomposites 41

Figure II.2: a) Schema of the three roll calendering, b) high shear zone between rolls 42

Figure II.3: Example of surface oxidation and fluorination of CNTs.....43

Figure II.4: Viscosity as a function of shear rate, for pristine epoxy and epoxy/CNT dispersions 44

Figure II.5: Viscosity vs shear rate for the neat resin and nanocomposites with CNT and fluorinated CNT. 46

Figure II.6: a) Solid-like behavior for CNTs dispersions and b) G´ vs frequency for a graphene/epoxy dispersion 47

Figure II.7: Extent of reaction vs temperature at 20 °C/min of MWCNTs filled epoxy systems 48

Figure II.8: Effect of graphene oxide on the activation energy as function of the extent of reaction 49

Figure II.9: Effect of carboxylic CNTs on the extent of reaction of an epoxy resin 50

Figure II.10: Stress–strain curves of the resin and its CNT composites 53

Figure II.11: Mechanical properties of poorly and well dispersed CNT, a) Young's modulus and b) tensile strength 54

Figure II.12: Microcracks generated in nanocomposites at a) 10 wt. % CNF and b) 20 wt. % CNF 55

Figure II.13: Mechanical comparison of nanocomposites containing CNTs and graphene nanoplatelets, a) tensile strength and b) Young's modulus (Halpin-Tsai model was used for the theoretical model) 56

Figure II.14: a) Stress-strain curves, b) Young's modulus, c) tensile strength and d) fracture strain 57

Figure II.15: a) Idealized structure of a hybrid nanocomposite containing graphene and CNTs and b) stress-strain curves of the hybrids and nanocomposites 58

Figure II.16: Optical micrographs of CNTs in a cured nanocomposite, a) and b) without electric field, c) and d) with electric field alignment 59

Figure II.17: SEM micrographs of CNT epoxy nanocomposites. a) Crack bridging and b) pull-out 60

Figure II.18: K_{IC} and G_{IC} as function of CNF content 61

Figure II.19: Toughness of graphene oxide (GO), silica (ATS) and silica/graphene (ATGO) nanocomposites..... 62

Figure II.20: Conductivity as a function of wt. % of CNT (p). The insert shows a log–log plot of the conductivity as a function of p−pc, pc is the percolation threshold which resulted to be 0.0025 wt. %..... 64

Figure II.21: Electrical resistance of epoxy nanocomposites containing aligned CNF 66

Figure II.22: EMI shielding effectiveness for epoxy/graphene nanocomposites 67

Figure II.23: κ enhancement as function of SWNT and CNF loading 69

Figure II.24: Thermal conductivity using different type of CNPs..... 70

Figure II.25: Thermal conductivity of 5.4 vol. % graphite nanoplatelet composites as function of the exfoliating temperature..... 71

Figure II.26: Thermal conductivity with various filler contents of MWCNTs/epoxy, graphene/epoxy, and Py-PGMA–graphene/epoxy 72

Figure II.27: *Tan δ* curves for epoxy nanocomposites filled with un-treated CNFs and silanized CNFs..... 75

Figure II.28: DMA curves of pristine graphene and amine functionalized graphene... 76

Figure II.29: LOI of epoxy nanocomposites with graphene oxide (EPGO) and GO functionalized with flame retardant molecules (EPGRF)..... 77

Figure III.1: Schematic view of a SWCNT and a MWCNT 83

Figure III.2: Schematic diagram showing a carbon nanotube with a) armchair chirality and b) zig-zag chirality..... 84

Figure III.3: Schematic illustration of an idealized single layer graphene sheet..... 85

Figure III.4: Schematic models representing different types of defects in CNTs and graphene..... 87

Figure III.5: Molecular structure of ferrocene 87

Figure III.6: Experimental set up for the synthesis of MWCNTs 88

Figure III.7: FT-IR spectra of MWCNTs and o-MWCNTs 89

Figure III.8: Raman spectra of MWCNTs and o-MWCNTs 90

Figure III.9: C_{1s} and O_{1s} XPS spectra of MWCNTs and o-MWCNTs 92

Figure III.10: TGA and DTGA curves of MWCNTs and o-MWCNTs 94

Figure III.11: SEM images of MWCNTs a) augmentation x500 b) x2000 95

Figure III.12: TEM images of the a) and b) pristine MWCNTs and c) and d) o-MWCNTs 96

Figure III.13: Diameter distributions of the MWCNTs a) outer diameter, b) inner diameter and for the o-MWCNTs c) outer diameter, d) inner diameter 97

Figure III.14: Scheme of the synthesis of TRG 99

Figure III.15: XRD patterns of natural graphite, GO and TRG. 100

Figure III.16: FT-IR spectrum of TRG 101

Figure III.17: Raman spectrum of TRG. The inset corresponds to the spectrum of natural graphite 102

Figure III.18: C_{1s} and O_{1s} XPS spectra of TRG. 103

Figure III.19: TGA and DTGA curves of TRG 104

Figure III.20: TEM images of TRG at a) low resolution and b) high resolution 104

Figure IV.1: Experimental procedure of the preparation of thermally cured composites 111

Figure IV.2: Experimental setup to measure the thermal conductivity of the uncured nanofluids 112

Figure IV.3: η^* evolution of the epoxy/nanofiller dispersions: (a) versus frequency where the symbols correspond to the experimental result and the solid line with the Herschel–Bulkley model and (b) versus the torque 114

Figure IV.4: Dynamic frequency sweeps for MWCNT and TRG dispersions. 116

Figure IV.5: Evolution of G' and G'' versus frequency at room temperature for the dispersions containing (a) MWCNTs and (b) MWCNTs and TRG at the same filler content 117

Figure IV.6: Loss tangent as a function of frequency for all the dispersions 118

Figure IV.7: Sequences of pulses 121

Figure IV.8: Superposition of raw data (I_{DQ} and I_{ref}, respectively) from DQ-NMR experiment based on the so-named 2-pulses and 3-pulses experiments at 100 °C for the cured ER 121

Figure IV.9: NMR signals at three different temperatures for the cured ER, a) I_{ref}, b) I_{DQ}, d) $I_{\Sigma MQ}$ and d) I_{nDQ} 123

Figure IV.10: Evolution of *C(t)* at short DQ evolution time 124

Figure IV.11: a) D_{res} distributions after Tikhonov regularization and b) D_{res} evolution with the temperature 125

Figure IV.12: Curing curves for a) neat epoxy resin at three different temperatures and b) nanocomposites at 1 wt. % of filler and 40 °C. 126

Figure IV.13: η^* versus curing time for the a) ER at 40 °C, 70 °C and 100 °C and b) nanocomposites at 40 °C 129

Figure IV.14: Evolution of $G´$ and $G´´$ with the curing time at 40 °C for a) ER, b) 1 wt. % MWCNT, c) 1 wt. % o-MWCNT and d) 1 wt. % TRG. 130

Figure IV.15: Extent of reaction by DSC for a) the ER at 40 °C, 70 °C and 100 °C and b) nanocomposites at 70 °C 131

Figure IV.16: TEM images of nanofluids: a) resin loaded with 1 wt. % MWCNTs and b) with 1 wt. % TRG 133

Figure IV.17: Schema of the phonon coupling losses and the boundary phonon scattering at the nanoparticle interphase. 135

Figure IV.18: Comparison of the measured data for MWCNT nanofluids and the theoretical values 136

Figure IV.19: TEM images of cured epoxy samples: a) resin loaded with 1 wt. % MWCNTs and b) with 1 wt. % TRG. 137

Figure IV.20: TEM images of the 0.75 wt. % MWCNT and 1.5 wt. % TRG nanocomposites 140

Figure IV.21: Stress–strain curves for the neat resin and nanocomposites containing 0.5 wt. % of MWCNT, o-MWCNT and TRG. 141

Figure V.1: Molecular structures of the a) dicycloaliphatic epoxy resin and b) photoinitiator 146

Figure V.2: Experimental procedure of the UV cured composites preparation 147

Figure V.3: Experimental set up for the a) real time FT-IR measurements and b) static UV lamp 148

Figure V.4: FT-IR spectra vs irradiation time for the pure epoxy resin over the entire region and a closed-up from 950 to 650 cm^{-1}. Curing time 3 min 150

Figure V.5: FT-IR conversion curves for a) nanocomposites at 1 wt. % of nanofiller content. Effect of filler content on the conversion for b) MWCNTs and o-MWCNTs, c) TRG and d) EG. 151

Figure V.6: FT-IR spectra of the formulation containing 1.5 wt. % TRG before and after 5 min of UV irradiation. Film thickness 25 μm 153

Figure V.7: AC conductivity and permittivity versus frequency for all the fillers at different loading fractions 155

Figure V.8: Values of the DC electrical conductivity of the epoxy nanocomposites as a function of the nanofiller content 156

Figure V.9: SEM images of a) neat CE (scale 20 μm) and b) 1.5 wt. % TRG nanocomposite (scale 10 μm). TEM images of the 1.5 wt. % TRG c) and d) 157

Figure V.10: SEM images of the fracture surface of the 5 wt. % EG nanocomposite. 158

Figure V.11: SEM images of the 1 wt. % a) MWCNTs and b) o-MWCNTs nanocomposites 158

Figure V.12: TEM image of the 1 wt. % MWCNTs nanocomposite 159

Figure V.13: DMTA curves for composites at 1 wt. % loading fraction 160

Figure V.14: DSC thermograms for all the nanocomposites 162

Figure V.15: a) Hit values and b) load vs depth curves at 1 wt. % filler content 164

Figure V.16: Persoz hardness as function of TRG content 164

Figure VI.1: Experimental procedure for the preparation of nanostructured thermally cured composites. 171

Figure VI.2: Configuration of the three point bend specimen 173

Figure VI.3: Digital image at room temperature of the samples in the a) uncured and b) cured states (2 mm thick) 174

Figure VI.4: TGA curves of the cured ER-BC blends 174

Figure VI.5: DSC thermograms of the cured blends. 175

Figure VI.6: Dynamic mechanical curves of the cured blends 176

Figure VI.7: TEM images of a) 10BC, b) 20BC and d) 40BC 178

Figure VI.8: Scheme of the hierarchical nanostructure 178

Figure VI.9: SAXS profiles of the neat epoxy resin, 10BC, 20BC and 40BC. 179

Figure VI.10: Tapping mode AFM images at 5x5 µm and 1x1 µm scales. 180

Figure VI.11: Tapping mode AFM images of 40BC-TRG and 40BC-MWCNT at 5x5 µm and 1x1 µm scales 181

Figure VI.12: SEM images of a) neat epoxy resin, b) 40BC, c) 40BC-TRG and d) 40BC-MWCNT 182

Figure VI.13: K_{IC} comparison 183

Figure VII.1: Scheme of the three roll calendar 190

Figure VII.2: Experimental procedure of the foams preparation. 192

Figure VII.3: Morphological characterization of Expancel. a) SEM image and b) diameter distribution. 194

Figure VII.4: DSC of Expancel 194

Figure VII.5: a) Premature curing without expansion (85 °C and 15 min) and b) full expanded epoxy foam (100 °C and 3 min) 195

Figure VII.6: Schematic diagram of the changes on the cell structure in nanocomposite foams 196

Figure VII.7: SEM images of the low density foams. a) pristine ER-LD, b) and c) 0.5 wt.% MWCNT-LD, d) and e) 1.5 wt.% TRG-LD. 197

Figure VII.8: SEM images of the high density foams. a) pristine ER-HD, b) and c) 0.5 wt. % MWCNT-HD, d) and e) 1.5 wt. % TRG-HD. 199

Figure VII.9: E' vs ρ at room temperature 200

Figure VII.10: E' vs temperature for a) low density and b) high density foams 201

Figure VII.11: a) LOI test of ER-LD at 20.3 vol. % of oxygen, b) LOI test of 0.5 wt. % MWCNT-LD at 21.1 vol. % of oxygen and c) LOI test of 1.5 wt. % TRG at 21 vol. % of oxygen. 203

Figure VII.12: Variation of κ with the foam density 204

Figure VII.13: κ / ρ for a) low density foams and b) high density foams 205

Figure VII.14: Electrical conductivity of the a) low density foams and b) high density foams. 206

Figure VII.15: Permittivity of the a) low density foams and b) high density foams .. 207

Figure VII.16: Application of conductive epoxy foams 208

Figure A.1: Schematic representation of possible molecular conformations in a polymer network. 217

Figure A.2: Schematic representation of $C_\alpha(t)$ for entangled melt and polymer networks above T_g 218

Figure A.3: Variation of I_{DQ} and I_{ref} with τ_{DQ} 219

Figure A.4: Evolution of I_{sDQ} with τ_{DQ} of PDMS rubber 220

Figure A.5: Evolution of I_{nDQ} 221

LIST OF TABLES

Table II.1: SSA and T_E of the neat epoxy resin and its composites 51

Table II.2: Summary of the experimental results concerning the electrical properties of CNT/epoxy nanocomposites 64

Table II.3: Shift of T_g in CNT/epoxy nanocomposites.....73

Table III.1: Peaks, binding energy, assignments and atomic percentage of MWCNT and o-MWCNT 93

Table III.2: Structural properties of the MWCNTs and o-MWCNTs.....98

Table III.3: Peaks, binding energy, assignments and atomic percentage of TRG 103

Table IV.1: Parameters of the Herschel–Bulkley fitting 115

Table IV.2: Values of λ for all the dispersions 119

Table IV.3: Kinetic parameters obtained by DQ-NMR 128

Table IV.4: t_{gel} values obtained by rheology. 130

Table IV.5: Kinetics parameters obtained by DSC 132

Table IV.6: Thermal conductivity of the epoxy nanofluids 134

Table IV.7: Thermal conductivity of the cured epoxy nanocomposites.....138

Table IV.8: Mechanical properties of the reinforced nanocomposites.....139

Table V.1: UV curing parameters of all the formulations studied.....152

Table V.2: T_g values obtained by DMTA of the cured nanocomposites at 1 wt. % loading fraction.....161

Table V.3: T_g values obtained by DSC for all the nanocomposites studied 163

Table VI.1: T_g values of the cured blends.....177

Table VI.2: Toughness of the cured nanocomposites. K_{IC} (MPa $m^{1/2}$) values 183

Table VII.1: Dispersing protocol.....191

Table VII.2: Cell size of the epoxy foams.....198

Table VII.3: LOI values for the low density foams.....203

SYMBOLS AND ABBREVIATIONS

a: Initial crack length

A: Consistency index

AFM: Atomic Force Microscopy

B: Thickness

BC: Block Copolymer

BE: Binding Energies

B-P: Baum-Pines

C(t): Second Legendre polynomial of the OAF

CB: Carbon Black

CE: Cycloaliphatic epoxy resin

CF: Carbon Fiber

CNFs: Carbon Nanofibers

CNPs: Carbon Nanoparticles

CNTs: Carbon Nanotubes

CVD: Chemical Vapor Deposition

ε^*: Dielectric permittivity

ε': Real part of the dielectric permittivity

ε'': Imaginary part of the dielectric permittivity

d: Bragg´s law spacing

DETA: Diethylenetriamine

ΔH: Heat of reaction

ΔH_{iso}: Heat of reaction during isothermal scans

ΔH_{dyn}: Heat of reaction during dynamic scans

ΔH_T: Total heat of reaction

ΔH_t: Heat of reaction at each time

DMTA: Dynamic Mechanical Analysis

DQ: Double Quantum

D_{res}: Residual dipolar coupling

DSC: Differential Scanning Calorimetry

DWCNT: Double Wall Carbon Nanotube

E_a: Activation energy

EG: Expanded Graphite

EMI: Electromagnetic Interference

ER: Epoxy Resin

FT-IR: Fourier Transform Infrared

$G´$: Elastic modulus

$G´´$: Storage modulus

G_{IC}: Energy absorbed for crack propagation

GO: Graphite Oxide

HD: High Density

Hit: Indentation hardness

I_{DQ}: Double quantum intensity

In_{DQ}: Normalized double quantum intensity

I_{ref}: Intensity reference

$I_{\Sigma MQ}$: Summation of multiple quantum intensities

I_{sDQ}: Summation of multiple quantum intensities

η^*: Complex viscosity

θ: Incidence angle

k: Polymerization rate constant

κ: Thermal conductivity

κ_e: Effective thermal conductivity

κ_f: Fluid´s thermal conductivity

κ_p: Nanoparticle´s thermal conductivity

K_{IC}: Stress intensity factor

λ: Characteristic time for $tan\ \delta_{max}$

LD: Low Density

LOI: Limit Oxygen Index

m: Nanoparticle shape factor

MDA: Methylenedianiline

MDI: Methylene Diphenyl Diisocyanate

MQ: Multiple Quantum

MWCNTs: Multi Wall Carbon Nanotubes

MWS: Maxwell-Wagner-Sillars

n: Flow behavior index

NMR: Nuclear Magnetic Resonance

OAF: Orientation Autocorrelation Function

o-MWCNTs: Oxidized Multi Wall Carbon Nanotubes

P: Critical load for crack propagation

PBA: Poly(n-butyl acrylate)

p_c: Percolation threshold

PCL: Poly ε-caprolactone

PEE: Poly(ethylene-b-ethylene)

PEO: Polyethylene oxide

PEP: Poly(ethylene-alt-propylene)

PGMA: Poly(glycidyl methacrylate)

POSS: Polyhedral Oligomeric Silsesquioxanes

PPO: Polypropylene oxide

PS: Polystyrene

PTFE: Polytetrafluoroethylene

Py: Pyrene

ρ: Density

q: Scattering vector

RBM: Radial Breathing Mode

RCD: Residual Dipolar Coupling

RFI: Resin Film Infusion

RIMS: Reaction Induced Microphase Separation

RT-FTIR: Real Time Fourier Transform Infrared

RTM: Resin Transfer Molding

S: Loading span

S_b: Dynamic order parameter

SEM: Scanning Electron Microscopy

SENB: Single Edge Notch Bending

σ: Electrical conductivity

σ_{DC}: Direct current electrical conductivity

SAXS: Small Angle X-Ray Scattering

SSA: Specific Surface Area

SWCNT: Single Wall Carbon Nanotube

Tan δ: Damping factor

T_c: Crystallization temperature

TEM: Transmission Electron Microscopy

t_{gel}: Gel time

T_m: Melting temperature

τ_o: Yield stress

$\tau_{DQ:}$ Double quantum evolution time

T_g: Glass transition temperature

T_E: Maximum of the exothermic heat flow of curing reaction

TGA: Thermogravimetric Analysis

TPS: Transient Plane Source

TRG: Thermally Reduced Graphene

φ: Volume fraction

UCST: Upper Critical Soluble Temperature

UV: Ultra Violet

$X_{A\text{-}B}$: Flory-Huggins parameter

XPS: X-Ray Photoelectron Spectroscopy

XRD: X-Ray Diffraction

W: Width

ω: Angular frequency

RESUMEN (ESPAÑOL)

ANTECEDENTES Y OBJETIVOS

Desde el descubrimiento de los nanotubos de carbono (CNTs) a principios de los 90, estas nanopartículas han despertado un gran interés en diversos campos de la ciencia. En particular, en la última década se han publicado un gran número de artículos describiendo el alto potencial de los nanocompuestos CNT/polímero en la producción de materiales compuestos con propiedades multifuncionales para aplicaciones avanzadas.

Las resinas epoxi representan un grupo importante dentro de las distintas clases de polímeros existentes hoy en día. Su importancia reside en las excelentes propiedades adhesivas y mecánicas, su alta estabilidad química, térmica y dimensional al igual que su buena resistencia a los disolventes. Estas propiedades intrínsecas de las resinas epoxi, junto con la posibilidad de modificar su composición química y física para obtener unas propiedades finales a la carta, hacen que cumplan los requerimientos de un amplio espectro de aplicaciones en áreas muy diversas. Por estos motivos existe una gran variedad de sistemas epoxídicos que van desde la clásica resina curada térmicamente a materiales nanoporosos, filmes curados por luz ultravioleta, espumas de baja densidad, resinas autoensambladas o nanoestructuradas por mencionar algunos.

Se espera que con la incorporación de CNTs en la formulación de las resinas epoxi no solo se mejore la respuesta mecánica de la matriz, sino que también se le añadan nuevas funcionalidades como son el caso de la conductividad eléctrica o térmica. Sin embrago, a pesar de las increíbles propiedades intrínsecas de los CNTs, la extrapolación de dichas propiedades a todo el material compuesto supone el gran reto en el desarrollo de estos nanocompuestos poliméricos. Los factores clave para lograr dicho objetivo pasan por alcanzar una dispersión óptima de los CNTs, una buena interfase carga/matriz y la orientación adecuada de la nanocarga.

Mientras el desarrollo de los compuestos basados en CNT/polímero maduraba, en 2004 se descubrió por primera vez las láminas aisladas de grafeno. Este hecho, junto con el posterior avance en los métodos de síntesis de grafeno reducido en grandes cantidades hizo que apareciera una nueva posibilidad dentro del campo de los nanocompuestos basados en nanoestructuras de carbono. Al igual que los anteriores, los

nanocompuestos de grafeno y resina poseen gran potencial pero su desarrollo también presenta los mismos obstáculos que en el caso de los CNTs en términos de dispersión, aglomeración, adhesión, etc. Sin embargo, la geometría plana del grafeno puede conferir ciertas peculiaridades y diferencias en cuanto a los medios de dispersión más óptimos, el procesado y las propiedades finales de sus nanocompuestos en comparación con los CNTs.

En este contexto, esta tesis doctoral tiene como principal premisa el desarrollo y la comparación de nanocompuestos de CNTs y grafeno en una matriz epoxídica. Los objetivos específicos que se definieron vienen desglosados en los siguientes puntos:

- Comparar y evaluar el efecto de los CNTs y grafeno en la reacción de curado de dos sistemas epoxídicos diferentes, en particular, el curado térmico con aminas y el curado ultravioleta, así como evaluar el efecto de las nanopartículas en las propiedades finales de los nanocompuestos obtenidos.

- Desarrollar nuevas técnicas de caracterización de polímeros termoestables y de seguimiento de reacciones de curado de resinas basadas en experimentos de resonancia magnética nuclear (NMR) de bajo campo.

- Desarrollar una estrategia *bottom-up* basada en la nanoestructuración de la resina epoxi usando copolímeros de bloque para mejorar la tenacidad de los nanocompuestos.

- Producir y caracterizar espumas epoxídicas de baja densidad y con alta conductividad eléctrica.

ESTRUCTURA DE LA TESIS Y METODOLOGÍA

La tesis está organizada en ocho capítulos y un anexo donde se presentan y discuten los resultados obtenidos.

El *capítulo I* presenta los principales aspectos de los materiales epoxídicos, tales como los métodos de producción y las características de los diferentes sistemas de resinas epoxi empleados durante la tesis: el clásico curado térmico, el curado ultravioleta, la nanoestructuración con copolímeros de bloque y las espumas epoxídicas de baja densidad.

El *capítulo II* muestra el estado del arte actual de los nanocompuestos de resinas epoxi basados en nanopartículas de carbono. Este capítulo representa una revisión bibliográfica de los aspectos clave necesarios en la producción de nanocompuestos epoxídicos descritos y presentados en orden cronológico: métodos de dispersión, procesado de las dispersiones, reacción de curado así como el efecto de las cargas en un amplio número de propiedades finales.

El método de síntesis y la caracterización de las nanopartículas empleadas en este trabajo vienen detallados en el *capítulo III*. Se describe en profundidad el método experimental usado en cada caso, la deposición en fase vapor (CVD) y la reducción térmica de grafito oxidado para los CNTs y el grafeno, respectivamente. Las nanopartículas obtenidas por estos métodos se caracterizaron mediante técnicas tales como FT-IR, XPS, SEM, TEM, Raman, XRD y TGA.

El *capítulo IV* detalla la preparación de los nanocompuestos curados con aminas alifáticas (curado térmico). Aspectos tales como la percolación de las cargas, su efecto en la cinética de curado, la conductividad térmica y las propiedades mecánicas del material curado final son descritos en este capítulo. Merece la pena mencionar que en este capítulo se presenta una nueva técnica de seguimiento de la reacción de curado para materiales termoestables basada en RMN de bajo campo.

La tecnología de curado por luz ultravioleta es empleada en el *capítulo V*. El efecto de las nanopartículas en la fotopolimerización, la morfología y las propiedades finales de los filmes están descritos en este capítulo.

El *capítulo VI* trata sobre la adición de copolímeros de bloque para nanoestructurar la matriz epoxídica. El principal objetivo de dicha nanoestructuración es incrementar la tenacidad del material. El efecto de las nanopartículas en la miscibilidad del copolímeros, la morfología de las fases y las propiedades finales es investigado. La morfología de las fases se evalúa mediante técnicas de microscopia de fuerza atómica (AFM) y microscopia electrónica de transmisión (TEM).

El último sistema epoxídico estudiado en la tesis son los nanocompuestos de espumas de baja densidad (*capítulo VII*). Se emplean microesferas expandibles térmicamente para espumar la resina. Este capítulo contiene todos los detalles experimentales de la producción de las espumas, así como la completa caracterización de la estructura celular de las espumas y sus propiedades finales. Las espumas desarrolladas en este capítulo presentan una alta conductividad eléctrica dotándolas de una alta aplicabilidad en sectores como el aeronáutico y la automoción.

El *capítulo VIII* resume las conclusiones generales obtenidas y algunas pautas para la continuación de la línea de investigación.

Finalmente, el *anexo* trata de explicar brevemente los principios y fundamentos de la técnica de RMN de bajo campo aplicada a la caracterización de redes poliméricas entrecruzadas.

CONCLUSIONES

Como se ha mencionado anteriormente, esta tesis trata sobre el desarrollo de nanocompuestos de resinas epoxi basados en nanoestructuras de carbono, como los nanotubos de pared múltiple (MWCNTs) y el grafeno reducido térmicamente (TRG). Estas nanopartículas fueron utilizadas en cuatro tipos de sistemas epoxídicos: resinas curadas térmicamente, filmes curados mediante luz UV, resinas nanoestructuradas y espumas de baja densidad. En los cuatro casos, analizamos y comparamos el efecto de cada nanopartícula en el procesado, reacción de entrecruzamiento y propiedades finales de los nanocompuestos.

Las conclusiones generales extraídas de la tesis son:

- Estudiamos la red de percolación de los MWCNTs y el TRG mediante el estudio reológico de las dispersiones de las nanopartículas en la resina sin curar. Los MWCNTs con una geometría tubular y con una alta relación de aspecto formaron la red de percolación a bajos porcentajes de carga, mucho menores que en el caso del TRG. Los MWCNTs cambiaron el comportamiento reológico de la dispersión pasando de un fluido Newtoniano a uno con comportamiento pseudoplástico. En comparación, el TRG no produjo un gran aumento de la viscosidad, incluso a elevadas concentraciones. Esta baja viscosidad de las dispersiones facilitó el procesado de los nanocompuestos con TRG permitiendo introducir mayores cantidades de carga. Los ensayos de propiedades mecánicas sobre los materiales curados térmicamente revelaron notables incrementos en el módulo de Young y la resistencia final del material, especialmente en el caso de los nanocompuestos con TRG.

- La caracterización mediante RMN de bajo campo demostró ser efectiva para el análisis de reacciones de curado, estudio de la estructura y la dinámica segmental de polímeros termoestables. Los resultados obtenidos por esta técnica novedosa sobre la cinética de curado de la reacción resultan ser complementarios a los obtenidos por otros métodos más tradicionales. Se observó un efecto autocatalítico de la reacción de curado en presencia de las nanopartículas, reduciéndose los tiempos de inducción y de gelificación, incrementándose la velocidad de reacción y bajando la energía de activación de la reacción. Este efecto acelerante de las nanopartículas se atribuyó a incrementos en la conductividad térmica de las dispersiones, la presencia de grupos funcionales en la superficie de las partículas y su elevada superficie específica. Cabe destacar que es la primera vez que se emplea la técnica de RMN para caracterizar este tipo de materiales.

- Se empleó un método directo y fácil basado en la técnica del hilo caliente para medir la conductividad térmica de las dispersiones sin curar. Analizando los diferentes mecanismos que intervienen en la transmisión de calor se concluyó que la estructura multicapa de los MWCNTs facilita el transporte de los fonones

a través de sus capas internas y que la presencia de grupos funcionales actúa como puntos de dispersión para las vibraciones fonónicas.

- En el caso de emplear la tecnología de curado por luz UV, se observó que las conversiones al final de la fotopolimerización y la propia velocidad de reacción disminuían con la presencia de las nanopartículas. Este hecho se basa en la competencia en la luz absorbida entre el fotoiniciador y las nanopartículas, que actuaría como un escudo, reduciendo la eficiencia del proceso de fotocurado. Las propiedades eléctricas de los filmes fotocurados mostraron límites de percolación diferentes dependiendo del tipo de carga empleada, obteniéndose el menor límite de percolación y el mayor valor de conductividad con los MWCNTs. Las diferencias se asociaron a la geometría de la partícula y al tipo de contacto entre partículas producido en una red percolada de MWCNTs. Sin embargo, el TRG produjo el mejor resultado desde un punto de vista de mecánico, mostrando incrementos en la dureza superficial del filme y aumentos en la T_g de más de 20 °C con tan solo un 1 % en peso de TRG.

- Se prepararon satisfactoriamente novedosos nanocompuesos híbridos formados por una matriz nanoestructurada con un copolímero de bloque y MWCNTs y TRG. Se observó un efecto sinérgico entre el copolímero y las nanopartículas en la tenacidad a fractura del material. Además, la presencia de las nanopartículas disminuyó el efecto negativo del copolímero en las propiedades dinamo-mecánicas.

- Finalmente, se estudió un cuarto sistema epoxídico espumando la resina curada térmicamente mediante microesferas expandibles. El objetivo primordial de este desarrollo era producir espumas eléctricamente conductoras mediante el empleo de los MWCNTs y TRG, que resultó ser independiente de la densidad de la espuma. Además, la presencia de las nanocargas mejoró otras propiedades de las espumas como su resistencia a la llama y las propiedades mecánicas.

- Un denominador común observado en los cuatro sistemas estudiados fue el hecho de que los nanocompuestos con MWCNTs se comportaron mejor que el TRG en las propiedades físicas que requieren transporte de carga o temperatura, como la conductividad eléctrica y térmica. El menor límite de percolación de los MWCNTs facilita dicho transporte a través de la red de percolación. Sin

embargo, la estructura plana y arrugada de las láminas de grafeno junto con la presencia de los grupos funcionales residuales hacen que sus nanocompuestos presenten mejores propiedades mecánicas que los correspondientes a los MWCNTs. Este hecho se debe fundamentalmente a una mayor inhibición de la generación y propagación de grietas por el grafeno y a la mejor adhesión en la interfase carga/polímero.

PREFACE: MOTIVATION, GOALS AND STRUCTURE OF THE THESIS

Since carbon nanotubes (CNTs) were reported for the first time in the early 1990s, these nanoparticles have attracted great attention in several fields of science and technology. In particular, a vast number of articles have been published in the sector of polymer composites over the last years, where CNT/polymer nanocomposites showed their potential to produce multifunctional and high performance composites for advanced applications.

Epoxy resins are an important class of polymers due to their strong adhesion and excellent overall mechanical properties, high chemical, thermal, and dimensional stability and solvent resistance. The intrinsic properties of epoxy resins make them suitable for a wide spectrum of applications in diverse areas due to the fact that epoxies can be chemically and physically tailored to fulfill specific requirements. Therefore, there are numerous epoxy systems ranging from the classical thermally cured resin, to nanoporous materials, ultraviolet cured coatings, low density foams, self-assembled polymers, nanostructured resins or specific formulations for adhesives and/or high mechanical and thermal properties.

Incorporation of CNTs into the epoxy formulation is expected to improve the mechanical performance of epoxy resins but also to bring new functionalities like enhanced electrical and thermal conductivities. However, despite the exceptional intrinsic properties of CNTs, the extrapolation of these properties to the bulk matrix has become the greatest challenge on the development of epoxy nanocomposites. The key aspects to reach this goal are the dispersion state of the CNTs, the filler-polymer interfacial adhesion and the orientation of the nanofillers.

In the meantime, the discovery of graphene in 2004 and the development of methods of synthesis to produce large quantities of exfoliated graphene sheets have opened a new class of possibilities to produce epoxy nanocomposites based on carbon nanostructures. Epoxy/graphene nanocomposites also possess great potential but present the same obstacles as the CNTs nanocomposites in terms of dispersion, agglomeration, adhesion, etc. However, the planar geometry of graphene sheets can confer some peculiarities and differences in the dispersion protocols, processing and final properties of its composites compared to CNT nanocomposites.

Therefore, the aim of this thesis is to develop and compare CNT and graphene epoxy nanocomposites with improved properties. The specific goals of the study are defined in the following points:

- Comparison of the rheology of CNT and graphene dispersions, the effect on the curing reaction with amines and the evaluation of the final properties of the thermally cured nanocomposites.
- Development of new techniques to analyze the curing reaction and network structure of epoxy resins based on low field NMR experiments.
- Use of UV curing technologies to produce epoxy UV cured coatings containing graphene and CNTs. Analysis of the influence of the carbon nanoparticles (CNPs) on the photopolymerization process and final properties of the coatings. Production of high electrical conductive epoxy coatings.
- Development of a *bottom-up* approach based on the nanostructuration of the epoxy resin using block copolymers in order to improve the toughness of the nanocomposites.
- Production and characterization of low density epoxy foams with improved electrical conductivity.

This thesis is organized into eight chapters and one annex in order to present all the work performed during this PhD.

Chapter I introduces the main generalities, production methods and characteristics of the different epoxy systems developed during the thesis: the classical thermal curing approach, the UV curing technology, the nanostructuration by block copolymers and the epoxy foams.

Chapter II presents the state of the art on epoxy nanocomposites based on carbon nanostructures. This chapter represents a review of the main aspects involved in the fabrication of epoxy nanocomposites which are described in chronological order: dispersion methods, processing of the dispersions, curing reaction and a wide set of properties are summarized analyzing the effect of the CNPs on each one.

The method of synthesis and characterization of the CNPs employed to prepare the epoxy nanocomposites is detailed in the *Chapter III*. A full description of the experimental procedure to obtain the multi-walled carbon nanotubes (MWCNTs) through the chemical vapor deposition (CVD) technique can be found in this chapter. The oxidation/functionalization of these MWCNTs is also described. In addition, the synthesis and characterization of graphene sheets obtained from the thermal reduction and exfoliation of graphite oxide is also reported.

Chapter IV details the preparation of epoxy nanocomposites cured with aliphatic amines (thermally cured). Aspects like the filler percolation, the effect of the CNPs on the curing kinetics, the thermal conductivity and the mechanical properties of the fully cured material are described in this chapter. It is worth mentioning that a new approach to follow the kinetics of thermosetting polymers based on NMR experiments is reported here for the first time.

A different curing technology based on UV light is employed in *Chapter V*. The effect of the CNPs on the photopolymerization, the morphology and the main properties of UV cured nanocomposite coatings are investigated.

Chapter VI deals with the addition of block copolymers to nanostructure the epoxy matrix. The main goal of this nanostructure is to increase the fracture toughness of the epoxy resin. The effect of CNPs on the miscibility, morphology of the phases and final properties are investigated.

The last epoxy system studied in this thesis is the epoxy nanocomposite foams (*Chapter VII*). A novel approach using expandable microspheres is used to reduce the density of the resin. A full description of the experimental conditions, morphology of the cell structure and CNPs distribution and the analysis of the final properties is reported. These electrically conductive epoxy foams possess high applicability in the aeronautical and automotive sectors.

Chapter VIII draws the general conclusions and suggestions for continuation of this research.

Finally, the *annex* briefly explains the principles and fundaments of low field NMR techniques to characterize polymer networks.

Chapter I. INTRODUCTION TO EPOXY RESIN SYSTEMS

There exist a vast number of epoxy systems varying from the type of epoxy monomer or hardener, the use of a catalysts or co-monomers, the curing technique employed (thermal, ultra violet (UV), electron beam or thermoplastic curing), use of a second phase like block copolymers (BC), rubbers, fibers (Kevlar, glass and carbon fibers), nanoparticles: carbon nanotubes (CNTs), clays, graphene, polyhedral oligomeric silsesquioxanes (POSS), silica nanoparticles, the use of foaming agents or even the origin of the epoxy monomer as in the case of the epoxy formulations from renewable resources. All these systems lead to a great variety of properties like self-healing polymers, recyclable epoxy resins, low or high glass transitions temperatures (T_g), high adhesion, high chemical resistance, enhanced toughness, high thermal o electrical conductivity or light weight structural materials, among others.

It would be impossible to give a brief description of each one in only one chapter, thus we will introduce only the epoxy systems employed during the realization of this thesis. The systems studied comprise the thermal curing with aliphatic amines, ultraviolet curing, epoxy resins nanostructured by block copolymers and rigid epoxy foams.

I 1. THERMAL CURING OF EPOXY RESINS

This is the most common technique to cure epoxy resins. In order to form the polymer network it is necessary to add a hardener into the formulation, in certain cases a catalyst is also desired to initiate the curing reaction. In principle, any molecule containing reactive hydrogens may react with the epoxide groups of the resin. Common classes of hardeners for epoxy resins include amines, acids, acid anhydrides, phenols, alcohols and thiols, but amines and acids are the most employed ones.[1, 2]

In the case of using catalyst, the epoxy monomer can be reacted with itself without the presence of any hardener. Anionic catalysts (Lewis bases such as tertiary amines or imidazoles) or cationic catalysts (Lewis acids such as a boron trifluoride complex) can produce this homopolymerization. The resulting network contains only ether bridges, and exhibits high thermal and chemical resistance, but it is brittle and often requires elevated temperature of curing. An example of the mechanism using

tertiary amines is depicted in Figure I.1. Cationic catalysts are often used in the UV curing processes and will be discussed in more detail in the next section.

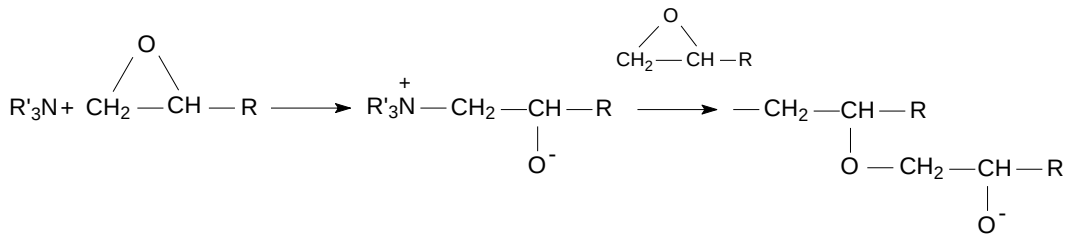

Figure I.1: Curing reaction with tertiary amines as catalysts.

Primary amines are the most employed class of epoxy hardeners. These amines undergo an addition reaction with the epoxide group to form a hydroxyl group and a secondary amine. The secondary amine can further react with an epoxy group to form a tertiary amine and an additional hydroxyl group as described in the scheme of the Figure I.2. In particular, the scheme represents the reaction between an epoxy resin and diethylenetriamine (DETA), which is the hardener used in this thesis. The group noted as *R* in the scheme usually contains more epoxy groups leading to additional crosslinking points. There is a wide variety of amines which determine the curing conditions and the final properties and applications of the material. Hence, it is possible to tailor the curing temperature ranging from 25 °C to 180 °C for example. The reactivity of aliphatic amines is higher than cycloaliphatic amines and aromatic amines in this order. These reactions are catalyzed by acids such as Lewis acids, phenols, and alcohols. Therefore, the hydroxyl groups generated by the amine epoxide addition are active catalysts, so that the curing reaction usually shows an accelerating rate in its early stages, typical of auto catalysis.

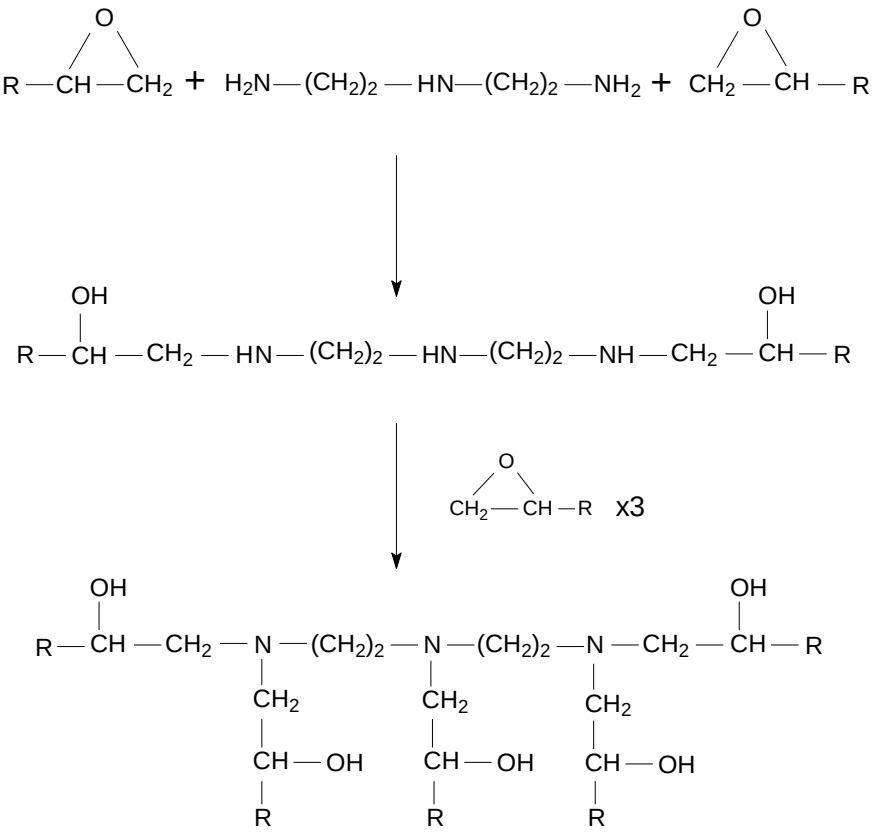

Figure I.2: Curing reaction with primary amines (DETA).

In comparison with amines, hardeners based on acid agents are less exothermic and produce networks with good physical, chemical and electrical properties but their chemical resistance is lower. The reaction mechanism is very complex but a simplified scheme is shown in Figure I.3.[3]

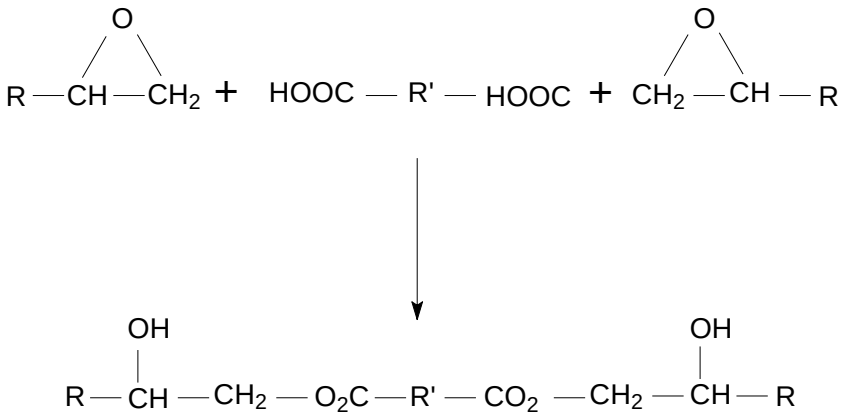

Figure I.3: Curing reaction with acid agents.

There have been many studies to analyze the cure reactions of epoxy resins and a variety of kinetic models have been used to relate the rate of the chemical reactions to the time, temperature, and extent of cure. In general, the kinetic models fall into two main categories: phenomenological and mechanistic models.

Phenomenological models are expressed in a relatively simple rate equation, and are developed ignoring the details of how reactive species take part in the reaction. On the other hand, mechanistic models are obtained from balances of reactive species involved in the reaction. In spite of a better prediction and interpretation offered by mechanistic models, in many cases it is not possible to derive such models due to the complexity of cure reactions. In addition, mechanistic models generally require more kinetic parameters than phenomenological models do.[4] So in most cases, phenomenological models are preferred in studying curing processes.

The simplest model to represent the curing kinetics of the autocatalytic reaction of epoxy resins is express by an nth order rate equation.

$$\frac{d\alpha}{dt} = k(1-\alpha)^n \qquad \text{Equation I.1}$$

Where *n* represents the reaction exponent and *k* is the rate constant obeying an Arrhenius temperature dependence. For the majority of curing systems, the efficiency of this model has been postulated by some workers.[5-8] Reactions obeying the nth order kinetics will exhibit a maximum reaction rate at time t=0, while an autocatalyzed reaction exhibits a maximum reaction rate at 30–40 % of the reaction and the formation of intermediate species which initiate and accelerate the reaction.[9-13] For these reasons, modifications of the nth order model have been proposed to represent more accurately the curing reaction of epoxy resins. These extended models introduce several reaction exponents and rate constants making the study more complex. One of the most common one is the model postulated by Kamal *et al.*[14, 15]

$$\frac{d\alpha}{dt} = (k_1 + k_2\alpha^m)(1-\alpha)^n \qquad \text{Equation I.2}$$

Where k_1 and k_2 are rate constants with Arrhenius temperature dependence and *m* and *n* are constants independent of temperature.

The result of the thermal curing process is a highly cross-linked material with very extensive applications including protective and decorative coatings, adhesives (Figure I.4a), paints, caulking compounds and matrices for composite materials (carbon and glass fiber composites) as shown in Figure I.4b.

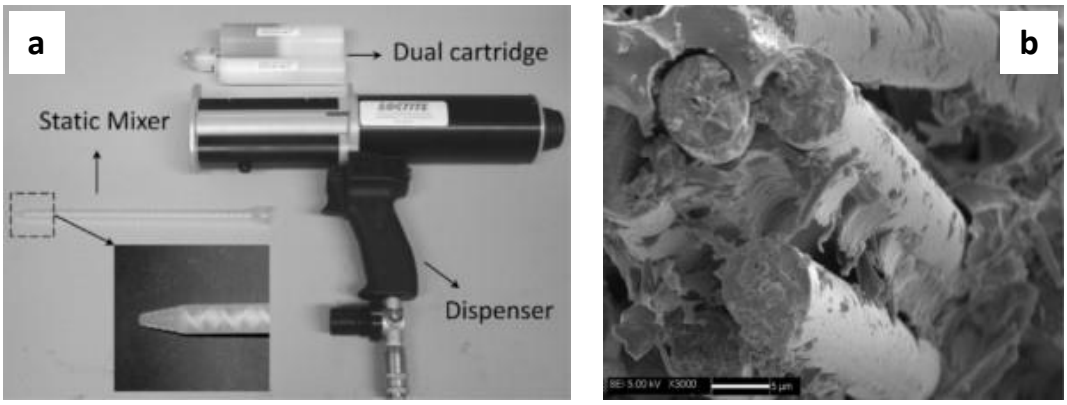

Figure I.4: Applications of thermally cured epoxy resins, a) dual-cartridge dispenser for adhesives and b) carbon fiber composite. Reprinted from.[16, 17] *Copyright (2011 and 2014) with permission from Elsevier.*

I 2. UV CURING EPOXY RESINS

The UV curing process, also known as photopolymerization, is a technique by which a photoinitiator is activated by UV light and initiates the cross-linking reaction of a monomer, in our case an epoxy monomer (Figure I.5). In some cases, the absorbed light can be in the visible region of the light spectrum.

Figure I.5: Scheme of the UV induced photopolymerization.

Photopolymerization techniques possess many advantages compared with the classical thermal curing. First of all, photocuring can be considered an environmentally friendly technique because of the absence of solvents and the low temperatures required. In addition, UV curing is very fast reaching high curing rates in only a few minutes with low energy consumption and low cost. It also allows the possibility of a selective curing using masks. Finally, a wide variety of monomers and/or oligomers are suitable for photopolymerization, allowing good adhesion to all kinds of substrates.[18]

In general, a photopolymerizable formulation contains the following three components:[19]

- The photoinitiator: it is the specie responsible for the light absorbance.
- A reactive diluent: it is not always employed but when used, it adjusts the viscosity of the system. Usually, it is also involved in the polymerization mechanism.
- The monomer or oligomer: it is generally a multifunctional molecule that gives rise to a cross-linking polymerization. The backbone of the monomer will confer the final properties of the material.

While the monomer plays a predominant role on the physical and chemical properties of the cured material, the photoinitiator rules on the curing rate. The molecular absorption coefficient of the photoinitiator determines the amount of light absorbed, i.e. energy utilized in the reaction. If the efficiency of the photoinitiator is high, its concentration could be reduced in the formulation decreasing the price of the formulation and improving the optical properties (yellowing after curing) at the same time.[20]

Depending on the reaction mechanism, we can identify two main types of processes: the first class is the free radical polymerization typical of acrylates, methacrylates and unsaturated polyester resins. The photopolymerization of these monomers is initiated, carried and finished by radicals. The whole process can be summarized into four steps (Figure I.6): photoinitiation (creation of radicals), propagation (addition of monomers), chain transfer and termination (recombination of radicals).

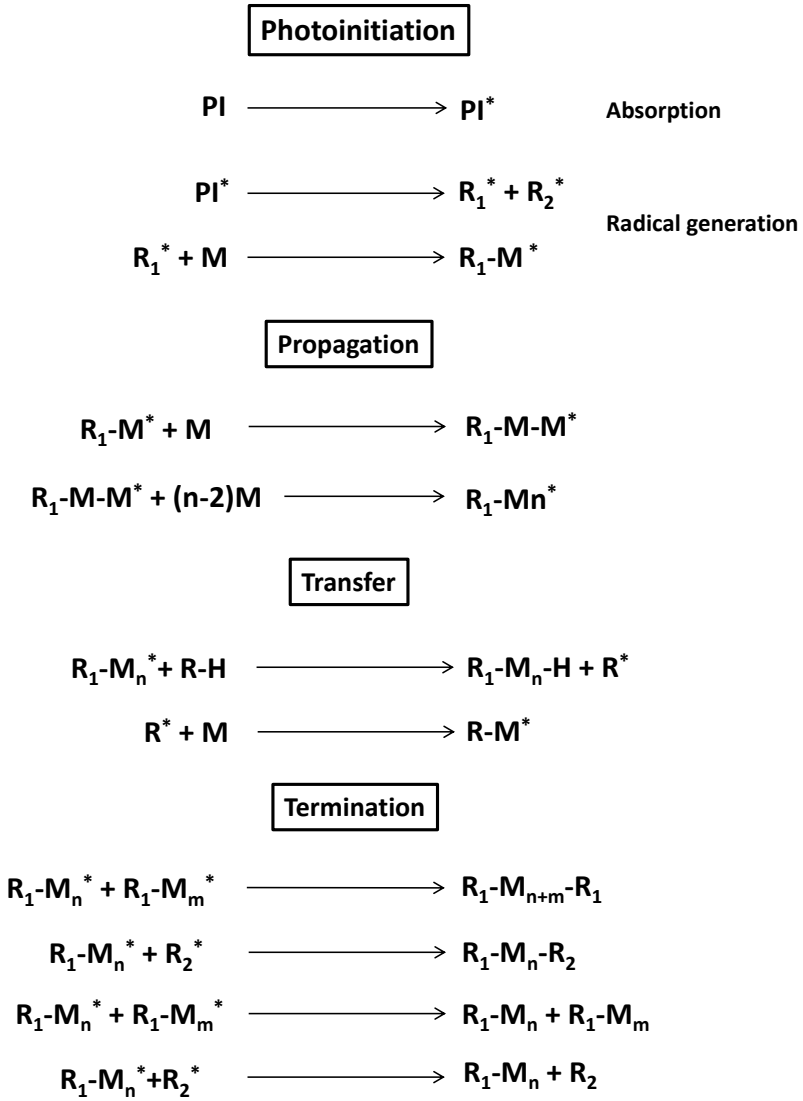

Figure I.6: Photoinitiated free radical polymerization mechanism (PI stands for photoinitiator, R for radical and M for monomer).

The second group of photopolymerization process is the cationic polymerization. Monomers like epoxy resins, vinylethers and propenylethers are suitable to be cross-linked through this process. As epoxy resins undergo cationic photopolymerization, photoinitiators, mechanisms and other features of this technique will be explained in detail in the next lines.

Onium salts represent the most widely used class of cationic photoinitiators. Their thermal stability and inactivity towards polymerizable monomers in absence of UV light makes these salts very attractive for practical application in photocurable formulations. Onium salts are formed by a cationic moiety and an anion. The cationic part is the light-absorbing component of the molecule. For this reason, the structure of the cation controls the UV absorption characteristics, the photosensitivity, whether the compound can be photosensitized or not and the ultimate thermal stability of the salt. However, the nature of the anion and its stability determine the strength of the acid formed during photolysis and its corresponding initiation efficiency, the kinetics of the polymerization and the termination of the reaction.[21]

Figure I.7 represents the chemical structure of an onium salt, in this case triarylsulfonium with a metal anion.

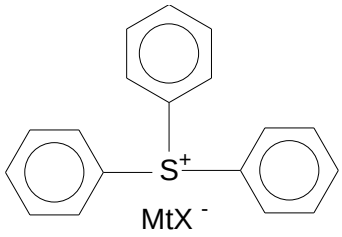

Figure I.7: Structure of an onium salt.

UV irradiation causes the excitation of the onium salt to an excited singlet state that leads to homolytic or heterolytic cleavages. The resulting species are highly reactive and further interact with solvents, monomers, or impurities to give protonic acids, which actually are the initiators of cationic polymerization. The strength and reactivity of the formed acid depends on the anion of the salt. The order of reactivity of the most common initiators is SbF_6>AsF_6>PF_6>BF_4. Epoxy monomers in the presence

of a photogenerated protonic acid leads to a ring-opening polymerization by the oxonium ion. If difunctional epoxides are used as monomers, the cross-linking readily occurs to generate a tridimensional polymer network. By contrast to radical initiated polymerization, the chain carrier species do not interact, so the living polymerization will continue even after the UV exposure and thus leads to a beneficial post-curing effect that can be further enhanced by a thermal treatment, this process is called *dark polymerization*. Termination occurs either by chain transfers, to give inactive species, or by reaction of the propagating species with nucleophilic impurities, in particular traces of water.[22] The cationic polymerization mechanism is depicted in Figure I.8.

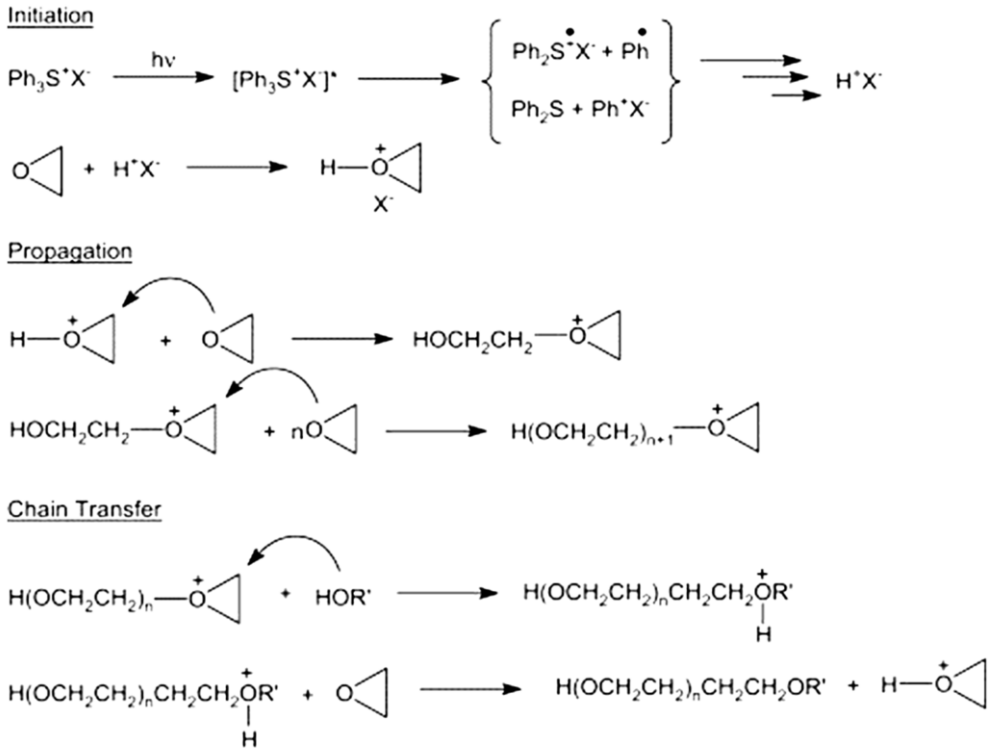

Figure I.8: Cationic photopolymerization mechanism via UV light.

If compared with the free radical photopolymerization, the cationic photopolymerization has several advantages. From an experimental point of view, one of the main differences and advantages of the cationic polymerization is the absence of air inhibition, fact that eliminates the need of inert atmosphere during curing. Cationic

polymerization, once initiated, may continue to proceed after the light source has been removed (*dark polymerization*). Furthermore, the cationic photopolymerizable systems are characterized by absence of toxicity or irritation properties being a good alternative to acrylates and methacrylates formulations usually employed in radical processes. Finally, the cured materials present lower shrinkage than acrylic and methacrylic resins leading to lower residual stress in the material which induces better adhesion properties on many different substrates.

The UV curing technology has found its major openings in sectors where its distinct advantages (fast curing, solvent-free formulation, selective curing, low curing temperature and energy consumption) have allowed it to replace other processing techniques. Applications of photocured resins are comprised in the next fields (see Figure I.9):

- Graphic arts: UV curing is used in the printing industry through UV curable inks with low residual odors, over-printed varnishes that further improve the surface properties of the printed material, in particular its gloss, smoothness, abrasion and scratch resistance, as well as its weathering resistance.
- Coatings: a thin layer of a UV cured polymer is widely used to protect or decorate the substrate (wood, plastic, metal optical fibers, paper…). Depending on the monomer, additives and thickness of the layer, the coating can also contribute with new functionalities to the final material.
- Adhesives: to bond together two pieces of an assembly, acting as a quick-setting glue. An important limitation to the use of UV curable adhesives for bonding an assembly is that one of the two parts must be transparent to UV radiation.
- Electronics: UV curable systems have found several applications in microelectronics where they serve not only as photoresist in the imaging step, but also as fast drying adhesives and protective coating of circuits.
- Dentistry: in this case, the formulations are usually cured with visible light and the resin is loaded with ceramic fillers to produce cements with high mechanical resistance.

Figure I.9: Applications of the UV curing in graphic arts, protective coatings, microelectronics and dentistry sectors.

I 3. NANOSTRUCTURATION BY BLOCK COPOLYMERS

It is well known that epoxy resins possess a wide set of interesting properties, starting from their good mechanical performance, chemical resistance to their optical properties just to mention some of them. But their highly cross-linked structure confers them very low toughness, this property is probably their greatest limitation for many applications. Therefore, important efforts have been made to overcome the brittleness of epoxy resins. One of the most successful routes is to incorporate soft polymer modifiers like elastomers,[23, 24] thermoplastics,[25] hyperbranched polymers[26] or rigid fillers.[27] In all cases, the finer and smaller the morphology of the second phase, the greater the enhancement in the toughness of brittle polymers is.[28, 29]

In this context, the use of nanostructured systems seems to be one of the most appropriate strategies to modify the final properties of thermosetting polymers. For this reason, nanostructures generated by the addition of amphiphilic block copolymers (BC) to the epoxy formulation have attracted great attention among researchers.[30] An amphiphilic BC is a class of polymer which consists of two or more chemically distinct subchains that are covalently bounded and at least one of them is miscible with the epoxy resin and another one is immiscible. Owing to the thermodynamic immiscibility

of the constituent subchains, BCs in the bulk are often microphase separated at the length scale of the polymer chains (typically tens of nanometers). Macroscopic phase separation is suppressed by the confinement of the covalent bonds between the subchains of the BC.[31] In the simplest case of a BC comprised of A and B blocks (i.e. A–B diblock copolymer), the temperature dependent Flory–Huggins parameter ($\chi_{A\text{-}B}$) describes the segmental interaction of the A and B subchains and governs the self-assembled microphase separation.[32] The final nanostructure achieved depends on the degree of curing and the relative fractions of each component of the BC.[33] The most common geometries are: body centered cubic spheres, hexagonally packed cylinders, bicontinuous gyroid, and lamellae. Therefore, it is possible to create phase diagrams for each BC in function of the concentration of the BC. The phase diagram of poly(ethylene oxide)–poly(ethylene-alt-propylene) (PEO-PEP) can be observed in Figure I.10 as an example.[34]

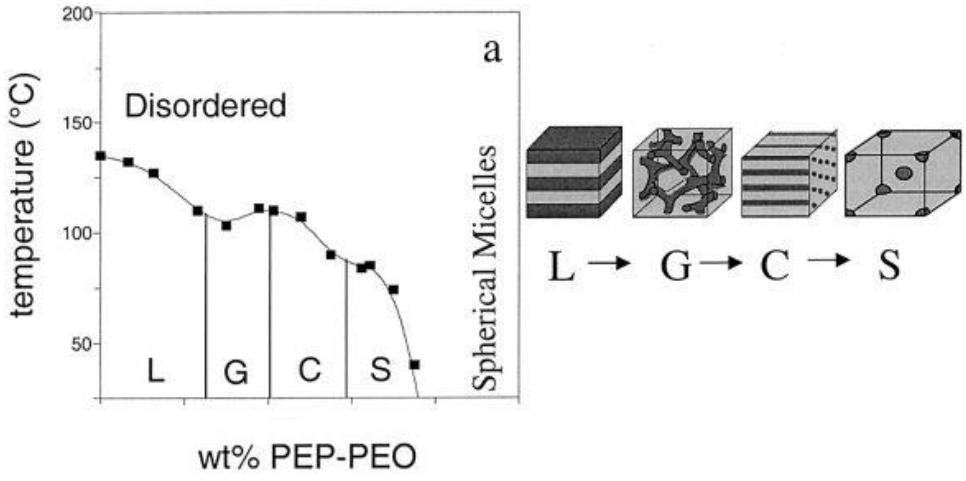

Figure I.10: PEO-PEP phase diagram in an epoxy matrix. Figure adapted from.[34] Copyright (2001) with permission from John Wiley & Sons, Inc.

Depending on the miscibility of the BC before and after curing, two different mechanisms have been postulated to explain the formation of nanostructures in thermosetting polymers by adding BC. The first approach is called *"self-assembly"* and is based on the amphiphilic character of the BC in the epoxy resin before curing.

Therefore, the epoxy monomer acts as a selective solvent of the BC and self-organized nanostructures are formed in the blend before curing. Then, the preformed nanostructuration is fixed by initiating the polymerization of the epoxy resin.[35, 36] An example of a self-assembled nanostructure of a poly(ethylethylene-b-ethylene oxide) (PEE-PEO) diblock in an epoxy matrix can be observed in Figure I.11.

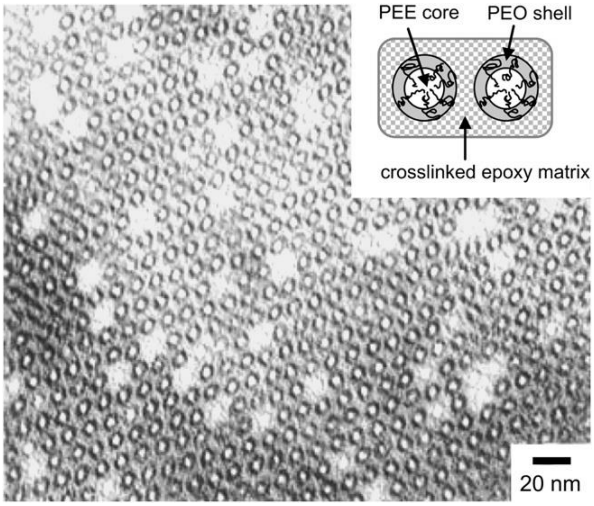

Figure I.11: TEM image of a self-assembled nanostructure of PEE-PEO in a cured epoxy resin. Reprinted with permission from.[35] Copyright (1997) American Chemical Society.

However, the self-organization of the BC in the un-cured epoxy precursors is not always possible. In many situations all the blocks of the BC are miscible in the monomers. In addition, the formation of the required self-organized nanostructure in the monomer at low temperature does not guarantee its existence at the high temperatures likely needed for the curing. Polymer blends often exhibit an upper critical soluble temperature (UCST) behavior.[37] In this context, self-assembly of BC is not possible but nanostructures are still found. The "*reaction induced microphase separation"* (RIMS) mechanism proposes that when a mixture of a BC and epoxy precursors with UCST behavior is heated for curing above its UCST point, the polymerization starts as in an homogeneous system. As the reaction continues, the block with less solubility starts to nucleate forming a microphase separated domains surrounded by an interphase of epoxy

resin rich in the other block of the BC.[38-43] An example of a nanostructured epoxy resin with polystyrene-block-poly(ε-caprolactone)-block-poly(n-butyl acrylate) (PS-b-PCL-b-PBA) is shown in Figure I.12.

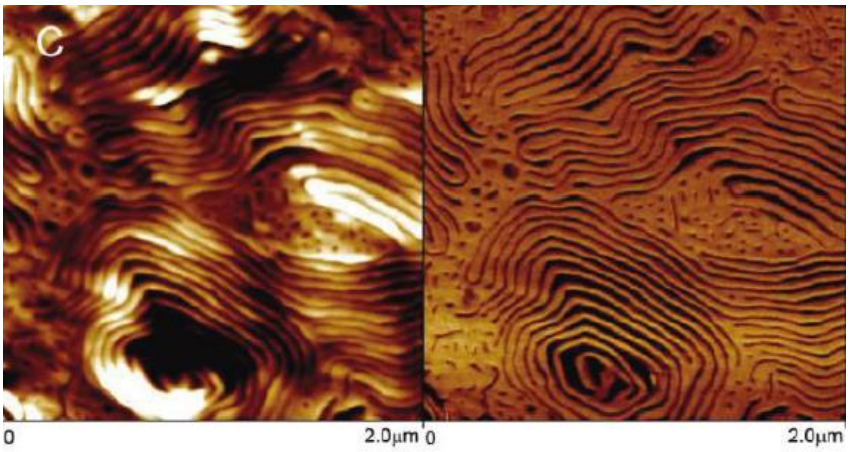

Figure I.12: AFM image of a nanostructure produced by RIMS of a 30 wt. % of PS-b-PCL-b-PBA in an epoxy matrix. Reprinted with permission from.[43] Copyright (2010) American Chemical Society.

Nanostructuration has been proved to be a successful route to enhance the toughness of epoxy resins. The morphology of the nanostructure developed by the BC has a major role on the enhancement of the toughness. For example, the vesicular morphology of PEO-PEP was found to increase the critical stress intensity factor (K_{IC}) by 45 % even at half the block copolymer concentration of the micelle forming systems.[34] The authors suggested that the resin inside the vesicle acts as another separated microparticle in a similar way to phase separated modifiers. In addition, vesicles and other geometries can be attached to the epoxy matrix through reactive BCs to further improve the toughness.[44] From the point of view of interactions between the matrix and the soft microphase/nanoparticle, where there is an interface, a propagating crack must extract the microphase/nanoparticle from the surrounding matrix to continue its path. Such pull-out or extraction from the matrix is associated with friction and energy dissipation which translates into substantial toughness.[45]

Finally, it is worth mentioning that the formation of self-assembled nanostructures is considered as a *bottom-up* strategy to modify the properties of polymers. Nanostructuration allows us to design materials from their core, handling the material at the nanoscale to obtain improvements at the macroscopic level. *Bottom-up* approaches are intended to play a key role in nanotechnology in the near future.

I 4. EPOXY RESIN FOAMS

Epoxy foams are low density materials especially attractive for their high specific properties (property divided by the density) which make them suitable for applications including shock, thermal, and vibration isolation of electronic components and the production of lightweight materials for the transportation industry.[31]

Inert or reactive blowing agents must be added to the epoxy resin formulation to provide the gas required for the blowing process. Compared to conventional polyurethane foams, epoxy foams are generally rigid and are used when greater thermal stability, solvent resistance, adhesion or a more controlled cellular structure is required. Additionally, isocyanate health problems are avoided. Moreover, a wide variety of monomers, hardeners and blowing agents are available to tailor the final properties to the product performance.[46] However, cellular foams made of epoxy resin are produced in a much lower volume than polyurethane foams and have remained for special products due to their higher cost.

There are two main types of epoxy foams, the syntactic and the cellular foams:

Syntactic foams are produced by mixing hollow microspheres (glass, plastic or carbon microspheres) to reduce the density,[47, 48] giving a close-cell structure as it is shown in Figure I.13. Many authors do not include the process of fabricating syntactic foams as a pure foaming or blowing process due to the fact that they are a simple mixture of two materials with different densities, the hollow microballoons and the epoxy binder.

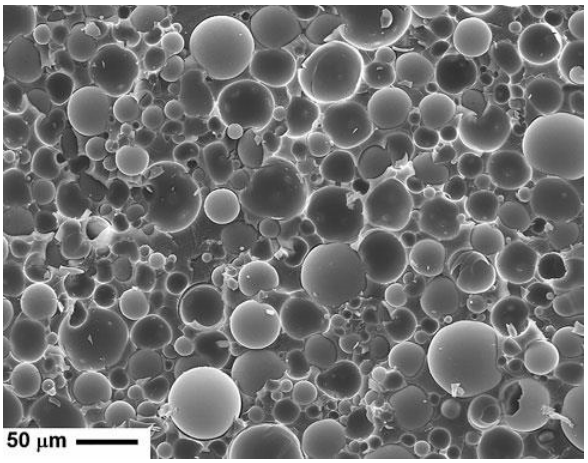

Figure I.13: SEM image of a syntactic epoxy foam with a 60 vol. % of glass microballoons. Reprinted from[49] with kind permission from Springer Science and Business Media.

Cellular or blown epoxy foams present either open or closed cells which have been generated by a specific blowing agent. It is essential to match the kinetics of the blowing process with the curing kinetics to avoid a premature curing or a collapse of the cells. Besides, the uniformity and stability of the cellular structure are strongly dependent on the rheology of the resin; i.e. very low viscosities let the blowing agent scape without forming an effective cellular structure. Inert and reactive blowing agents can be used to prepare epoxy foams:

- Inert gas: like nitrogen, carbon dioxide or air are pumped into un-cured formulations at high pressure. This technique is generally used in automated processes for the fabrication of sheets and molded pieces.[50]
- Inert liquid: similar to the previous technology but using low-boiling liquids (ethers, ketones, hydrocarbons).
- Reactive agents: reactive substances are added into the epoxy formulation to initiate a chemical reaction which generates gaseous products. Acid anhydrides,[51] azodicarbamides, sodium borohydride[52] and p-toluenesulfohydrazide[53] are some examples of reactive blowing agents.
- Expanding syntactic fillers: unlike traditional hard syntactic filler, the expandable microspheres are made of a thermoplastic shell which encloses a gas or low-boiling point liquid. When heated, the polymeric shell gradually

softens, and the liquid hydrocarbon begins to gasify and expand, when the heat is removed, the shell stiffens and the microsphere remains in its expanded form as in Figure I.14. These microspheres are commonly known by their trade name, *Expancel*.

- Emulsions: frothed epoxy emulsions can be used to make epoxy foams in a very simple process just mixing vigorously the formulation. The open-cell structure obtained depends on the ingredients of the formulation.[54]

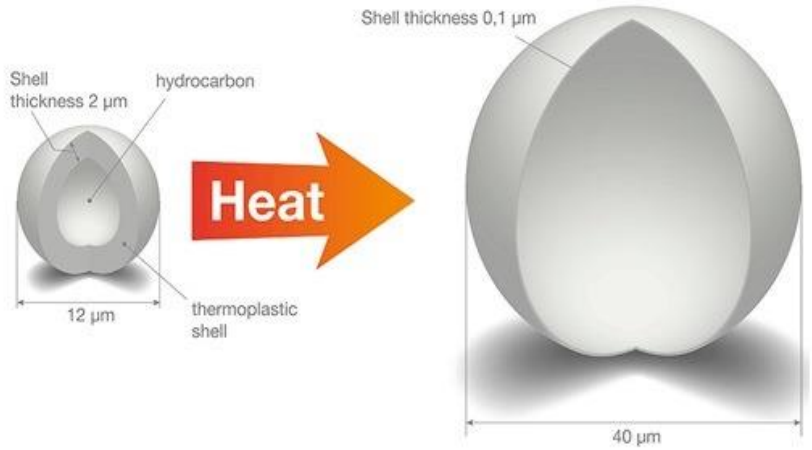

Figure I.14: Expancel microspheres.

Finally, a less common type of epoxy foam, namely "solid-state foaming"[55-57] in which no blowing agents or low density fillers are employed, should also be mentioned. In this case the epoxy foam is fabricated by pressing an epoxy powder to form a porous tablet. This tablet is then heated at high temperature. Foaming occurs because of the temperature is set above the boiling point of the uncured resin. During boiling, the resin polymerizes and freezes the bubbles in the final structure.

The applications of epoxy foams are usually related to the weight reduction of structural materials and to their insulating properties (Figure I.15). One of their initial applications was in marine structures due to their naturally buoyant behavior coupled with their low moisture absorption and high compressive strength. Remotely operated vehicles and submarines incorporate structures made of epoxy foams as well as in flotation modules.[49] The transport sector has also been beneficiary of the high rigidity and vibration damping of the epoxy foams. In the automotive field; bumpers, doors and

hollow pillars are filled with epoxy foams. Aircrafts also use these lightweight materials for thermal insulation.[49] The dielectric performance of epoxy foams also makes them attractive in electronics encapsulation due to their high volume resistivity.[46] Finally, less technological applications like sports equipment (surfboards and skies[58]) and furniture use epoxy foams among their components.[59]

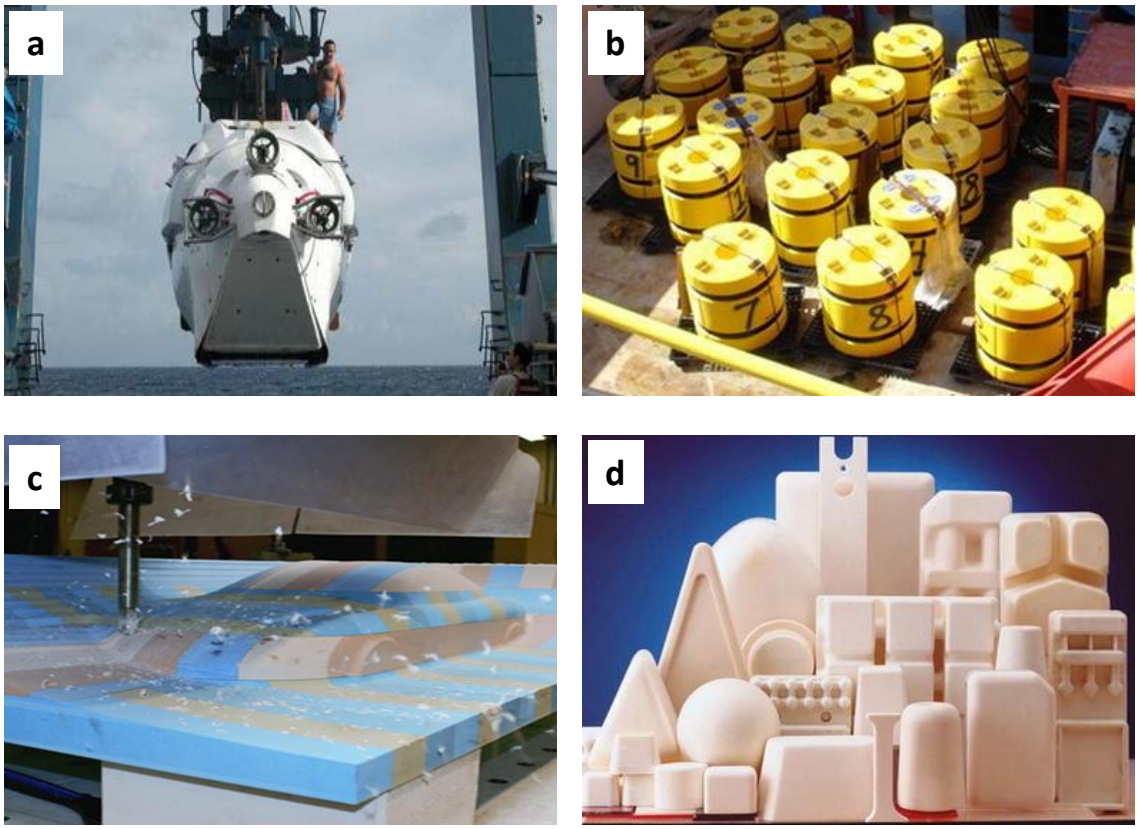

Figure I.15: Marine applications of epoxy foams a) human-operated vehicle and b) flotation modules, c) epoxy panel and d) plug assists. Reprinted and adapted from[49] with kind permission from Springer Science and Business Media.

Chapter II. EPOXY NANOCOMPOSITES: STATE OF THE ART

Epoxy nanocomposites can be defined as a composite material in which the matrix is an epoxy resin and the second phase and/or filler has one, two or three dimensions of less than 100 nm. There are many systems that can be considered as nanocomposites like the nanostructured or nanoporous epoxies[60] but the most common approach is to modify the epoxy matrix with nanofillers. Indeed, it is common to associate the word "nanocomposite" to the concept of "nanofilled" polymers.

The nanofillers employed in the fabrication of nanocomposites usually possess structural properties like high specific surface area (SSA) and long aspect ratio. In addition, they also have exceptional intrinsic mechanical, electrical, thermal, optical, electrochemical and catalytic properties. The combination of the structural and intrinsic properties of nanofillers is used to modify the properties of epoxy systems or to introduce new functionalities; for example, the addition of conductive nanofillers reduces the resistivity of an epoxy matrix rendering it conductive and broadening its applications.

Depending on the application and/or the property desired to enhance, many different nanoparticles can be used as fillers of epoxy resins. The most common ones are: titania, silica, carbon nanotubes (CNTs), carbon nanofibers (CNFs), graphene, fullerenes, nanoclays, cellulose nanowhiskers and magnetite. When it comes to developing epoxy nanocomposites, the selection of the most appropriate type of nanoparticle, the dispersing tool and protocol employed to disperse the particles, their effect on the processing of the resin and on the curing reaction are key aspects to obtain an effective enhancement of the final properties.

This section of the thesis tries to summarize the state of the art of all the steps necessaries to produce nanocomposites with carbon nanoparticles (CNPs), as well as the final properties of epoxy nanocomposites. Among all the allotropes and possible forms of carbon we will focus on carbon nanotubes (CNTs), carbon nanofibers (CNFs), expanded graphite (EG), carbon black (CB), fullerenes and graphenes.

II 1. DISPERSING METHODS

The biggest challenge in order to gain the desired nanocomposite properties is to disperse the nanoparticles as individual particles in the epoxy matrix. So far, commercially available particle powders and in-house synthetized nanoparticles include agglomerates where the nanoparticles stick strongly together due to adhesive forces. Furthermore, adhesives forces increase with increasing SSA and decreasing particle size. It has been proved that a poor dispersion of CNTs not only dramatically reduces their reinforcing efficiency, caused by the CNTs slipping by each other when forces are applied, but also results in the formation of micro-voids in the nanocomposites.[61] Therefore, the way to disperse nanofillers into separated individual particles is considered the most important stage in nanocomposite processing. Ultrasonication and high shear mixing are the two main methods to disperse nanoparticles in epoxy resin.

Ultrasonication techniques, both bath and tip sonication, are able to combine the breakage of particle agglomerates with an effective mixing of the epoxy formulation at a molecular level. Ultrasonication can be applied straight to the nanoparticle/epoxy mixture[62-64] but the common practice is the use of solvents to decrease the viscosity of the system.[65-70] In some cases, the use of surfactants and solvents has also disentangled effectively CNTs agglomerates.[71, 72] However, high intensity and long duration ultrasonication treatments can lead to localized damage and shortening of the CNPs.[73] Besides, the removal of solvents becomes a key step in the processing of nanocomposites because any trace of solvent in the final material will considerably affect its properties. On the other hand, the volume dispersion of the nanoparticles in the matrix is very low due to the decrease of vibrational energy with increasing distance from the tip. For these reasons, sonication has also been used together with mechanical stirring or other high shear forces methods.[74-76]

Mechanical dispersion of CNPs in epoxies is also widely employed. High speed rotation tools like ultraturrax, toroidal mixers and mechanical stirrers use high shear forces to break the agglomerates and disperse the individual CNPs. A scheme of a rotating disc and the flow generated in the resin is depicted in Figure II.1.

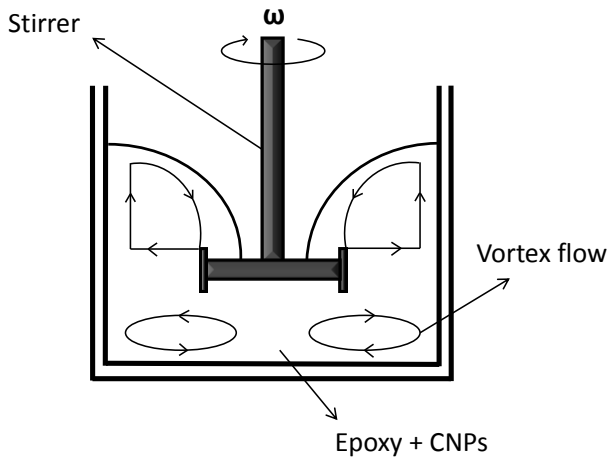

Figure II.1: Rotating stirrer for the manufacturing of nanocomposites.

Finally, three-roll calendering has gained popularity among the approaches to disperse nanoparticles in epoxies over the years. The configuration of three adjacent rolls rotating at different angular velocities combined with small gaps between the rolls results in high shear forces at the gaps.[77] The equipment let the user adjust the angular velocity, the gaps and the temperature of the rolls to optimize the shear intensity. One advantage of this technique compared to other mechanical dispersers is the fact that all the volume of the mixture must pass through the gaps between rolls, thus the shear is applied uniformly to all the mixture without dead zones. In addition, calendering represents a significant advance towards the development of solvent free and scalable manufacturing processes. A schematic configuration of the calendering is shown in Figure II.2. Gojny *et al.*[78] published the first paper where calendering was applied to CNP, in this case amine functionalized nanotubes. Since this work, many other authors have used the three roll technique to disperse CNTs,[77, 79-83] EG,[75] CNFs,[84, 85] CB[86] and graphene sheets.[87-89]

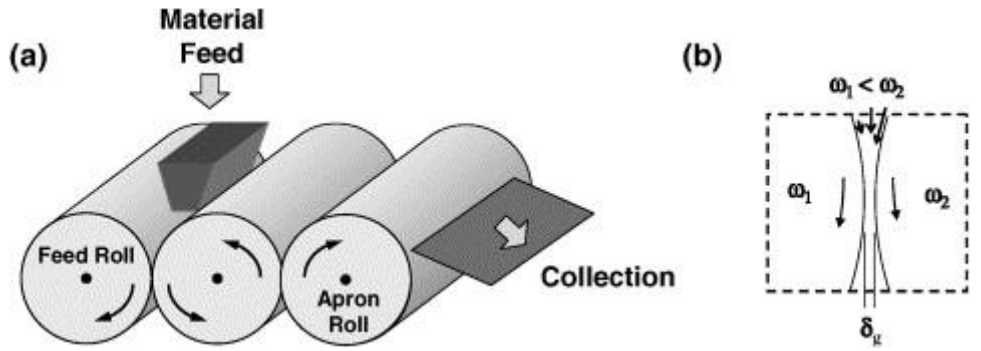

Figure II.2: a) Schema of the three roll calendering, b) high shear zone between rolls. Reprinted with permission from.[77] Copyright (2006) from Elsevier.

Prolongo *et al.*[90] compared a high shear mixing method with the three roll calendering technique and the combination of both in a mixture of graphene nanoplatelets and an epoxy monomer. The authors concluded that the high shear forces originated by high speed rotating tools reduced the lateral size of the graphene platelets, while calendering preserved the geometry and increased the exfoliation of the filler. Nanocomposites obtained by calendering presented better dispersion and final properties. Meanwhile, the combination of both techniques did not give any advantages to the calendering by itself.

Depending on the type of CNP and their agglomeration state, the methods explained above may not be sufficient to guarantee an optimum dispersion state of the filler within the matrix. Thus, surface treatment of CNPs is still essential, especially for structural applications where mechanical properties are more relevant. Covalent functionalization of the nanofiller surface not only improves the dispersibility but also enhances the adhesion of the filler to the epoxy matrix. To maximize the interactions, functionalizations are designed to act as cross-linkers of the epoxy resin. For example, amine, fluorinated and/or oxidized CNTs and graphenes with different functionalities showed better solubility and stability of the dispersions as well as better performance.[91-97] Other possibility is to tailor the surface of the CNPs with similar groups to those presented in the matrix of the composite to improve the final properties preserving the thermosetting architecture.[98] One drawback of such functionalizations is that they degrade the length of individual CNPs.[99] An example of the functionalization process of CNTs is shown in Figure II.3

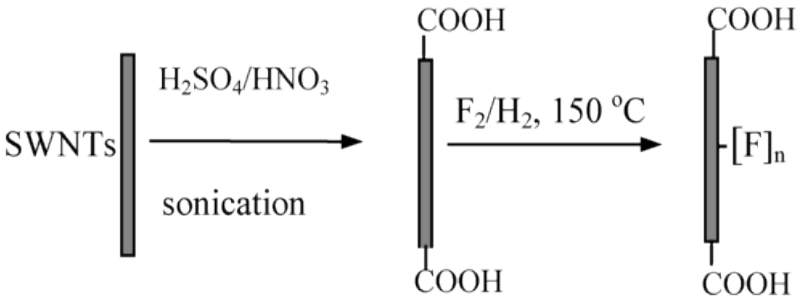

Figure II.3: Example of surface oxidation and fluorination of CNTs. Reprinted with permission from.[93] Copyright (2003) American Chemical Society.

Another strategy is the non-covalent functionalization. In this case, no further improvement of the CNP/matrix interphase is obtained and its purpose is only to enhance the dispersion of the particles and prevent their re-agglomeration. The major advantage of the non-covalent functionalization is the maintenance of the original structure of the particle. The most common non-covalent functionalization is the use of amphiphilic molecules, like surfactants. The hydrophobic subchain interacts with the CNP and the hydrophilic one with the epoxy resin and induces electrostatic repulsions between adjacent CNPs. Non-ionic surfactants improved the tensile properties of graphene/epoxy nanocomposites,[100, 101] the mechanical and fracture toughness of CNT nanocomposites[102-104] and CNFs.[105] Ionic surfactants have also been employed with success with the same purpose.[106, 107]

II 2. RHEOLOGY OF THE EPOXY/NANOPARTICLE DISPERSIONS

It is well known that the greatest enhancements on the properties of nanocomposites are reached when a network of the filler is formed within the polymer matrix. A very useful approach to study and evaluate the formation of CNP networks in epoxy resins is to evaluate the rheological properties of the dispersion. Furthermore, the rheology of the dispersions plays a key role from a processing point of view due to the big increments in the viscosity of the system when nanoparticles are added, favoring the presence of voids and hindering the transport of the blend to the mold in resin transfer molding (RTM) processes or the infusion in resin film infusion (RFI).

The network formation of nanoparticles are closely related to the rheological properties of suspensions, which can be clearly measured by viscosity tests under shear flow.[108] CNPs are usually flexible or semiflexible nanoparticles with a very high aspect ratio, thus it might be expected that above a critical concentration they would show rheological characteristics related to entangled flexible, semirigid, or rigid polymer fluids. In a shear rate sweep, epoxy resins clearly follow a Newtonian behavior where the viscosity is independent of the shear rate applied to the resin. Meanwhile, the flow behavior of CNT and CNF suspensions shows a deviation from the matrix response. At low filler loadings, a similar Newtonian behavior has been observed but with a slight rise in the viscosity. Then, at higher filler loadings, the apparent viscosity progressively increases at low shear rates. Thus, the suspension presents an evident shear-thinning behavior with increasing CNT loading, as can be seen in Figure II.4.[109-114] The increased viscosity is mainly induced by the formation of a network structure of CNPs within the polymer matrix.

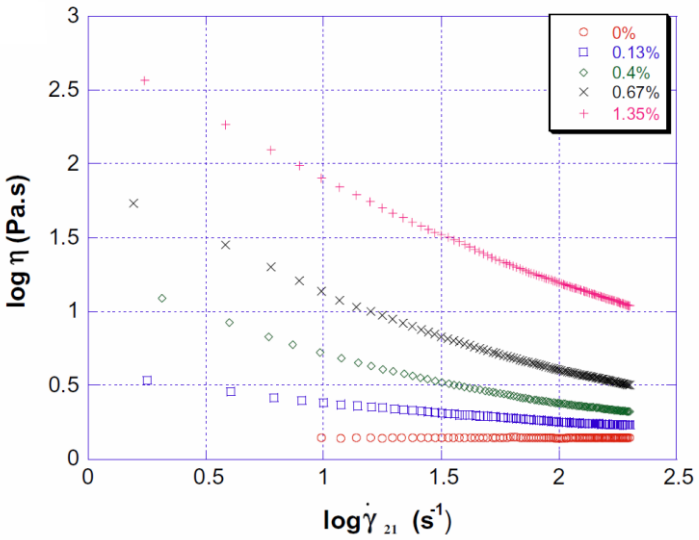

Figure II.4: Viscosity as a function of shear rate, for pristine epoxy and epoxy/CNT dispersions. Reprinted from,[112] copyright (2010) with permission from Elsevier.

The shear-thinning behavior of CNTs was found to be dependent on the synthesis method to produce the CNTs. Arc-grown nanotubes formed networks at higher concentration that chemical vapor deposited nanotubes CVD-CNTs. Arc-grown

CNTs and aligned CVD-CNTs showed lower viscosity increments than random CVD-CNTs due to different nanofiller network formation.[115] In addition, the dispersion state of the CNPs also influenced the rheological variables of the epoxy suspension. The epoxy composites filled with poorly dispersed CNTs exhibit stronger non-Newtonian behavior than the ones with well dispersed CNTs and the viscosity of the former specimen increases more rapidly with an increase in the CNT loading.[116] On the other hand, some authors confirmed that well distributed CNTs form a broader filler network that leads to a stronger shear-thinning behavior.

The effect of surface functionalization is not fully clear since some authors claim that functionalization of the particles decreases the viscosity of the dispersions. Zhu *et al.*[117, 118] observed that amine functionalization of CNFs improved the dispersion of the filler and let the CNFs orientate at high shear rates decreasing the shear thinning of the suspension. However, an opposite result was obtained by Kim *et al.*,[119] they observed higher viscosities for amine and acid treated CNTs. In this case, the authors suggested that stronger interactions between the filler and the matrix lead to stronger percolated networks and higher viscosities. Abdalla *et al.*[120] observed the same behavior for carboxylated and fluorinated CNTs (Figure II.5). Fan *et al.*[121] investigated the effect of the aspect ratio of CNTs in the resin, their results supports the hypothesis that larger aspect ratios lead to form an interconnecting network which increases the viscosity of the resin. Then, Sydlik *et al.*[122] explained that the lower viscosities obtained in functionalized CNT epoxy dispersions are due to shortening effects during the synthesis and functionalization process.

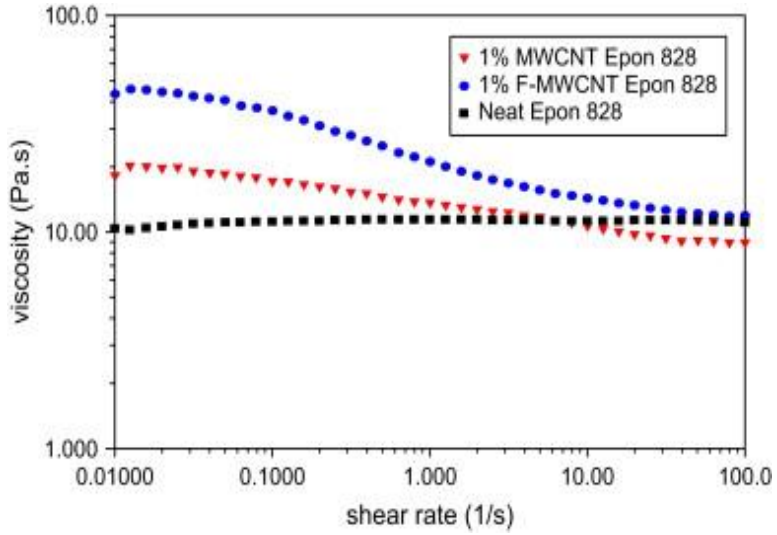

Figure II.5: Viscosity vs shear rate for the neat resin and nanocomposites with CNT and fluorinated CNT. Reprinted from,[120] copyright (2007) with permission from Elsevier.

In the case of planar and spherical geometries, as in the case of CB, EG and exfoliated graphene, the increments on the viscosity are not as high as in the case of the tube-like nanofillers. The lower shear-thinning behavior of these CNPs has been attributed to the fact that their aspect ratio is usually lower than CNTs increasing the minimum concentration to form the percolated system.[123-125]

A common procedure to analyze the rheological percolation threshold of CNP/epoxy suspensions is to plot the elastic (G') and storage (G'') moduli. Suspensions of CNPs above the percolation threshold shows a "solid-like" behavior characterized by a plateau in the G' at low shear rates where $G' > G''$ (see example in Figure II.6a for CNTs). The filler concentration in which $G' = G''$ is considered as the percolation threshold. In addition, an increase in G' is usually obtained with an increase in CNP content,[112, 116, 125] as shown in Figure II.6b for graphene/epoxy dispersions.

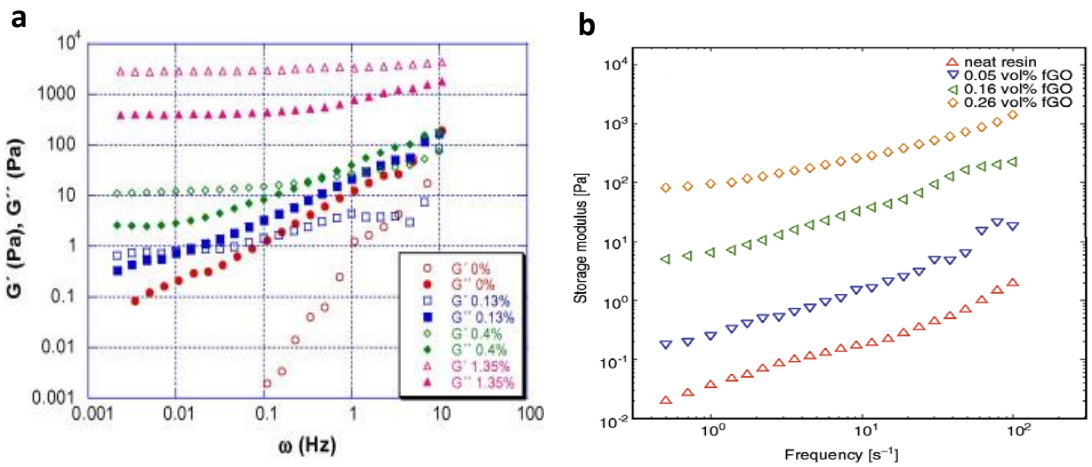

Figure II.6: a) Solid-like behavior for CNTs dispersions and b) G´ vs frequency for a graphene/epoxy dispersion. Reprinted from,[112, 125] *copyright (2010) with permission from Elsevier.*

Sumfleth *et al.* compared the *G´* and *G´´* of dispersions containing CB and CNTs. CB exhibited a four-time higher percolation threshold than CNTs, which can be explained by the spherical shape of the CB particles in contrast to the fibrous CNTs. Thus, a network throughout the suspensions was created at subsequently lower filler contents in the case of CNT suspensions.[126]

II 3. EFFECT OF THE NANOPARTICLES ON THE CURING REACTION

The study of the curing reaction is of great importance because the final properties of the material are strongly linked to the good progress of the reaction. Moreover, the control of the curing kinetics plays also a relevant role from the processing point of view. Variables like the amount of heat necessary for curing, curing conditions (temperature and time) and the gel time are important to control.

CNPs possess high thermal conductivity, functional groups, high SSA among other features. Thus, they are expected to have some effect on exothermic reactions, like the curing of epoxy resins. Calorimetry has been one of the most employed techniques for the analysis of curing reaction in epoxy resins.[127] Puglia *et al.*[62, 63] performed

isothermal and dynamic tests to epoxy resin formulations containing CNTs observing a decrease in the heat of reaction (ΔH_r) and in the exothermic peak temperature in dynamic scans and a decrease of the time in isothermal scans with the CNTs while the particles did not affect the final extent of reaction. The decrease of ΔH_r with increasing CNT content was associated to the proportional reduction of the epoxy concentration in the sample. The accelerating effect of the CNTs (see Figure II.7) was attributed to the high thermal conductivity of the CNTs and the ability of the epoxy resin to open the CNT bundles creating a higher surface for heat propagation. These results were confirmed by other authors.[128-132]

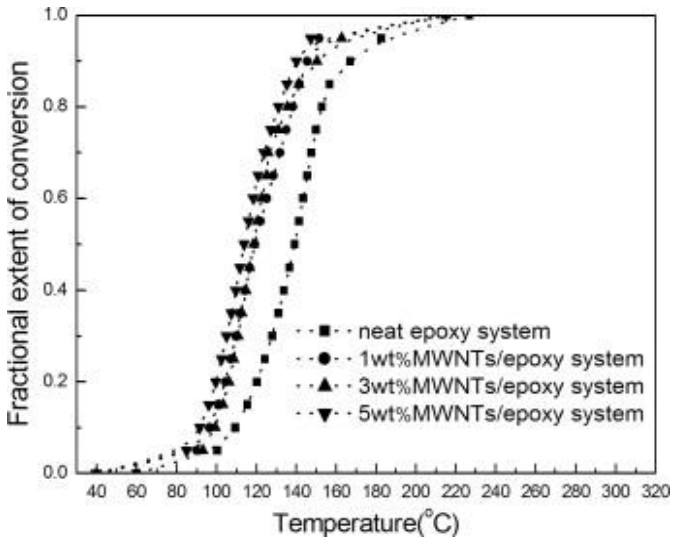

Figure II.7: Extent of reaction vs temperature at 20 °C/min of MWCNTs filled epoxy systems. Reprinted from,[128] copyright (2009) with permission from Elsevier.

Similar effects were found in epoxy resins containing milled graphite which also decreased the ΔH_r and activation energy (E_a) accelerating the reaction.[133] Baochun *et al.*[134] reported that, at low concentrations of EG, the E_a of the nanocomposite was lower than the neat epoxy resin. While at high concentrations of EG, however, the composite with EG showed a higher E_a compared with the epoxy resin. Graphite oxide also showed a similar catalytic effect to the one produced by CNTs.[135]

Also, the graphene oxide accelerated the curing reaction reducing the E_a with the graphene concentration as shown in Figure II.8. Graphene oxide decreased the onset and

peak temperatures of the exothermic peak indicating that the graphene acted as catalysts and facilitated the curing reaction. This catalytic effect increased with the graphene oxide content in the composite. However, the ΔH_r increased due to the epoxy and hydroxyl groups on the surface of the filler but the mechanism of the reaction was considered to be the same.[136]

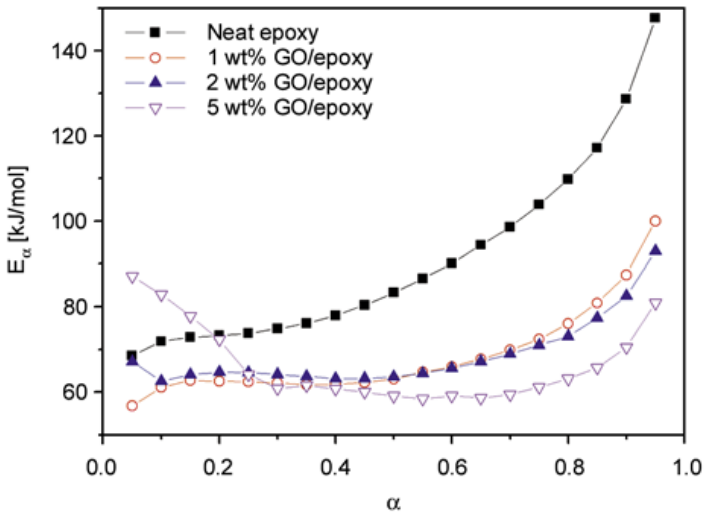

Figure II.8: Effect of graphene oxide on the activation energy as function of the extent of reaction. Reprinted from[136] with permission from IOPScience.

Low concentrations of CNFs in the bulk had only a negligible effect on the curing kinetics of the epoxy, just some improvements were found in the early stages of the reaction suggested by a decrease of the activation energy, after that point CNFs hindered the reaction.[137-139] Whilst an accelerating effect of CNFs was found in nanopapers with high contents of CNFs.[140] The lower SSA of the CNFs compared to other CNPs can be the reason for this discrepancy.[141]

Covalent modification of the CNPs might also influence the cross-linking reaction of epoxy resins. Abdalla *et al.*[142] investigated the effect of carboxyl and fluorine surface modification of CNTs on the curing behavior of epoxy resins, and reported that the E_a and rate constant were not affected by the fluorine modification whereas the resins with carboxylated CNTs exhibited an increase in the E_a and a lower rate constant for the curing reaction. They attributed the delay of the reaction to the

higher viscosity of the carboxylated CNTs dispersion which hinders the mobility of the reactive species. Zhou *et al.*[143] reported that the effect of carboxylic functionalization of CNTs did not change the autocatalytic curing reaction mechanism of epoxy nanocomposites and had catalytic effect on the curing process. In a different study, the authors analyzed the effect of a silane treatment of carboxylic functionalized CNTs obtaining a supplementary accelerating effect promoting the vitrification of the system.[144] Wang *et al.*[145] obtained similar results with carboxylated CNTs which also accelerated the reaction decreasing the onset of the exothermic peak to lower temperatures (Figure II.9). The differences between these works can be due to the different intrinsic properties of the carboxylated CNTs which depending on the functionalization process may possess different aspect ratio, degree of functionalization and crystallinity.

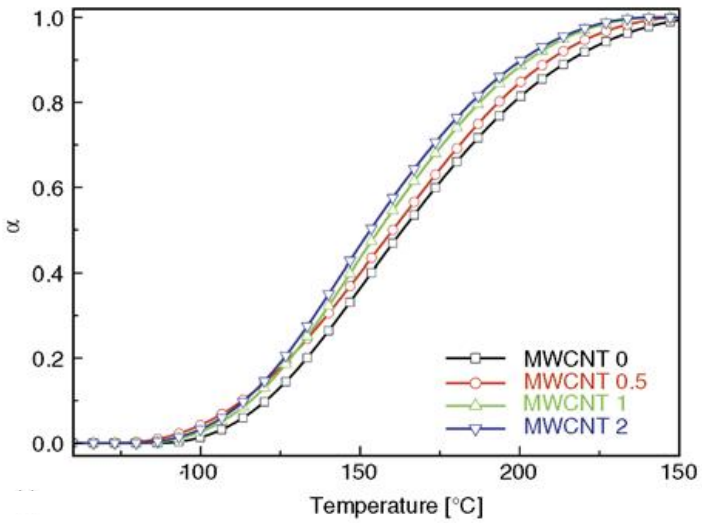

Figure II.9: Effect of carboxylic CNTs on the extent of reaction of an epoxy resin. Reprinted from.[145] Copyright (2009) John Wiley & Sons, Inc.

The presence of amine groups on the surface of CNT[146, 147] and graphene[148] also accelerated the curing reaction compared to the untreated fillers due to the reaction of the amine groups with the epoxy ring, which decreased the E_a. Covalent functionalization of CNFs also influenced the kinetics of the reaction. In particular,

silane groups attached onto CNFs modified and accelerated the curing reaction of the epoxy matrix to some extent.[138]

Chung *et al.*[141] compared the effect of CB, CNFs and chopped carbon fibers (CF) with different treatments (ozone treated fibers and activated fibers with CO_2 at high temperature) on the curing reaction of an epoxy/amine formulation. They measured the Brunauer Emmet Teller (BET) SSA of each filler by nitrogen adsorption and matched the SSA with the maximum of the exothermic heat flow (T_E). The reaction was catalyzed in all cases, but according to the data reported in Table II.1, it seems that the acceleration effect was closely related to the SSA of the filler. The higher the SSA was, the higher the temperature drop. High SSA of CNPs leads to a large interphase polymer/filler which improved the heat transfer through the material facilitating in this way a faster curing.

Table II.1: SSA and T_E of the neat epoxy resin and its composites. Reprinted from,[141] copyright (2004) with permission from Elsevier.

Material	**SSA of the filler (m^2/g)**	**T_E (°C)**
Neat epoxy resin	-	93.4 ± 0.7
10 vol. % CF	7.6 ± 0.6	85.2 ± 0.5
10 vol. % ozone CF	7.6 ± 0.6	84.5 ± 0.5
10 vol. % activated CF	90 ± 8	79.8 ± 0.4
10 vol. % CNFs	12 ± 2	82.1 ± 0.6
10 vol. % CB	254 ± 22	71.8 ± 0.3

As discussed before, CNPs have a direct or indirect effect on the curing process of epoxy resins which can lead to a modification of the final cross-linked structure of

the polymer network and the final properties of the material. This way, other properties evaluation turns out to be more difficult. For this reason, a large number of publications were found dealing with this issue. Nevertheless, the full understanding of the effect of CNPs on the curing reaction mechanism has not been achieved.

II 4. MECHANICAL PROPERTIES

The purpose of enhancing the mechanical properties of epoxy resins incorporating CNPs as reinforcing fillers is considered a great challenge, even from the theoretical point of view. Compared to thermoplastics, shear forces generated during mixing CNPs in thermosets are much lower and the achieved dispersion state has to be maintained during the curing process. In addition, the CNP contribution to the load transfer is more effective in compression,[149] while many of the structural applications of epoxy resins require high mechanical performance in other modes. Nevertheless, notable improvements on the mechanical performance of carbon based epoxy nanocomposites have been made.

In 1998 one of the first publications on CNT/epoxies reported an improvement of about 20 % of the Young's modulus with high loadings (5 wt. %).[149] Other authors doubled the elastic modulus by adding 1 wt. % of CNT and quadrupled it with 4 wt. % CNT with significant improvements on the final tensile strength (Figure II.10).[150, 151] It is important mentioning that the improvements were carried out in a rubbery epoxy matrix with high ductility, otherwise the enhancements in brittle resins are moderate.[152]

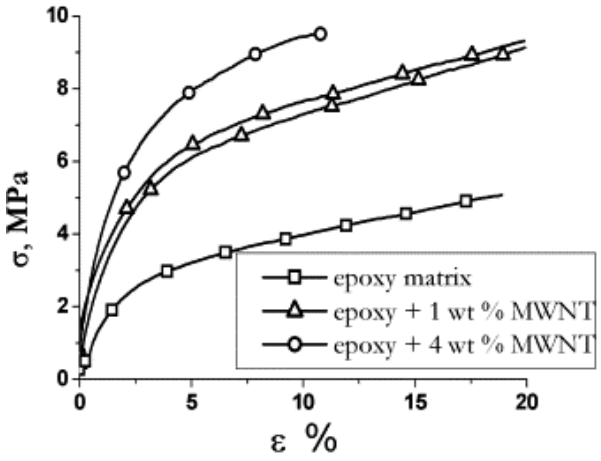

Figure II.10: Stress–strain curves of the resin and its CNT composites. Reprinted from,[150] copyright (2002) with permission from Elsevier.

Song *et al.*[116] evaluated the tensile properties of epoxy nanocomposites containing poorly dispersed CNTs and well dispersed CNTs. The elastic modulus increased regardless of the dispersion state but, surprisingly, the poorly dispersed CNT nanocomposite exhibited a slightly higher modulus (Figure II.11a). This behavior was explained by the fact that the agglomerates in the poorly dispersed CNTs nanocomposites act as large particles as if higher filler loading were present. The agglomerates trap polymer resin in the void between CNTs and the nanocomposites behave as if it had lower volume fraction of polymer matrix. However, tensile strength was found to be higher in the case of the well dispersed CNTs, in fact, the tensile strength decreased with the amount of poorly dispersed CNTs because the agglomerates acted as crack nucleates (Figure II.11b).

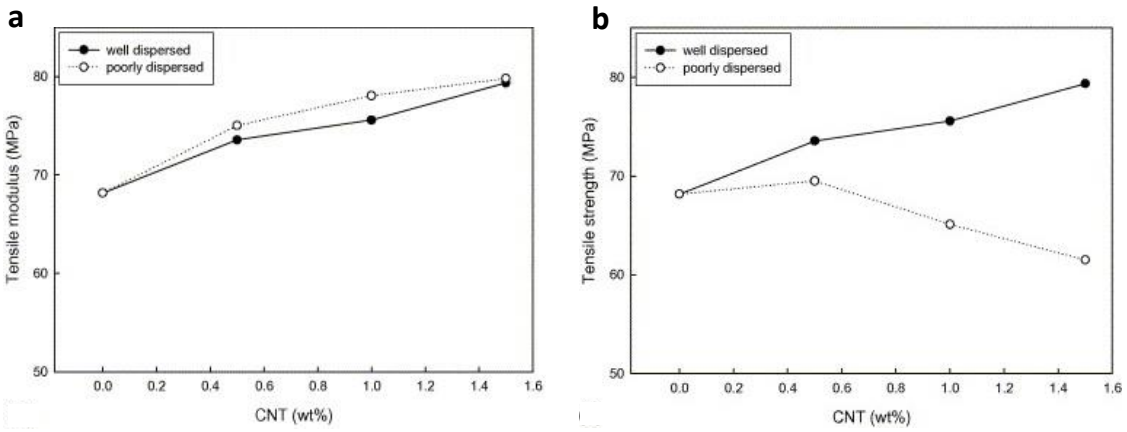

Figure II.11: Mechanical properties of poorly and well dispersed CNT, a) Young's modulus and b) tensile strength. Reprinted from,[116] copyright (2005) with permission from Elsevier.

In the same context, Choi *et al.*[153] added CNFs to the epoxy resin up to a 20 wt. % showing that the reinforcement effect reaches a maximum for tensile strength and Young's modulus at 5 wt. %. At higher contents, the mechanical properties decreased with filler loading. The negative effect of the CNFs at concentrations above the 5 wt. % was explained by a heterogeneous dispersion above this critical filler content; a decrease of the ductility with the increase of the load and the higher number of voids, produced during processing, which promotes the formation of microcracks as shown in Figure II.12. A similar optimum CNFs concentration was also detected elsewhere.[154-161] As in the case of rubbery epoxies filled with CNT, the enhancements in this type of matrix were higher.[162] Amine functionalization of CNFs also improved the adhesion of the filler/matrix interface enhancing the mechanical performance compared to the un-treated CNFs.[163]

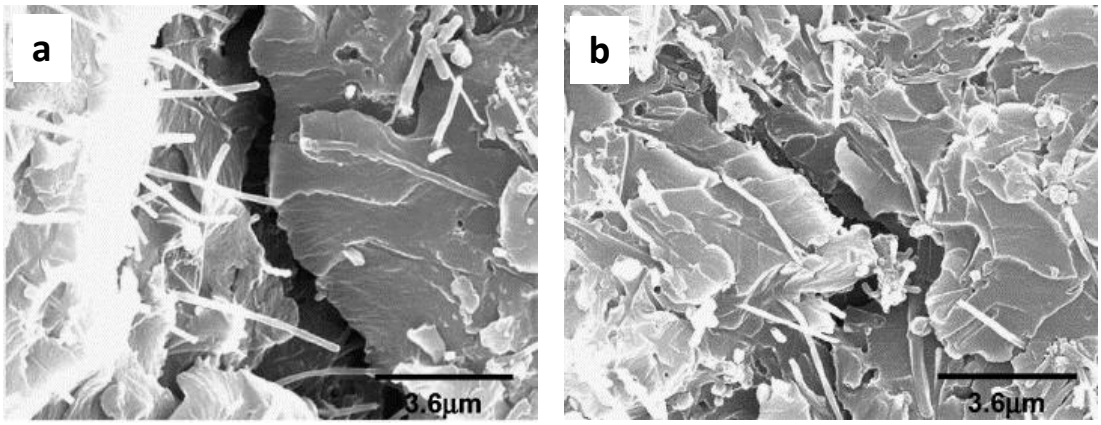

Figure II.12: Microcracks generated in nanocomposites at a) 10 wt. % CNF and b) 20 wt. % CNF. Reprinted from,[153] copyright (2005) with permission from Elsevier.

Fullerenes epoxy nanocomposites outperformed other epoxy composites with spherical geometry of the filler, like SiO_2, Al_2O_3 or TiO_2. The better mechanical performance of the fullerenes was associated to their hollow shell structure, which reduces the weight and increases the SSA in conjunction to the excellent sp^2 carbon bonding.[70] Amino acid functionalization of fullerenes also resulted in the improvement of the mechanical properties of epoxy resins.[164]

Rafiee *et al.*[74] reported a comparative study of the mechanical properties of CNTs and graphene nanoplatelets at low weight fractions. The Young's modulus obtained was about 30 % higher than the epoxy resin with just a 0.1 wt. % of graphene. The fatigue behavior was also notable improved by the addition of graphene. The authors confirmed that graphene outperformed SWCNT and MWCNT due to several reasons, which include enhanced specific area of graphene platelets, improved mechanical interlocking/adhesion at the nanofiller/matrix interface and the planar geometry of graphene platelets. The comparison of the mechanical properties among the cited fillers is represented in Figure II.13. Other authors corroborated the good performance of low content graphene nanocomposites.[165-168]

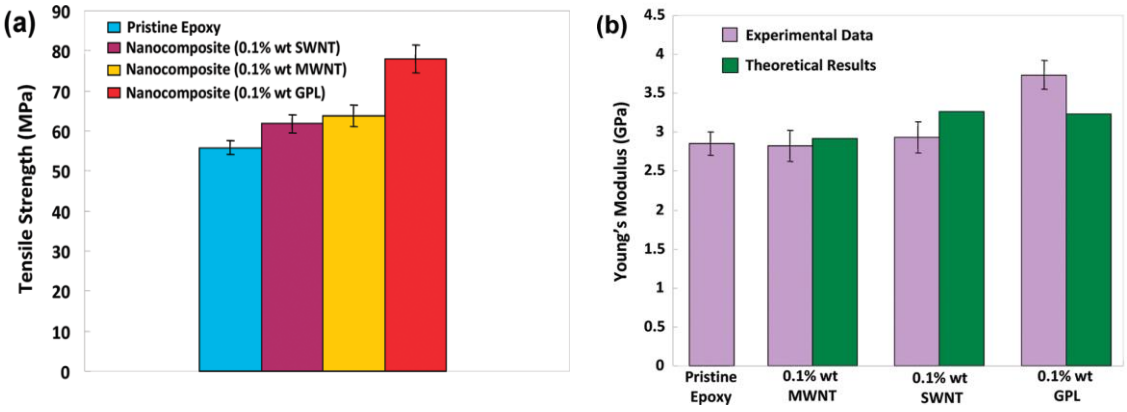

Figure II.13: Mechanical comparison of nanocomposites containing CNTs and graphene nanoplatelets, a) tensile strength and b) Young's modulus (Halpin-Tsai model was used for the theoretical model). Reprinted (adapted) with permission from.[74] *Copyright (2009) American Chemical Society.*

Regarding covalent bonding, the oxidation of the CNTs to improve the interfacial adhesion between the filler and the matrix enabled also a step forward towards the enhancement of mechanical properties. The addition of oxidized CNT resulted in approximately a 30 % increase in modulus and 15 % increase in tensile strength.[93, 169, 170] Amine functionalized CNT/epoxy nanocomposites also exhibited a 25 % higher modulus at 0.5 wt. %, in contrast they obtained a poor 3.2 % increase with the un-functionalized CNT reinforced composite.[147, 171] Gojny *et al.*[78, 95] studied the influence on the mechanical properties of different types of CNT. In particular they used double-wall carbon nanotubes (DWCNTs), amine functionalized DWCNTs and CB. The Young's modulus already increased at low contents of DWCNTs, whereas CB did not show any significant effect. The amino-functionalized DWCNTs had a more significant influence on the modulus due to the better dispersibility and improved interphase adhesion, as corroborated by other authors.[172] Meanwhile, non-functionalized DWCNT and CB had a negative effect on the tensile strength, probably due to the presence of agglomerates and the weaker interface compared to the amine DWCNTs. These results are summarized in Figure II.14. Zhu *et al.*[93] combined the acid treatment with a subsequent fluorination to functionalize CNT. They performed mechanical tests

obtaining a 30 % increase in modulus and 18 % increase in tensile strength. Silanized CNTs behaved in a similar way.[173-176]

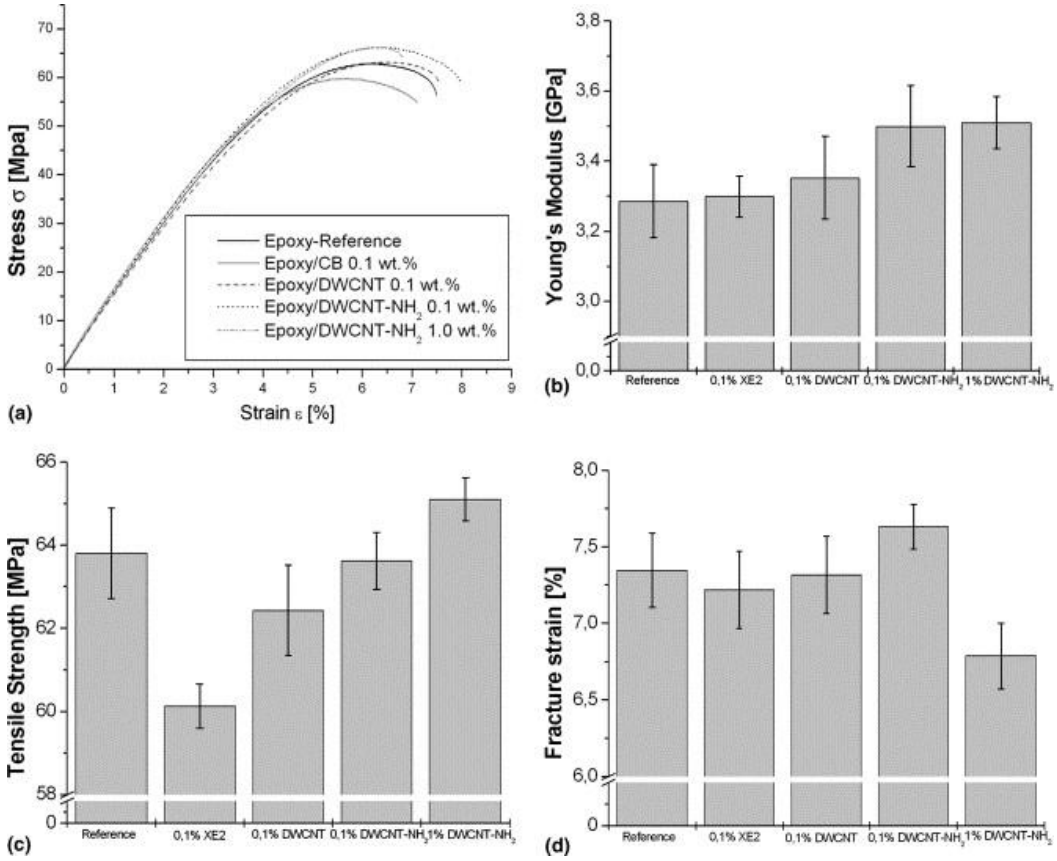

Figure II.14: a) Stress-strain curves, b) Young's modulus, c) tensile strength and d) fracture strain. Reprinted from,[78] copyright (2004) with permission from Elsevier.

The epoxy functionalization of graphene oxide led to significant improvements. In particular, the ultimate tensile strength of the resin increased a 75 % with a 0.25 wt. % of the functionalized graphene which was also superior to the one obtained without the treatment. The fracture surface analysis revealed a better interfacial interaction between the epoxy functionalized graphene and the matrix.[177] Similar functionalization was also carried out for expanded graphite with similar results.[178] Other chemical routes involving isocyanates, aminobenzoyles and silanes improved the interaction between graphene and the matrix with success.[179-182]

In the very last years, hybrids nanocomposites containing a combination of graphene nanoplatelets and CNTs have attracted great attention. These hybrids showed a synergic effect in flexural modulus when the ratio CNT/graphene was 9/1 and 5/1[89] and in uniaxial tension.[183-185] Flexible CNTs can interact with graphene to form 3-D hybrid structure, which inhibited face to face aggregation of the graphene platelets. The result was a large surface area of the carbon structure that was able to entangle the polymer chain of the epoxy matrix and improve the mechanical properties (Figure II.15b). The idealized morphology is depicted in Figure II.15a.

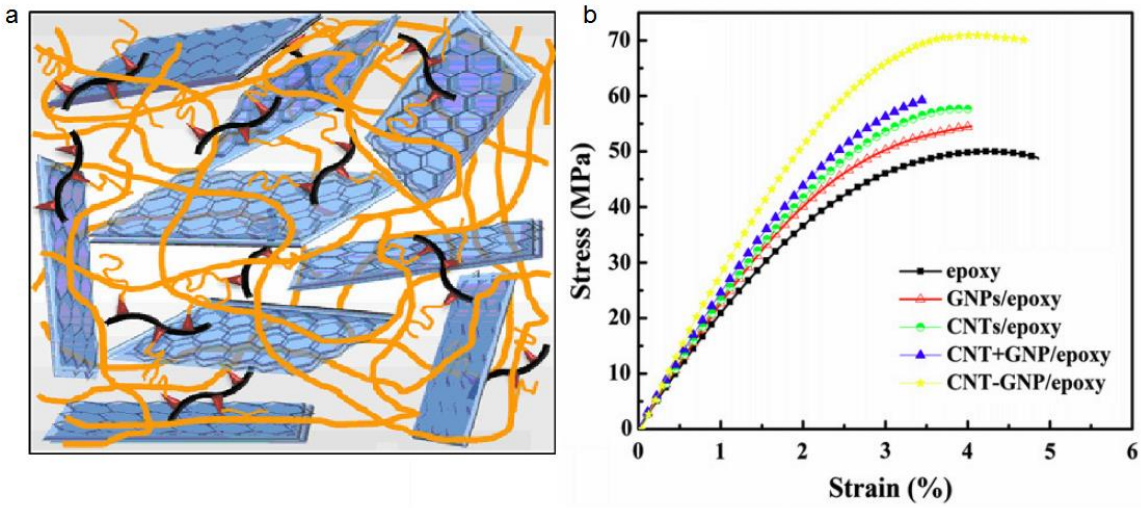

Figure II.15: a) Idealized structure of a hybrid nanocomposite containing graphene and CNTs and b) stress-strain curves of the hybrids and nanocomposites. Reprinted from,[183, 185] copyright (2011 and 2013) with permission from Elsevier.

It is worth mentioning that it is possible to generate a specific orientation of the CNPs within the matrix through the application of magnetic and electric fields while the dispersion of the epoxy resin is still in the liquid state.[186, 187] Electrically and magnetically aligned CNTs/epoxy nanocomposites raised the Young's modulus and tensile strength with the increase of SWNT concentration. Moreover, they presented well differentiate properties in perpendicular directions evidencing the anisotropic character of the nanocomposite after the alignment.[188-191] An example of the morphology achieved with electrically aligned CNTs can be observed in Figure II.16. Another possibility to produce aligned CNT composites is by infusing epoxy into arrays

of vertically aligned CNTs. This process permits to incorporate up to 39 wt. % of CNT into the resin and improve the elastic modulus (measured by DMA) a 400 %.[192] Compression mode Young's modulus increments obtained by this technique are over 200 % at 2 vol. %.[193]

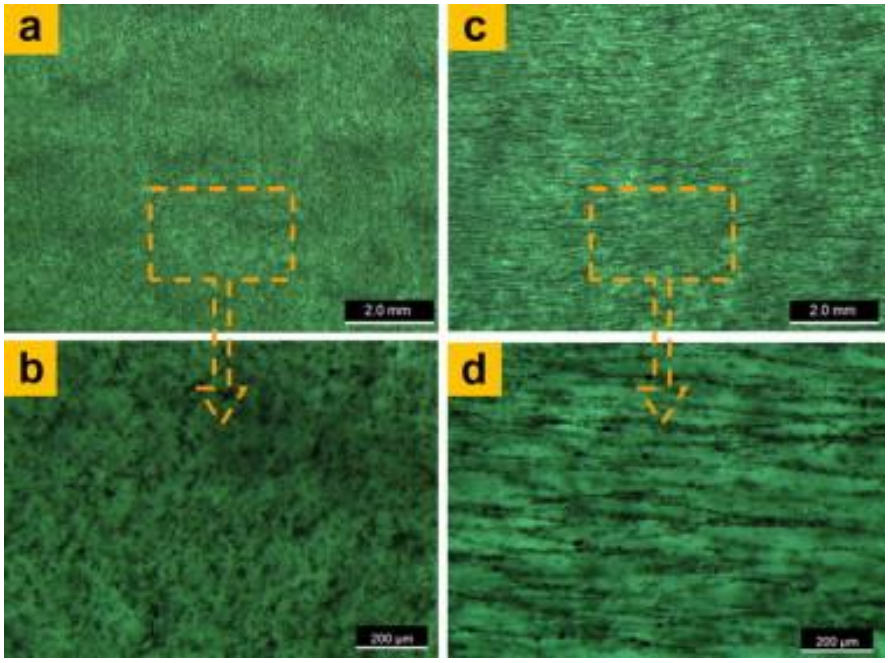

Figure II.16: Optical micrographs of CNTs in a cured nanocomposite, a) and b) without electric field, c) and d) with electric field alignment. Reprinted from,[188] *copyright (2013) with permission from Elsevier.*

In the field of epoxy foams, CNPs have also been employed to modify the final properties of the foam, in particular syntactic foams with low density glass microballoons whose concentration vary from 20 wt. % to 60 wt. % respect to the resin. CNT reinforced epoxy foams showed an improvement in compressive modulus by 35-41 % while the strength remained unchanged.[194] Guzman *et al.*[195] used functionalized CNT and various commercially available microballoons to produce syntactic epoxy foams showing significant increase in compressive strength and apparent shear strength. CNFs also improved the mechanical properties of syntactic foams in tension mode[196, 197] while the compressive modulus and strength were slightly affected.[196, 198, 199]

II 5. TOUGHNESS

Due to the highly cross-linked structure of epoxy resins, they present high brittleness limiting their applications in many cases. The addition of CNPs has been considered as one of the strategies to improve the toughness of epoxy resins. Even though, the study of the toughening mechanisms is not the goal of this section, a brief description of the toughening mechanisms involved in CNP/epoxy nanocomposites is described in the following lines:[200] shear yielding is one of the most accepted mechanisms. It involves the plastic deformation of the matrix at the crack tip under the application of stresses. The particle bridging mechanism supposes that the particles act as bridges compressing the crack path (example in Figure II.17a). Crack path deflection, in this case, the role of the particles is to cause the crack to deviate from its plane. The microcracking mechanism supposes that the CNPs generate microcracks increasing the toughness. Crack pinning and particle pull-out (Figure II.17b) are also very common toughening mechanisms.

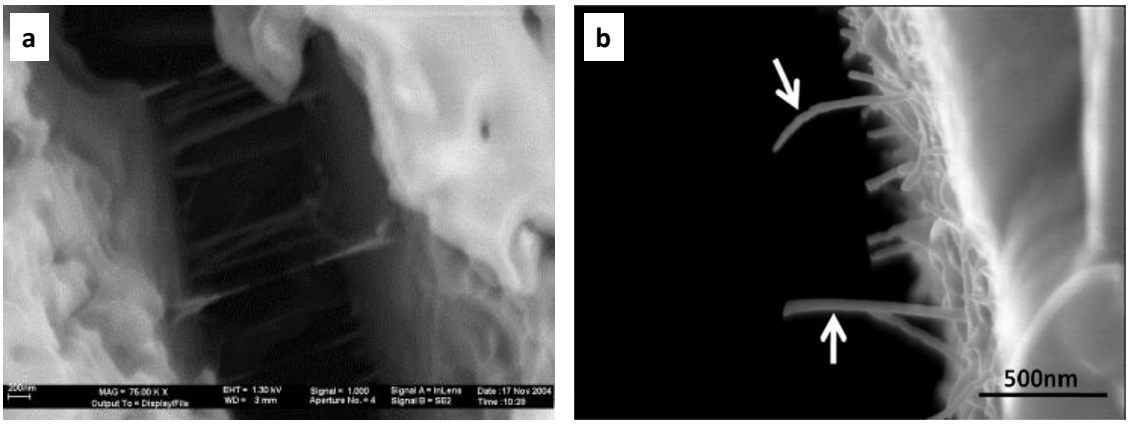

Figure II.17: SEM micrographs of CNT epoxy nanocomposites. a) Crack bridging and b) pull-out. Reprinted from,[170, 200] copyright (2006 and 2011) with permission from Elsevier.

Gojny *et al.*[78] were the first authors to study the fracture behavior of different CNPs on epoxy resins. Pristine CNTs, functionalized CNTs and CB presented significant higher fracture toughness (evaluating the critical stress intensity factor, K_{IC})

than the unfilled matrix. CB and pristine CNTs behaved very similar in this case, probably due to the high SSA of the CB. Amine functionalized CNTs outperformed the other CNPs due to their better wettability and adhesion with the matrix. Similar results using CNTs and functionalized CNTs where the improvements in K_{IC} varied from 20 % to 50 % were published afterwards.[74, 77, 95, 115, 170, 200-202]

CNFs also improved the fracture toughness, CNFs epoxy composites revealed that adding 0.5 wt. % and 1.0 wt. % CNFs to the matrix enhanced the resistance to fracture by 66 % and 78 % respectively.[203] The energy absorbed by the crack propagation (G_{IC}) followed the same trend, as shown in Figure II.18.

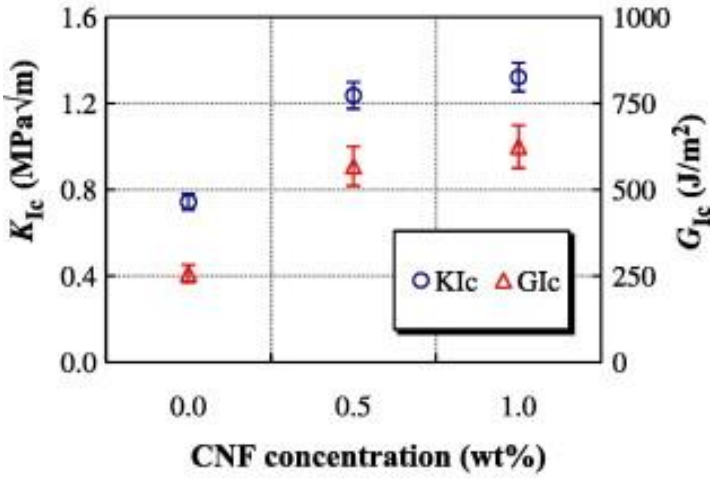

Figure II.18: K_{IC} and G_{IC} as function of CNF content. Reprinted from,[203] copyright (2011) with permission from Elsevier.

Toughness of graphite nanoplateles/epoxy nanocomposites was tested using single edge notch bending (SENB) obtaining the most significant improvement at 1 wt. % where a 43 % improvement was observed.[30] More moderate enhancements of the toughness were obtained with expanded graphite.[204]

Comparative studies between CNTs and graphene nanocomposites revealed that the wrinkled and planar morphology of the graphene sheets played a crucial role to enhance the toughness and fatigue properties of epoxy resins at low filler content

compared to the cylindrical shape of CNTs.[205] The potential of graphene as a toughening agent was corroborated by other authors.[163-164, 204] Enhancements of 63 % in K_{IC} and 112 % in G_{IC} were reported through the addition graphene to an epoxy system.[165, 166] The effect of the dispersion state of graphene also influenced the toughness, poorly and highly dispersed graphene at 0.2 wt. % loading resulted in about 24 % and 52 % improvement in K_{IC} of cured epoxy thermosets, respectively.[206] By adding small amounts of graphene oxide (0.1 wt. %) an improvement in the fracture toughness (K_{IC}) was obtained but higher loadings lead to a negative effect on the property. However, the same graphene with silica functional particles on their surface extended the range of concentration where the nanocomposite presented enhanced toughness (Figure II.19).[181] Methylene diphenyl diisocyanate (MDI) modified graphenes also presented improved interfacial adhesion showing a 85 % higher value of K_{IC} and a doubled G_{IC} than the matrix.[179]

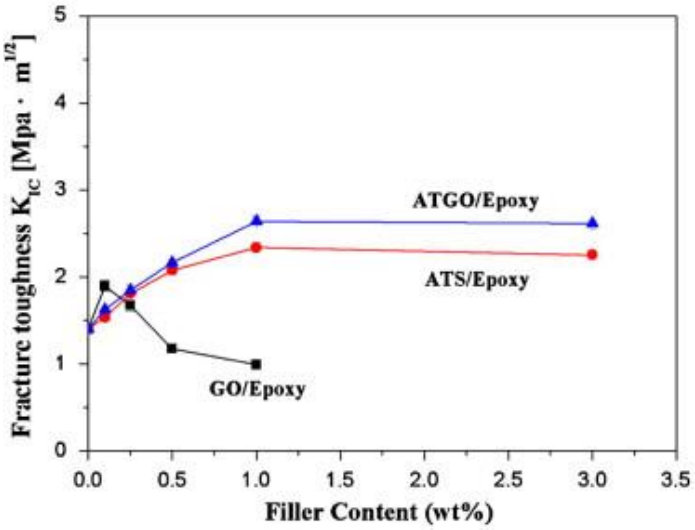

Figure II.19: Toughness of graphene oxide (GO), silica (ATS) and silica/graphene (ATGO) nanocomposites. Reprinted from,[181] copyright (2013) with permission from Elsevier.

II 6. ELECTRICAL PROPERTIES

While the initial intention to incorporate CNPs in epoxy resins was to improve the mechanical properties for structural applications, the extremely high intrinsic electronic and phonon transport of CNPs has broadened the experimental findings of CNP/epoxy nanocomposites. Thereby, the modification of the insulating character of epoxy resins became one of the most popular challenges. The goal to achieve the mentioned modification is to disperse the CNPs in such way that a continuous filler network guarantees conductive pathways within the polymeric matrix. Hence, the minimum concentration of the CNP needed to form the filler network is denoted as the electrical percolation threshold.

It is important to consider that the functionalization approaches of CNPs usually improves the final dispersion state of the CNPs which is positive to obtain the required percolated network, but functionalization processes often alters the molecular structure and/or geometry of the CNPs decreasing their intrinsic electrical properties. In addition, CNPs are surrounded by a thin layer of polymer matrix. Surface functionalization can promote the formation of this insulating polymer layer coating the CNP with a barrier to the electronic transport through the filler network.[207, 208] In conclusion, a determined functionalization can lead either to an improvement on the electrical conductivity as a result of the enhanced dispersibility or to a decrease on the electric conductivity generated by the lower intrinsic properties of the CNP and the formation of an insulating polymeric layer on the surface of the particle.

Sandler and coworkers[65, 187, 209, 210] studied the electrical conductivity of CNT epoxy nanocomposites obtaining very low percolation thresholds, their analysis resulted in a threshold of 0.0025 wt. % for CVD MWCNTs (Figure II.20). Since their first publication[65] in 1999 a huge number of papers dealing with the electrical properties of CNT/epoxy nanocomposites can be found in the literature, Table II.2 tries to summarize the main results obtained about electrical percolation in CNT/epoxy nanocomposites.

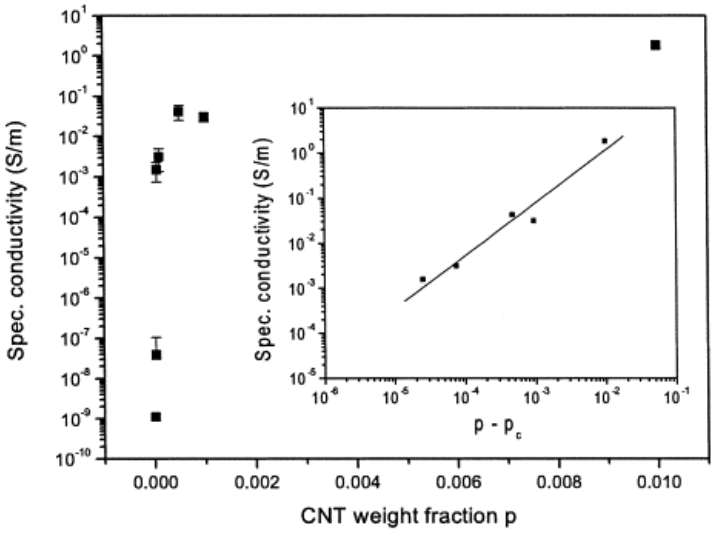

Figure II.20: Conductivity as a function of wt. % of CNT (p). The insert shows a log–log plot of the conductivity as a function of p−pc, pc is the percolation threshold which resulted to be 0.0025 wt. %. Reprinted from,[209] copyright (2003) with permission from Elsevier.

Table II.2: Summary of the experimental results concerning the electrical properties of CNT/epoxy nanocomposites.

Filler	Funct.	Dispersion method	p_c (wt. %)	σ_{max} (S/m)	Ref
MWCNT	-	Stirring	0.0021	10^{-3} @0.01 wt.%	210
MWCNT	-	Stirring	0.0025	$2 \cdot 10^{0}$ @1 wt. %	209
MWCNT	-	Stirring	0.0025	$4 \cdot 10^{-1}$ @0.5 wt. %	211
MWCNT	-	Stirring	0.0039	$2 \cdot 10^{-4}$ @0.01 wt. %	211
SWCNT	-	Sonication	0.005	$2 \cdot 10^{-2}$ @0.1 wt. %	212
MWCNT	-	Stirring	0.011	$4 \cdot 10^{-1}$ @1 wt. %	213
MWCNT	-	Sonication + stirring	0.03	$5 \cdot 10^{-1}$ @0.15 wt. %	65
MWCNT	-	Calendering + stirring	0.03	$1 \cdot 10^{-2}$ @0.3 wt. %	214

MWCNT	Acid	Sonication	0.034	$1 \cdot 10^{-1}$ @2 wt. %	215
SWCNT	-	Sonication + stirring	0.04	$1 \cdot 10^{1}$ @4 wt. %	216
SWCNT	Thermal ox.	Sonication + pump	0.074	$1 \cdot 10^{-3}$ @0.2 wt. %	217
SWCNT	Acid	Stirring	0.08	$2 \cdot 10^{-2}$ @0.4 wt. %	218
SWCNT	Acid	Sonication	0.1	$2 \cdot 10^{-6}$ @0.1 wt. %	219
MWCNT	-	Sonication	0.1	$2 \cdot 10^{-1}$ @1 wt. %	220
DWCNT	-	Calendering + stirring	0.15	$1 \cdot 10^{-2}$ @0.6 wt. %	214
MWCNT	Amine	Calendering + stirring	0.25	$1 \cdot 10^{-2}$ @0.6 wt. %	214
DWCNT	Amine	Calendering + stirring	0.25	$3 \cdot 10^{-4}$ @0.6 wt. %	214
MWCNT	UV/O_3	Sonication	0.27	$2 \cdot 10^{-2}$ @1 wt. %	220
SWCNT	-	Infiltration	0.3	$5 \cdot 10^{-1}$ @3 wt. %	221
SWCNT	-	Sonication + stirring	0.3	$1 \cdot 10^{-2}$ @2.5 wt. %	222
SWCNT	-	Manual	0.6	$1 \cdot 10^{-2}$ @14 wt. %	223
MWCNT	-	Stirring	0.6	$5 \cdot 10^{-3}$ @10 wt. %	224
MWCNT	-	Stirring	0.7	$5 \cdot 10^{0}$ @4 wt. %	150
MWCNT	Acid	Sonication + stirring	3.5	$1 \cdot 10^{-5}$ @8 wt. %	103
MWCNT	-	Calendering + stirring	<0.5	$3 \cdot 10^{-2}$ @2 wt. %	82
MWCNT	-	Sonication + stirring	<0.5	$3 \cdot 10^{-1}$ @1.5 wt. %	116
MWCNT	-	Calendering	-	$1 \cdot 10^{-2}$ @0.5 wt. %	115
SWCNT	Acid	Sonication	0.05	$1 \cdot 10^{-4}$ @5 wt. %	189
MWCNT	Surfactant	Sonication	0.06	$1 \cdot 10^{-2}$ @0.25 wt. %	104

When comparing the electrical properties of CNTs and CNFs or CB, the first ones showed lower percolation threshold. This difference was attributed to the intrinsic differences between the nanofillers, mainly their aspect ratio.[153, 225-228] Silanized CNFs improved the dispersion state of the filler enhancing the electrical properties two orders of magnitude above the un-treated CNFs.[117] Prasse *et al.*[229] detected anisotropy on the electrical conductivity of electrically aligned CNF, for a CNF content of 1 wt. % and above, one can estimate a maximal anisotropy of the electric resistance of about 10 as represented in Figure II.21.

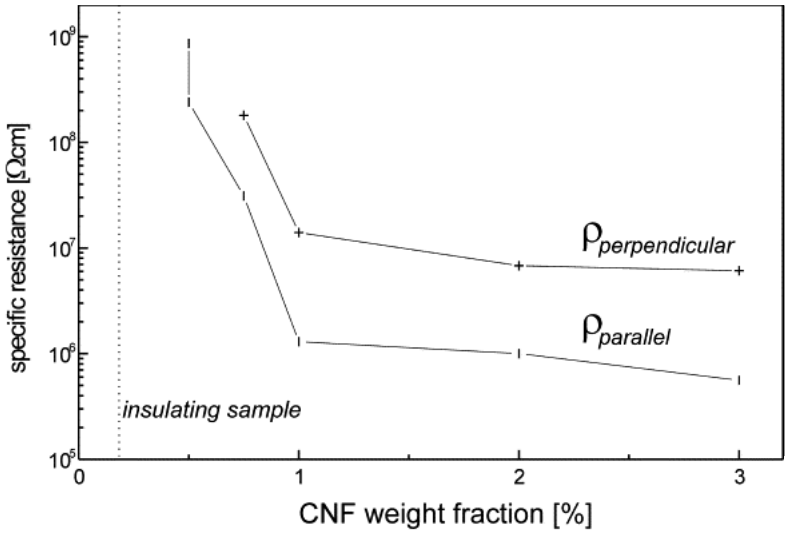

Figure II.21: Electrical resistance of epoxy nanocomposites containing aligned CNF. Reprinted from,[229] copyright (2003) with permission from Elsevier.

Graphite nanoplatelets also showed a higher percolation threshold than CNTs nanocomposites, at 0.3 wt. %, and the maximum value of conductivity ($1.8 \cdot 10^{-03}$ S/m) was obtained adding 1 wt. % of graphite.[30] Expanded graphite with epoxy functionalization raised the electrical conductivity five orders of magnitude at a loading of 0.5 wt. %.[178] Electrical resistivity of nanocomposites containing expanded graphite, treated with UV/O_3, showed a decreasing trend with the UV/O_3 exposure time. However, silane treatments of expanded graphite reduced the electric properties of the final composite.[230] As can be observed, depending on the functionalization treatment, it is possible to improve or reduce the conductivity of the nanocomposite. The final result

will be determined by the effect of the treatment on the intrinsic properties of the filler and the better dispersability achieved with the functionalization.

In the case of graphene nanocomposites we find a similar behavior. In particular, the electrical percolation threshold was found in the range of 1–2 wt. % of graphene nanoplatelets.[69, 168, 231] The electromagnetic interference shielding effect (EMI) of graphene was also measured and probed that the shielding effectiveness of the nanocomposite increases with the loading of graphene, which is mainly attributed to the formation of conducting interconnected graphene-based sheets networks in the insulating epoxy matrix. The target value of the EMI shielding effectiveness needed for commercial applications is around 20 dB, value that was obtained for a concentration of 15 wt. % of graphene as shown in Figure II.22. The dispersion state also played an important role in the electrical properties of graphene nanocomposites. Highly dispersed graphene produced one or two orders of magnitude higher electrical conductivity than the corresponding poorly dispersed, a value of $1.47 \cdot 10^{-6}$ S/m was reached with a 0.2 wt. % of well dispersed graphene oxide.[206]

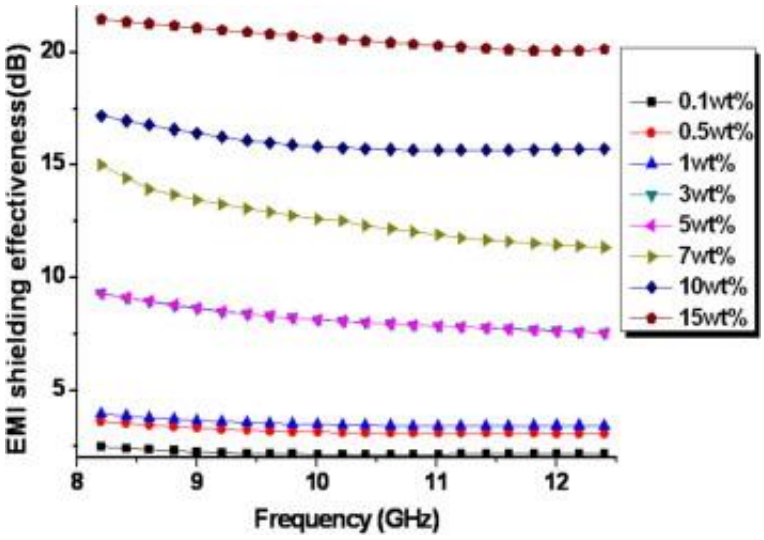

Figure II.22: EMI shielding effectiveness for epoxy/graphene nanocomposites. Reprinted from,[69] copyright (2009) with permission from Elsevier.

II 7. THERMAL CONDUCTIVITY

As for the electrical conductivity, the thermal conductivity (κ) enhancement of CNP/epoxy nanocomposites strongly depends on the formation of a conductive filler network through the matrix. Researchers have revealed two main issues associated with CNPs/polymer nanocomposites for heat transfer: the first one is that CNPs tend to aggregate into ropes or bundles when dispersed in polymers due to the strong intrinsic Van der Waals forces and the inert graphite-like surface, causing poor dispersion and making it a challenging task to disperse CNPs properly; the second is related to interfacial thermal resistance caused by the phonon mismatch at the interface of the CNPs and the polymer results in a high interface thermal resistance, leading to severe phonon scattering at the interface and a drastic reduction of thermal transport properties. In addition, the thermal transport through CNP network by phonons will be strongly hindered by the gaps between adjacent particles. The attainment of CNP/polymer nanocomposites with high thermal conductivity is challenged to address these two critical issues and build effective conductive networks for heat transfer.

Biercuk *et al.*[232] obtained great improvements of the κ at room temperature, about 120 %, at 1 wt. % loading of SWCNT. The authors also observed that the enhancement in SWCNT/epoxy samples rises much more rapidly than in CNF/epoxy composites (Figure II.23). Similar results can be found elsewhere.[233]

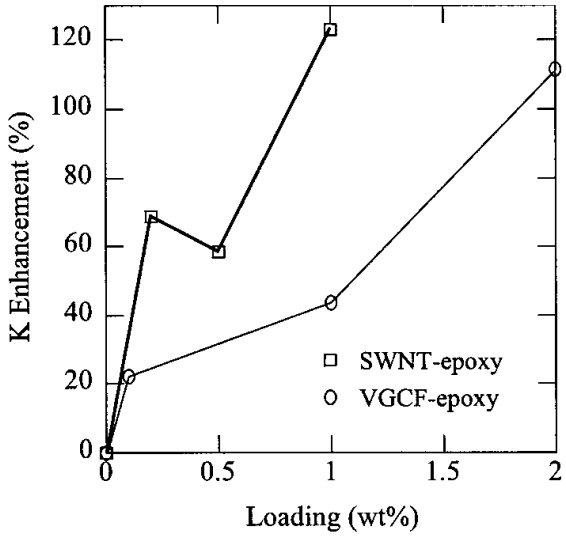

Figure II.23: κ enhancement as function of SWNT and CNF loading. Reprinted with permission from.[232] Copyright (2002) AIP Publishing LLC.

As with the electronic transport, functionalization not always improves the heat transfer of the final material. Dispersion of CNPs can be improved by functionalization of the CNPs but it also disrupts the phonon transport characteristics of CNPs increasing phonon scattering at the interface. Examples of the beneficial effect of covalent functionalization was given by Yu *et al.*[216] using oxidized SWCNTs and Yang *et al.*[234] for amine functionalization. Silanized CNFs also presented an improved thermal conductivity than the un-treated CNFs nanocomposites.[163] However, Gojny and coworkers[214] obtained lower values of the κ for amine functionalized MWCNTs than for the un-treated ones. They also observed lower κ for SWCNT and CB compared to the MWCNT (as shown in Figure II.24) due to their smaller SSA which reduced the interfacial resistance for phonon transport. This hypothesis was corroborated by other authors that reported a reduction of *κ* for an epoxy filled with high SSA SWCNT.[211] An effective method to reduce the interfacial resistance between CNTs and the matrix can be achieved by resin infusion of a CNT framework.[221]

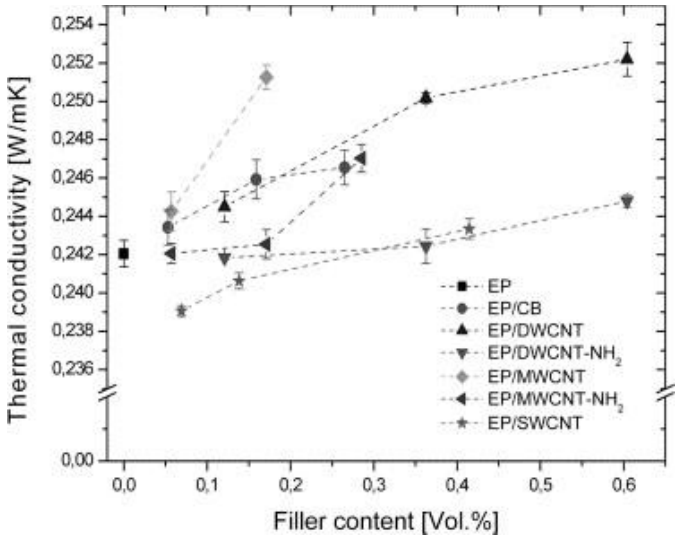

Figure II.24: Thermal conductivity using different type of CNPs. Reprinted from,[214] copyright (2006) with permission from Elsevier.

Expanded graphite slightly improved the heat transfer by 20 % at 2 wt. % loading.[30] While Yu *et al.*[235] studied the effect of different exfoliation temperatures to expand graphite on the thermal properties of epoxy nanocomposites obtaining greater improvements. Figure II.25 shows the positive effect of the expanding temperature of the graphite nanoplatelets on the thermal conductivity because of the higher aspect ratio of the nanoplatelets obtained at higher temperatures.

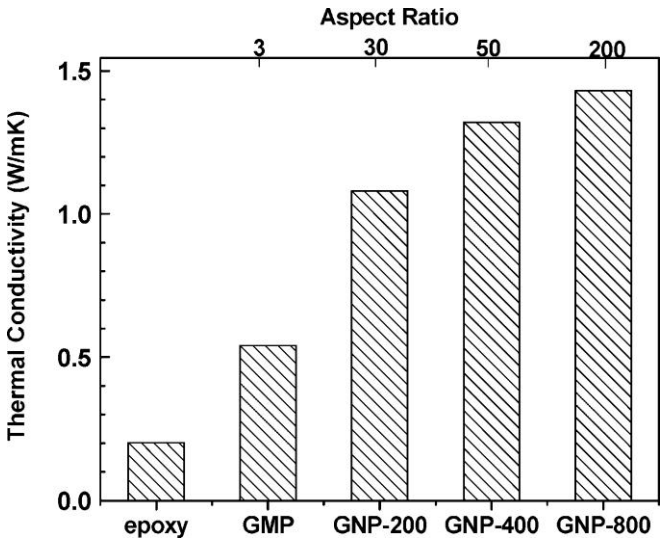

Figure II.25: Thermal conductivity of 5.4 vol. % graphite nanoplatelet composites as function of the exfoliating temperature. Reprinted with permission from.[235] *Copyright (2007) American Chemical Society*

The success of non-covalent functionalization with surfactants for thermal management of epoxy/SWCNT nanocomposites was reported by Bryning *et al.*[236] who obtained increments of 65 % in κ. A comparison of the effect of different carbon fillers (MWCNT, graphene, non-covalent functionalized graphene and exfoliated graphite) on κ of epoxy resin revealed that the thermal conductivity is affected by the carbon nanofiller structure, loading, dispersion, and the thermal resistance of the interface between nanofillers and the polymer matrix. Figure II.26 shows significant increase in κ of the epoxy composites with the increasing graphene content, which is superior to the MWCNT/epoxy composites.[237] The best results were obtained with the non-covalent functionalization, in particular a segmented poly(glycidyl methacrylate) containing localized pyrene groups (Py-PGMA), of graphene due to the better dispersion and lower interfacial resistance. The 4 wt. % Py-PGMA-graphene sample produced a 20% (higher than that of pristine graphene/epoxy) and 267% (higher than pristine MWCNT/epoxy) thermal conductivity. The authors of the study attributed the better performance of graphene to the thinner polymer layer coating the functionalized graphene reducing the barriers of phonon transport. Similar results were obtained by Song *et al.*[238]

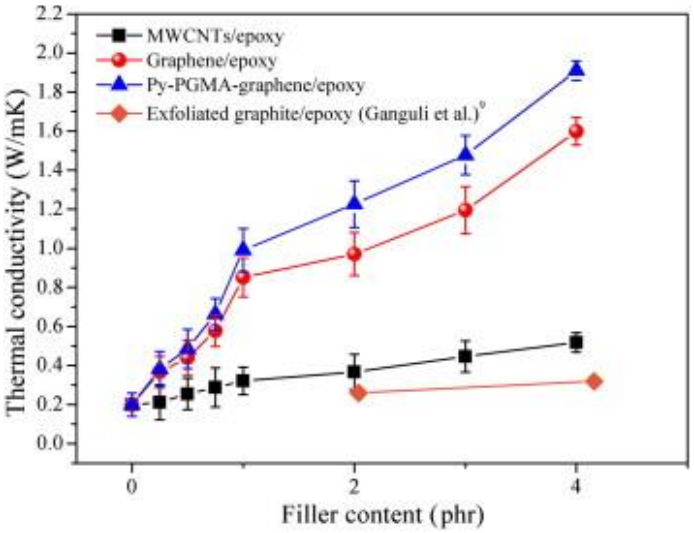

Figure II.26: Thermal conductivity with various filler contents of MWCNTs/epoxy, graphene/epoxy, and Py-PGMA–graphene/epoxy. Reprinted from,[237] copyright (2011) with permission from Elsevier.

Hybrids of graphene or graphite with MWCNT showed an important synergism improving κ more than 120 % respect to the neat epoxy resin and 90 % respect to the composites containing individual MWCNT or graphene due to the higher number of contacts and paths for phonon transport.[183, 239, 240]

II 8. GLASS TRANSITION TEMPERATURE

The effect of CNPs on the glass transition temperature (T_g) of epoxy resins is not trivial. T_g of epoxy resins depends on the molecular structure of the polymer network generated after the curing reaction and this final structure is function at the same time of several factors like the molecular architecture of the epoxy monomer and hardener, the degree of conversion of the reaction, curing conditions, etc. Thus, the addition of CNPs can modify some of these variables affecting the final T_g of the material. Besides, CNPs are expected to hinder the molecular motion of the polymer chains enhancing the T_g.

The number of articles dedicated to the shift of the T_g with CNTs is very high and many different results were obtained. Table II.3 summarizes the most relevant results in epoxy matrix CNT nanocomposites.

Table II.3: Shift of T_g in CNT/epoxy nanocomposites.

filler	Functionalization	Dispersion	T_g Method	ΔT_g (°C) $T_{g.composite} - T_{g.resin}$	Ref
SWCNT	-	Sonication	DMA	-5.9 @1 wt. %	[201]
SWCNT	Amine	Sonication	DMA	-7.7 @1 wt. %	[201]
MWCNT	Amine	sonication	DSC	-20 @1 wt. %	[241]
MWCNT	Amine	Sonication	DSC	8 @1 wt. %	[242]
SWCNT	-	Manual	DSC	-14 @1 wt. %	[129]
SWCNT	Fluorinated	Sonication	DMA	-20 @0.1 wt. %	[243]
MWCNT	-	Sonication	DMA	22 @0.4 wt. %	[152]
MWCNT	-	Shear + sonication	DMA	24 @1 wt. %	[244]
SWCNT	Surfactant	Sonication	DMA	-7.5 @0.5 wt. %	[71]
MWCNT	-	Shear + sonication	DSC	3 @1 wt. %	[245]
MWCNT	Plasma	Shear + sonication	DSC	10 @1 wt. %	[245]
MWCNT	O_3	High speed	DMA	1 @1 wt. %	[170]
MWCNT	Oxidized	Sonication	DMA	0 @1 wt. %	[246]
MWCNT	-	Sonication	DMA	16 @0.75 wt. %	[247]
MWCNT	Amine	Sonication	DMA	19 @0.75 wt. %	[247]
MWCNT	-	Sonication	DMA	25 @1 wt. %	[76]

MWCNT	Surfactant	Stirring	DMA	25 @1 wt. %	[72]
SWCNT	Amine	Sonication	DMA	-11 @0.5 wt. %	[171]
SWCNT	Oxidized	Sonication	DMA	-2.4 @1 wt. %	[248]
SWCNT	Amine	Sonication	DMA	10 @0.1 wt. %	[91]
SWCNT	-	Sonication	DSC	0 @0.05 wt. %	[249]
MWCNT	Silane	Sonication	DMA	13 @0.25 wt.%	[250]
MWCNT	Surfactant	Sonication	DMA	27 @0.25 wt.%	[104]

As can be observed in Table II.3, most of the papers which used SWCNTs in their experiments reported a negative effect on the T_g due to the tendency of this filler to agglomerate in bundles. One of the possible reasons to the great variety of the results summarized in the previous table can be the effect of the likely presence of small traces of solvent. Lau *et al.*[251] analyzed the effect of traces of solvents commonly employed to disperse CNTs on the mechanical properties observing an important reduction of the properties. Solvents with high boiling temperature showed stronger influence on the final properties of the nanocomposite. Therefore, solvent free processes are preferred.

CNFs behave in a similar way to CNTs. When a well dispersed state, an unmodified stoichiometry of the curing reaction and molecular structure were not achieved, the T_g was maintained unaffected[137] or negatively affected[85] by the presence of CNFs. On the other hand, silane and amine functionalizations together with more effective dispersion methods led to progressive increments of the T_g with the amount of CNFs,[117, 163] as shown in Figure II.27.

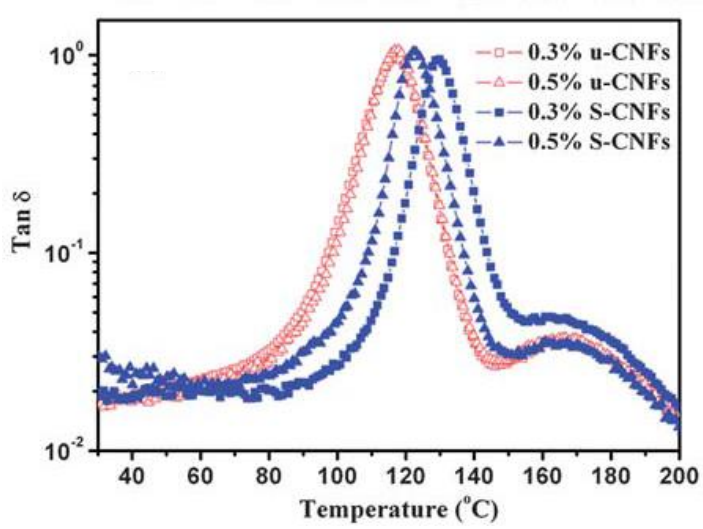

Figure II.27: Tan δ curves for epoxy nanocomposites filled with un-treated CNFs and silanized CNFs. Reproduced from[117] with permission of The Royal Society of Chemistry.

Expanded graphite nanoplatelets also had a variable performance. Graphite nanoplatelets dispersed by sonication and calendering did not show any profound influence on the T_g.[30, 204] Meanwhile Ganguli *et al.*[230] detected a critical concentration of expanded graphite (around 20 wt. %), below which the improvements obtained were minimal.

The results reported for graphene are more consistent and most of the results indicated a reinforcing effect of graphene, even simulations evidenced the potential of graphene sheets to improve the T_g of epoxy resins.[252] Experimentally, the T_g was increased by nearly 10 °C with the addition of 0.2 wt. % well dispersed graphene oxide to epoxy[206, 231] and 20 °C with 0.5 wt. %.[90] In most cases, covalent functionalization of graphene was also proved to be positive to hinder the polymer chain mobility resulting in enhanced T_g, reaching increments of 33 °C in the *tan δ* peak with amine functionalized graphenes (Figure II.28).[96, 177, 179] However, a slight decrease of T_g with amine graphene was also obtained and attributed to the plasticizer effect of the functionalization.[166] Prolongo *et al.*[253] studied the effect of the lateral size and thickness of different grades of graphene nanoplatelets. The authors observed that a major thickness and flake size of nanoparticles induced lower improvement of T_g while the smallest graphene sheets showed a more constraining effect on the molecular motion.

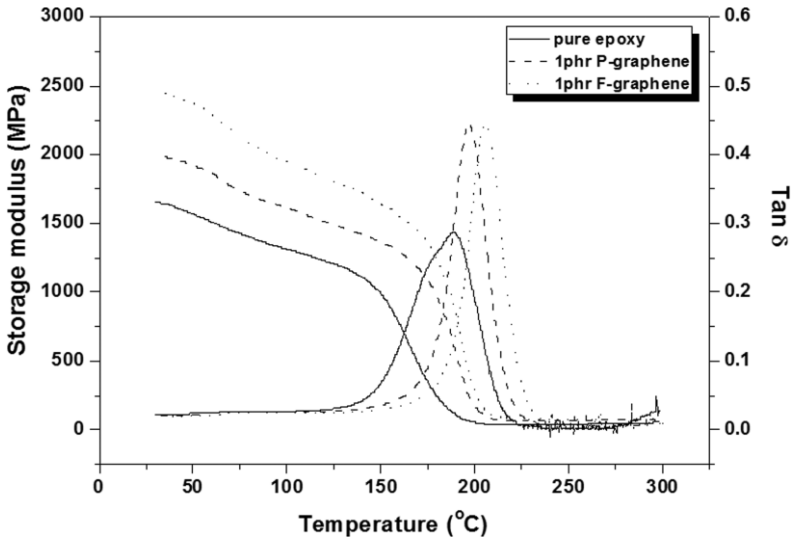

Figure II.28: DMA curves of pristine graphene and amine functionalized graphene. Reprinted from.[96] Copyright (2012) from John Wiley & Sons, Inc.

II 9. THERMAL STABILITY AND FIREPROOF PROPERTIES

The thermal stability of CNPs epoxy nanocomposites plays a relevant role for applications at elevated temperatures. While the incorporation of CNTs into epoxy led to significant thermal conductivity improvement, some reports revealed that they negatively affect the thermal stability of epoxy matrices accelerating their thermal degradation.[63, 130] The presence of metallic catalysts[130] which can catalyze degradation reactions and in some cases lower degree of curing were the reason to these negative results.

Introducing amine functionalized and silanized CNTs to epoxy resin enabled the increase of the initial decomposing temperature of neat resin. Because of the strong interaction between the epoxy resin matrix and functionalized CNTs, the diffusion of small molecules could be retarded under high temperature.[242, 250] In the case of CNFs, no significant effects on the degradation processes of epoxy resins were observed.[117, 160]

Thermogravimetric and flame retardant properties analysis indicated that graphene composites showed the highest onset temperature and maximum weight loss temperature compared with those added with graphite oxide and organic phosphate functionalized graphite oxides.[254] In a different study, the limit oxygen index (LOI) was

clearly raised by the presence of graphene oxide. More evident were the LOI values obtained for graphene functionalized with flame retardant molecules (Figure II.29).[255]

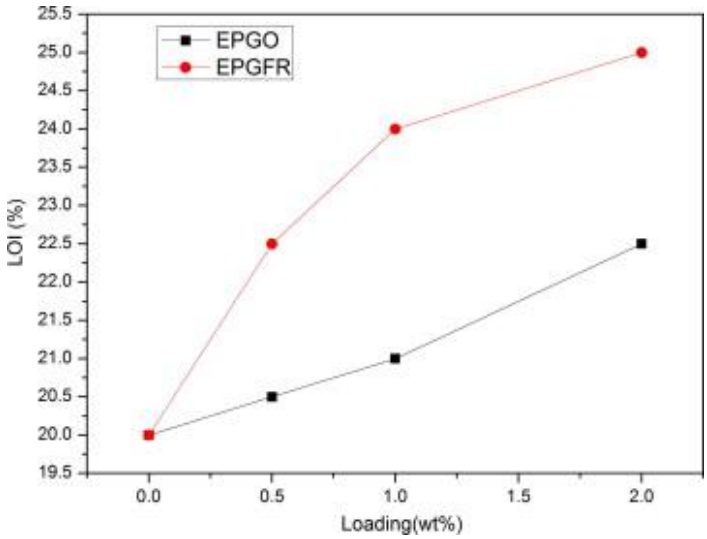

Figure II.29: LOI of epoxy nanocomposites with graphene oxide (EPGO) and GO functionalized with flame retardant molecules (EPGRF).Reprinted from,[255] copyright (2014) with permission from Elsevier.

II 10. SUMMARY

In this chapter we have reviewed the research up to date of CNPs/epoxy nanocomposites. The review reports the influence of CNPs on the variables involved in the processing and curing of epoxy nanocomposites and the final properties of the material. The improvement of such properties will strongly depend on several factors like the dispersion state, optimum degree of curing and maintenance of the intrinsic properties of the CNP during the whole manufacturing process.

The dispersion techniques available today to disperse CNPs comprise ultrasonication, high speed rotational tools and high shear forces devices like calendering. Ultrasonication and calendaring are effective to break the CNP agglomerates but the requirement of solvents in ultrasonication and the low quantities

that this technique allows to prepare per batch make calendering as the most suitable processing technique to prepare CNPs/epoxy nanocomposites.

The viscosity of the dispersions shows a clear shear-thinning behavior due to the presence of a filler network or to the presence of agglomerates that increase the viscosity and storage modulus of the epoxy dispersions. This effect is particularly noticeable in the case of CNTs and CNFs composites due to the high aspect ratio of the fillers. CB, graphene and expanded graphite show higher rheological percolating thresholds.

CNPs generally accelerate the curing reaction, decreasing the maximum heat temperature and the E_a. When the CNPs are functionalized, their effect will depend on the nature of the surface groups and their interaction with the reactive species which may vary the stoichiometry of the reaction. The catalytic effect is more pronounced for CNPs with higher SSA like CB and graphenes.

The mechanical properties of the epoxy resins can be improved by adding CNPs. In particular, toughness, Young's modulus and final strength increase with the amount of CNPs. The interfacial adhesion of the filler through covalent functionalization plays an important role enhancing the stress transfer from the matrix to the filler. The most outstanding CNP from the mechanical point of view is graphene due to the high SSA, wrinkled shape, planar geometry and usual functionalization derived from its processing that make it reinforce epoxy resin in a more efficient way.

The insulating behavior of the epoxy resin can be modified with the CNPs. In particular, CNTs clearly change the electrical properties of the matrix due to their exceptional intrinsic properties and high aspect ratio that lead to very low percolation thresholds. CNFs exhibit similar behavior but at higher loadings and proportionating lower values of the final electrical conductivity. Covalent functionalization can have a positive effect on the electrical conductivity if the dispersion state improves enough to overcome the loss of intrinsic electronic transport of the particle by the functionalization. CB, graphite nanoplatelets and graphene possess higher percolation thresholds due to the lower aspect ratio and wrinkled geometry.

Thermal conductivity is characterized by a more linear dependence with the CNP concentration. CNPs with functional groups and high SSA present stronger

interfacial resistance to the phonon transport. Pristine MWCNTs seem to be most appropriate CNP to enhance the thermal conductivity due to their lower SSA, high aspect ratio and the presence of inner graphitic layer that minimizes the coupling loses by phonon scattering. Nevertheless, some significant improvements have been reported using graphene in the presence of surfactants.

The shift of the epoxy T_g in CNPs/nanocomposites is not always towards higher temperatures. Pristine SWCNTs show great tendency to agglomerate into bundles reducing their reinforcing potential, and in many cases decreasing the T_g of the matrix. CNFs and MWCNTs produce improvements in the T_g when an homogeneous dispersion is achieved. The results are better when a correct functionalization of the CNP surface is done without altering the stoichiometry of the reaction and the final molecular structure of the resin. On the other hand, the presence of traces of solvent has a great impact on the T_g reducing its value even when well dispersed CNPs are employed. Graphene sheets have a greater potential to hinder the molecular motion of the polymer chains resulting in higher increments of the T_g when added.

Finally, the degradation process is not significantly affected by CNPs. However, strategic functionalizations of the CNPs with flame retardant molecules can enhance the fireproof properties of epoxy nanocomposites.

Chapter III. CARBON NANOPARTICLES

III 1. INTRODUCTION

Carbon nanotubes (CNTs) are one allotropic form of carbon with an atomic structure consisting in covalently bonded carbon atoms forming cylinders, where the edges of these cylinders can be capped by hemifullerenes. The chemical bonding in CNTs is essentially sp^2 carbon-carbon bonds; however, as the radius of curvature of the cylinders decreases in CNTs the sp^3 character of the carbon atoms increases.[256] CNTs are considered as one-dimensional carbon materials with large aspect ratio, high surface area, high flexibility,[257] low mass density and a unique combination of mechanical, electrical and thermal properties.[258, 259]

There are two main types of CNTs depending on the process of their structure: single-walled carbon nanotubes (SWCNTs) and multi-walled carbon nanotubes (MWCNTs). SWCNTs consist of a single graphene sheet rolled into a seamless cylinder while MWCNTs are formed by two or more graphene cylinders coaxially arranged around a central hollow core with an interlayer distance of ~0.36 nm (see Figure III.1). Consequently, nanotube diameters range from 0.4 to 3 nm in the case of SWCNTs and from 1.4 to 100 nm for MWCNTs.[256]

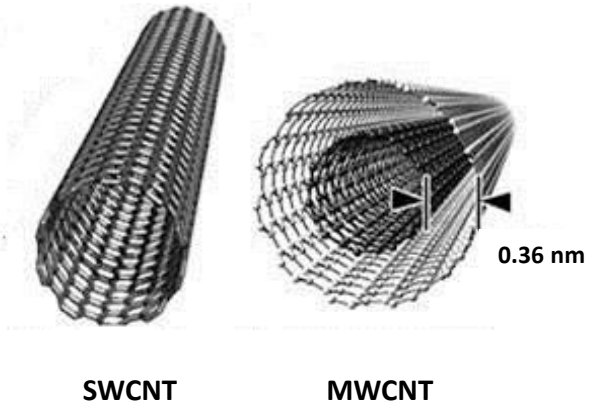

Figure III.1: Schematic view of a SWCNT and a MWCNT. Adapted from.[260]

The different conformations in which graphene can be rolled into tubes have been described by the tube chirality or helicity and it determines the atomic structure of the nanotubes. There are two main chiralities which are represented in Figure III.2, the first one is called "armchair" and the second one is the "zig-zag" chirality. The chiralities are determined by the chiral vector and the chiral angle. The chirality of CNTs has an important impact on their electronic properties, because nanotubes can show metallic or semiconducting behavior depending on the tube chirality. Hence, armchair SWCNTs are metallic (band gap = 0 eV) and zig-zag SWCNTs are semimetallic (band gap on the order of few meV) or semiconductors (band gap of 0.5 - 1 eV). On the other hand, MWCNTs present a wide variety of tube chiralities and thus, their properties are complicated to predict.[261]

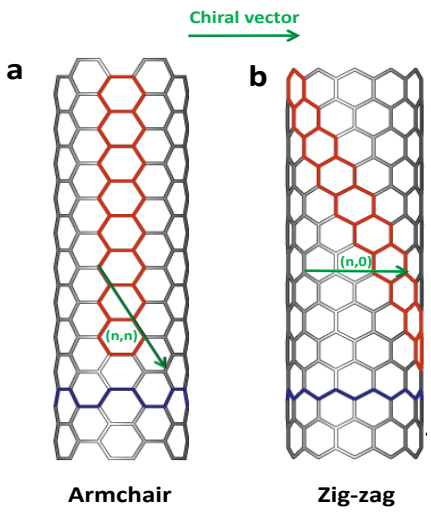

Figure III.2: Schematic diagram showing a carbon nanotube with a) armchair chirality and b) zig-zag chirality.

CNTs are usually produced by three techniques: arc discharge, laser ablation and chemical vapor deposition:[256, 262-264]

- Arc discharge: this technique involves the use of two high-purity graphite rods as electrodes. The electrodes are brought together and a voltage is applied until a stable arc is achieved. Then, a gap between the rods should be maintained at 1

mm or less and the anode is consumed while the material is deposited on the cathode.

• Laser ablation: in this method, a laser is used to vaporize a graphite target doped with small amounts of a catalyst in an oven at high temperatures and inert atmosphere. This method produces high-quality SWNTs; however the cost of the laser is very high and the process is not effective for a large scale synthesis.

• Chemical vapor deposition (CVD): this method consists on the catalytic decomposition of a hydrocarbon gas source in a furnace at high temperature (500-1000 °C). CNTs synthetized by this method possess low carbon-based impurities, minimizing the successive purification steps, but lower crystallinity than the previous methods. In addition, the supported CVD techniques produce aligned arrays of nanotubes and offer the possibility to control the diameter and length of the CNTs, thus allowing a large scale production of the nanotubes.

Recently, graphene has attracted a tremendous amount of attention and has emerged to be an exciting material with potential applications as a conductive and reinforcing material for polymer nanocomposites.[265, 266] Graphene is a two-dimensional (2D), one-atom-thick carbon sheet composed of sp^2 carbon atoms arranged in a honeycomb structure (Figure III.3).

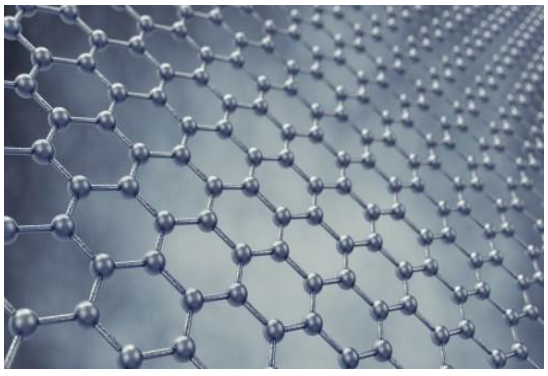

Figure III.3: Schematic illustration of an idealized single layer graphene sheet.

Defect-free graphene presents outstanding physical properties, such as high thermal conductivity (5000 W/m·K), Young's modulus (1 TPa) and ultimate strength of 130 GPa. Furthermore, graphene possess a large specific area (theoretical limit: 2630 m^2/g), gas permeability, and high electron mobility.[267-271]

To produce graphene, various approaches have been used including chemical vapor deposition (CVD),[272, 273] micromechanical cleavage,[274] epitaxial growth,[275] longitudinal "unzipping" of CNTs[276] and the reduction of graphite oxide.[277, 278] Among all the synthesis methods cited above, the oxidation of natural graphite and the later reduction of graphite oxide have been widely studied due to its simplicity, low cost and the possibility to scale-up the process. This method consists on the oxidation of graphite with concentrated acids and oxidizing agents to generate graphite oxide (GO). The reduction of GO into graphene can be performed via chemical or thermal reduction. In the chemical reduction, the reducing agents commonly used are hydrazine,[279] hydroquinone[280] or sodium borohydride.[281] The thermal reduction and exfoliation of GO is based on the rapid exfoliation of dried GO at high temperatures (above 1000 °C) and under an inert gas atmosphere.[282, 283] Graphene produced by this method is usually denoted as thermally reduced graphene (TRG).

Finally, it is worth mentioning that both carbon nanoparticles, CNTs and graphene, are complex structures and the synthesis methods to obtain them generally produce particles with defects that will affect the intrinsic properties of the final material. The most general defects are described in Figure III.4 and comprise structural defects, topological defects, doped elements, non-sp^2 carbons (vacancies, edges, and interstitials) and folding.[284]

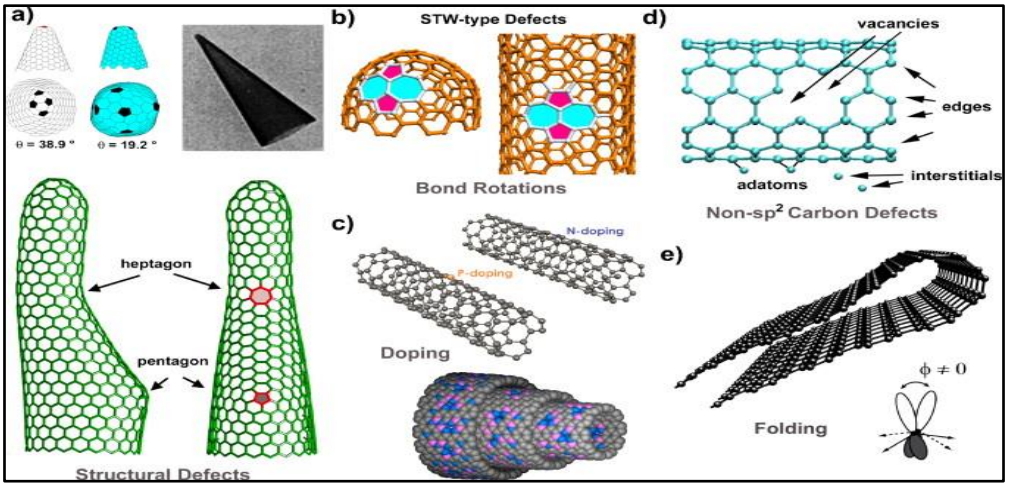

Figure III.4: Schematic models representing different types of defects in CNTs and graphene. Reprinted from,[284] copyright (2010) with permission from Elsevier.

III 2. SYNTHESIS, FUNCTIONALIZATION AND CHARACTERIZATION OF CARBON NANOTUBES

Multi-wall carbon nanotubes (MWCNTs) were grown by chemical vapor deposition (CVD) on the wall of a quartz tube which acted as a substrate.[285] First a solution of 3 wt. % of ferrocene (Figure III.5) in toluene was prepared. Ferrocene decomposes to provide the iron catalyst required to start the heterogeneous nucleation of the carbon nanotubes whilst toluene acts as the carbon atoms feedstock.[286] This solution is then injected in a tubular furnace at 760 °C where it is vaporized and carried through the furnace using 325 mL/min of argon.

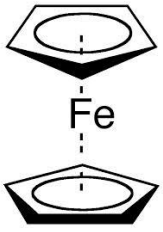

Figure III.5: Molecular structure of ferrocene.

The reaction time was calculated taking into the account the injection rate plus 1 h and 30 min to ensure a good quality of the outer CNT walls. Once the deposition is finished and room temperature is reached, MWCNTs were removed from the wall of the tube and stored in a container. No further purifications steps were performed prior to use. Figure III.6 illustrates the experimental set up for the synthesis described above.

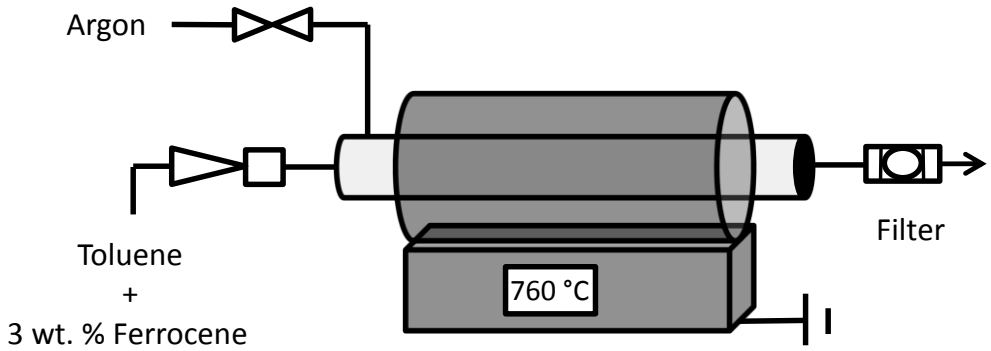

Figure III.6: Experimental set up for the synthesis of MWCNTs.

As it is well known, the functionalization of the external layer of CNTs can improve the dispersion of the nanoparticles within the polymer matrix.[287] The end caps and defect positions on the walls of MWCNTs can be opened using high oxidizing conditions leading to functional groups such as hydroxyl, carboxylic and carbonyl groups.[288] These oxidized nanotubes (o-MWCNTs) show more stable dispersions in epoxy resins[289] and polar solvents.[290]

In order to produce o-MWCNTs, the previously described MWCNTs were refluxed in a 3:1 concentrated sulfuric/nitric acid mixture at 120 °C for 30 min, filtered, washed until neutral pH and dried at 120 °C for a night.

Both types of CNTs were characterized by infrared and Raman spectroscopy, X-ray photoelectron spectroscopy (XPS), thermogravimetrical analysis (TGA) and scanning (SEM) and transmission (TEM) electron microscopy

Fourier transform infrared spectra (FT-IR) for the pristine MWCNTs and o-MWCNTs were collected using a Perkin-Elmer Spectrum One FT-IR spectrometer with a resolution of 4 cm^{-1}. The CNT powder was mixed and pressed with KBr to make KBr-

MWCNT and KBr-o-MWCNT disks. Their infrared spectra can be observed in Figure III.7.

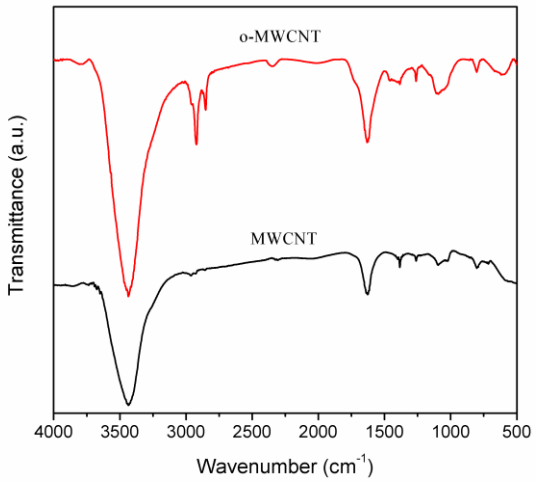

Figure III.7: FT-IR spectra of MWCNTs and o-MWCNTs.

In Figure III.7, o-MWCNTs show characteristic peaks at 2920 cm^{-1} and 2850 cm^{-1} corresponding to sp^3 CH stretching or asymmetric stretching of sp^3 CH_2 group and to symmetric stretching of sp^3 CH_2 groups, respectively. [288] These high bands related to the sp^3 hybridization are an evidence of the presence of functional groups after oxidation process. The bands at 1040–1150 cm^{-1} correspond to the C-O stretching and also corroborate the presence of a higher number of oxidized species in the o-MWCNTs.[291] The characteristic band of the C=C stretching at 1600 cm^{-1} is observed in both samples while in the case of the o-MWCNTs appears with a shoulder at 1730 cm^{-1} which is attributed to the C=O stretches.

Raman spectroscopy is a useful technique to study the crystalline and structure quality of carbonaceous materials. In particular, Raman spectra of the CNTs can provide information of their diameter, chirality and defects.[292]

Raman measurements were performed on a Renishaw Invia Raman Microscope. The analyses were done using an argon laser at 514.5 nm excitation wavelength. The

CNTs were placed on a glass slide and air-dried before the measurements were taken. Figure III.8 depicts the Raman spectra of the pristine MWCNTs and after oxidation.

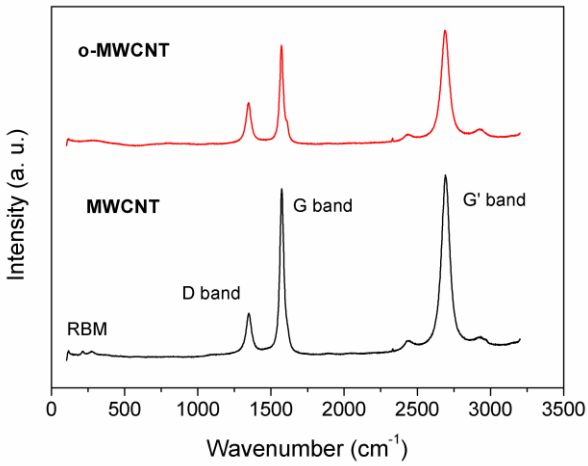

Figure III.8: Raman spectra of MWCNTs and o-MWCNTs.

The most characteristics bands of the CNT spectrum are marked in the Figure III.8. It is possible to define the radial breathing mode (RBM) band at 100-300 cm^{-1}. The RBM band is related to the diameter of single and double layer CNTs and their chirality.[293] In MWCNTs these bands are usually too weak since MWCNTs have several graphitic layers as well as the effect of the broadening of the signal by the average diameter of the inner tubes.[292] In our case, the presence of these peaks indicates the possible presence of any single or double layer CNT. Therefore, the most important bands for MWCNTs are the defect (D band) and graphitic bands (G band), located at 1350 cm^{-1} and 1570 cm^{-1}, respectively. Finally, the G' band appears at 2700 cm^{-1} and it is an overtone band. The G band is a common peak for graphitic materials and it corresponds to the vibrational mode of carbon-carbon bonds in the graphitic plane. On the other hand, the D band is originated by the defects on the crystalline structure or presence of amorphous carbon of graphitic materials.[294] The most common approach to measure the quality of CNTs is to calculate the ratio of the relative intensity of the D band and G band (I_D/I_G).[286] Thus, the higher is the value of this ratio the higher is the number of defects. The values of I_D/I_G for both samples were calculated using the

relative intensity of a Lorentzian deconvolution of the D and G bands. The value obtained for the MWCNTs was 0.28 while for the o-MWCNTs was 0.72. The higher I_D/I_G for the o-MWCNTs is a clear evidence of the higher number of defects generated after the oxidation process. The functional groups disrupt the aromatic sp^2 structure of the CNT. Moreover, it is possible to observe the formation of a shoulder in the G band near 1600 cm^{-1} which corresponds to the D' band and its intensity grows when the number of defects is very high.[295]

XPS was employed to determine the chemical composition of the surface of the nanoparticles. The experiments were performed on a VG Escalab 200R spectrometer equipped with a hemispherical electron analyzer operated on a constant pass energy mode and non-monochromatized Mg X-ray radiation ($h\upsilon$ = 1253.36 eV) at 10 mA and 12 kV. The samples were first placed in a copper holder mounted on a sample rod in the pre-treatment chamber of the spectrometer and then, degassed at room temperature for 1 h before being transferred to the analysis chamber. Data analysis was performed with a XPS peak program. The spectra were decomposed by the least-squares fitting routine using a Gauss Lorentz product information after subtracting a Shirley background. The binding energies (BE) were normalized by using the C_{1s} peak (284.8 eV) of carbon as an internal standard.

In Figure III.9 are represented the C_{1s} and O_{1s} spectra for the MWCNTs and o-MWCNTs as well as their fitting curves.

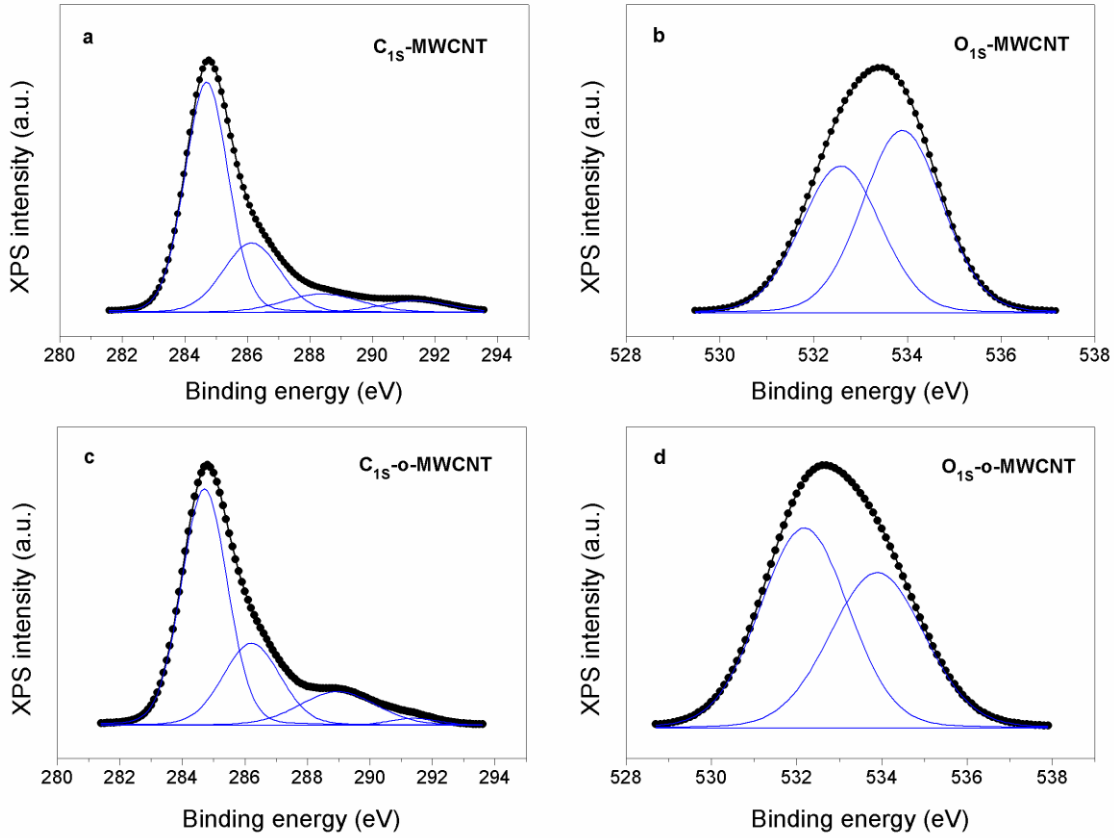

Figure III.9: C_{1s} and O_{1s} XPS spectra of MWCNTs and o-MWCNTs.

The C_{1s} spectra are dominated by a single peak at 284.8 eV assigned to the sp^2 C-C bonds of graphitic carbon. The deconvolution of the C_{1s} peak into different fitting curves has been assigned to a peak between 285-286 eV of sp^3 C-atoms and the peaks in the region 286.3-290.5 eV assigned to carbon attached to different oxygen groups. It can be observed that C_{1s} spectra show a broad weak component at around 291.5 eV which corresponds to the π-π^* transition of carbon atoms in graphene structures.[296-298] The O_{1s} spectrum shows a broad peak indicating that different oxygen-containing groups are present on the surface of the carbon nanofillers. The deconvoluted peaks are centered at 532.2 eV and 533.6 eV, corresponding to O=C surface groups and O-C bonds, respectively.[298] The information provided by the C_{1s} spectra is complemented analyzing the O_{1s} spectra. The O_{1s} spectra are more surface specific than the C_{1s} because the O_{1s} photoelectron kinetic energies are lower than those of the C_{1s}, and the O_{1s} sampling depth is smaller.[299]

The binding energies, peak assignments and relative atomic percentage are reported in Table III.1. As can be observed, the oxidation of MWCNTs introduces new oxygen groups on the surface of the fillers and a decrease on the carbon graphitic layer. The surface atomic ratios of oxygen to carbon are calculated from the area of the O_{1s} peak divided by the area of the C_{1s} peak normalized by the atomic sensitivity factors.[300]

Table III.1: Peaks, binding energy, assignments and atomic percentage of MWCNT and o-MWCNT.

Peak	Binding energy (eV)	Assignment	Atomic % in MWCNTs	Atomic % in o-MWCNTs
C_{1s}	284.6-285.8	C-C sp^2 C-C sp^3	86	63
	286.3-286.5	C-O-C	-	20
	288.0-289.0	-O-C=O	11	16
	291.0-291.5	π-π*	3	1
O_{1s}	532.0-532.5	C=O	43	56
	533.5-533.9	C-O-C	57	44

The thermal stability of the nanotubes was evaluated by TGA. A TA Q500 thermogravimetric analyzer was employed. The experiments were carried out in air atmosphere (200 ml/min) to study the oxidative stability of the nanoparticles. Approximately 5 mg of each sample were heated up from room temperature to 800 °C at a heating rate of 10 °C/min.

The Figure III.10 represents the weight loss and the derivate for both types of CNTs. In the case of the pristine MWCNTs the thermal degradation occurs basically in one step with a maximum in the derivate at 600 °C. This degradation corresponds to the oxidation of the carbon backbone of the MWCNTs. Occasionally, it may be possible to obtain small weight losses around 400 °C which would correspond to the degradation of amorphous carbon on the surface of the CNTs.[301] In our case, the amount of amorphous carbon is close to 0.3 wt. %. After the oxidation, o-MWCNTs present two degradation steps: the first one is centered at 372 °C and is associated to the functional moieties

attached on the external wall of the CNT. In particular, it corresponds to the decarboxylation of the COOH groups.[295] Besides, it can also be observed a slight weight loss (5 wt. % approximately) between 150 °C and 300 °C which is due to the loss of OH groups and water. Finally, the second step is again due to the degradation of the carbon backbone of the particles taking place this time at lower temperatures. Bom *et al.*[302] reported a decrease on the air thermal stability when the crystalline structure presents defects facilitating the thermal oxidative degradation of the CNTs which is the case of the o-MWCNTs. In this context, is possible to correlate the Raman I_D/I_G ratio and the thermal oxidative stability of CNTs.[303] The lower the I_D/I_G, the higher the crystallinity and the energy required to degrade them.

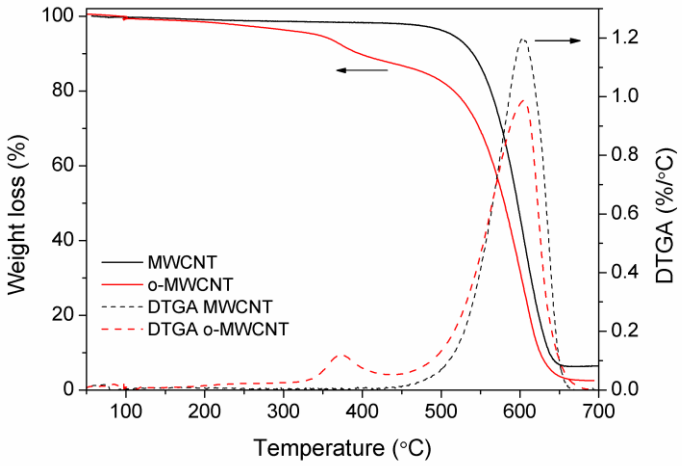

Figure III.10: TGA and DTGA curves of MWCNTs and o-MWCNTs.

Eventually, the morphology of the CNTs was analyzed by scanning (SEM) and transmission (TEM) electron microscopy. The images were obtained on a Philips XL30 ESEM at 25 kV and on a Philips Tecnai 20 TEM apparatus using a voltage of 200 kV, respectively. SEM analysis was performed on the surface of a mat extracted from the wall of the quartz tube while for the TEM the samples were prepared by immersion of the TEM grid in a dilute solution of nanoparticles in THF and letting the solvent evaporate.

Two SEM images of the neat MWCNTs are shown in Figure III.11. It can be observed that MWCNTs are aligned and disentangled in the mat, this fact would enable to disperse them in the epoxy resin in an easy way. The length measured from the low magnification image is approximately 160 μm.

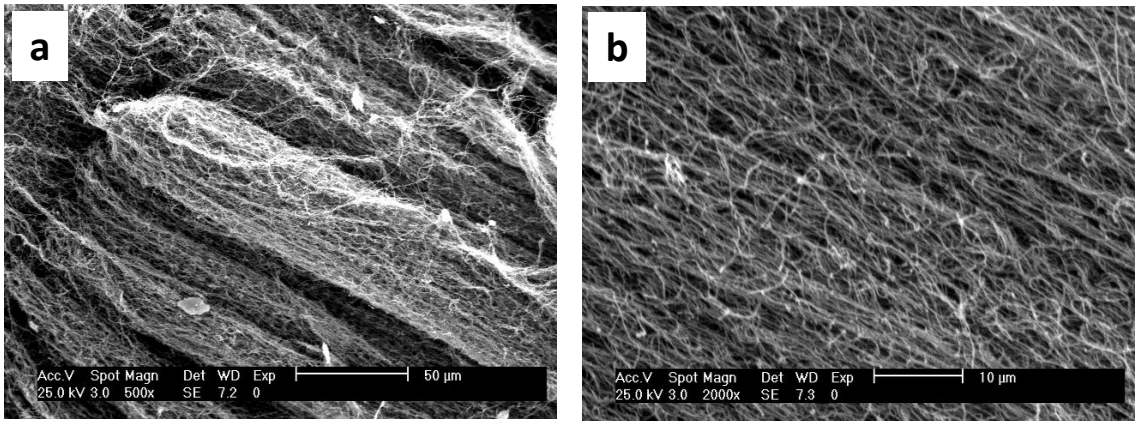

Figure III.11: SEM images of MWCNTs a) augmentation x500 b) x2000.

In the TEM images (Figure III.12) we can observe the flexible tube-like geometry with the characteristic high aspect ratio of these nanoparticles. In some of the MWCNTs it is possible to detect some catalyst residues (black dots). Figure III.12b is a high resolution image of an individual MWCNT where it is possible to observe the hollow space inside the tube (it determines the inner diameter) and the different carbon layers with a concentrically configuration with an interlayer distance of 0.34 nm. The effect of the oxidation process can clearly be detected in Figure III.12c and d. The acid treatment of MWCNTs causes severe etching of the graphitic surface and hence the size of the nanofillers is affected in length and diameter.[304] The length is reduced to 25-30 μm.

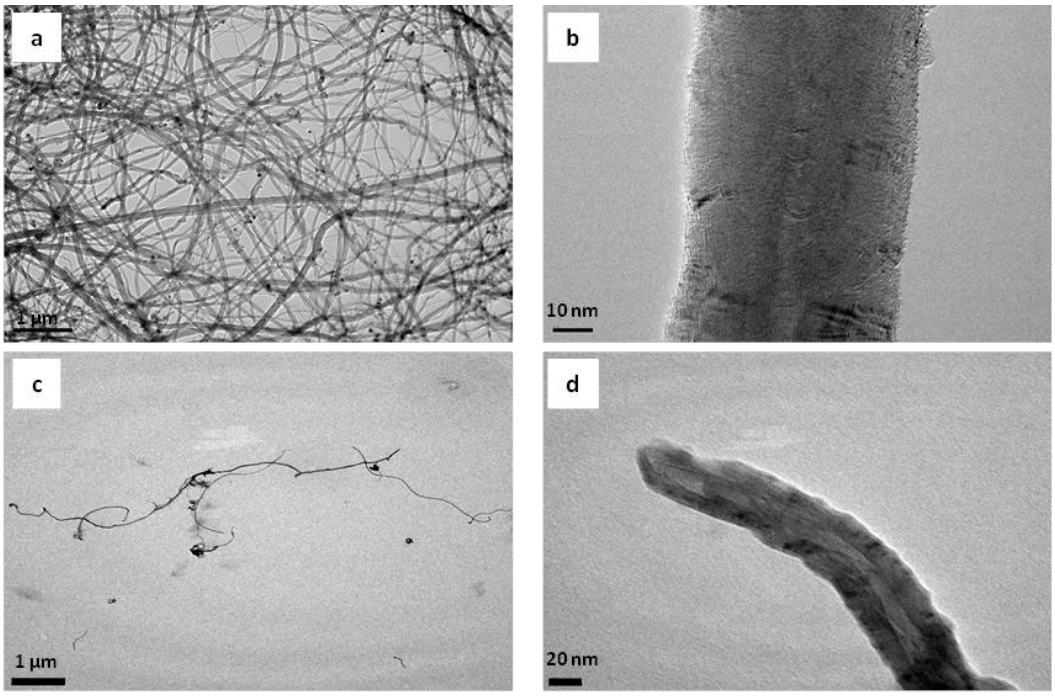

Figure III.12: TEM images of the a) and b) pristine MWCNTs and c) and d) o-MWCNTs.

Diameter distribution of the inner and outer diameter of the nanotubes was carried out using ImageJ software (W.S. Rasband, US. National Institutes of Health, Bethesda). Histograms are presented in Figure III.13 where distributions with only one head are obtained for the outer and inner diameter for MWCNTs and o-MWCNTs. We can observe how the oxidation process reduces the outer diameter of the MWCNTs from 43.8 ± 12.7 nm to 32.7 ± 9.8 nm while the inner diameter is maintained constant.

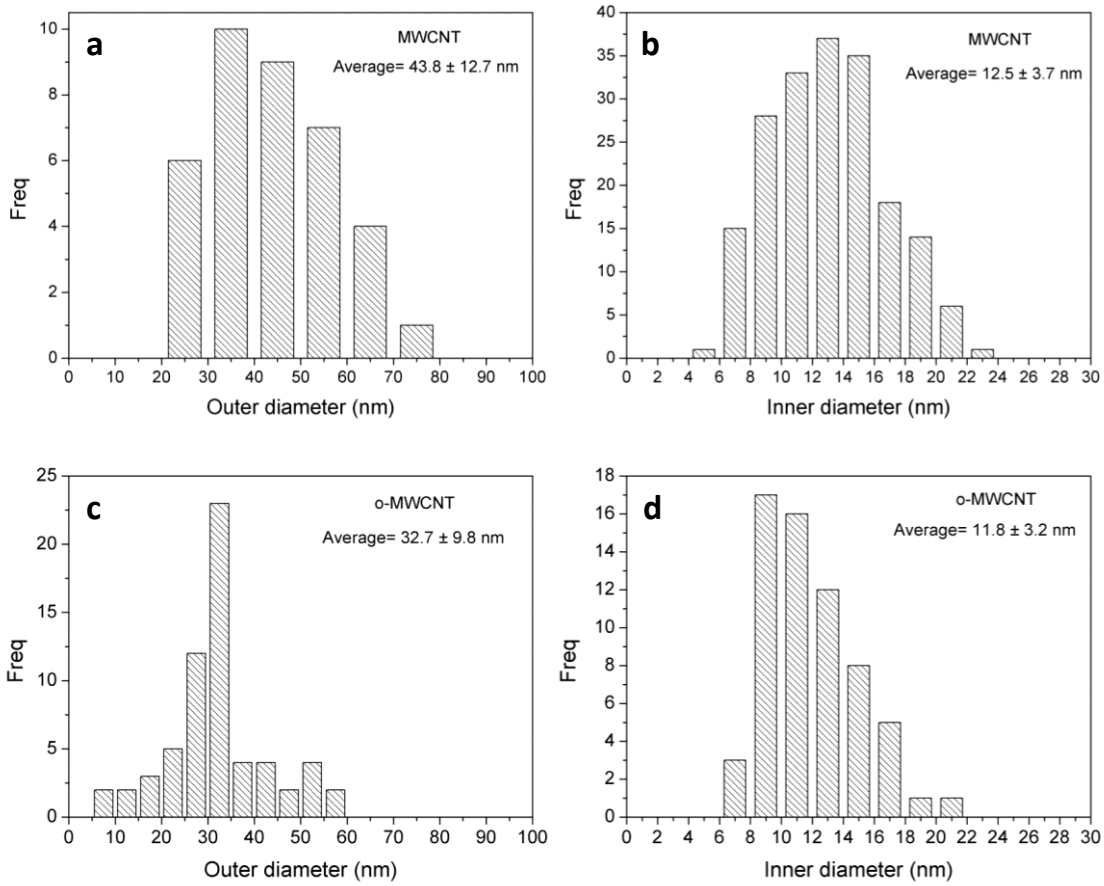

Figure III.13: Diameter distributions of the MWCNTs a) outer diameter, b) inner diameter and for the o-MWCNTs c) outer diameter, d) inner diameter.

Considering the length measured by SEM and the outer diameter of the CNTs, we can calculate the L/D aspect ratio of the MWCNTs which is higher than 3600 and 900 for the o-MWCNTs. Thostenson *et al.*[305] developed the Equation III.1 to calculate the density of CNTs with their inner and outer diameters, the results are summarized in the Table III.2:

$$\rho_{CNT} = \frac{\rho_{graphite} \cdot (d_{outer}^2 - d_{inner}^2)}{d_{outer}^2} \qquad \text{Equation III.1}$$

Finally, following the indications of Peigney *et al.*[306] the specific surface area of the MWCNTs and o-MWCNTs produced would be close to 50 m^2/g and 60 m^2/g, respectively.

Table III.2: Structural properties of the MWCNTs and o-MWCNTs.

	Length (μm)	**d_{outer} (nm)**	**d_{inner} (nm)**	**L/D**	**ρ (g/cm^3)**	**SSAA (m^2/g)**
MWCNTs	160	43.8	12.5	1600	2.05	50
o- MWCNTs	30	32.7	11.8	900	1.95	60

III 3. SYNTHESIS AND CHARACTERIZATION OF THERMALLY REDUCED GRAPHENE

The synthesis of thermally reduced graphene sheets (TRG) was carried out following the steps illustrated in Figure III.14. First, graphite oxide (GO) was produced using natural graphite powder (universal grade, 200 mesh, 99.9995 %, Fluka) according to the Brödie method.[307, 308] In a typical preparation procedure, a reaction flask with 100 mL of fuming nitric acid was cooled to 0 °C in a cryostat bath for 20 min. Then, the graphite powder (5 g) was carefully added and stirred to avoid its agglomeration. After that, $KClO_3$ (40 g) was gradually added over 1 h, in order to avoid sudden increases in temperature due to the exothermic nature of the reaction. The mixture was stirred for 21 h maintaining the reaction temperature at 0 °C. Next, it was diluted in distilled water and filtered using a PTFE membrane until the filtrate reached a neutral pH. The GO obtained was dried and stored in a vacuum oven at 50 °C until use. Then, the GO was thermally exfoliated at 1000 °C and under an inert argon atmosphere for a short time, usually less than 1 min, to produce the TRG. Finally, TRG was stored in a sealed container prior to use.

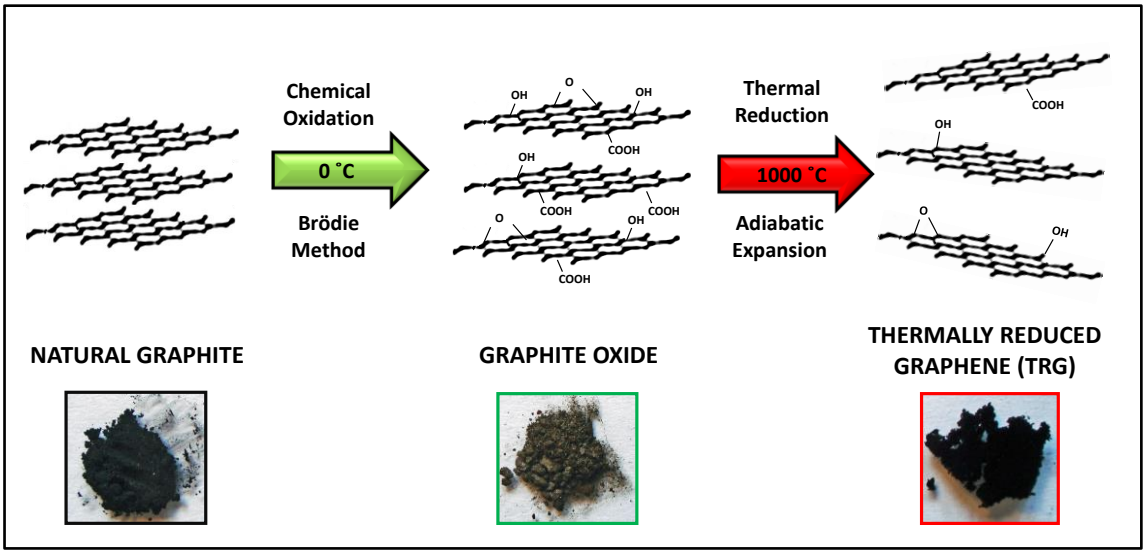

Figure III.14: Scheme of the synthesis of TRG.

As for the MWCNTs, TRG was characterized by FT-IR, Raman spectroscopy, XPS, TGA and TEM. In addition, X-ray diffraction (XRD) was employed to evidence the oxidation and the exfoliation of the sheets after the thermal treatment.

XRD data were obtained for natural graphite, GO and TRG. A diffractometer (Bruker, D8 Advance) was employed with a radiation source of CuK_{α} and wavelength λ_w= 1.54 Å operated at 40 kV and 40 mA. The incidence angle (2θ) was fixed between 3° and 70° and the scan rate was 0.02 °/s.

The successful exfoliation of TRG is corroborated by the changes on the interlayer distance calculated from the XRD data. X-ray diffraction patterns of the natural graphite, GO and TRG are shown in Figure III.15. Natural graphite presents a peak at 2θ = 26° corresponding to d = 0.34 nm graphite interlayer spacing calculated from the Bragg's law (Equation III.2).

$$n\lambda_w = 2d\ sin(\theta)$$ Equation III.2

During the oxidation process, graphite flakes break down into smaller GO flakes. The value of the 2θ diminishes to 17° (d = 0.52 nm) due to the intercalation of oxygen groups.[282] While the XRD pattern of the TRG does not present any diffraction

peak indicating that a high degree of exfoliation was achieved during the thermal reduction.[309]

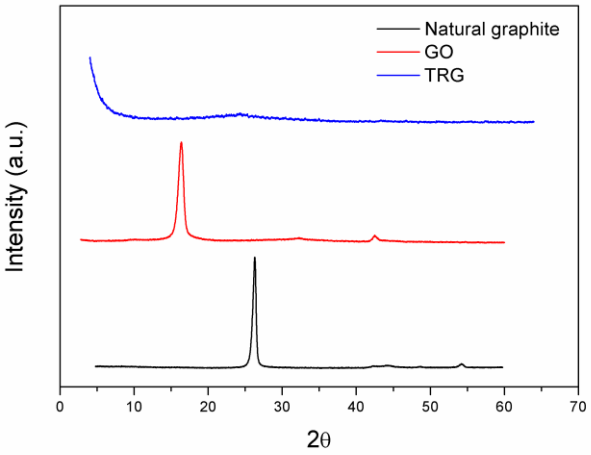

Figure III.15: XRD patterns of natural graphite, GO and TRG.

The infrared spectrum of TRG is shown in Figure III.16. It can clearly be observed a broad absorption band in the region 3700-3000 cm^{-1} corresponding to stretching vibration of surface hydroxyls (~ 3400 cm^{-1}) and water absorption (~ 3200 cm^{-1}). The features at 2920 cm^{-1} and 2851 cm^{-1} are attributed to asymmetric and symmetric stretching of sp^3 CH_2 groups.[310] There is a shoulder at 1730 cm^{-1} and a broad absorption band at ~ 1630 cm^{-1}, respectively, corresponding to C=O stretching and skeletal vibrations of un-oxidized aromatic domains as well as vibrations of the cyclic ether groups (C-O-C) or water molecules.[311] The band at ~1400 cm^{-1} is assigned to C-OH groups in amorphous defects (sp^3 hybridization) or particle edges and the significant band at 1261 cm^{-1} represents C-O stretching indicating the presence of the –COOH bonding.[312]

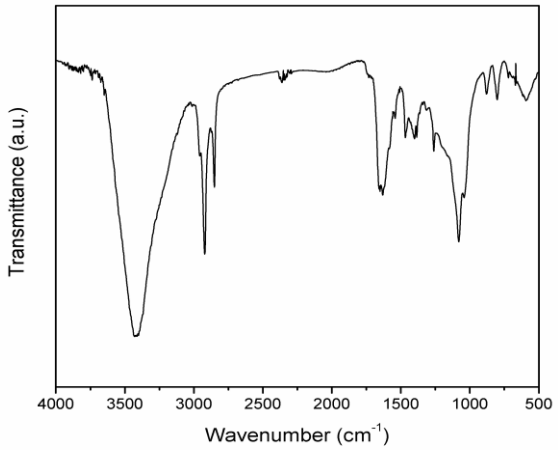

Figure III.16: FT-IR spectrum of TRG.

Raman spectroscopy was employed to evaluate the crystallinity and structure of TRG. Therefore, Raman measurements of natural graphite and TRG were performed in order to confirm the changes on the graphic structure of the TRG produced by the rapid exfoliation (Figure III.17) of GO. Both Raman spectra present the two well-known relative intensity D and G bands, previously explained in the characterization of MWCNTs. The Raman spectrum of natural graphite (inset of Figure III.17) displays the intensity of the G band at 1575 cm^{-1} while it upshifts towards 1587 cm^{-1} for TRG which has been attributed to the single-layer graphene sheets.[313, 314] Furthermore, it is worth noting that the D and G bands broaden for TRG compared to natural graphite thereby increasing the I_D/I_G ratio. This ratio takes a value of 0.77 for the TRG and 0.06 for natural graphite. The changes observed on the G and D bands for TRG and the differences on the I_D/I_G ratio are ascribed to a higher disorder in the graphite structure of TRG, confirming that some sp^3 carbon remain in TRG due to intercalation of oxygenated groups between the layer of natural graphite to produce GO.[315]

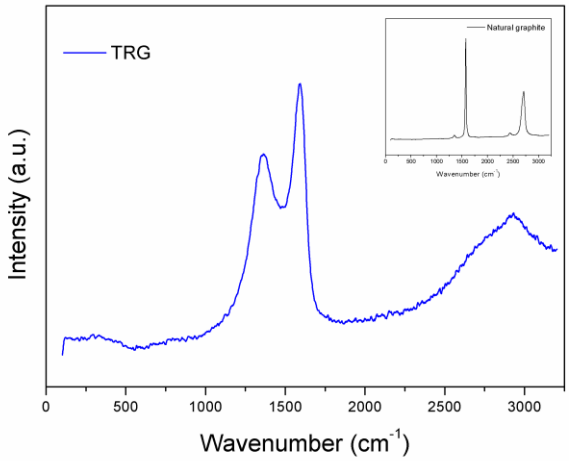

Figure III.17: Raman spectrum of TRG. The inset corresponds to the spectrum of natural graphite.

XPS was employed to analyze the nature and the relative amount of oxygen-containing functional groups present on the graphene surface.

The C_{1s} and O_{1s} XPS spectra are shown in Figure III.18 and the relative amount and the corresponding assignment of binding energy are summarized in Table III.3. All peaks are decomposed into several symmetrical components (four for C_{1s}, two for O_{1s}). The most intense peak between 284.6-285.8 eV in the C_{1s} spectra is assigned to sp^2 and sp^3 carbon atoms. Meanwhile, the peaks on the region 286.3-286.5 eV and 288.0-289.0 eV correspond to C-O-C and –O-C=O functional groups, respectively.[283, 299] It is worth noting that the peak corresponding to the signature of graphitic carbon (291.0-291.5 eV) is still present in the TRG. This peak is known as the shake-up satellite of the 284.5 eV peak and it is characteristic of graphitic systems.[316]

Although the C_{1s} spectrum provides information about the possible functional groups on TRG, some conflicts can be found on the correct assignments of these groups. Therefore, the O_{1s} spectrum complements the C_{1s} spectrum as has been previously said. Deconvolution of the O_{1s} spectrum resulted into two peaks: (i) at 531.5 eV corresponding to –O-C=O groups and (ii) between 533.5-533.9 eV assigned to C-O-C groups.

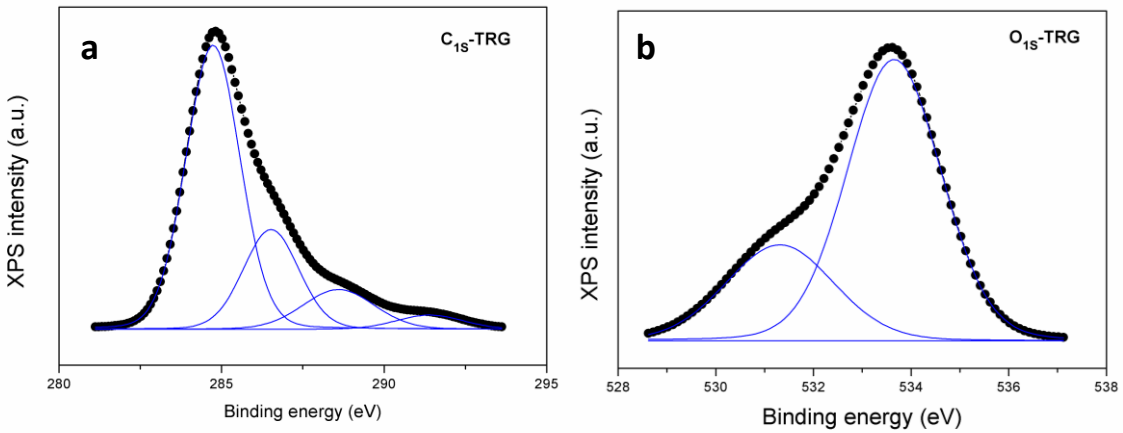

Figure III.18: C_{1s} and O_{1s} XPS spectra of TRG.

Table III.3: Peaks, binding energy, assignments and atomic percentage of TRG.

Peak	Binding energy (eV)	Assignment	Atomic % in TRG
C_{1s}	284.6-285.8	C-C sp^2 C-C sp^3	65
	286.3-286.5	C-O-C	17
	288.0-289.0	-O-C=O	16
	291.0-291.5	π-π*	3
O_{1s}	531.5	-O-C=O	26
	533.5-533.9	C-O-C	74

The thermogravimetric analysis of TRG in air atmosphere is presented in Figure III.19. The TRG sample shows two degradation temperatures at 285 °C and 575 °C. The first degradation temperature corresponds to the functional groups such as hydroxyl, carboxyl and epoxy groups on the surface of the graphene sheets, as it has been observed by FT-IR and XPS. The second step at 575 °C is due to the degradation of the carbon backbone.

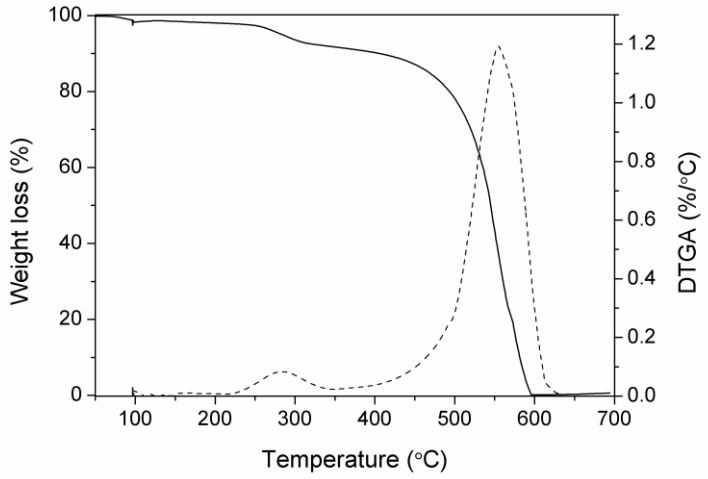

Figure III.19: TGA and DTGA curves of TRG.

TEM images (Figure III.20a) show the characteristic wrinkled structure of the particle due to the thermal shock to which it has been subjected. Figure III.20b shows the presence of stacks of a small number of graphene sheets, of up to 7 layers, with inter-graphene spacing of 0.6 nm. The selected area electron diffraction pattern of those stacks presents only weak and diffuse rings, confirming the loss of long range ordering. This result is in agreement with a study where the exfoliation of TRG particles on single sheets was found to be roughly 80 % of the material.[282]

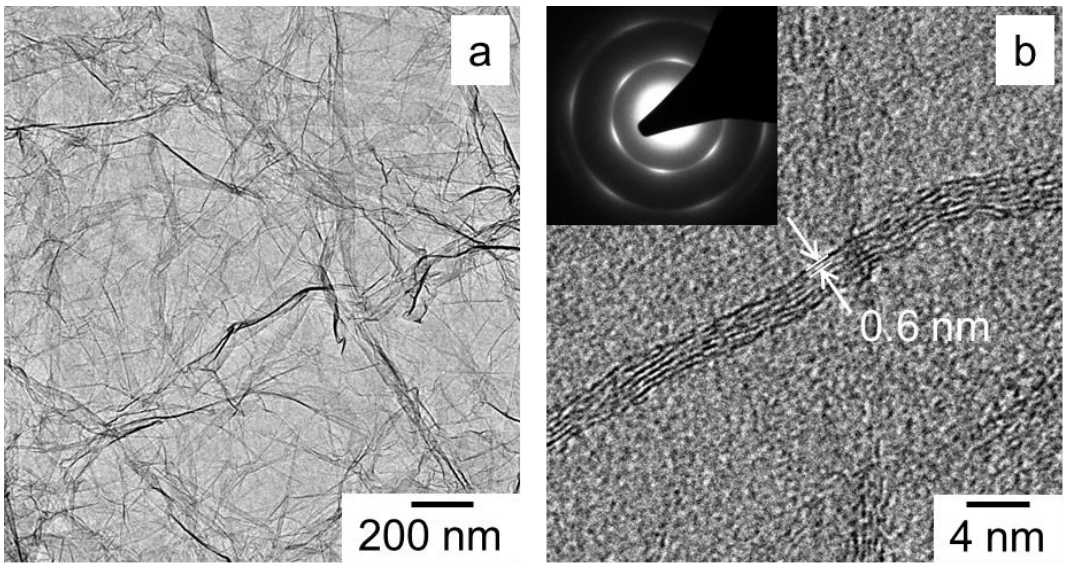

Figure III.20: TEM images of TRG at a) low resolution and b) high resolution.

III 4. SUMMARY

In this chapter, carbon nanoparticles (MWCNTs, o-MWCNTs and TRG) have been synthesized, functionalized and characterized to be used as reinforcements of the epoxy resin composites.

MWCNTs were synthesized by the CVD method obtaining nanotubes with high crystallinity and low defects as it could be observed thorough Raman spectroscopy. A high degree of alignment was detected by SEM while TEM let us measure the diameter distribution and final aspect ratio (L/D > 3600) of the MWCNTs. These nanoparticles were oxidized to obtain the so called o-MWCNTs which presented functional groups on their surface determined by the XPS and FT-IR analyses. Besides, the Raman study showed that the oxidation process affected the crystallinity of the MWCNTs, due to the disruption of the aromatic structure by the functional groups. The thermal oxidative stability of the nanotubes was affected by the oxidation and a reduction on the temperature of decomposition of the carbon backbone was observed. Finally, TEM images showed the effect of the acid treatment on the sidewalls of the nanotubes, reducing the diameter and the length of the nanotube.

Finally, TRG was synthesized by the thermal expansion of the GO. The exfoliation of TRG was confirmed from the XRD data where the peak corresponding to the natural graphite almost disappeared. Meanwhile, Raman spectroscopy displayed an increase of the relative intensities for TRG and an upshift of the G band attributed to the single-layer graphene sheets. Additionally, XPS spectra confirmed the presence of some functional groups attached to the layers that could also be observed in the FT-IR spectrum. Finally, TEM images established the exfoliation of the TRG on single sheets or stacks of a few layers.

Chapter IV. THERMALLY CURED EPOXY NANOCOMPOSITES

Part of the work described in this chapter has been published in the following journals:

- *Nanoscale Research Letters*, Vol. 6: 610 - 617 (2011).
- *European Polymer Journal*, Vol. 49: 1347 - 1353 (2013).
- *RSC Advances* (2014) - Article submitted.

IV 1. INTRODUCTION

The addition of CNPs into epoxy resins has become a popular strategy to modify and add new properties to the resin. Since the discovery of graphene in 2004, graphene/epoxy nanocomposites have attracted the same attention as the previously developed CNTs. This chapter compares the differences obtained between CNT and graphene epoxy nanocomposites cured via thermal treatment. First, we analyzed the filler percolation in the pre-cured state and the effect of the CNPs on the curing reaction. Finally, the properties of the cured nanocomposites were compared differentiating the geometry and functionalization of the nanoparticle's surface.

It is well known that the greatest enhancements on the properties of nanocomposites are reached when a network of the filler is formed within the polymer matrix. There are two main strategies to analyze filler networks when we use conductive particles. The first one is by analyzing the rheological response of the dispersion in the liquid state and the second one is by evaluating the electrical properties.[116, 317-319] In both cases, the material presents a clear change of the variables involved in the analysis when we pass from a non-percolated system to a percolated one. It is worth mentioning that the rheology of the dispersions plays a key role from a processing point of view due to the large increments in the viscosity of the system when CNPs are added, favoring the presence of voids.

The study of the curing process in thermosetting polymers is particularly relevant since the final properties of the material depend on the good progress of the reaction and hence, it will determine the applications of the material as well as the processing variables and cost. For this reason, the knowledge about the curing reaction and the dynamics of the polymer chains throughout the whole process is of great interest. Traditionally, curing kinetics of epoxy resins have been studied by Fourier Transform Infrared Spectroscopy (FT-IR), Differential Scanning Calorimetry (DSC) and rheology. In this chapter, we present a new approach based on NMR experiments to obtain the extent of reaction which is consistent and/or complementary to the traditional methods mentioned before. In addition, double-quantum (DQ) NMR experiments can provide information of the chain mobility and final structure of the network.

Finally, enhancements on the thermal conductivity in the liquid and cured state of the nanocomposites were observed. The increment on the conductivity in the pre-cured state was correlated with the catalytic effect of the CNPs on the curing reaction. In addition, the thermal conductivity of the cured nanocomposites was enhanced depending on the type of CNP. Comparisons of the mechanical performances of the nanocomposites were also evaluated.

IV 2. EXPERIMENTAL

Diglycidyl ether of bisphenol-A epoxy resin (product number: D3415), and diethylene triamine curing agent (D93856) used in this study were purchased from Sigma–Aldrich. For some comparative studies with the CNPs described in the previous chapter, SWCNTs (519308; diameter 1.2 to 1.5 nm; length 2.5 μm; and specific surface area 1300 m^2/g) from Sigma-Aldrich were also employed.

TRG and MWCNTs were directly dispersed in the epoxy resin by means of Ultraturrax and sonication bath. A mixing procedure at 30000 rpm for 10 min and then 60 min in an ultrasonic bath at 60 °C was carried out to reach a good dispersion of the carbon filler in the epoxy resin. The following protocol was carried out to cure the formulations: the liquid formulations containing CNPs and epoxy resin were mixed with diethylene triamine in a stoichiometric ratio; the blends were degassed for 15 min in a vacuum chamber and casted in Teflon molds. Thermal treatments of 60 min at 70 °C and 90 min at 130 °C were applied to complete the curing reaction. The whole experimental procedure is summarized in Figure IV.1.

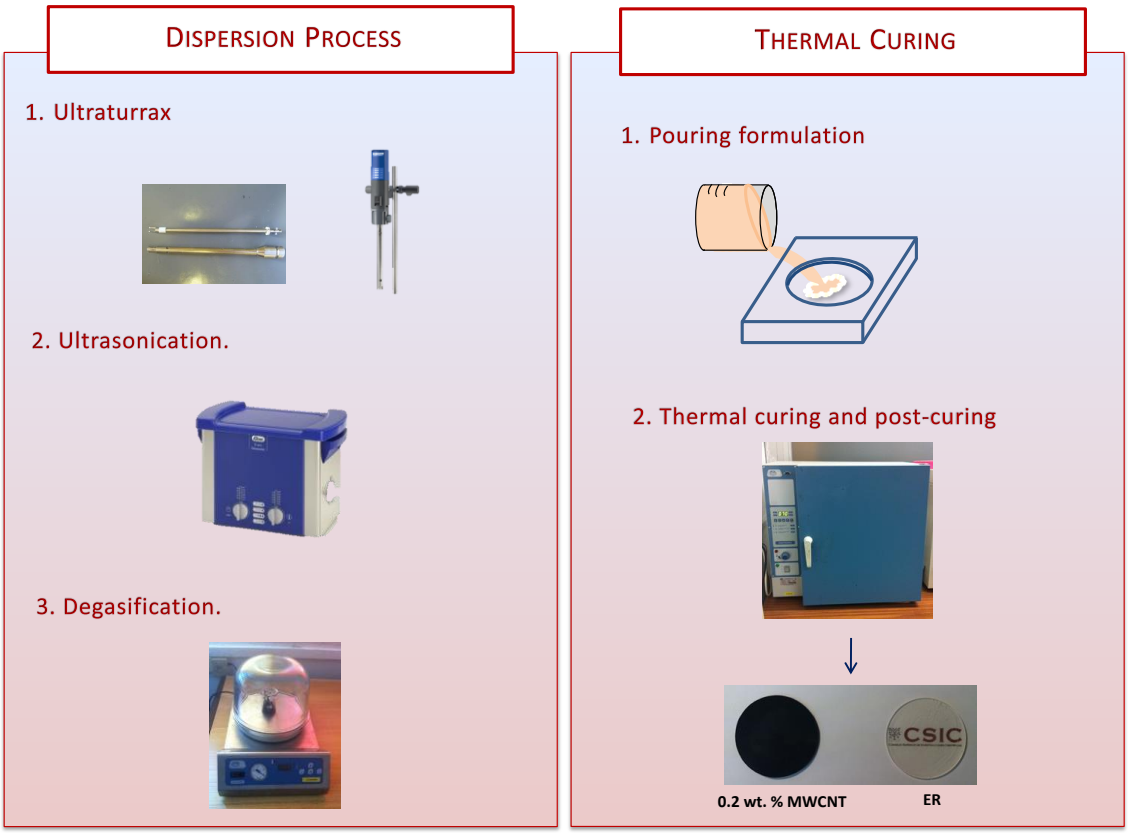

Figure IV.1: Experimental procedure of the preparation of thermally cured composites.

The rheological measurements were performed using a TA Instruments Advanced Rheometer AR1000. The geometry used was a stainless-steel parallel plate with a diameter of 25 mm. The gap was fixed to 0.25 mm and the measurements were recorded in frequency from 0.01 to 100 Hz at 21 °C and at amplitude of 1 % in order to be within the linear viscoelastic range. The results are averaged over three different samples. The standard error for each set of samples was less than 1 %. When the rheometer was used to analyze the curing reaction, time sweeps at 1 Hz and 15 µNm at three different temperatures (40 °C, 70 °C and 100 °C) were carried out.

DSC measurements were performed to characterize the curing reaction using a Mettler Toledo822e. The curing process was studied through dynamic scans from 25 ºC to 250 ºC at a heating rate of 10 ºC/min and isothermal scans at 40 °C, 70 °C and 100 °C. After the isothermal scans, a dynamic scan was programmed to evidence the post-curing heat release.

^{1}H DQ-NMR measurements were performed on a low-field Bruker Minispec DQ20 spectrometer at 20 MHz proton resonance frequency (0.5 T) with 90° pulses of 3 μs length and a dead time of 12 μs. The sample temperature was controlled with a BVT3000 heater working with air. More details about this technique can be found in the Annex I of this thesis.

The thermal conductivity of the uncured nanofluids (the samples do not contain the curing agent) was measured with a KD2 probe (Decagon Devices Inc., Pullman, WA, USA), based on the hot wire technique, and consisting of a needle located inside the sample, as can be seen in the experimental setup in Figure IV.2. The hot wire enabled us to obtain the thermal conductivity in a direct and easy way. The needle had a waiting time of 30 s until the sample temperature was stable and heated up the sample for 30 s. Then, it was used to monitor the cooling rate and calculate the thermal conductivity with an accuracy of 5 %. The measurements were carried out over a temperature range from 30 °C to 60 °C. In this range of temperature, no convection was present in the liquid. The results were the average of at least six measurements for each sample.

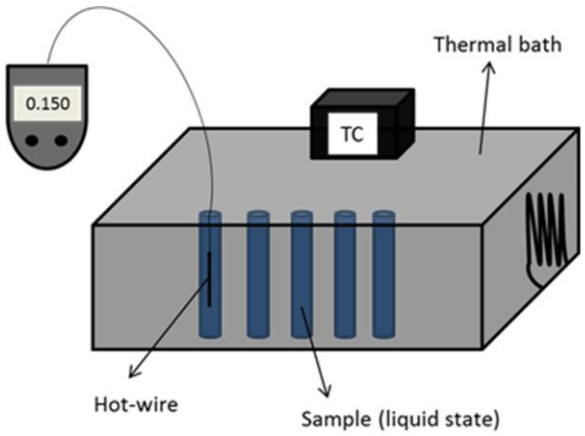

Figure IV.2: Experimental setup to measure the thermal conductivity of the uncured nanofluids.

On the other hand, the thermal conductivity of the cured samples was measured using a hot disk apparatus. This method was based on a heat balance in the steady state between the sample and the three disks of the apparatus that allowed us to calculate the

thermal resistivity of the solid sample. Testing samples with different thicknesses were used to obtain the thermal conductivity of the material.

The dispersion state of the nanoparticles was examined using transmission electron microscopy (TEM Leo 910 microscope at an acceleration voltage of 80 kV). Ultra-thin sections of the cured samples were prepared by cryo-ultramicrotomy at -140 °C (Leica EM UC6).

Tensile tests were performed with dog-bone specimens using an Instron model 3366 tensile tester at a crosshead speed of 1 mm/min. The results are the average of at least five measurements.

IV 3. RHEOLOGICAL FILLER PERCOLATION

The formation of filler networks in nanocomposites can be determined evaluating the rheological response in the melt state of the system. In the case of epoxy resins, the rheological measurements have to be performed before the curing reaction takes place.

Figure IV.3a shows the variation of the complex viscosity versus frequency for the studied systems. Epoxy resin clearly has a Newtonian flow behavior with the viscosity independent of the frequency. The addition of MWCNTs significantly alters the flow behavior of the epoxy dispersions. The viscosity gradually increases as the MWCNT content increases. This effect is particularly evident in the low frequency range and decreases with increasing frequency due to shear-thinning behavior. When the viscosity is plotted versus the applied torque (Figure IV.3b), MWCNT dispersions present a yield stress where the viscosity tends asymptotically to infinite at a certain value of torque. Below that stress limit the material does not flow, showing a solid-like behavior. These changes in the rheological behavior are attributed to the formation of a randomly dispersed nanotube network. At high shear rates, this network breaks down and CNTs can then align in the direction of the flow and/or disaggregate[320] causing the decrease in the viscosity. The o-MWCNT dispersion does not present a shear-thinning behavior as strong as the pristine MWCNTs due to their lower aspect ratio. On the other hand TRG does not change the Newtonian regime of the pristine epoxy resin. Therefore,

the effect of TRG concentration on the viscosity is much smaller compared with the viscosity enhancement produced by MWCNTs.

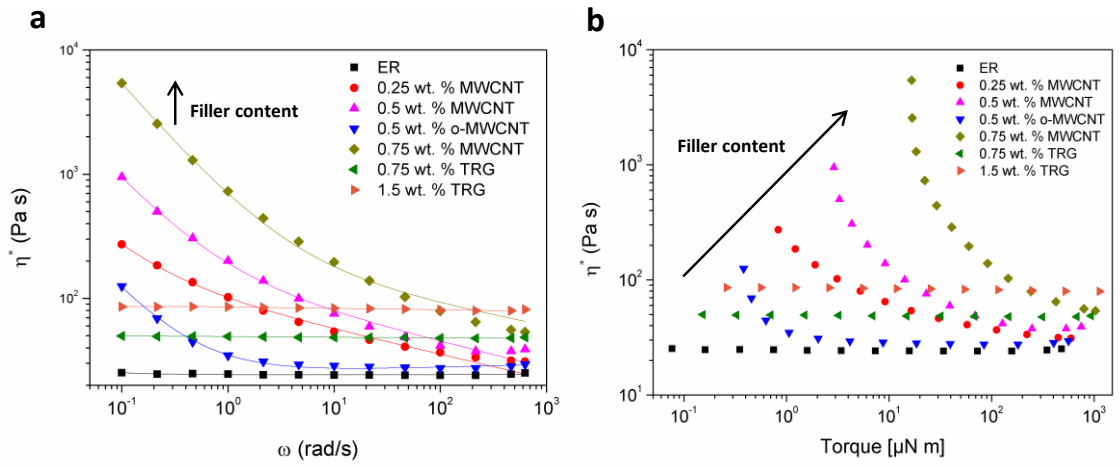

Figure IV.3: η evolution of the epoxy/nanofiller dispersions: (a) versus frequency where the symbols correspond to the experimental result and the solid line with the Herschel–Bulkley model and (b) versus the torque.*

The increase in the viscosity as a function of MWCNT loading fraction and the change from Newtonian to shear-thinning response can be ascribed to the particle–particle and/or polymer–particle interactions. Poetschke *et al.*[321] found similar empirical results between CNTs and expanded graphite while Knauert *et al.*[322] performed simulations comparing the effect of nanoparticle shape, spherical, rod-like, and sheet-like nanoparticles, on polymer nanocomposite rheology. They found the largest increase in viscosity for the rod-like nanoparticles and the least for the sheet-like. The authors explained this phenomenon based on the number of ‘‘bridging chains’’, or polymer–particle interactions, present in the system. However, it has also been demonstrated that the destruction of a combined carbon nanotube/polymer network is feasible for polymers of high molecular weight[323] but is not contemplated for systems of low molecular weight. In our case, the system under study is a pre-polymer with a molecular weight of 337 g/mol, and, hence, it is assumed that a physical MWCNT network is the mechanism that takes place. Such consideration was proposed by Chapartegui *et al.* for CNT/epoxy dispersions.[112] Here, we observe that MWCNTs readily form a nanofiller network compared to TRG. This extended nanoparticle network is responsible for the increase in the viscosity and the change from Newtonian to shear-thinning response.

Other experimental results with sheet-like CNPs suspensions corroborate this assumption.[123, 124]

Several empirical equations have been proposed to describe the shear-thinning behavior of nanofiller dispersions. In our case the evolution of the frequency dependence of the viscosity is fitted by applying the Herschel–Bulkley model (Equation IV.1):

$$\eta^* = \frac{\tau_0}{\omega} + A\omega^{(n-1)} \qquad \text{Equation IV.1}$$

Where η^* is the complex viscosity, ω the angular frequency, τ_0 the yield stress, A the consistency index and n is the flow behavior index. When $n > 1$, the fluid exhibits a shear-thickening behavior; for $n = 1$ the fluid has a Newtonian behavior; when $n < 1$ the fluid shows shear-thinning behavior. The fitting parameters are summarized in Table IV.1 and the curves are represented with solid lines in Figure IV.3a. This model has already been used to describe the non-linear viscoelastic behavior of CNTs dispersions.[320, 324-326]

Table IV.1: Parameters of the Herschel–Bulkley fitting.

	τ_0 (Pa)	A (Pa·s^n)	n	R^2
ER	≈0	24.4	1	0.91
0.25 wt. % MWCNT	14	88.2	0.8	0.99
0.5 wt. % MWCNT	76	116.9	0.8	0.99
0.5 wt. % o-MWCNT	10	25.1	1	0.99
0.75 wt. % MWCNT	510	191.3	0.8	0.99
0.75 wt. % TRG	≈0	49.3	1	0.96
1.5 wt. % TRG	≈0	85.6	1	0.99

We can observe a good correlation of the Herschel–Bulkley model with the experimental data, providing a good prediction of the rheological behavior of the filled epoxy dispersions. The decrease of the flow behavior index with the addition of MWCNTs means that the dispersion behaves like a shear-thinning fluid. This theoretical model corroborates the tendency of the yield stress to increase with the amount of MWCNTs that is attributed to the nanofiller network which possesses certain strength by itself.

In the plot of the frequency sweep (Figure IV.4), the storage modulus (*G´*) of the neat epoxy resin follows a classical linear viscoelastic curve, this is called terminal or liquid-like behavior. In the case of the mixtures containing MWCNTs we can observe a plateau in the low frequency zone of the *G´* curves, termed as non-terminal or solid-like behavior. As the nanotube content increases the storage modulus also increases, becoming more independent of frequency and, hence, the plateau becomes larger. According to this idea and observing the curves, we are able to confirm that the rheological percolation thresholds are close to 0.25 wt. % and above 1.5 wt. % for MWCNT and TRG, respectively. These values agree with those found in the literature.[112, 327] The *G´* values for the mixtures with MWCNTs are larger than those obtained with TRG which support our theory that the MWCNTs form a stronger and more interconnected network of particles. In addition, due to their planar geometry TRG could slip one from each other when the rotational force is applied to the system leading to lower storage moduli.

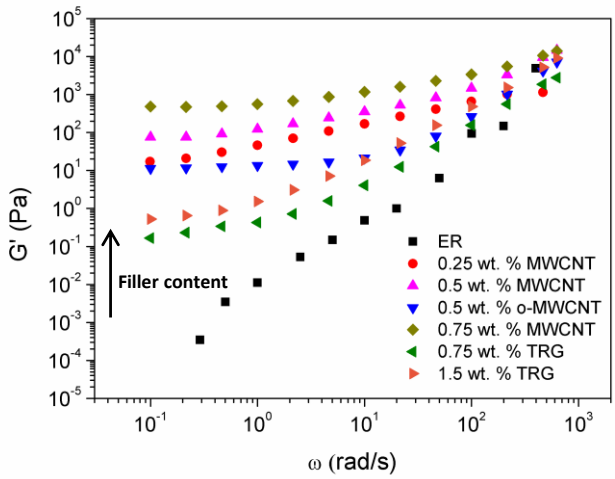

Figure IV.4: Dynamic frequency sweeps for MWCNT and TRG dispersions.

When we represent the storage and loss modulus together for the formulations with different contents of MWCNT (Figure IV.5a) we can observe that at low frequency values, the *G´* became higher than the *G´´* at 0.5 and 0.75 wt. % of MWCNT. This also evidences a solid-like behavior. The solid response characterized by *G´ > G´´* started with the lowest concentration (0.25 wt. % of MWCNT) where *G´ = G´´* at 0.1 rad/s, which indicates that the rheological percolation threshold is in the proximity of that concentration of filler. Comparing the effect of MWCNT and TRG at the same concentration (Figure IV.5b), we clearly observe the solid-like response of the MWCNT characterized by *G´ > G´´* at low frequencies while the TRG dispersion still presents a liquid- like behavior (*G´ < G´´*). This liquid-like behavior is also observed at 1.5 wt. % of TRG.

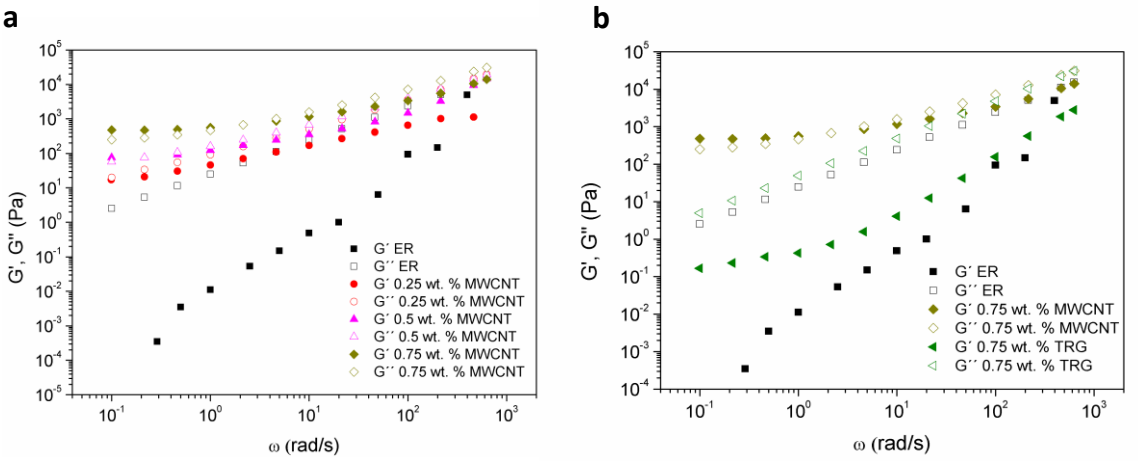

Figure IV.5: Evolution of G´ and G´´ versus frequency at room temperature for the dispersions containing (a) MWCNTs and (b) MWCNTs and TRG at the same filler content.

If we consider the damping factor (*tan δ*) definition like the ratio between *G´´/ G´*, we can represent it in a frequency sweep as in the Figure IV.6. We are able to observe the presence of a maximum that becomes broader and appears at higher frequencies when the nanoparticles are included. This peak in *tan δ* is related to molecular motions in polymers and marks a certain limit in the mobility of polymer chains in the nanocomposite.[328] It is important to notice how the presence of MWCNTs

largely reduces the value of *tan δ* due to the increase in the elastic response discussed earlier.

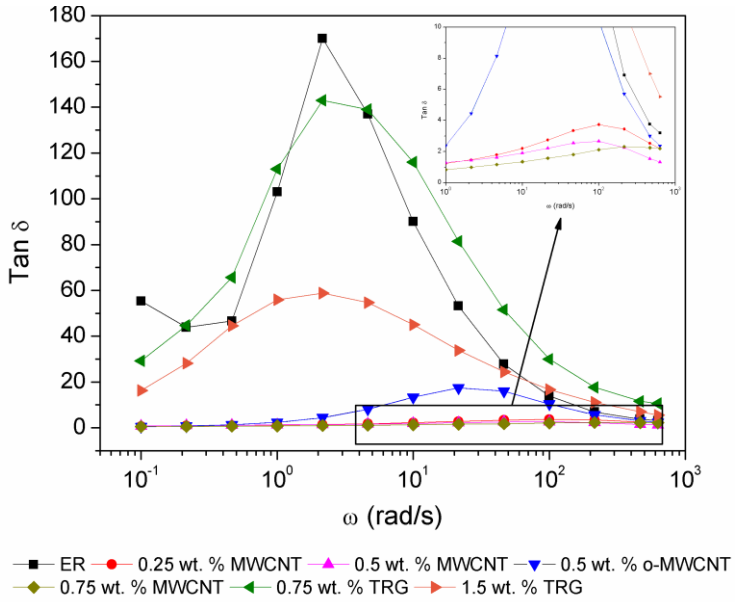

Figure IV.6: Loss tangent as a function of frequency for all the dispersions.

From the Figure IV.6, it is possible to define a characteristic time λ at which *tan δ* maximum occurs ($\lambda = 1/\omega$). At a constant temperature, the chain mobility which requires times larger than λ implies that the terminal zone is hindered. On the other hand, motions involving times shorter than λ in the high frequency zone correspond to motions across entanglements and are not hindered by the presence of any of the nanoparticles. Thus, when the *tan δ* peak appears at short times this means that the blocking effect of the particles is more effective and the mobility of polymer chains is more restricted. Looking at Table IV.2, the values of λ are notable shorter for MWCNTs than for TRG and the pristine epoxy resin. This feature is an indication that TRG blocking effect in the un-cured resin is delayed compared to the MWCNT.

Table IV.2: Values of λ for all the dispersions.

	λ (sec)
ER	$4.7 \cdot 10^{-1}$
0.25 wt. % MWCNT	10^{-2}
0.5 wt. % MWCNT	10^{-2}
0.5 wt. % o-MWCNT	$4.7 \cdot 10^{-2}$
0.75 wt. % MWCNT	$4.7 \cdot 10^{-3}$
0.75 wt. % TRG	$4.7 \cdot 10^{-1}$
1.5 wt. % TRG	$4.7 \cdot 10^{-1}$

IV 4. CURING KINETICS

Conventional techniques to analyze curing reactions of epoxy resins (FT-IR, DSC) are sensitive to the actual number of bonds created during the curing reaction.[329-332] In consequence, they provide accurate information about the initial steps of this process, but they are less sensitive to the last stages when a small number of reactions promote an abrupt increase of viscosity and mechanical properties. These changes at high conversion ratios are better characterized by rheology, but this approach is limited by the impossibility of measuring the fully cured epoxy resins.

In this section, we present a new approach based on time-domain NMR experiments to obtain the extent of reaction which is consistent and/or complementary to the traditional methods mentioned before. NMR provides molecular evidences about the evolution of epoxy resins during the curing process, being especially accurate in the final steps when the curing reaction has a direct relevance on the resin properties. In addition, double-quantum (DQ) or more generally multiple-quantum (MQ) NMR

experiments can provide additional information on the chain mobility and final structure of the resin network.

DQ-NMR has been demonstrated as one of the most effective experimental approaches to measure the residual dipolar couplings (RDCs) of soft polymers.[333] The RDC is null in isotropic mobile polymer systems, whereas it takes positive values in polymers where crosslinking points and/or entanglements hinder the chain motions leading to anisotropic systems[334, 335] (more details about the use of DQ-NMR for polymer characterization can be found in the annex of this thesis). Thus, DQ-NMR spectroscopy has successfully been used to determine the polymer dynamics in melts,[334] the gel point[336] and vulcanization kinetics,[337] and the complete and quantitative characterization of polymer network structures.[333, 336, 338] In those works, DQ experiments are based upon the lengthy but quite robust Baum-Pines (B-P) sequence,[333, 337, 339, 340] which shows ideal performance for studying soft weaker dipolar-coupled polymers systems such as elastomers[338, 341-344] and gels.[336, 345] Nevertheless, the use of the B-P sequence is limited to characterize high dipolar coupled polymers (epoxy resins would belong to this type of samples), as it was recently demonstrated for ionic elastomers.[346] The main problem is the fast decay of the associated NMR signal that almost completely vanishes during a single cycle of the B-P sequence (~ 0.09 ms). In this context, we have applied and combined two simplified versions of the B-P sequence based on the so-named five-pulse sequence.[347-349] This sequence reduces the cycle time being able to record the entire DQ-NMR signals from the epoxy resin. Therefore, studies of the structure and dynamics of the cured polymer as well as the analysis of the curing reaction are possible with the new method. Figure IV.7 shows the pulses for the B-P sequence and the shorter three and two pulses sequences respectively.

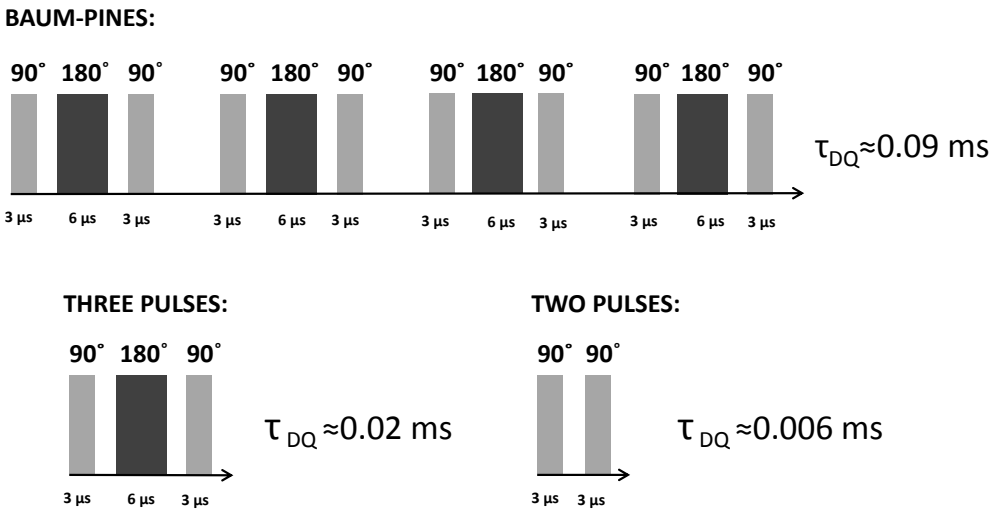

Figure IV.7: Sequences of pulses.

Before analyzing the effect of the CNPs on the curing reaction, we first evaluated the suitability of DQ-NMR experiments for the neat epoxy resin. The first step is to perform DQ experiments in the fully cured resin. The results from two different DQ-NMR sequences named as two and three-pulse sequences, respectively, are combined in order to get the complete information about the network structure of the epoxy resin (Figure IV.8).

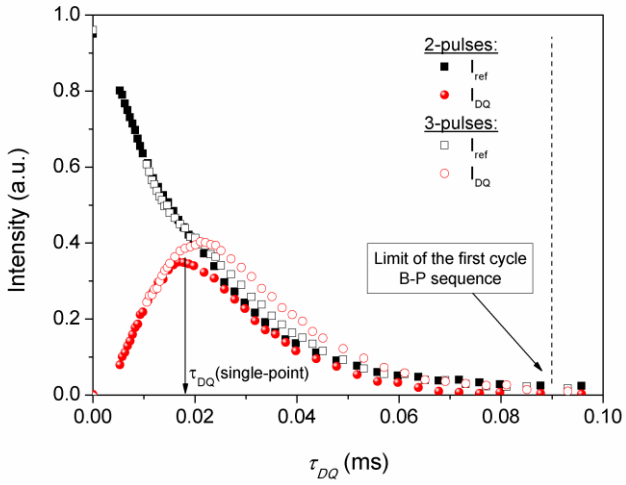

Figure IV.8: Superposition of raw data (I_{DQ} and I_{ref}, respectively) from DQ-NMR experiment based on the so-named 2-pulses and 3-pulses experiments at 100 °C for the cured ER.

Epoxy resins are high dipolar coupled polymers (closer to the rigid limit ~ 30 kHz) whose associated signal decays almost completely during a single cycle of the B-P sequence (~ 0.09 ms). For that reason DQ-NMR experiments based on the so-named five-pulse sequence are required for reaching the minimum pulse sequence cycle time of ~ 0.0053 ms (named 2-pulse sequence).[348, 350, 351] In order to provide better stability and long-time performance of the two-pulse segment for DQ excitation and reconversion, a refocusing π pulse was also introduced in each sequence block, reaching a minimum sequence cycle time of ~ 0.01 ms (named 3-pulse sequence). According to the results shown in Figure IV.8, the signals from both experimental approaches perfectly superimpose at times close to the minimum 3-pulse cycle time. This pulse sequence shows better efficiency at longer excitation times, but it is too lengthy to access to the highest dipolar coupled segments that compose the complex network structure of the studied epoxy resin. For that reason, the combination of both experimental approaches are required to get the complete picture of these highly dipolar coupled samples.

As it is shown in Figure IV.9, the combined raw signals (I_{ref} and I_{DQ} in Figure IV.9a and Figure IV.9b, respectively) are normalized to properly separate the temperature dependent segmental dynamics (defined in $I_{\Sigma MQ}$, Figure IV.9c) from the temperature-independent network structure effect (encoded in I_{nDQ}, Figure IV.9d), according to the procedure explained elsewhere.[333, 338] To take into consideration the duty-cycle dependent scaling factor, the DQ pulse sequence (evolution) time τ_{DQ} was scaled by a pre-factor of 3/2 and thus renders the data directly comparable with the results obtained from the widely used B-P sequence.[333]

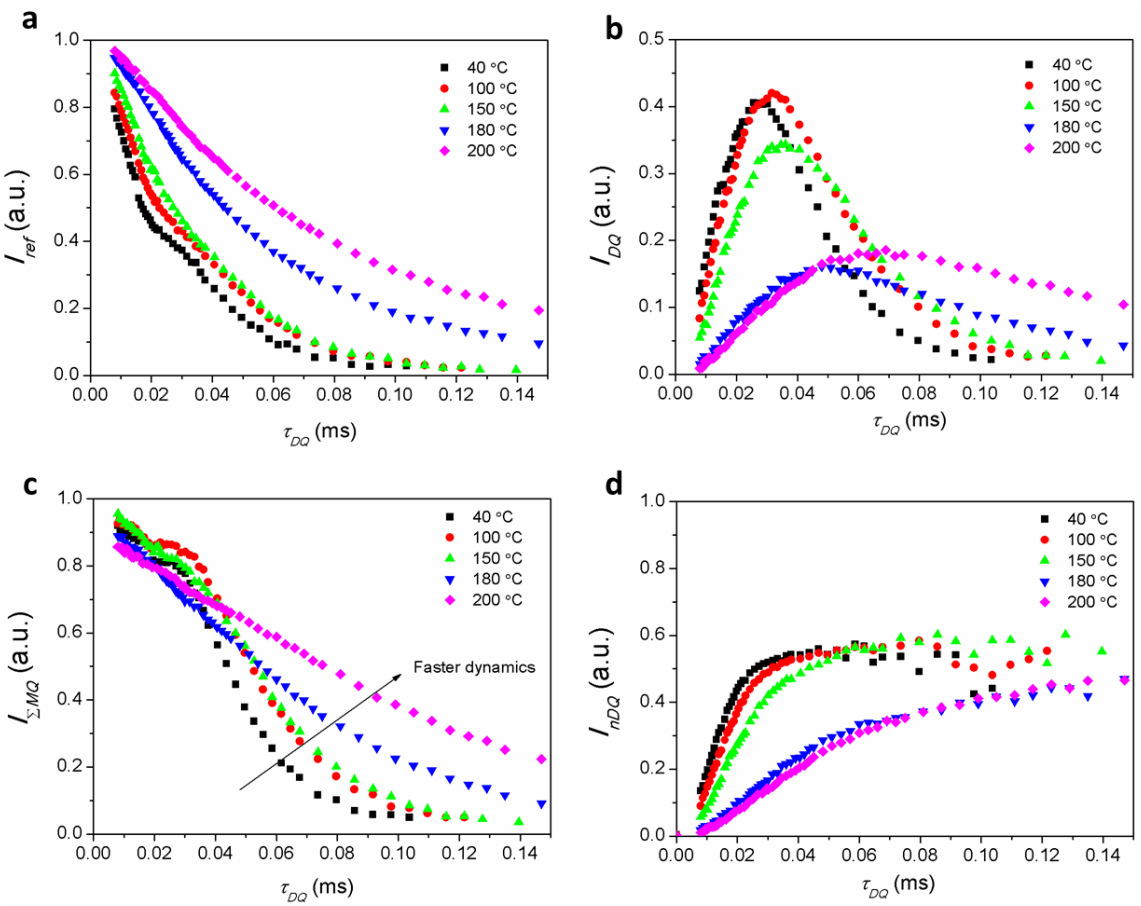

Figure IV.9: NMR signals at three different temperatures for the cured ER, a) I_{ref}, b) I_{DQ}, d) $I_{\Sigma MQ}$ and d) I_{nDQ}.

The evolution of NMR signals at different temperatures reflects the dependence of both segmental dynamics and the dynamic order parameter (S_b). The slower decay in the $I_{\Sigma MQ}$ signal reveals faster dynamics of the resin at higher temperatures. It is important to appreciate the significant change in the y-intercept value and function shape at temperatures above 150 °C. Up to 150 °C, the epoxy resin does not show any long (with slowly relaxation behavior) exponential tail related to uncoupled (isotropically mobile) protons, coming from small molecules or network defects.[352] This behavior becomes apparent at higher temperatures (180 °C - 200 °C), reaching values around 10 % of the total protons in the sample (y-intercept in Figure IV.9c). This temperature dependence of uncoupled protons has been previously described in rubber samples, being related with dynamic constraints.[338, 353, 354]

The change in the shape of $I_{\Sigma MQ}$ could be related to the different dynamics regimens experimented by the sample with temperature according to the evolution of the segmental orientation autocorrelation function (OACF) of the second Legendre polynomical, *C(t)*, for this epoxy resin, partially described in Figure IV.10. The small section of the complete *C(t)* is directly obtained from the analysis of the I_{nDQ} build-up curve at short τ_{DQ}, according to the procedure described elsewhere.[334, 335] The combination of data from different temperatures allows constructing the OACF on the basis of the time-temperature superposition principle. However, the absolute value of *C(t)* cannot be calculated neither the full correlation function given on a properly referenced time scale, because of the lack of information about the quasi-static reference value (D_{stat}/k) and the entanglement characteristic time (τ_e) for this epoxy resin.[334]

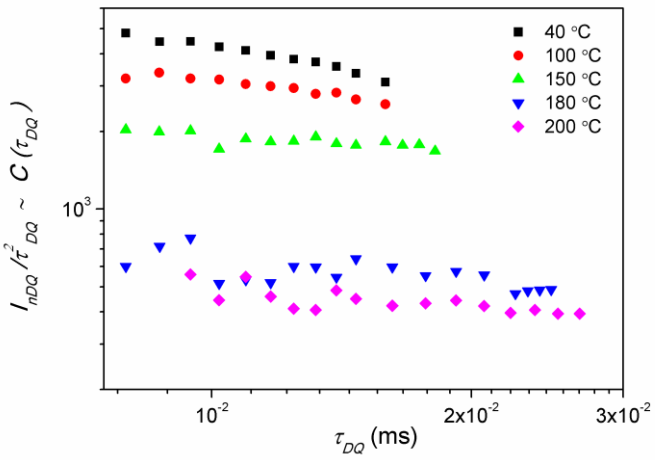

Figure IV.10: Evolution of C(t) at short DQ evolution time.

Finally, an improved numerical inversion procedure based on fast Tikhonov regularization was used to analyze the I_{nDQ} signal and determine the actual dipolar coupling distribution[355] that is related to the spatial cross-linking distribution[333, 338, 356] of the epoxy resin (see Figure IV.11).

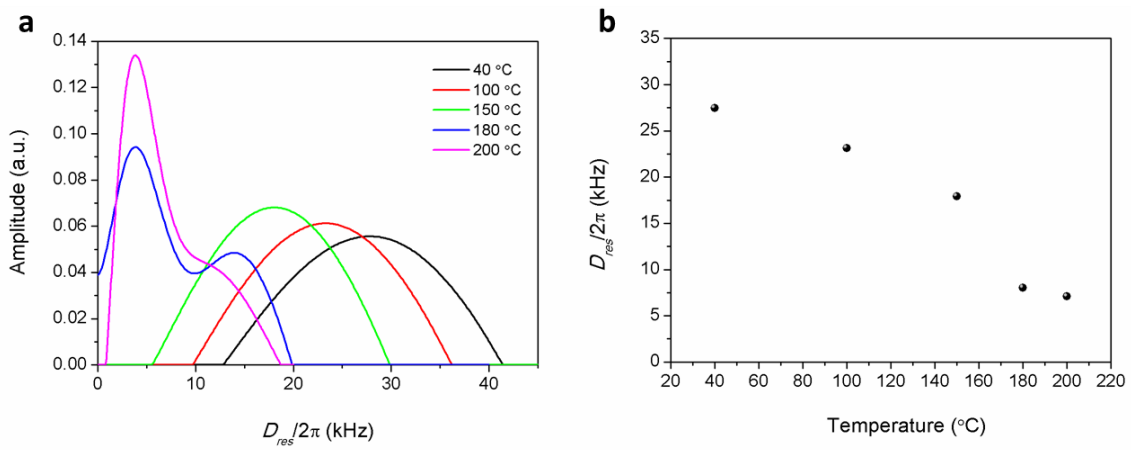

Figure IV.11: a) D_{res} distributions after Tikhonov regularization and b) D_{res} evolution with the temperature.

By comparing the different pieces of *C(t)*, there is a clear change in the time scaling exponent derived from different dynamic regimens at 150 °C (Figure IV.10). At lower temperatures, the epoxy resin is below the glass transition temperature (T_g = 116 °C according to DMA analysis) and close to the static regimen (~ 30kHz) as shown in Figure IV.11a. When the temperature rises, the faster dynamics allows enlarging the analyzed length-scale in the time window explored by the NMR experiments. Hence, the dynamic local parameter (directly proportional to the measured $D_{res}/2\pi$ in Figure IV.11b) decreases until it reaches a plateau close to the highest temperature (limited by the used low-field spectrometer). At that temperature, dynamics are fast enough to average out all the available segmental configurations between constraints and consequently, the measured dipolar coupling distribution (Figure IV.11a) is directly related to the actual spatial distribution of cross-links as it has been demonstrated in other works.[333, 338, 342, 356]

These results demonstrate that the application of short DQ-NMR sequences at the appropriate temperature is a valid method to obtain molecular evidences about the different factors that describe the network structure of the epoxy resins, *i.e.* the fraction of non-coupled segments/molecules, the cross-linking density and the spatial distribution of cross-links.

With the five-pulse sequence described above, the measurement of the full DQ evolution time is useful to quantitatively evaluate the invariant network structures of fully cured epoxy resins, but it is not applicable to networks under evolution, e.g. epoxy resins during the curing process. Thus, a faster method (but still sensitive to the cross-linking density) involving the evaluation of the DQ intensity in a single DQ time is required to characterize the curing kinetics of epoxy resins.

The single-point approach has been successfully used before to study the gelation and vulcanization kinetics of soft polymers.[336, 337] In the case of higher dipolar coupled epoxy resins, it is possible to follow the same experimental procedure explained elsewhere,[336] but now it is mandatory to use the shorter 3-pulse sequence approach in order to have access to the DQ intensity (I_{DQ}) that codifies the information about the cross-linking density. The most appropriate DQ time (~ 0.02 ms whose intensity is used to define the extent of the reaction, see Figure IV.8) is selected next to the maximum in I_{DQ} from a fully cured sample, which would be used for the subsequent curing under isothermal conditions (40 °C, 70 °C and 100 °C). It means that fast changes on the cross-linking density during curing can be followed by using single-point detection, obtaining the classical reaction kinetic curve with a sigmoidal shape as in Figure IV.12.

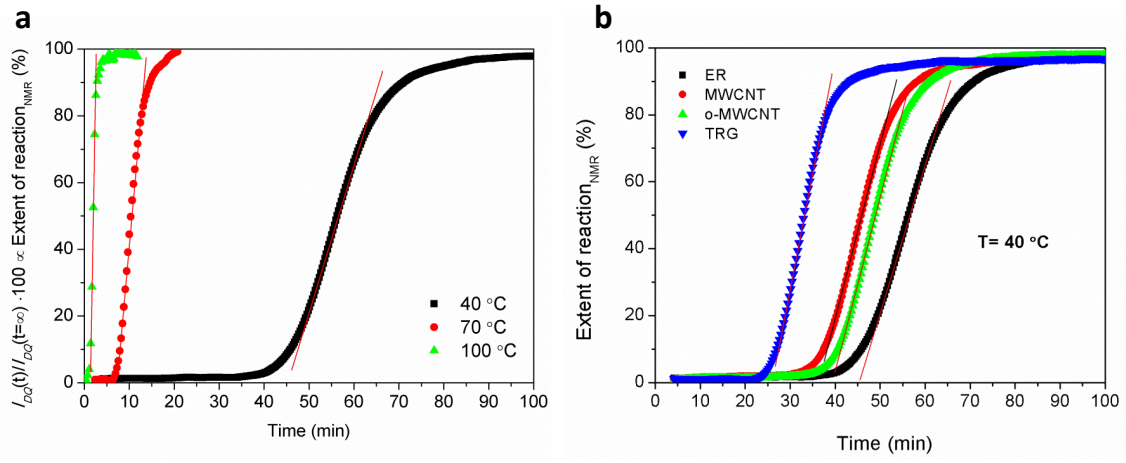

Figure IV.12: Curing curves for a) neat epoxy resin at three different temperatures and b) nanocomposites at 1 wt. % of filler and 40 °C.

In order to compare the kinetic parameters obtained by NMR with some other complementary techniques, it is important to point out that I_{DQ} only rises up when the initial isotropic liquid system is transformed during the curing reaction in a polymer network with non-isotropic movements. The formation of enough cross-links and topological constraints promote the persistence of some RDCs at the measured temperature. We can define this moment as the NMR induction time of the curing reaction. Opposite to other complementary techniques (e.g. FT-IR or DSC), during the induction time (measured by DQ-NMR) there are numerous initial reactions between monomers and curing agent that have no relevance in the NMR signal because the formed products (at that reaction time) are non-dipolar coupled low molecular weight oligomers. The subsequent reactions after the induction time increase the total amount of constraints, limiting the conformational space of the polymer segments and increasing the RDCs. Therefore, the NMR signal increases with the curing time according to the reaction rate, giving molecular evidences about the structural evolution.

At larger curing times, the curves exhibit a decrease on the extent of reaction associated to the vitrification of the system. This process is difficult to characterize by FT-IR and DSC because of the small number of reactions involved in the process (as compared with the initial stages) and also it is quite problematic to follow it by rheology measurements because of the dramatic rise of viscosity. However, DQ-NMR is a more sensitive approach to characterize these latest stages of the reaction or even the structure of epoxy resins when they are completely cured.

Table IV.3 shows the kinetic parameters that define the curing reaction of the epoxy resin and nanocomposites at three different temperatures: 40 °C, 70 °C and 100 °C. As one can expect, the temperature facilitates the movement of reactive species and decreases the NMR induction and vitrification times and increases the polymerization rate. Figure IV.12b and the values reported in the Table IV.3 evidence a catalytic effect of the CNPs characterized by a significant reduction of the induction time and an increase on the polymerization rate and reduction of the activation energy (E_a). This effect is attributed to the increase of the thermal conductivity of the sample and to the high SSA of the CNPs.[63, 141] The oxidation of MWCNTs does not really affect the results obtained with the pristine MWCNT. Only a slight delay of the o-MWCNTs respect to the untreated ones is detected, fact that is mainly associated to the lower aspect ratio of the o-MWCNTs.

Table IV.3: Kinetic parameters obtained by DQ-NMR.

Temp.		ER	MWCNT	o-MWCNT	TRG
40 °C	**Induction time (min)**	35	30	32	22
	Vitrification time (min)	84	77	76	63
	Polymerization rate[a] (sec^{-1})	0.07	0.09	0.09	0.12
70 °C	**Induction time (min)**	7.0	3.6	4.0	2.0
	Vitrification time (min)	20	9.7	11	5.5
	Polymerization rate[a] (sec^{-1})	0.28	0.59	0.48	0.95
100 °C	**Induction time (min)**	1	0.5	0.6	0.3
	Vitrification time (min)	4	3.2	3.6	3.0
	Polymerization rate[a] (sec^{-1})	1.15	1.10	1.24	1.24
	E_a (kJ/mol)	44.6	41.9	42.6	38.8

[a]*Obtained from the slope of the linear part of the curing curve.*

The results obtained by DQ-NMR are correlated by the conventional techniques employed to analyze the curing reaction of epoxy resin. We first compare the results with rheological analysis of the epoxy resins during the cross-linking reaction. Figure IV.13a shows the evolution of the viscosity with the curing time for the ER at 40 °C, 70 °C and 100 °C, while Figure IV.13b depicts the effect of the CNPs on the viscosity at 40 °C. The rise of the viscosity is generated at the final stages of the curing reaction (as in the case of DQ-NMR signals), when each reaction involves two large polymer chains and results a chain with very high molecular weight. The viscosity curves corroborate the same trends obtained by DQ-NMR (Figure IV.12). But in this case, the signal (η^*) increases abruptly and the shape of the curves tends asymptotically to infinite because the plates of the rheometer, at the very last moments, get stuck/glued precluding the correct characterization of the last steps of the process.

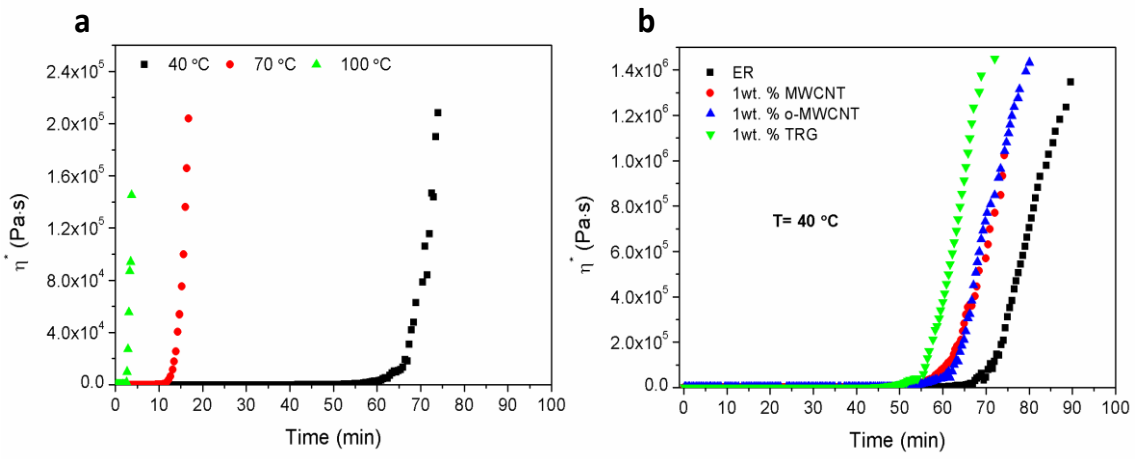

Figure IV.13: η versus curing time for the a) ER at 40 °C, 70 °C and 100 °C and b) nanocomposites at 40 °C.*

As in the study of the filler percolation by rheology, we can also plot the *G´* and *G´´*, in this case with the curing time (Figure IV.14). The ER (Figure IV.14a) presents a G´´ curve that takes higher values than the G´ indicating that the resin is still behaving as a liquid. At a certain point *G´* is higher than *G´´* evidencing that the resin is now a solid. Thus, we can define the gel time of the reaction (t_{gel}) as the point when *G´= G´´*. The samples containing 1 wt. % of MWCNTs and 1 wt. % of o-MWCNTs show an initial solid behavior, as described before in the study of the filler percolation, that is lost as the reaction continuous. Finally, we have a second point when *G´= G´´* which is now due to the formation of the cross-linked structure of the matrix. We will consider the second crossing point of the curves for the consideration of the t_{gel}.

Table IV.4 summarizes the t_{gel} values obtained for all the samples studied. The vitrification times obtained by DQ-NMR are well correlated with the gel times obtained by rheology (the small differences are attributed to the heat transfer resistance of the glass tube in the NMR experiments). Therefore, we confirm the suitability of the DQ-NMR approach developed in this thesis to study the curing reaction of thermosetting polymers. In addition, as in the case of the vitrification time from the DQ-NMR analysis, the t_{gel} decreases with the temperature and with the addition of the CNPs, obtaining the greatest accelerating effect with the addition of TRG.

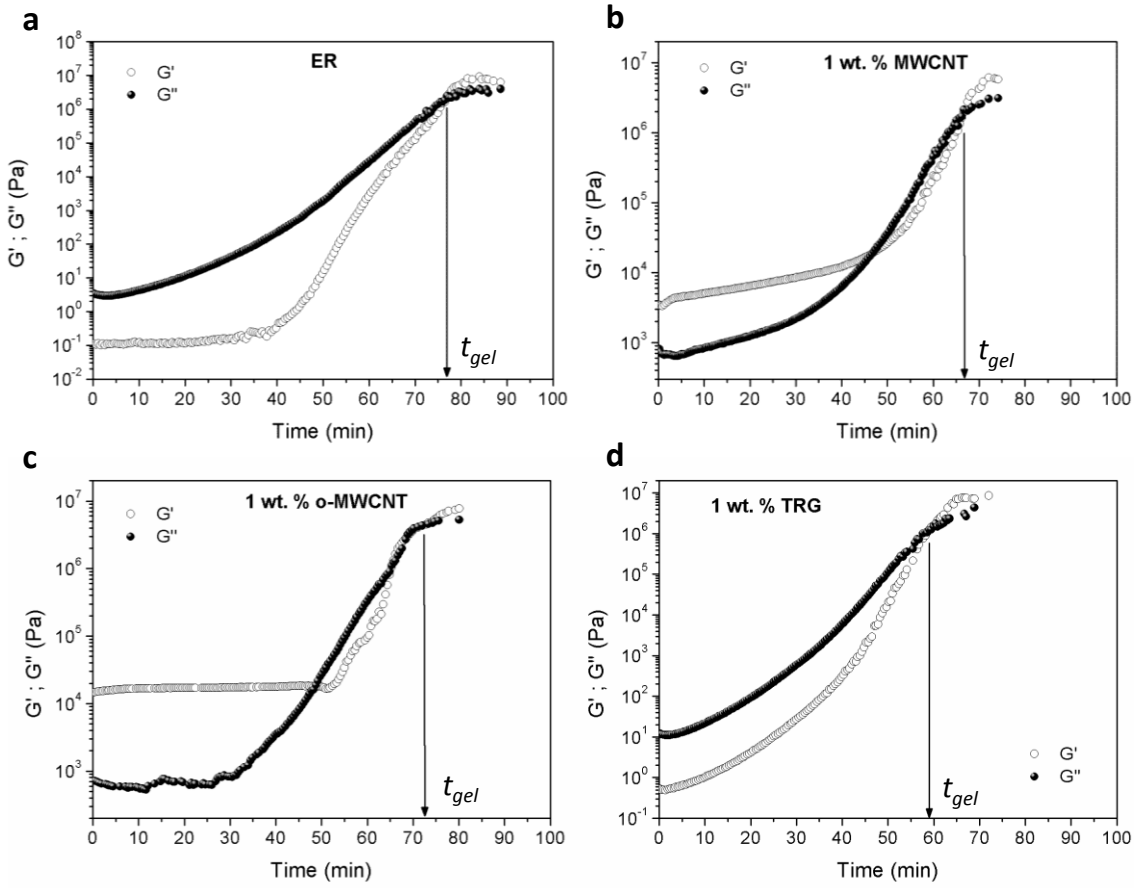

Figure IV.14: Evolution of G´ and G´´ with the curing time at 40 °C for a) ER, b) 1 wt. % MWCNT, c) 1 wt. % o-MWCNT and d) 1 wt. % TRG.

Table IV.4: t_{gel} values obtained by rheology.

t_{gel} (min)	40 °C	70 °C	100 °C
ER	77.0	13.9	2.7
MWCNT	66.7	10.9	2.5
o-MWCNT	72.0	11.1	2.5
TRG	59.1	9.4	1.7

Finally, a third technique is employed to study the curing kinetics. Isothermal scans at 40 °C, 70 °C and 100 °C followed by dynamic scans were carried out by DSC. This approach provides the extent of reaction through the Equation IV.2:

$$Extent\ of\ reaction\ (t)_{DSC} = \frac{1}{\Delta H_{iso} + \Delta H_{dyn}} \cdot \frac{dH}{dt} = \frac{\Delta H_t}{\Delta H_T} \qquad \text{Equation IV.2}$$

Where ΔH_{iso} is the heat generated during the isothermal scan, ΔH_{dyn} is the heat released during the dynamic scan (or post-curing), and ΔH_t is the heat released at each time. Figure IV.15 shows the extent of reaction for the epoxy resin and nanocomposites at 1 wt. % of filler. From Figure IV.15a, it is clear that, at 40 °C, a big amount of reactive groups remain trapped in the cross-linked network when the T_g of the system is closed to the curing temperature. These unreacted species further react during the post-curing scan. In the case of the loaded resin, the CNPs accelerate again the reaction. As the reaction during the isothermal scan is faster, the nanocomposites release higher amount of heat resulting in a slight increase of the final extent of reaction at the end of the isothermal scan.

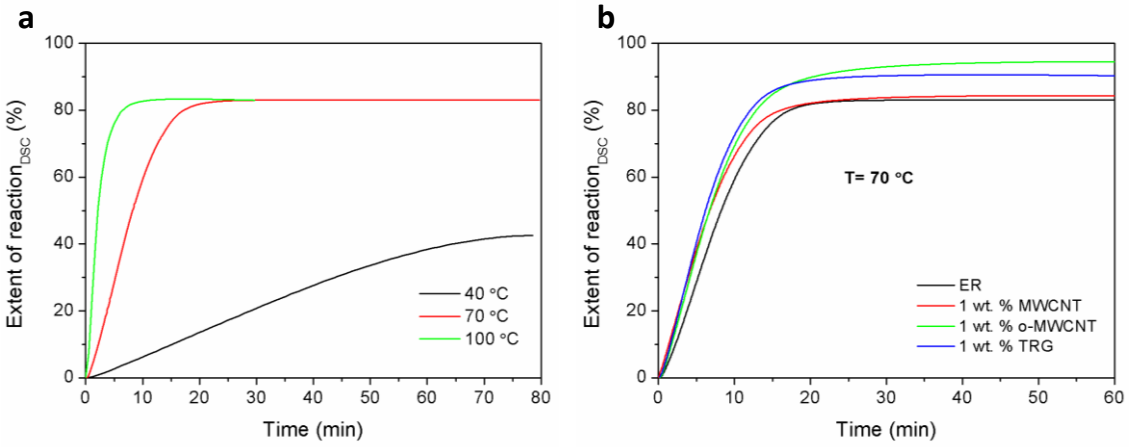

Figure IV.15: Extent of reaction by DSC for a) the ER at 40 °C, 70 °C and 100 °C and b) nanocomposites at 70 °C.

The values of the polymerization rates and activation energies are summarized in Table IV.5. In this case, the values of the polymerization rate do not show such big differences as in the case of the DQ-NMR. Actually, the E_a is slightly increased in the presence of the CNPs. As commented before, DSC is more sensitive to the first steps of the reaction when there are an important number of reactions involved. Therefore, we

associate the lower accelerating effect of the CNPs in the first stages of the reaction to the lower mobility of the reactive species caused by the higher viscosity of the loaded systems.[142]

Table IV.5: Kinetics parameters obtained by DSC.

Polymerization rate (sec^{-1})[a]	**40 °C**	**70 °C**	**100 °C**	**E_a (kJ/mol)**
ER	0.011	0.106	0.398	58.3
MWCNT	0.015	0.122	0.623	60.2
o-MWCNT	0.014	0.129	0.533	59.3
TRG	0.014	0.142	0.603	60.7

[a]*Obtained from the slope of the linear part of the curve.*

IV 5. THERMAL CONDUCTIVITY

The thermal conductivity of the uncured liquid resin plays an important role to define the variables involved in the transformation process, such as time, applied heat, or cooling time, which will then have a profound effect on the cross-link density and hence, on the final properties of the system. Thus, we aimed at studying the effect of MWCNT and TRG on the thermal conductivity of the uncured epoxy dispersions as well as in the cured nanocomposites.

The thermal conductivity (κ) of CNTs depends on several factors such as the morphology, the chirality, the diameter and length of the tubes, the number of structural defects, and the specific surface area.[357, 358] Thus, a description of the thermal conduction mechanisms is not trivial. Liu *et al.*[359] reported a κ for a SWCNT and a MWCNT of 2400 W/mK and 1400 W/mK, respectively, measured using the non-contact Raman spectra shift method. The lower intrinsic conductivity of MWCNTs was ascribed to the fact that thermal transport mainly occurs by the outermost wall and by

the existence of intertube Umklapp scattering processes. In addition, SWCNTs exhibit a higher number of phonon vibrational modes and a lower defect density in relation to MWCNTs, leading to a higher intrinsic κ.[360, 361] CNTs are characterized by a large aspect ratio and a huge surface area. It is assumed that the κ of CNTs will be higher for CNTs with a greater aspect ratio.[362] In this study, we used both SWCNTs and MWCNTs with a similar aspect ratio, so this issue does not seem to affect the κ of the nanofluid. Another factor that determines the κ of CNTs is the presence of structural defects. Cagin *et al.*[363] revealed that the κ of CNTs decreased with increasing defect concentration. Finally, the heat transfer mechanism of CNTs takes place with phonons and electrons and depends on their chirality.[364] However, to simplify the discussion, we assumed that the thermal conductance mainly occurs via a phonon conduction mechanism since the aim of this section is to provide a general description of the experimentally determined κ.

In Figure IV.16, we show the morphology of the un-cured formulations with 1 wt. % of MWCNT and TRG by TEM analysis. In both cases, a homogeneous dispersion state was obtained.

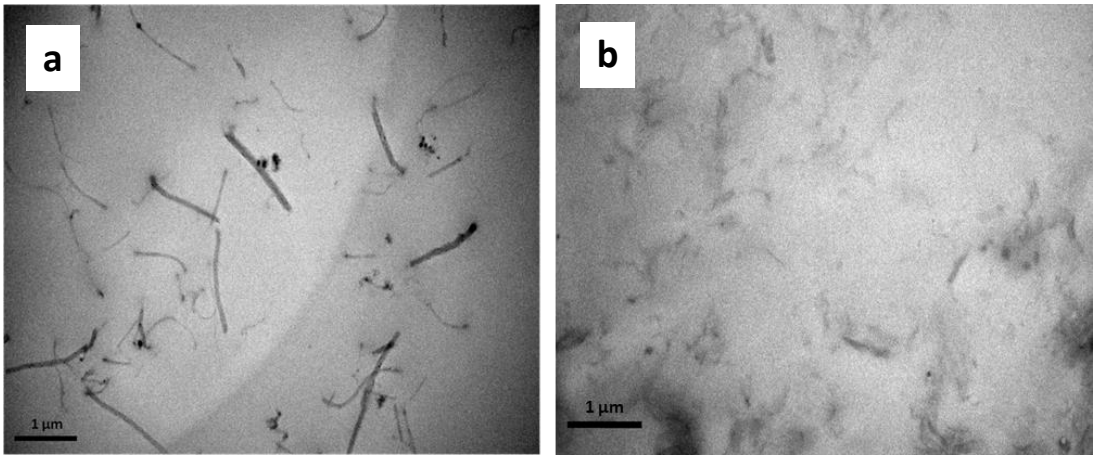

Figure IV.16: TEM images of nanofluids: a) resin loaded with 1 wt. % MWCNTs and b) with 1 wt. % TRG.

Table IV.6 presents the κ measurements of the nanofluids only at 30 °C as no significant changes with the temperature were observed. The results indicate that

MWCNTs are the most effective carbon nanofillers to improve the κ of liquid resins. Indeed, the κ of the nanofluids gradually increased as a function of MWCNT content, reaching a 70 % improvement at 1 wt. % loading. The better performance of MWCNTs can be due to their lower SSA, as compared with SWCNTs, and to the presence of the internal layers which enable phonon conduction and hence minimize coupling losses. κ of nanocomposites is sensitive to the quality of the interfacial bonding between the filler and the matrix, intimately related to a phonon coupling mechanism. This mechanism is influenced by numerous factors such as the length of free path for phonons, the boundary surface scattering, the number of vibration modes, and the resistance to heat flow at the interface, known as Kapitza resistance.[365] In general, the Kapitza resistance increases with the SSA, decreasing the efficiency of phonon transport. A lower improvement was obtained with the acid-treated carbon nanotubes (o-MWCNTs), even though the functionalization decreases the SSA of the nanotubes. This result can be explained by the presence of the functional groups, hydroxyl and carbonyl, that act as scattering points on the surface where phonons can be transferred from the nanotube crystalline structure into the insulating polymer matrix. This behavior has already been observed in cured resins,[211, 214] but not in the pre-cured state.

Table IV.6: Thermal conductivity of the epoxy nanofluids.

	κ (W/mK)
ER	0.150 ± 0.001
0.2 wt. % MWCNT	0.162 ± 0.004
0.4 wt. % MWCNT	0.176 ± 0.009
0.6 wt. % MWCNT	0.202 ± 0.004
0.8 wt. % MWCNT	0.220 ± 0.001
1 wt. % MWCNT	0.250 ± 0.001
0.6 wt. % o-MWCNT	0.180 ± 0.001

0.6 wt. % SWCNT	0.180 ± 0.001
1 wt. % TRG	0.150 ± 0.001
1 wt. % Graphite	0.176 ± 0.005
1 wt. % GO	0.150 ± 0.001

The addition of nano-dispersed TRG caused no improvement of the κ in the liquid resin. To better understand this result, we also measured dispersions of both the starting natural graphite and GO. The natural graphite showed a slight enhancement of κ, while no improvement was observed in the oxidized system. These results support the previous discussion of the negative effect of the presence of functional groups on the nanoparticle surfaces,[366] the presence of only one carbon layer, and the large SSA (see Figure IV.17). Hence, TRG cannot be considered as suitable fillers to enhance the κ of liquid resins.

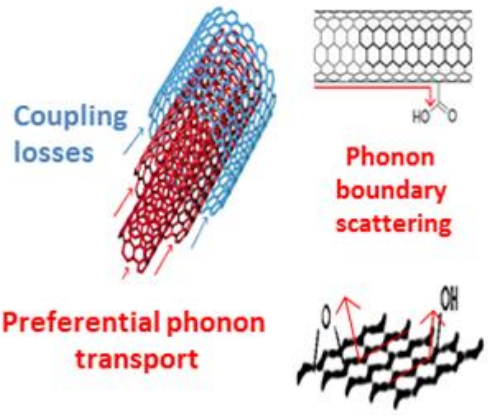

Figure IV.17: Schema of the phonon coupling losses and the boundary phonon scattering at the nanoparticle interphase.

The enhancement in the κ of MWCNT nanofluids were fitted with the Hamilton-Crosser[367] model (Equation IV.3) traditionally used to predict the thermal enhancement of solid/liquid suspensions:

$$\frac{\kappa_e}{\kappa_f} = 1 + \frac{m(\alpha - 1)\varphi}{(\alpha + m - 1) - (\alpha - 1)\varphi}$$ Equation IV.3

Where κ_e and κ_f are the effective thermal conductivities of the suspension and the base fluid, respectively; $\alpha = \kappa_p/\kappa_f$ is the κ ratio, κ_p is the particle conductivity, m is the particle shape factor (m = 6 for cylinders, m = 3 for spheres in which case, Equation IV.3 reduces to the Maxwell model), and φ is the particle volume fraction calculated using the true density of the nanotubes.[305] The theoretical thermal conductivities are calculated with both values due to the bent conformation adopted by CNTs when dispersed in a matrix; thus, their shape factor would be between 3 and 6. Figure IV.18 compares the experimental results for the MWCNT samples with the theoretical ones from the proposed model.

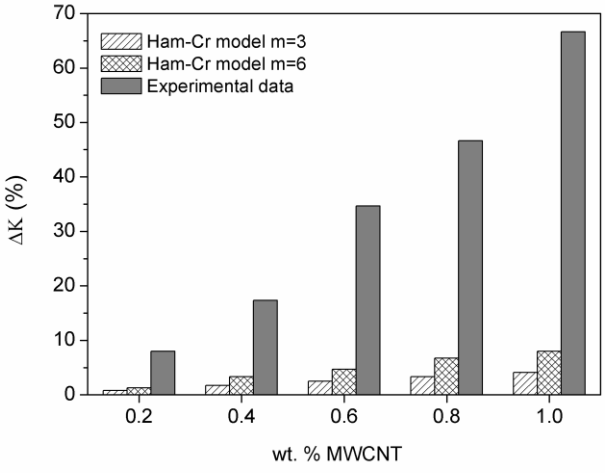

Figure IV.18: Comparison of the measured data for MWCNT nanofluids and the theoretical values.

We observe an anomalous enhancement of the experimental κ. This behavior has also been observed in other nanofluids and could be related to two effects. The first effect is the presence of an organized structure of the molecules in the liquid state at the solid/liquid interface that facilitates the coupling between the solid particles and the fluid.[368] The second effect could be contributions from the Brownian motions of the particles that modify the heat transfer in the fluid.[369]

We finally measured the κ of the cured samples for some of the nanocomposites with a classical hot-plate apparatus. TEM microphotographs also show a finely and homogeneous dispersion of the CNPs in the cured epoxy samples (Figure IV.19).

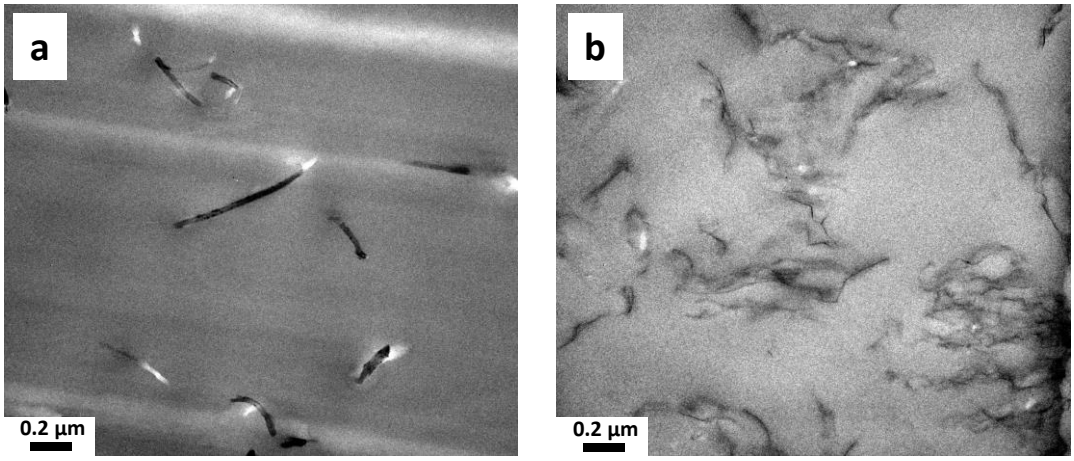

Figure IV.19: TEM images of cured epoxy samples: a) resin loaded with 1 wt. % MWCNTs and b) with 1 wt. % TRG.

The κ obtained for the cured epoxy nanocomposites are summarized in Table IV.7. The improvements obtained for the cured MWCNT nanocomposites are approximately the same as those in the liquid state and are in agreement with the data found in the literature.[77, 211, 214] The cured TRG sample revealed a similar enhancement of the κ as the MWCNT sample. This increase of κ in cured epoxy resin due to the addition of TRG has already been reported,[235, 370] but not the uncured/cured transition. This transition suggests that the results can be attributed to the differences in the media surrounding the nanoparticles when the resin is in the liquid or solid state. While the TRG are dispersed in a liquid media, they are not able to transfer the heat because the

vibrational modes are not compatible. However, when the TRG are surrounded by the more rigid cured matrix, the differences between the frequencies of vibrational modes are smaller and enable phonon coupling. This result corroborates a current theory postulating that the dominant factor in nanocomposite heat conduction is the low frequency modes and their coupling with high vibrational modes at the interface.[371, 372] This transition does not exist in the MWCNT samples because the phonon transport through the inner tubes should be relatively unperturbed by the surrounding matrix.

Table IV.7: Thermal conductivity of the cured epoxy nanocomposites.

	κ (W/mK)
ER	0.22 ± 0.007
0.6 wt. % MWCNT	0.29 ± 0.005
1 wt. % MWCNT	0.38 ± 0.007
1 wt. % TRG	0.36 ± 0.004

IV 6. MECHANICAL PROPERTIES

Tensile tests were performed in order to obtain the stiffness, strength and elongation of the composites. The results are summarized in Table IV.8. It can be clearly noted how Young's modulus increases with the filler content for both types of reinforcements, MWCNTs and TRG. We could only reach 0.75 wt. % of MWCNT due to the extremely high viscosity of the system which caused some difficulties to prepare the dog-bone specimens. Nevertheless, the addition of 0.75 wt. % of MWCNT produces an enhancement of 38 % in Young's modulus and 20 % in the final strength while the final elongation is reduced. The explanation to this stiffening effect without reducing

the strength of the material is attributed to an appropriate impregnation with the matrix and good adhesion at the filler/matrix interphase.[78]

On the other hand, the lower viscosity of the TRG dispersions allows us to double the maximum MWCNT concentration. The improvement obtained with 1.5 wt. % of TRG is higher than 50 % and 15 % for Young's modulus and final strength, respectively. This means that with TRG we are able to use a broader range of concentrations leading to better improvements of the final properties compared to CNT composites.

Table IV.8: Mechanical properties of the reinforced nanocomposites.

	E (MPa)	**σ (MPa)**	**ε (%)**
ER	1631 ± 37	58.9 ± 3.5	5.9 ± 0.5
0.25 wt. % MWCNT	1954 ± 97	68.4 ± 3.1	5.4 ± 0.7
0.5 wt. % MWCNT	2005 ± 32	69.1 ± 6.8	4.8 ± 0.7
0.75 wt. % MWCNT	2267 ± 21	72.1 ± 3.6	4.9 ± 0.6
0.5 wt. % o-MWCNT	2039 ± 51	75.4 ± 2.0	5.7 ± 0.4
0.25 wt. % TRG	2163 ± 72	65.2 ± 4.0	4.3 ± 0.3
0.5 wt. % TRG	2296 ± 55	64.4 ± 6.6	3.8 ± 0.7
0.75 wt. % TRG	2393 ± 62	68.1 ± 7.6	3.7 ± 0.6
1.5 wt. % TRG	2466 ± 34	68.5 ± 8.3	3.7 ± 0.8

We investigated the dispersion states on the fracture surface by TEM. Figure IV.20a corresponds to the sample with 0.75 wt. % of MWCNT presenting a good dispersion state with isolated MWCNT. It is possible to see some overlapping connections among them (marked with arrows) which are responsible for the increase on the viscosity. Figure IV.20b shows the morphology of the 1.5 wt. % TRG

nanocomposite where it is possible to observe the wrinkled shape of the sheets and their more staked structured with different type connections such as plane-to-plane, edge-to-plane and edge-to-edge.

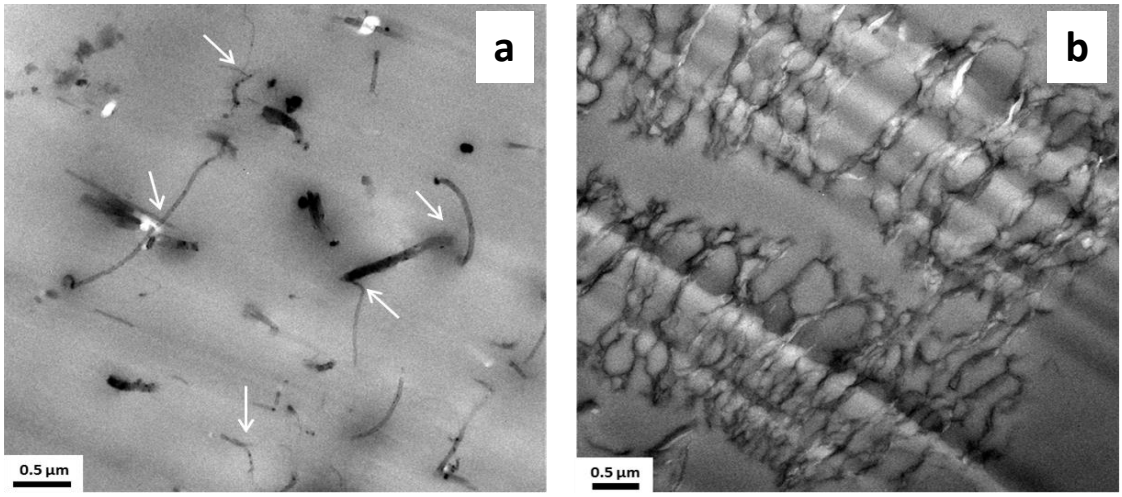

Figure IV.20: TEM images of the 0.75 wt. % MWCNT and 1.5 wt. % TRG nanocomposites.

Figure IV.21 shows a comparison of the tensile curves for the neat epoxy resin and the nanocomposites containing 0.5 wt. % of MWCNT and TRG. We observed that the TRG outperform the MWCNTs nanocomposites. This could be the result of the morphological differences and/or the presence of functional groups. To elucidate these effects, we also tested the o-MWCNTs which possess barely similar functional groups than the TRG. We can observe that even though the o-MWCNTs possess lower aspect ratio,[99] the final properties of their composites exceed the performance of the un-treated nanotubes due to their more affective wettability and interfacial adhesion produced by the chemical bonding of the functional groups with the epoxy matrix and the hardener.[95] TRG nanocomposites shows the most outstanding mechanical performance as previously reported.[74] This fact can be attributed to both effects, the functionalization and the planar geometry, predominantly to its morphology because the small thickness of the sheets with a much wrinkled topology at the nanoscale results in a better mechanical interlocking with the polymer chains and a more impeded crack propagation.[373]

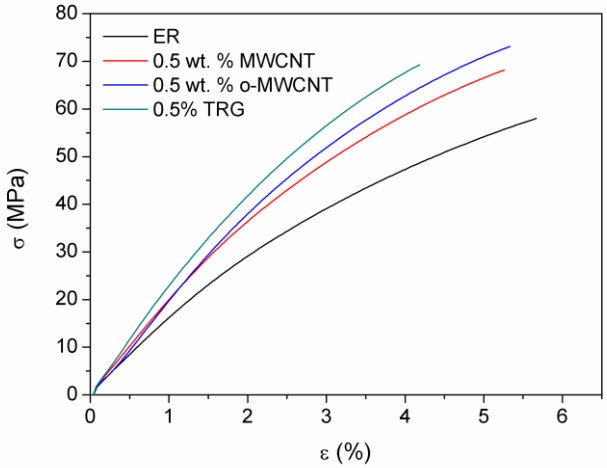

Figure IV.21: Stress–strain curves for the neat resin and nanocomposites containing 0.5 wt. % of MWCNT, o-MWCNT and TRG.

IV 7. SUMMARY

We studied the percolation network of MWCNT and TRG epoxy nanocomposites through the rheology behavior of the dispersions. MWCNTs with a rod-like geometry and a very high aspect ratio readily form the filler network. A lower rheological percolation threshold for MWCNTs was observed. MWCNTs changed the rheological behavior from a Newtonian fluid to a shear-thinning response while the planar structure and functional groups on the TRG did not raise the viscosity of the dispersions even at high concentrations. This low viscosity played a key role in their processing which allows us to introduce higher contents of TRG.

We demonstrated that DQ-NMR experiments performed in low-field spectrometers are well suited to analyze the curing reaction, network structure and segmental dynamics of thermosetting polymers. This non-destructive approach had not been employed before in the field of epoxy resins because of the technical difficulties related to the fast decay of the NMR signal associated to the high dipolar couplings. These issues were overcome by using DQ-NMR experiments based on the so-named five-pulse sequence to reach a shorter minimum sequence's cycle time. All CNPs

employed caused an accelerating effect on the curing reaction of the resin. The results obtained by DQ-NMR were corroborated by more conventional techniques (DSC, rheology).

The catalytic effect of the CNPs was mainly attributed to the increment of the thermal conductivity of the dispersions and cured nanocomposites. We measured the thermal conductivity of the epoxy nanofluids with an easy and direct method based on the hot wire technique. We also studied the differences in heat conduction mechanisms using graphene sheets and different types of CNTs analyzing the role of surface functionalization and resistance to heat flow at the interface in the thermal conductivity. The results showed that the layered structure of MWCNTs enables an efficient phonon transport through the inner layers and o-MWCNTs have functional groups on their surface acting as scattering points for the phonon transport. The dominant role of coupling vibrational modes between the matrix and the filler was evident in the case of TRG which induced a transition from a non-thermal conductive nanofluid into a thermal-conductive nanocomposite in the solid state.

The tensile tests performed on the cured samples revealed notable enhancements in the elastic moduli and final strength of the composites, especially in the case of the nanocomposites containing TRG. This combination of good processing properties with low viscosities and enhanced final mechanical properties makes TRG great candidates to develop multifunctional polymer materials.

Chapter V. UV CURED EPOXY NANOCOMPOSITES

Part of the work described in this chapter has been published in the following journals:

- *Polymer*, Vol. 52: 4664 - 4669 (2011).
- *Polymer*, Vol. 53: 1831 - 1838 (2012).

V 1. INTRODUCTION

Polymer nanocomposite coatings are attracting great attention in recent decades due to the possibility of adding valuable properties to the matrix. This multifunctionality is essential since polymer coatings should not only meet decorative or protective functions, they should also provide other requirements like electrostatic discharge, high mechanical performance, large operating temperature range and chemical resistance among others.[374] One approach to reach these features is the addition of nanofillers with remarkable mechanical, electrical and thermal properties. In this sense, carbon based nanofiller like CNTs and TRG appear as promising candidates for the reinforcement of the polymer matrices employed in the coating industry.

On the other hand, the UV polymerization of multifunctional monomers is one of the most efficient methods available to generate three-dimensional polymer networks. Among the advantages of this technology the high curing speed, the reduced energy consumption, and absence of volatile organic compounds emissions are the most remarkable.

This chapter reports the effect of MWCNTs, o-MWCNTs and TRG on the UV curing reaction and final properties of the polymer coatings. The curing process was studied in real time using FT-IR spectroscopy and gel permeation techniques. The effect of the nanofiller on the dielectric, dynamic mechanical (DMTA) and surface hardness properties was evaluated. In addition, an analysis of the influence of different structural parameters of the carbon nanofillers, such as geometry, structure and chemical composition was also performed. For comparative purposes and to elucidate certain issues, expanded graphite (EG) composites were also prepared and characterized.

V 2. EXPERIMENTAL

The UV-curable system selected for this chapter was a dicycloaliphatic epoxy resin, 3,4-epoxycyclohexylmethyl-3',4'-epoxycyclohexyl carboxylate (CE), and triphenylsulfonium hexafluoroantimonate was used as photoinitiator. Their chemical

structures are represented in Figure V.1. Both products were purchased from Sigma Aldrich and used as received without any further purification. These reactants were chosen because of the advantages of the cationic reaction mechanism involved in the crosslinking process that were previously described in the chapter I.2.

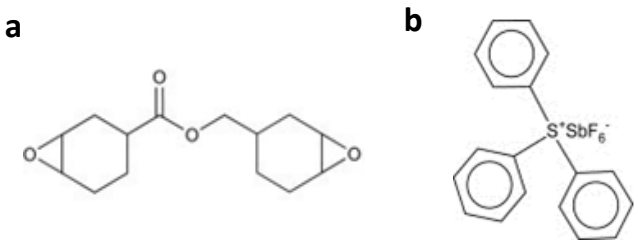

Figure V.1: Molecular structures of the a) dicycloaliphatic epoxy resin and b) photoinitiator.

Expanded graphite was prepared using a mixture of graphite flakes with concentrated sulfuric acid and nitric acid (4:1, v/v) stirred at room temperature. This acid treated natural graphite was washed and dried to remove any remaining solvent. The dried filler were treated at 1050 °C for 30 s to obtain expanded graphite filler.

Carbon-based nanofillers were directly dispersed into the epoxy resin using an IKA Ultraturrax at 30000 rpm for 10 min. Then, the mixtures were placed in an ultrasonic bath for another 10 min. The photoinitiator was added just before UV irradiation in a proportion of 2 wt. % with respect to the resin. For characterization tests, the formulations were coated on glass substrates and cured with UV light. The UV induced polymerization was promoted by UV irradiation (UV lamp Italyquartz), with a light intensity on the surface of the sample of about 55 mW/cm^2 during 15 min (7.5 min each side of the sample) while 3 min were applied to the transparent pristine epoxy resin. Homogeneous disc-shaped and rectangular nanocomposite coatings of about 150 µm in thickness were produced. The whole experimental procedure is summarized in Figure V.2.

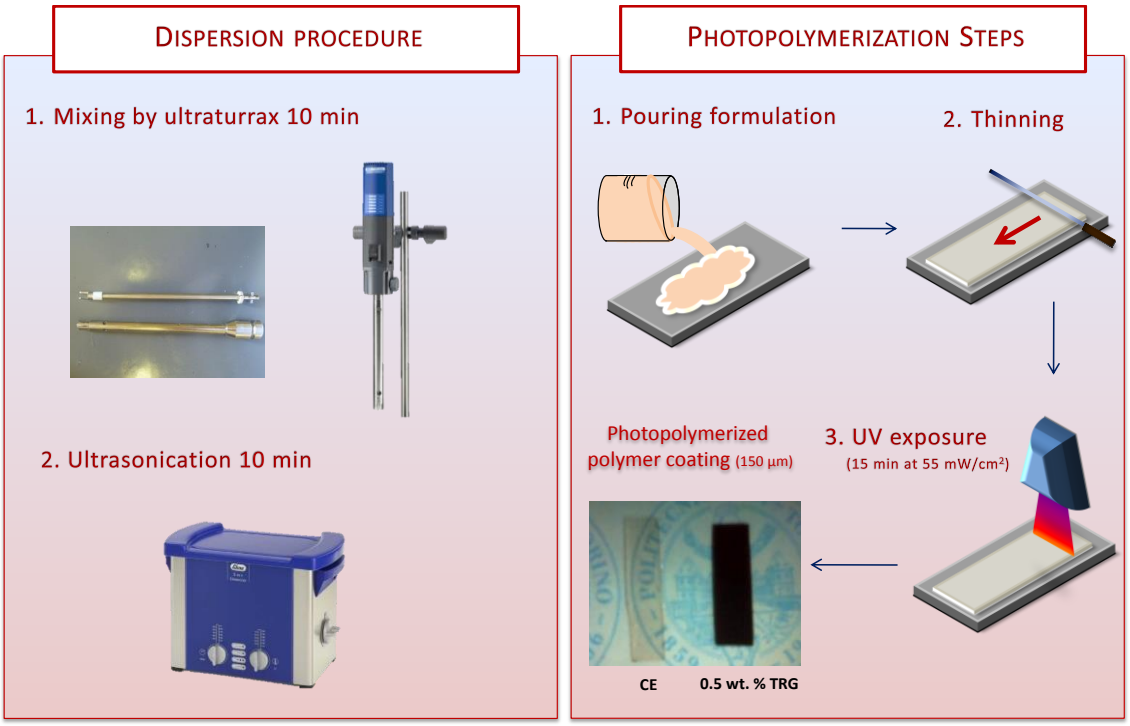

Figure V.2: Experimental procedure of the UV cured composites preparation.

The progress of the photopolymerization process was followed by real time FT-IR in a Thermo-Nicolet 5700 spectroscopy. During RT-FTIR analyses, the spectra were obtained co-adding 7 individual scans at 8 cm^{-1} resolution. 25 mm-thickness films were coated on silicon wafers and simultaneously exposed to the UV beam (Hamamatsu LC8 portable UV lamp) with an intensity of 35 mW/cm^2 for 3 min to induce polymerization, and to the IR beam, to make an in-situ evaluation of the extent of reaction (experimental set up in Figure V.3a). The conversion of the epoxy group was followed by monitoring the decrease in the absorbance of the epoxy groups centered at 750 cm^{-1} and normalized by the carbonyl peak centered at around 1700 cm^{-1}. The conversion curves as a function of irradiation time is the result of the average of 3 runs for each sample. As the UV lamps used to cure the final coatings is not the same as the lamp to perform the real time IR measurements, the conversion of the cured samples used for the dielectric and mechanical tests was determined by carrying out single spectrum before and after 5 min of irradiation with a static UV lamp (Italyquartz) at a light intensity of 55 mW/cm^2 on a coated film of about 25 µm-thickness (Figure V.3b).

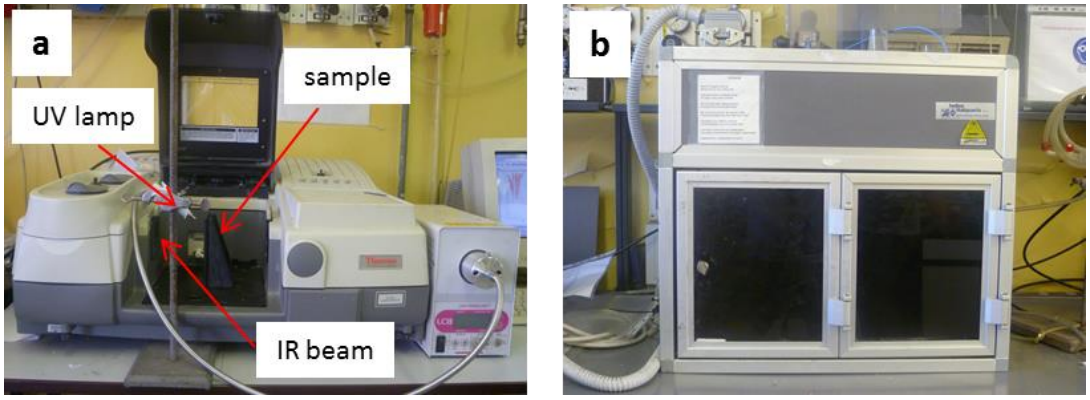

Figure V.3: Experimental set up for the a) real time FT-IR measurements and b) static UV lamp.

Gel content values of the cured coatings were obtained by measuring weight loss after 24 h in chloroform at room temperature (ASTM D2765-84).

Broadband dielectric spectroscopy was performed on an ALPHA high-resolution dielectric analyzer (Novocontrol Technologies GmbH, Hundsangen, Germany). The photocured films were held in the dielectric cell between two parallel gold-plated circular electrodes. The dielectric response of each sample was assessed by measuring the complex permittivity (Equation V.1) over a frequency range window of 10^{-1}-10^{7} Hz at room temperature.

$$\varepsilon^*(\omega) = \varepsilon'(\omega) - j\varepsilon''(\omega) \qquad \text{Equation V.1}$$

The amplitude of the alternating electric current applied to the samples was 1 V. The AC conductivity was measured in the same conditions as ε^* and the results were given directly by the dielectric analyzer. In a conducting composite, the conductivity is composed of two terms:

$$\sigma^*(\omega) = \sigma_{DC} - A\omega^x \qquad \text{Equation V.2}$$

Where σ_{DC} is the direct current conductivity and x is an exponent which describes the frequency (ω) dependence of $\sigma(\omega)$. For insulating materials x = 1. The term σ_{DC} appears as a plateau at low frequencies in the experiments and it was obtained extrapolating the broadband AC conductivity to 10^{-1} Hz when a plateau is reached.

SEM and TEM were carried out on a Philips XL30 ESEM at 25 kV and a TEM Leo 910 microscope at an acceleration voltage of 80 kV to study the morphology and dispersion states of the samples. For TEM analysis, ultra-thin sections of the samples containing 1 wt. % of TRG and MWCNTs were prepared by cryo-ultramicrotomy (Leica EM UC6) at -140 °C.

Dynamic mechanical analysis was performed on a Mettler Toledo 861e instrument at 1 Hz frequency in tensile configuration. The loss factor (tan δ) and elastic modulus (E´) were measured from room temperature to 250 °C. The experimental error was below 5 %.

Differential scanning calorimetric (DSC) measurements were performed under nitrogen flux of 2 ml/min, in the range of 25 °C – 250 °C with a heating rate of 20 °C/min, with a Mettler TC 10A/TC15 TA controller instrument.

Surface hardness tests were performed at room temperature with a standard microhardness tester Shimadzu model DUH211S. A load of 10 mN with a loading speed of 1.46 mN/s was applied and held for 5 s before unloading.

The pendulum hardness (Persoz, ASTM D4366) was measured from the damping of the oscillation of the pendulum. Pendulum hardness values are expressed in number of pendulum oscillations and are related directly to the softness of the surface of the sample. The shorter the damping time, the lower is the hardness.

V 3. PHOTOPOLYMERIZATION PROCESS

The influence of the different carbon fillers on the cationic photopolymerization reaction of an epoxy resin was evaluated by real time FT-IR, keeping the filler content constant at 1 wt. %. Figure V.4 shows the evolution of the spectra as function of

irradiation time recorded for the pure epoxy resin. The decrease of the epoxy group band centered around 750 cm^{-1} as a function of time provides an indication of the extent of the reaction.

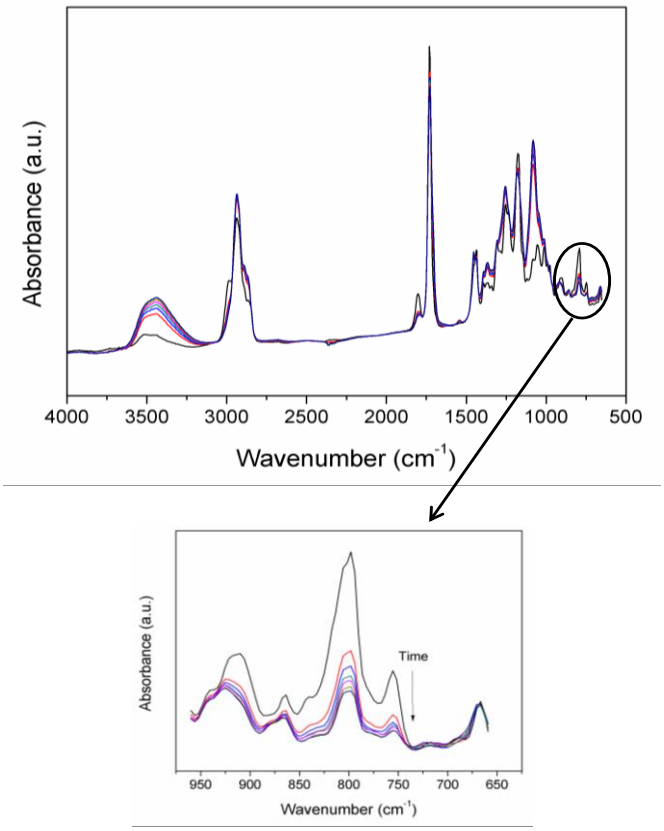

Figure V.4: FT-IR spectra vs irradiation time for the pure epoxy resin over the entire region and a closed-up from 950 to 650 cm^{-1}. Curing time 3 min.

Figure V.5a shows the conversion curves of all samples at 1 wt. % filler content calculated from the normalized absorbance of the epoxy by the carbonyl band. From this plot, we can get some qualitative and quantitative information; the slope of the initial linear segment of the curves is related to the photopolymerization rate and the final value to the epoxy group conversion reached at the end of the UV curing process.

At the initial stages, the reactivity of the epoxy groups is very high for the pristine CE resin, and after 3 min of irradiation the final conversion of the epoxy band is around 80 %. This phenomenon is caused by the gelification of the system, due to the formation of a crosslinked polymer network hindering the mobility of active groups

while the reaction progresses. We can observe that all carbon nanofillers decrease both the polymerization rate and the final conversion. Besides, the results suggest that the more staked structure of the graphite sheets in the EG leads to higher reaction rates and a final conversion of 71 % while the fillers at nanometer scale with higher specific surface area (SSA), TRG and MWCNTs, have a greater absorption of the UV light leading to a stronger shielding effect with a final conversion between 50 % and 60 %. No significant differences between MWCNT and TRG are observed.

The effect of the nanofiller content on the photopolymerization process was also analyzed by FT-IR spectroscopy. It is possible to observe how the polymerization rate and the final conversion decrease with the amount of both types of MWCNTs and TRG (Figure V.5b and c) while the effect of the load content is not so evident in the case of the EG (Figure V.5d). Values of the conversion and polymerization rates for all the samples are summarized in the Table V.1.

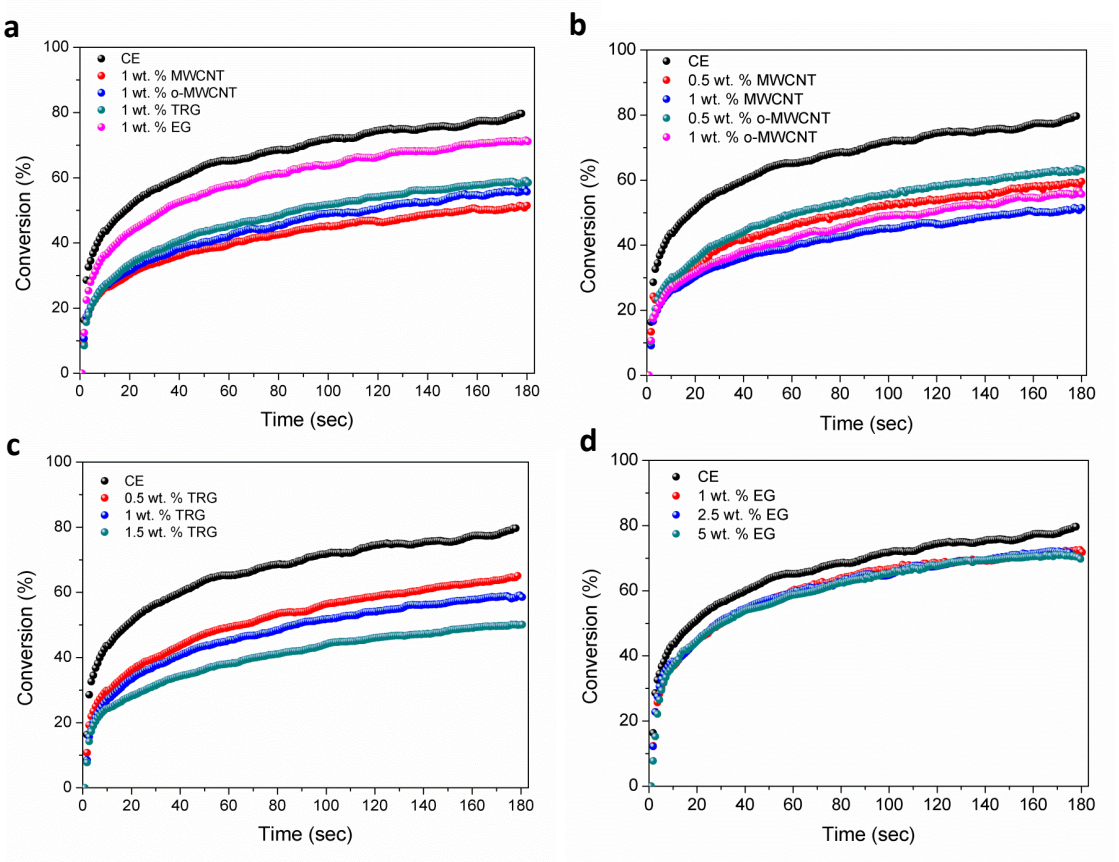

Figure V.5: FT-IR conversion curves for a) nanocomposites at 1 wt. % of nanofiller content. Effect of filler content on the conversion for b) MWCNTs and o-MWCNTs, c) TRG and d) EG.

The observed slowdown of the epoxy group conversion was due to the addition of highly light-absorbing fillers that reduce the generation of reactive species at the beginning of the photoinduced reaction. Hence, this competition in terms of light absorption between the nanofiller and the photoinitiator leads to a less effective UV curing process. In fact, the efficiency of the photo-initiation process can be described by two quantum yields: the *quantum yields of initiation*, which represents the number of starting polymer chains per photons absorbed, and the *quantum yields of polymerization*, which is the number of monomer units polymerized per photons absorbed. Therefore, it is clear that the competition in absorption with the carbon filler implies a decrease of the photons absorbed by the photo-initiator decreasing the quantum yields.[375] In addition to the shielding effect, it can be expected that the rigid nanofillers reduce the mobility of the epoxy chains by increasing the viscosity of the photo-curable formulation, and as consequence the mobility of the reactive species is reduced decreasing the overall reactivity.[142]

Table V.1: UV curing parameters of all the formulations studied.

	wt. % of filler	Polymerization rate (s^{-1})	Conversion[a] (%)	Conversion[b] (%)	Gel content (%)
CE	-	9.6	80	100	100
MWCNT	0.5	5.9	60	100	100
	1	5.5	51	98	99
o-MWCNT	0.5	6.1	63	100	100
	1	5.6	56	88	100
TRG	0.5	8.4	65	99	100
	1	5.6	59	95	100
	1.5	5.4	50	96	99
EG	1	7.5	71	98	100
	2.5	6.9	70	100	99
	5	6.2	69	100	100

[a] *Value of the plateau in the conversion curves (UV intensity 35 mW/cm^2)*
[b] *Determined by single spectra taken before and after 5 min of irradiation at 55 mW/cm^2*

In order to overcome this shielding effect, the formulations were cured for 5 min at a higher UV light intensity, 55 mW/cm^2. By increasing irradiation time and light intensity we could achieve fully cured networks. In the Figure V.6, FT-IR spectra in the region between 950 and 650 cm^{-1} are reported for the epoxy formulation containing 1.5 wt. % of TRG before and after 5 min of UV irradiation. It is possible to observe the almost complete disappearance of the epoxy group band centered at around 750 cm^{-1}. The high gel content obtained for all formulations (above 99 %, see Table V.1) indicates the absence of any extractable oligomer or unreacted monomer evidencing as well that fully cured composites were obtained.

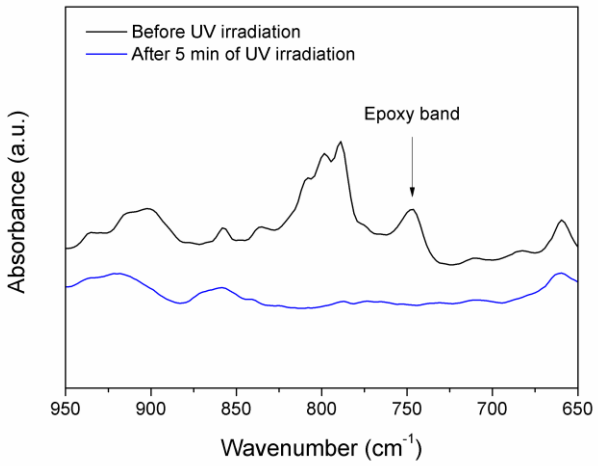

Figure V.6: FT-IR spectra of the formulation containing 1.5 wt. % TRG before and after 5 min of UV irradiation. Film thickness 25 µm

V 4. DIELECTRIC PROPERTIES

The dielectric properties of the photocured epoxy composites at different nanofiller contents measured at room temperature are depicted in Figure V.7. The electrical conductivity and dielectric permittivity are significantly increased by the addition of all nanofillers in different ways. We can observe how the geometry of the

filler plays a dominant role in the formation of conductive pathways. The conductivity with just a small percentage (0.1 wt. %) of non-functionalized rod-like filler becomes independent of the frequency in almost all the range of study. While the dielectric permittivity has the opposite behavior, passing from being independent of the frequency to reveal a negative slope when the concentration is above the percolation threshold due to polarization effects between clusters inside the percolated system. This shift on the dielectric behavior is also attributed to the well-known Maxwell-Wagner-Sillars (MWS) effect in heterophase systems, which basically consists on the polarization of the polymer-filler interface. The MWS interfacial polarization depends on several variables like: volume fraction of the conducting phase, the geometry of the filler, the dielectric permittivity of the matrix and the conductivity of the occluded phase.[376] These two drastic enhancements on the conductivity and permittivity are evidences of the formation of an effective conductive MWCNT percolated network in the epoxy matrix. This is confirmed by the morphological investigation, discussed below. On the other hand, when the resin is loaded with sheet-like nanofiller the increase of these two properties is much lower than for MWCNT and the thresholds appear at higher concentrations, but in all cases the antistatic limit of 10^{-8} S/m is reached.

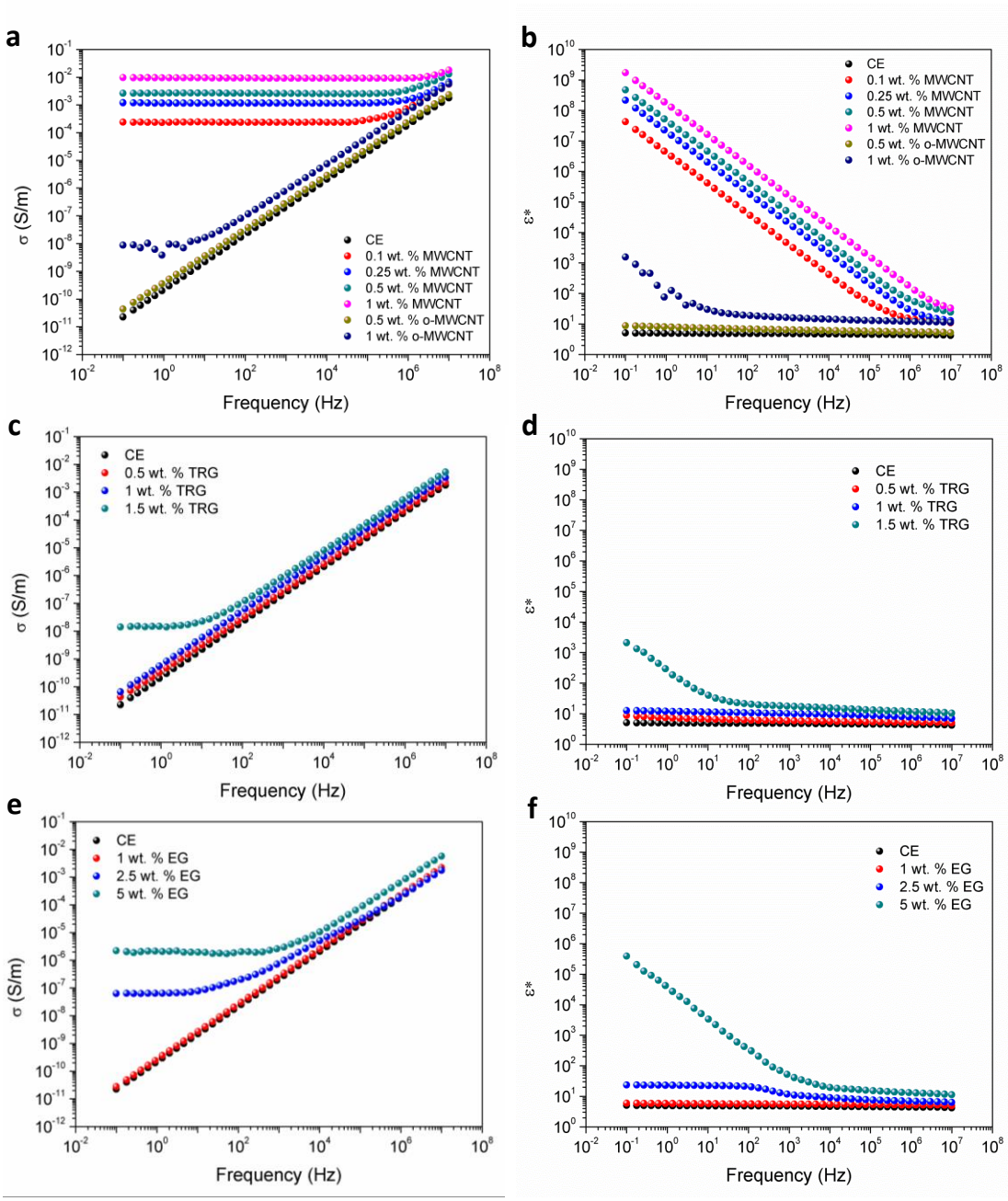

Figure V.7: AC conductivity and permittivity versus frequency for all the fillers at different loading fractions.

Extrapolating the broadband AC conductivity to 10^{-1} Hz it is possible to obtain DC conductivity values. Figure V.8 shows DC conductivity for the nanocomposites studied as a function of nanofiller content. The shaded areas correspond to the electrical percolation region for each system. We observe that the most effective filler in terms of

the electrical percolation threshold is the MWCNTs. The threshold values for the different fillers used agree with those found in the literature.[69, 204, 377, 378]

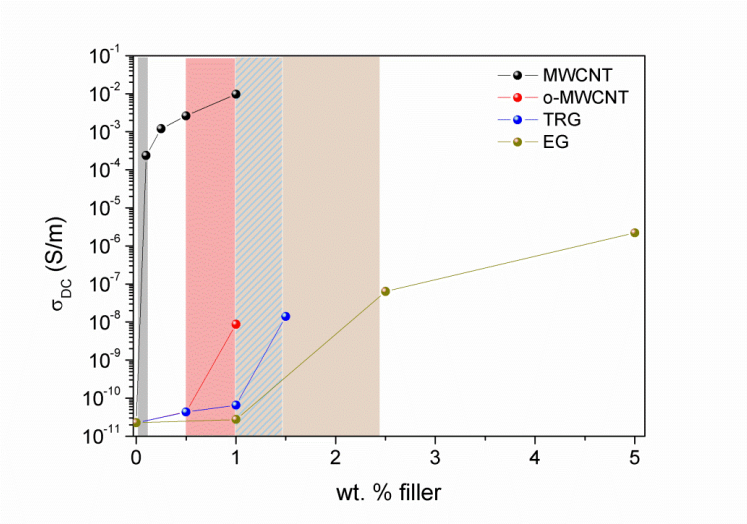

Figure V.8: Values of the DC electrical conductivity of the epoxy nanocomposites as a function of the nanofiller content.

The differences in the percolation thresholds obtained are attributed to the geometry of the fillers. First of all, it would be easier for polymer chains to intercalate between MWCNTs than between sheets facilitating the disentanglement of the MWCNTs. Moreover sheet-like nanofillers would be more likely to form aggregates due to their in-plane interactions and higher SSA. TRG has a wrinkled shape reducing the aspect ratio of the filler, in addition they are able to roll themselves up into a tube-like structure with diameters larger than those of MWCNTs.[379] This is confirmed by morphological investigation, as discussed below: EG sheets are found forming big agglomerates leading to higher percolation thresholds. The rod-like geometry of the MWCNT could generate a huge number of overlapping contacts among them causing an effective electronic transport, while sheet-like nanofillers are connected through a shorter number of connections, such as plane-to-plane, edge-to-plane and edge-to-edge, which are not equally efficient from the electrical point of view.[380] The higher percolation threshold of o-MWCNTs compared to as-synthesized MWCNT is attributed to the disturbance of the crystalline graphitic structure of the MWCNT, reducing the number of π-electrons and generating more sp^3-carbons which do not cause an electronic transport as high as the produced by π-electrons. Additionally, the reaction of

the epoxy resin with the functional groups of the o- MWCNT could form an electrically insulating polymer layer around the nanotubes and, hence, would hinder the electron tunneling between MWCNTs.[381]

V 5. MORPHOLOGY

We investigated the dispersion states of the different nanofillers in the epoxy resin by SEM and TEM inspections on cured materials in order to get some conclusions of the morphology effect of the nanocomposites on their electrical properties. We choose the highest loading fraction for each set of samples. Figure V.9a corresponds to the neat epoxy resin presenting a typical fragile behavior of epoxy matrices with a flat surface and the river-like pattern, whereas a less brittle-like fracture is observed for the nanocomposite with 1.5 wt. % of TRG in Figure V.9b. The different magnifications of the TEM images in Figure V.9c and d show a random and homogeneous distribution of single graphene sheets or stacks of a few nanometers adopting a wrinkled configuration.

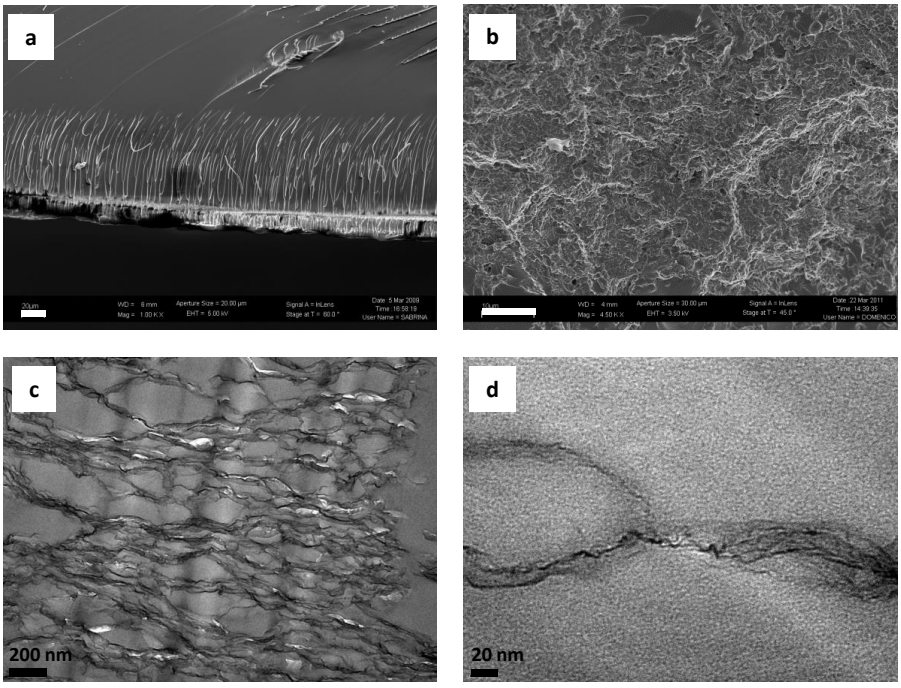

Figure V.9: SEM images of a) neat CE (scale 20 µm) and b) 1.5 wt. % TRG nanocomposite (scale 10 µm). TEM images of the 1.5 wt. % TRG c) and d).

Figure V.10 contains two SEM images of the 5 wt. % EG nanocomposite surface fracture where it is important to notice the scale of the filler. We observe aggregates of several microns dispersed in the polymer matrix. The presence of these micrometer agglomerates makes that the formulation absorbs less UV light than the other fillers in the nanometer scale but also, as discussed above, the electrical conductivity is lower.

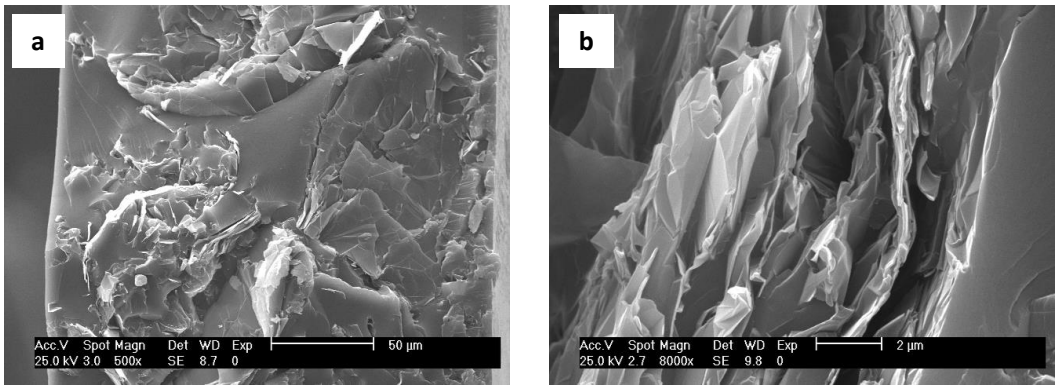

Figure V.10: SEM images of the fracture surface of the 5 wt. % EG nanocomposite.

The SEM images shown in Figure V.11 correspond to the analysis of the cryo-fractured surface of the 1 wt. % MWCNTs and o-MWCNTs nanocomposites. In both cases, the nanotubes are very well dispersed and spread out in the epoxy matrix without forming agglomerates.

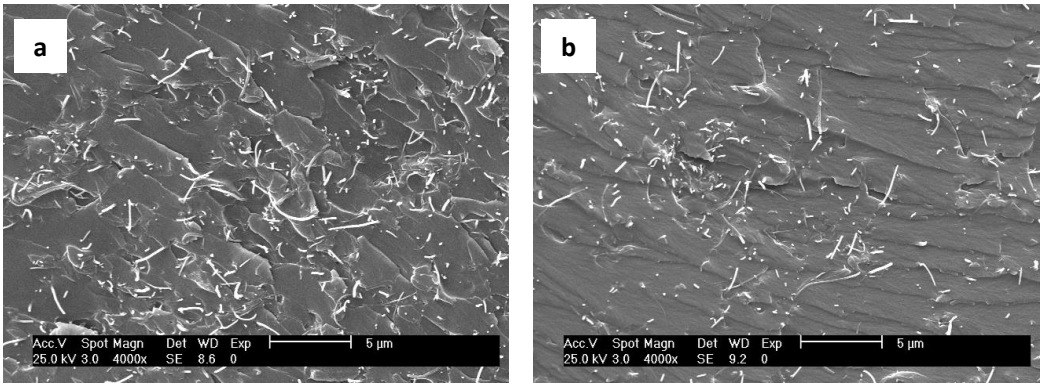

Figure V.11: SEM images of the 1 wt. % a) MWCNTs and b) o-MWCNTs nanocomposites.

It is important to mention that we find isolated MWCNTs in the matrix while TRG with their sheet-like morphology formed stacked groups of a few wrinkle graphene sheets. This dispersion together with the geometry of the nanofillers influence on the final electrical properties of the nanocomposites, as previously discussed. Therefore the morphological investigations agree with the measured electrical properties.

In Figure V.12, we show a TEM image of the 1 wt. % MWCNTs nanocomposite where it is possible to see the MWCNTs network with overlapping between particles, responsible for the highly effective electronic transport of these nanocomposites.

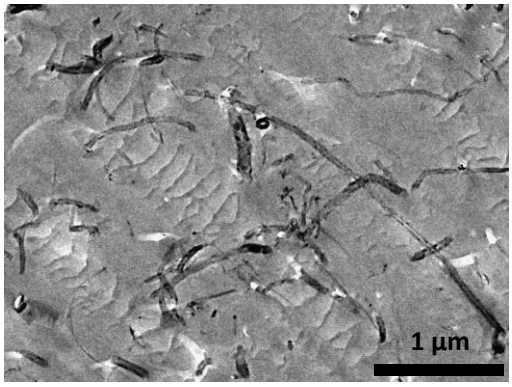

Figure V.12: TEM image of the 1 wt. % MWCNTs nanocomposite.

V 6. DYNAMIC MECHANICAL AND THERMAL ANALYSES

The choice of a given application for epoxy is often based on the glass transition temperature, noted as T_g. This is the temperature at which the mechanical properties of a polymer drop and corresponds to a second-order phase transition at which the polymer goes from a glassy to a rubbery behavior as the temperature increases. The T_g is closely linked to the thermo-mechanical stability, it is thus one of the properties that dictates the potential application of a given epoxy resin as a function of the service temperature range.

Viscoelastic characterization, glass transition temperature (T_α associated to T_g and expressed as the maximum value of loss factor, *tan* δ_{max}) and damping values, of the cured materials was carried out by DMTA analysis. Figure V.13a shows the *tan* δ curves as a function of temperature for the different prepared materials. CE resin shows a main relaxation process α assigned to the glass transition temperature. It is possible to observe that the filled materials show always higher T_g values compared to the pristine cured epoxy matrix (Table V.2), evidenced by the shift of the maximum of the tan δ peaks to higher temperatures, together with a decrease of the damping. The DMTA results show that the dynamic mechanical properties of the nanocomposites are greatly affected by the carbon nanofiller type. It is well known that in particulate-filled polymers, the addition of rigid fillers can hinder the polymer chain movements leading to a damping reduction and a shift of T_g values to higher temperatures. In this study a significant reduction of damping (here evaluated as *tan* δ_{max}) is observed in the nanocomposites, together with a strong increment in T_g values.

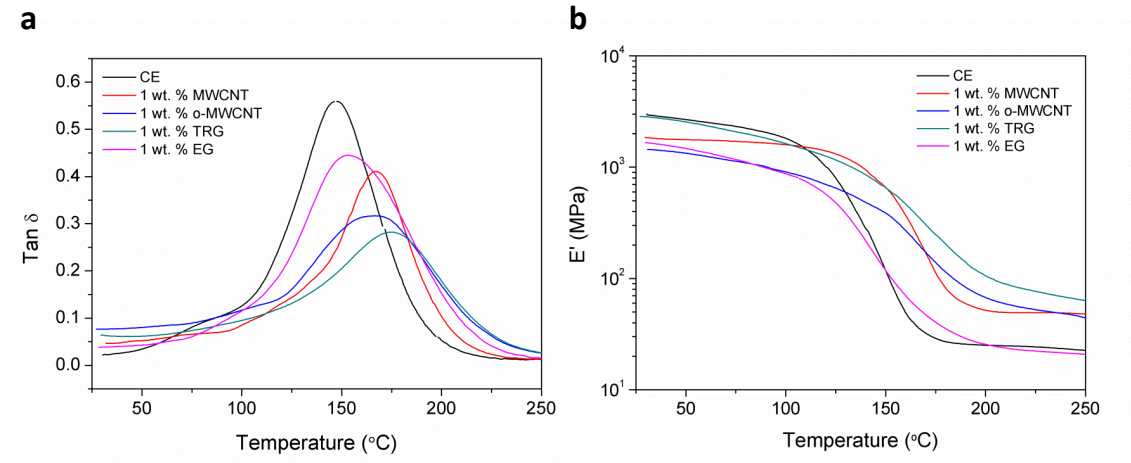

Figure V.13: DMTA curves for composites at 1 wt. % loading fraction.

These changes in both T_g and damping are generally attributed to a strong filler-matrix interfacial interaction; thus, nanofillers with functional groups on their surface (TRG and o-MWCNTs) evidence higher damping effect because of the covalent bonding between the filler and the polymer chains. The largest enhancement in the T_g is obtained with TRG (around 20 °C with 1 wt. %) due to the formation of a large and

chemically bonded interface at the proximity of the filler. TRG nanocomposite behaves even better than the o-MWCNTs and MWCNTs from the dynamic mechanical point of view. Raffie *et. al.*[74] already concluded that graphene systems outperform the mechanical properties of MWCNT nanocomposites because of the more efficient adhesion to the matrix and higher SSA of the graphene sheets.

No significant changes were observed in the modulus values by the addition of the nanofillers (Figure V.13b). However, an increase was detected in the rubbery region, being this effect more evident when TRG is used as nanofiller extending the mechanical performance to higher temperatures.

Table V.2: T_g values obtained by DMTA of the cured nanocomposites at 1 wt. % loading fraction.

Sample	**CE**	**1 wt. % MWCNT**	**1 wt. % o-MWCNT**	**1 wt. % TRG**	**1 wt. % EG**
T_g **(°C)**	152	167	165	173	154

The effect of the filler content on the T_g was analyzed by DSC. Thermograms of the second heating scan are shown in Figure V.14 while the values of the T_g are summarized in Table V.3. In all the cases the transition is shifted to higher temperatures with the amount of the filler.

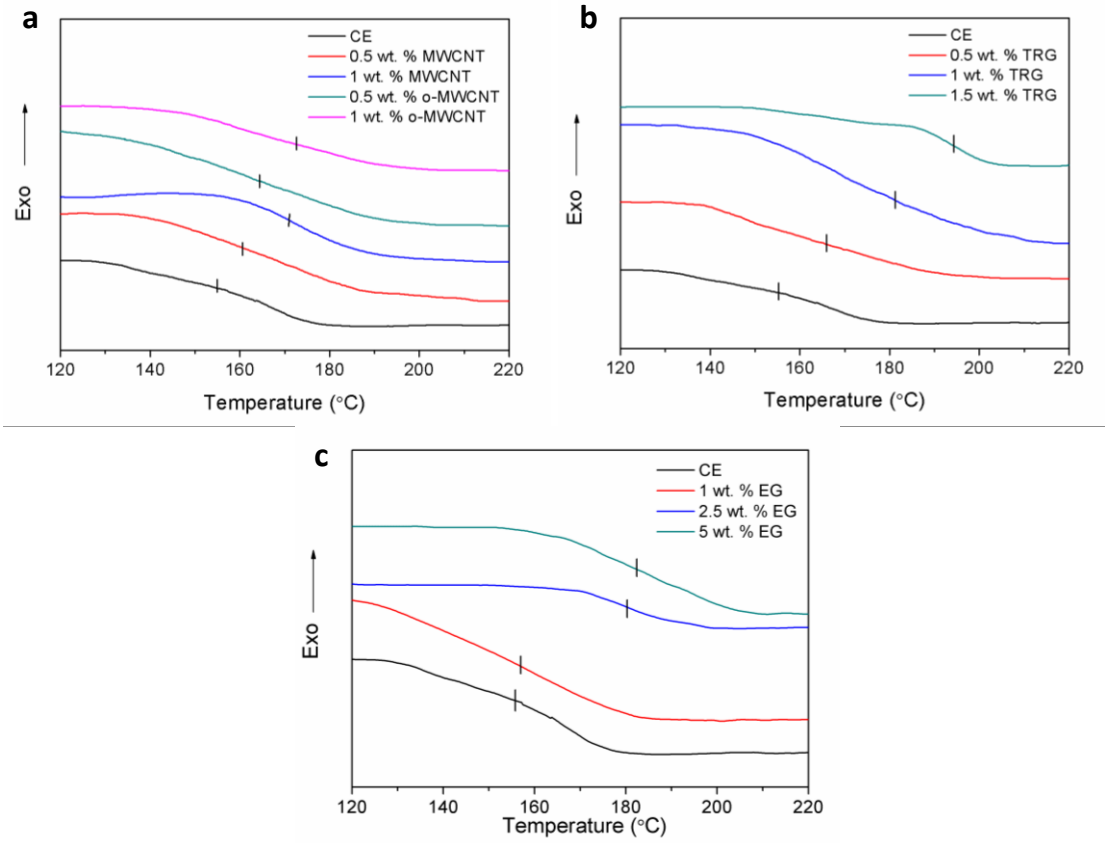

Figure V.14: DSC thermograms for all the nanocomposites.

The highest enhancements on the T_g are obtained with the addition of TRG as we observed in the DMTA results. In particular, an increment of 40 °C is obtained by adding only a 1.5 wt. % of TRG.

Table V.3: T_g values obtained by DSC for all the nanocomposites studied.

	wt. % of filler	T_g (°C)
CE	-	155
MWCNT	0.5	161
	1	172
o-MWCNT	0.5	164
	1	173
TRG	0.5	167
	1	181
	1.5	195
EG	1	155
	2.5	181
	5	183

V 7. SURFACE HARDNESS

The good dynamic mechanical behavior of the nanocomposites can be accompanied by an enhancement of the surface hardness. The results of microindentation tests performed on the surface of the photocured samples are shown in Figure V.15. Surface hardness values (Figure V.15a) show that the un-filled epoxy resin and its nanocomposites have very similar responses. Although, a slight increase in the indentation hardness (Hit) can be observed particularly for the sheet-like nanofillers. Again, the better mechanical performance of the sheet-like nanofillers is attributed to the enhanced specific area and geometry of the TRG and/or to a better mechanical interlocking of the nanofiller/matrix interface.[74]

We also plotted in Figure V.15 the loading-maintenance-unloading process of the microindentation test. In these plots, the differences in the mechanical response between samples are more evident. At the same load the indentation depth for the nanocomposites is lower than for the pristine epoxy resin evidencing the reinforcing effect of the nanofillers.

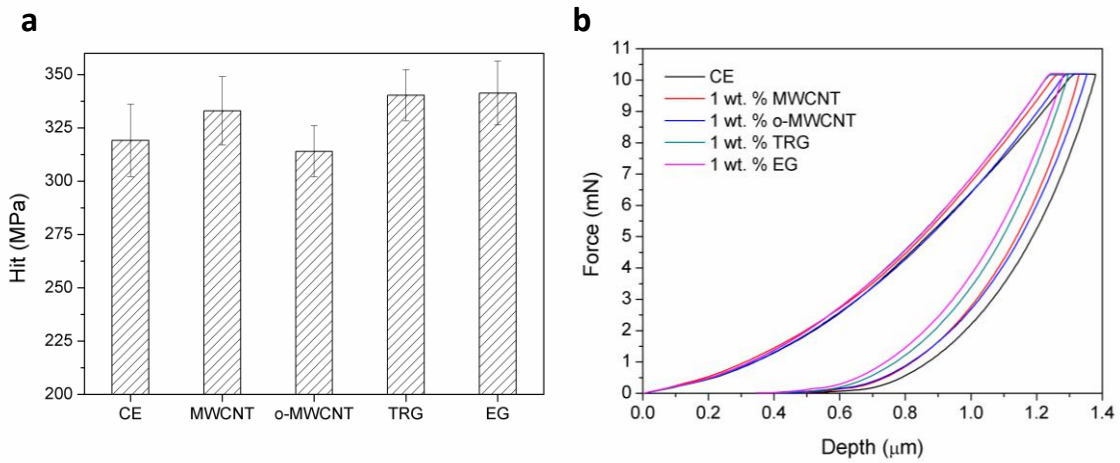

Figure V.15: a) Hit values and b) load vs depth curves at 1 wt. % filler content.

As TRG outperformes MWCNTs and EG in the dynamic mechanical and surface hardness test we selected TRG to study the effect of the filler content on the surface hardness of the UV cured coatings. In this case the Persoz pendulum technique is employed. Figure V.16 shows the surface hardness values as a function of TRG content. The Persoz hardness shows a clear increase of the cycles with TRG content.

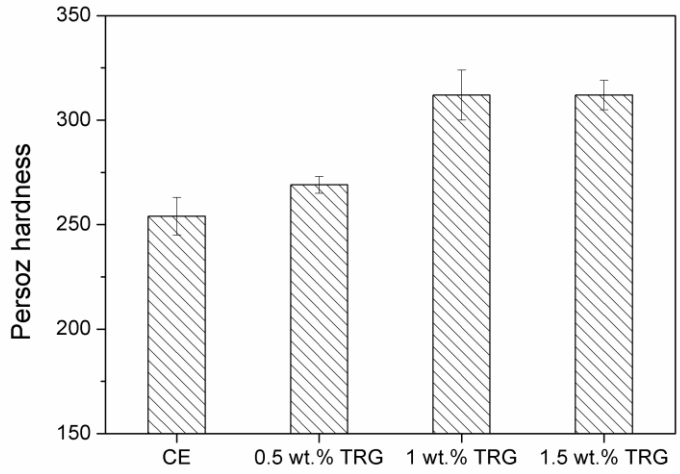

Figure V.16: Persoz hardness as function of TRG content.

V 8. SUMMARY

Four different types of carbon based nanofillers, i.e. MWCNTs, o-MWCNTs, TRG and EG, were introduced into a photo-curable epoxy resin formulation. The extents of reaction and polymerization rate were slightly delayed due to both a shielding effect and an increase of the viscosity of the filled-formulation, which decreased the *quantum yields* and the mobility of the reactive species. This phenomenon was more pronounced with nanometric fillers with higher aspect ratio and SSA (MWCNTs and TRG). Adjusting the processing conditions, we were able to develop nanocomposites characterized by high final conversion and gel values.

By analyzing the dielectric properties of the cured nanocomposites we found different percolation thresholds depending on the type of filler. The highest enhancement in electrical properties was achieved in the MWCNTs composites while in the sheet-like based nanocomposites were lower. These differences were attributed to the geometry of the filler, the filler dispersion and the more effective MWCNTs network to the electronic transport through overlapping of nanotubes. Nevertheless, all types of nanocomposites evaluated shifted the insulating behavior of the pristine epoxy resin to an antistatic material. However, TRG had the best behavior in terms of the dynamic mechanical and microindentation performances showing an increase on the surface hardness with the TRG content. An increase of more than 20 °C in the glass transition temperature was observed with the addition of 1 wt. % of TRG.

These results highlight the possibility to achieve advanced UV cured epoxy films with multifunctional properties.

Chapter VI. EPOXY NANOSTRUCTURATION BY BLOCK COPOLYMERS

Part of the work described in this chapter has been submitted to the following journal:

- *Composites Part A: applied science and manufacturing* (2014).

VI 1. INTRODUCTION

Since the first work reported by Hilmyer *et al.*[35] describing self-assembled structures in thermosetting polymers, two key types of block copolymers (BC) have been used as toughening agents. The first type are reactive BCs whose epoxy miscible group is reactive towards the epoxy monomer or hardener and the developed nanostructure can be fixed before macrophase separation occurs. A reactive BC can be produced by the epoxidation of one of its groups[382] or by synthesizing the full BC through complex reactions.[383, 384] The second type are nonreactive BCs which are the most widely studied, and includes a range of variants such as, poly(styrene)-poly(2-vinylpyridine),[385] polystyrene-block-poly(ethylene oxide)[386] or poly(epsilon-caprolactone)-block-polybutadiene-block-poly(epsilon-caprolactone),[40] among others. Poly(ethylene oxide)-poly(propylene oxide)-poly(ethylene oxide), (PEO-PPO-PEO) represents one of the most important BCs employed to nanostructure epoxy resins.

The popularity of PEO-PPO-PEO is due to its commercial availability, including different ratios of each block as well as the simplicity of the experimental procedure and the absence of any chemical synthesis or reaction with the epoxy system. For PEO-PPO- PEO epoxy blends, the formation of the self-assembled nanostructure depends on the curing conditions and the inner characteristics of the BC.[387-391] A common problem with adding BCs to epoxy resins is that poor miscibility between the two materials can result in a macrophase separation of one block of the BC, which minimizes the toughening effect of the BC. In addition, the BCs can have a negative effect on the Young's modulus and glass transition of the cured resin.

In addition to BCs, nanoparticles like carbon nanotubes and graphene have also been used to enhance the mechanical properties of epoxy resins and in particular the toughness.[74, 78]

In this chapter, we have analyzed the possible synergic effect between the self-assembled nanostructure of the BC and the CNPs on the toughness of the cured resin. The idea is that the addition of PEO-PPO-PEO should induce a nanostructure within the epoxy matrix that would enable a better dispersion of the nanofillers. Meanwhile, the

carbon nanotubes and graphene sheets minimize the negative effect of the BC on the elastic modulus and glass transition temperature of the resin.

VI 2. EXPERIMENTAL

The epoxy resin (ER) used in this study was diglycidyl ether of bisphenol A (DGEBA) and methylenedianiline (MDA) was used as curing agent and mixed in a epoxide/amine stoichiometric ratio. The block copolymer (BC) employed was poly(ethylene glycol)-block-poly(propylene glycol)-block-poly(ethylene glycol) (PEO-PPO-PEO), with average molecular weight, Mw= 8400 and 80 wt. % ethylene glycol. The BC possesses a melting point of 57 °C, crystallization temperature of ~ 36 °C and a glass transition temperature at -56 °C. All the chemicals were purchased from Sigma-Aldrich.

To prepare the cured samples, the block copolymer was added into the epoxy resin at 100 °C under continuous stirring at three different concentrations: 10 wt. % (10BC), 20 wt. % (20BC) and 40 wt. % (40BC) with respect to the epoxy resin. When a homogenous mixture was obtained, 0.25 wt. % (respect to the whole formulation) of carbon nanoparticles (MWCNT or TRG) was added and mechanically stirred at 100 °C and 2400 rpm for 2 h. Then, the mixture was degassed at 70 °C for 1 h in a vacuum chamber to remove the air bubbles trapped in the system. Finally, the curing agent was added to the mixture at 100 °C with continuous stirring until the hardener was completely dissolved. The final mixture was then poured into preheated aluminum pans and teflon molds, degassed again at 90 °C, cured at 80 °C for 8 h, and then post-cured successively at 150 °C for 2 h and 175 °C for 1 h. The whole experimental procedure is summarized in Figure VI.1.

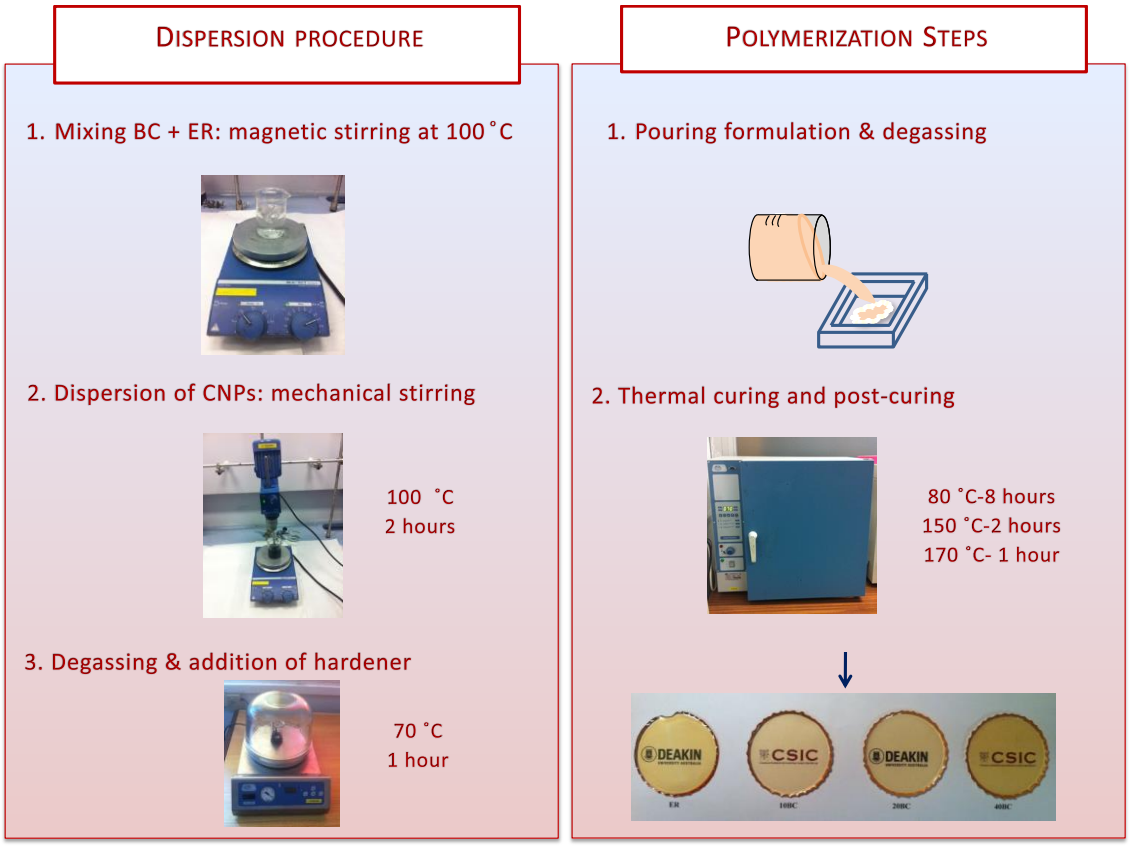

Figure VI.1: Experimental procedure for the preparation of nanostructured thermally cured composites.

TGA measurements were carried out on a TGA/SDTA851 from Mettler. The sample was placed on a ceramic holder and heated to 700 °C at a heating rate of 10 °C/min under a nitrogen flow of 20 mL/min to avoid any oxidation.

Calorimetric measurements were made on a TA Q200 differential scanning calorimeter in a dry nitrogen atmosphere (50 ml/min). Indium and tin standards were used for calibration purposes. Samples of 7-10 mg were placed in an aluminum DSC pan. All samples were first heated to 100 °C from -60 °C at 20 °C/min and kept at 100 °C for 2 min. Subsequently, they were cooled at a rate of 20 °C/min to -60 °C. Finally, a second heating scan to 250 °C at the same heating rate was carried out. The crystallization temperature (T_c) was assumed equal to the maximum of the exothermic peak, whereas the melting temperature (T_m) was the minimum of the endothermic peak.

Dynamic mechanical tests were performed on a TA Q800 dynamic mechanical analyzer in a single cantilever tension mode. The specimen dimensions were 30·5·2

mm. The storage modulus (E') and loss factor ($tan\ \delta$) were measured from room temperature to 250 °C at a heating rate of 3 °C/min and at a frequency of 1 Hz. The glass transition temperature (T_g) was taken at the maximum of the $tan\ \delta$ curve.

The cured samples were cryo-ultramicrotomed at -140 °C with a Leica EM UC6. The ultra-thin films obtained were placed on copper grids and stained with vapor of an aqueous solution of RuO4. The TEM images were taken using a Leo 910 microscope at an acceleration voltage of 80 kV.

Small angle X-ray scattering (SAXS) experiments were conducted at the Australian Synchrotron on small/wide angle X-ray scattering beam-line utilizing an undulated source that allowed measurement at a very high flux to moderate scattering angles and a good flux at the minimum q limit (0.012 nm^{-1}). The intensity profiles were interpreted as the plot of scattering intensity versus scattering vector, $q = (4/\lambda) \sin(\theta/2)$ (θ = scattering angle).

Analysis of the morphology of the system was carried out by atomic force microscopy (AFM) in a Bruker MultiMode 8 SPM instrument in PeakForce QNM mode on a flat trimmed surface generated by ultramicrotomy. AFM images correspond to the adhesion map.

SEM was carried out on a Philips XL30 ESEM at 25 kV to study the morphology and dispersion states of the cryo-fractured samples, which were previously metallized with a 5 nm coating of gold/palladium.

The fracture toughness of the cured samples was evaluated by means of the plane strain critical stress intensity factor (K_{IC}). Three point bending tests were carried out with an Instron mechanical tester according to ASTM D5045 standard. Three point bend single notch specimens (SEN-3PB) were prepared by casting and tapping with a fresh blade in order to initiate a pre-crack (see Figure VI.2).

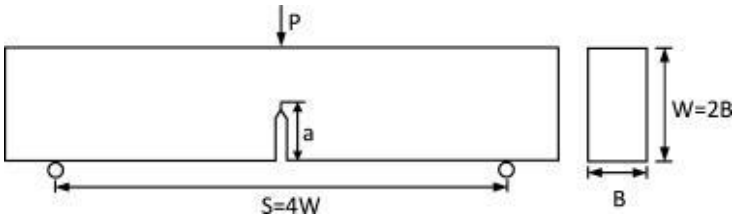

Figure VI.2: Configuration of the three point bend specimen. Note that W=12 mm, B=6mm and 0.45<a/W<0.55.

For the given configuration where the loading span (*S*) is 4 times the depth of the sample, K_{IC} can be calculated from Equation VI.1 and Equation VI.2.

$$K_{IC} = \frac{P}{B \cdot W^{1/2}} \cdot f\left(\frac{a}{W}\right) \qquad \text{Equation VI.1}$$

$$f\left(\frac{a}{W}\right) = \frac{\left\{6x^{\frac{1}{2}}[1.99 - x(1-x)(2.15 - 3.93x + 2.97x^2)]\right\}}{\left[(1+2x)(1-x)^{\frac{3}{2}}\right]} \quad x = \left(\frac{a}{W}\right) \qquad \text{Equation VI.2}$$

Where *P* is the critical load for crack propagation, *B* the specimen thickness, *W* the specimen width, *a* the initial crack length (crack prenotch plus razor tapping notch).

VI 3. MISCIBILITY AND CRYSTALLIZATION

The uncured s and the cured samples in all the range of composition used in this study are transparent at room temperature suggesting that macrophase separation before and during the curing process does not happen (Figure VI.3). This indicates the miscibility of both components at these compositions.

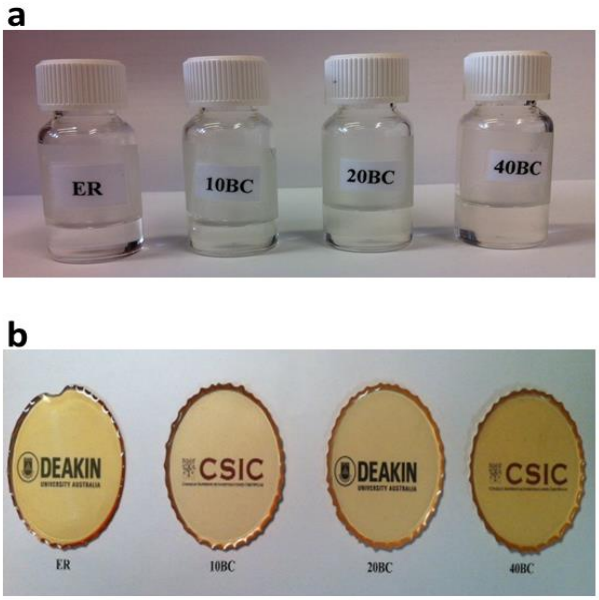

Figure VI.3: Digital image at room temperature of the samples in the a) uncured and b) cured states (2 mm thick).

The miscibility of the blends is also corroborated by the TGA results. The degradation curves of the epoxy resin and its blends with or without nanoparticles take place in a one-step degradation process. Besides, all the curves are overlapped (Figure VI.4) suggesting that there is not macrophase separation in any of the systems and indicating that the good thermal stability of the ER is not compromised by the addition of the BC.

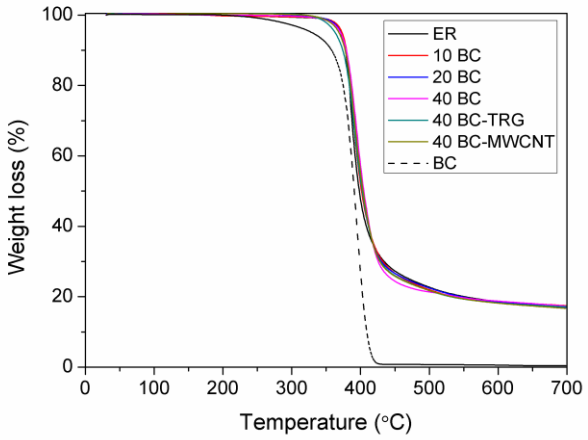

Figure VI.4: TGA curves of the cured ER-BC blends.

In Figure VI.5, DSC thermograms of the second heating scan are depicted. The T_g of the cured resin gradually decreases with the BC content in the blend, indicating the miscibility or at least partial miscibility of the two components. This reduction in T_g can result from the plasticization effect of the PEO chains that results in a reduction of the crosslinking density of the epoxy resin network. The effect of the nanofillers on the T_g will be analyzed by DMA measurements.

On the other hand, both 20BC and 40BC unfilled samples present a small endothermic peak in the proximity of the melting point of PEO. Hence, it appears these samples have just enough PEO to start the crystallization of small crystallites of PEO in the resin but not sufficient to cloud the sample. The disappearance of this peak in the loaded samples could be ascribed to three main causes: the first one is the local perturbation of the PEO crystalline order produced by the presence of nanoparticles;[392] the second cause is the lower mobility of polymer chains and higher viscosity of epoxy resin in the presence of MWCNT and TRG.[393] Thirdly, it has been reported that carbon nanoparticles accelerate the curing reaction of epoxy resins,[62] therefore PEO chains have less time to crystalize in systems with quick curing reactions.

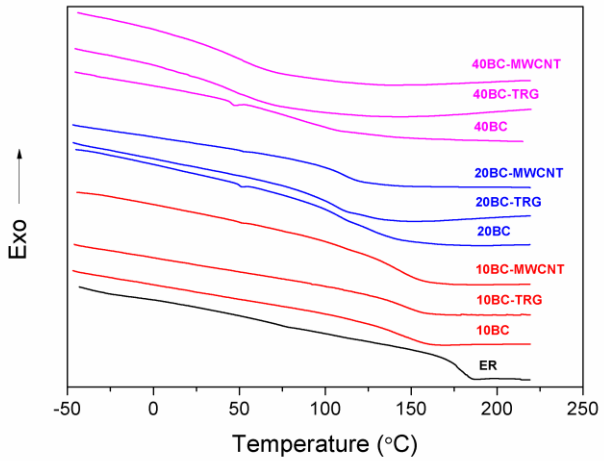

Figure VI.5: DSC thermograms of the cured blends.

VI 4. DYNAMIC MECHANICAL ANALYSIS

Figure VI.6 shows the dynamic mechanical response of all the samples. As already mentioned, the addition of BC significantly decreases the T_g due to the lower crosslinking degree of the PEO rich areas and the highly mobile microphases of PPO. However, in all cases the T_g of the nanoparticle filled mixtures is higher compared to the unfilled system (see values in Table VI.1). TRG is the most effective filler achieving increments higher than 20 °C with only a 0.25 wt. % of TRG in the formulation. These changes in the T_g are attributed to a strong filler-matrix interface, thus nanofillers with functional groups on their surface, like the TRG, produce a larger increment on the T_g. It is also important to point out how the storage modulus of the materials with nanoparticles is higher in the glassy and rubbery region balancing the negative effect of the BC on this property.

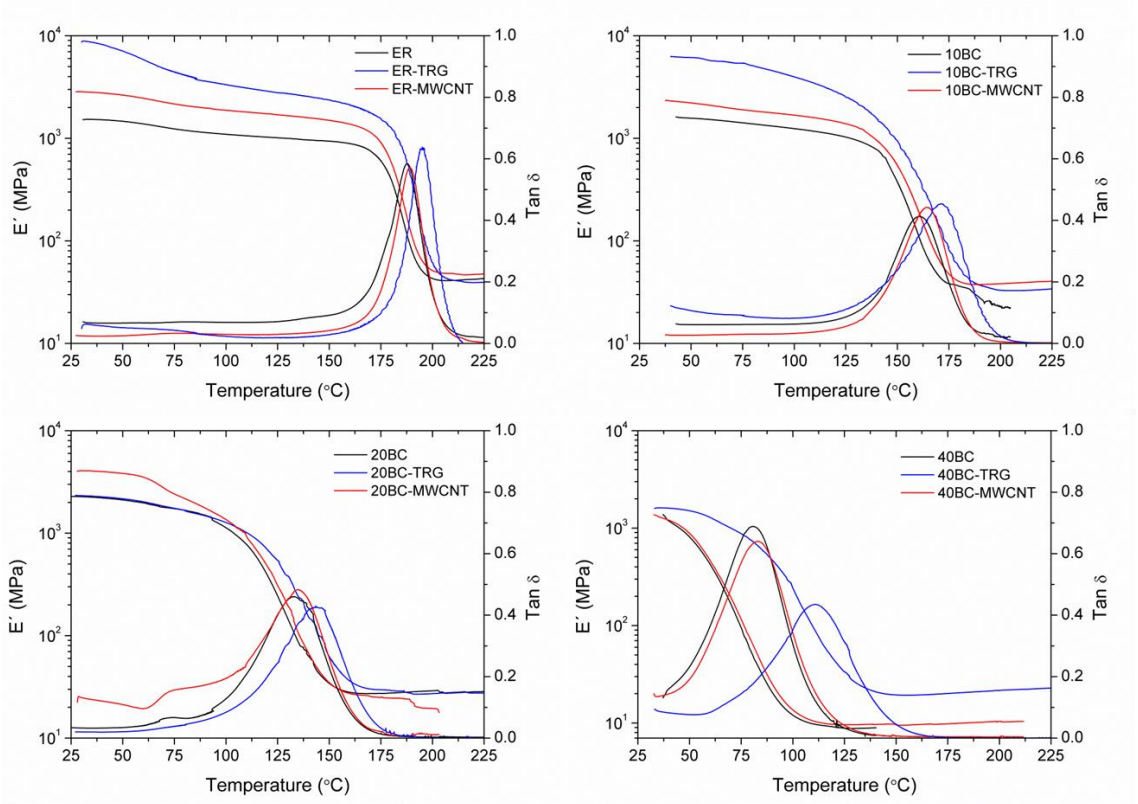

Figure VI.6: Dynamic mechanical curves of the cured blends.

Table VI.1: T_g values of the cured blends.

	Control (°C)	**TRG (°C)**	**MWCNT (°C)**
ER	187	195	189
10BC	160	171	164
20BC	133	143	135
40BC	81	109	84

VI 5. MORPHOLOGY

The morphology of the cured epoxy resin containing different amounts of BC was examined by TEM. Figure VI.7 shows the TEM micrographs for the 10BC, 20BC and 40BC. The sample with the smallest amount of BC displays the most homogeneous morphology, while the blends with BC content above 10 wt. % show a more heterogeneous morphology at the nanoscale. The tiny black spots are the PPO nanodomains, rendered black by the preferential staining with RuO_4 compared to the cured ER matrix.[394] The 40BC sample (Figure VI.7c) shows a hierarchical nanostructure formed by the PPO spherical domains with diameters of about 20-30 nm dispersed within the continuous ER matrix. The dark grey areas are the epoxy resin rich in PEO and the grey areas the epoxy resin rich phase. This hierarchical nanostructure was previously described by Guo *et al*.[388]

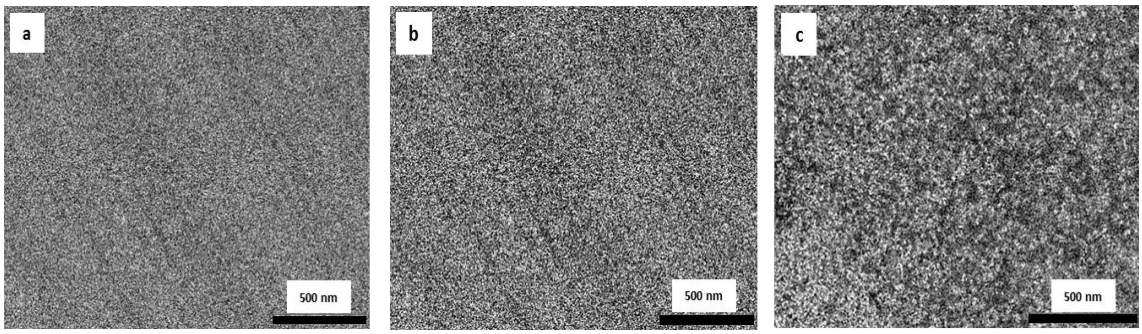

Figure VI.7: TEM images of a) 10BC, b) 20BC and d) 40BC.

The hierarchical nanostructure can be considered as a nanophase separated system driven by a reaction-induced microphase separation (RIMS) during the curing process due to the immiscibility of the PPO and the weaker miscibility of PEO in the cross-linked thermosetting resin.[42] At the beginning of the curing reaction the BC is miscible with the resin, as the reaction continues, the PPO central blocks start to nucleate in self-assembled nanodomains. Eventually, in the fully cured resin, PEO is located in the proximity of the PPO domains forming an interphase of partially cured epoxy resin rich in PEO acting as a bridge between the PPO nano-separated phase and the fully cured epoxy resin matrix.[395] As the miscibility of PEO in the fully cured resin is not as good as in the pre-cured resin, high amounts of the BC could lead to the orientation of some PEO chains in the right direction to partially crystallize. A schematic representation of the final self-assembled structure is shown in Figure VI.8.

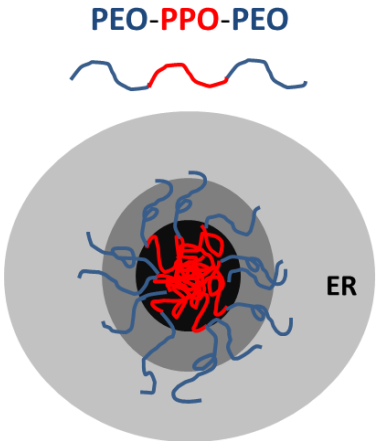

Figure VI.8: Scheme of the hierarchical nanostructure.

SAXS experiments were also performed to further characterize the morphology of the BC loaded resin. Their profiles are depicted in Figure VI.9. For the plain epoxy resin and the 10BC samples no scattering peaks are observed. A broad scattering peak can be seen for the 20BC and 40BC samples indicating the presence of phase separated structures at the nanometer scale. These peaks are centered at the scattering vector *q* for a long spacing of 23 nm, corresponding to the average distance between neighboring spherical domains.

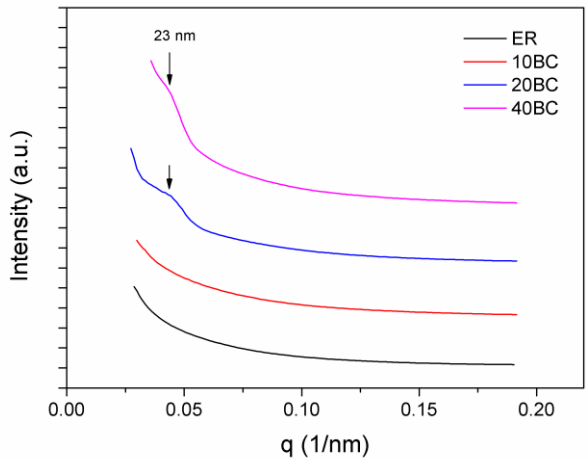

Figure VI.9: SAXS profiles of the neat epoxy resin, 10BC, 20BC and 40BC.

The effect of the addition of carbon nanoparticles on the morphology of the system was analyzed by AFM on an ultramicrotomed surface. Figure VI.10 shows the morphology obtained by tapping mode AFM for the samples without nanoparticles. As already observed in the TEM analysis, the 10BC sample presents a very homogeneous morphology at both micro and nanoscale. While, 20BC only shows the nanoseparated PPO domains at the nanoscale, seen in the 1x1 µm image. Finally, the 40BC sample presents a separated phase, with size domains around 0.6 to 1 µm, which corresponds to the PEO-rich microphases, seen in the 5x5 µm image, and the PPO nanodomains 1x1 µm image (PEO-rich microphases were intentionally avoided at the 1x1 µm scale image).

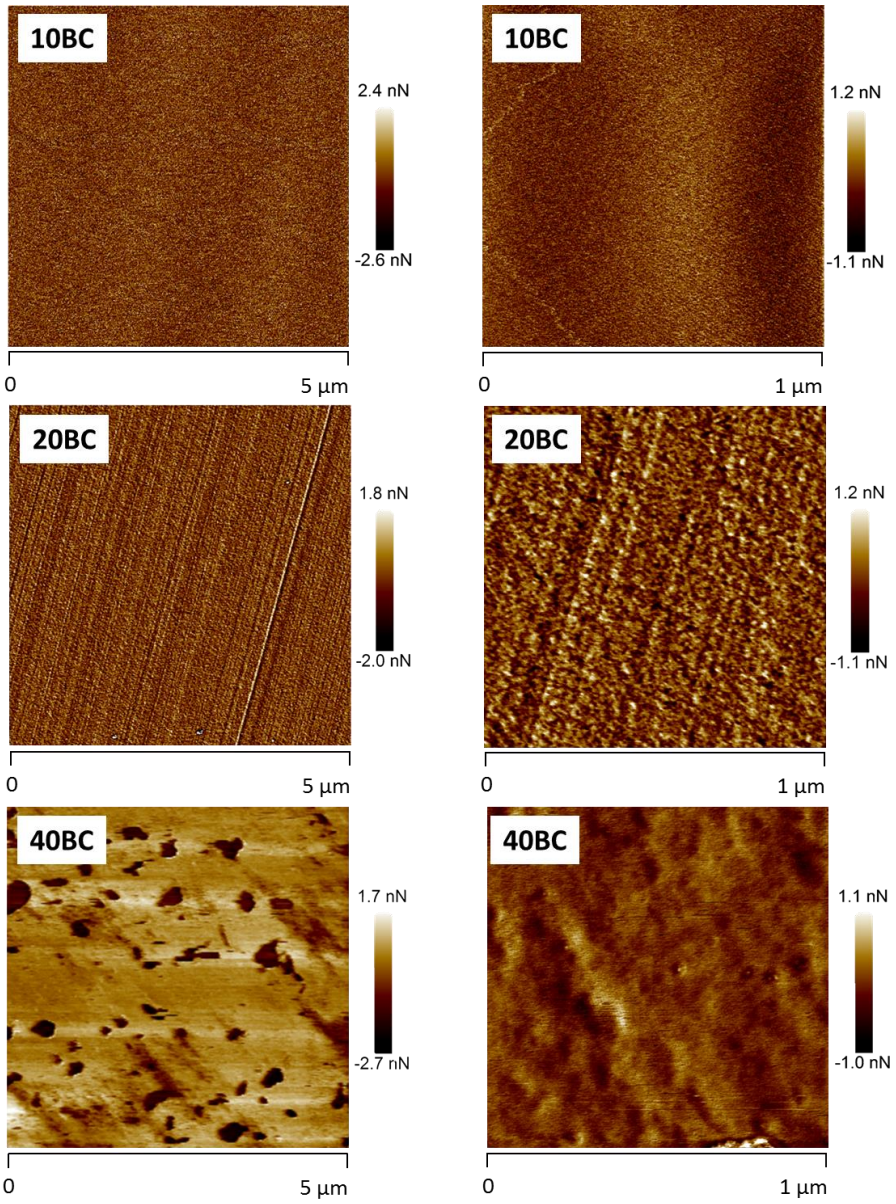

Figure VI.10: Tapping mode AFM images at 5x5 µm and 1x1 µm scales.

Figure VI.11 shows the effect of the nanoparticles on the morphology of the nanostructured epoxy resin containing 40 wt. % of BC. The addition of carbon nanoparticles inhibits the microphase separation of PEO-rich microphases as evidenced by the 5x5 µm scale images, resulting in a more homogeneous morphology.[396] On the other hand, the morphology of the samples at a nanoscale (1x1 µm frames) is not affected by the local perturbation of the nanoparticles and the spherical nanodomains of PPO are found in the samples examined. In all cases the size of the spheres is around 20-30 nm as also observed in the Figure VI.10 (1x1 µm image) of the 40BC sample.

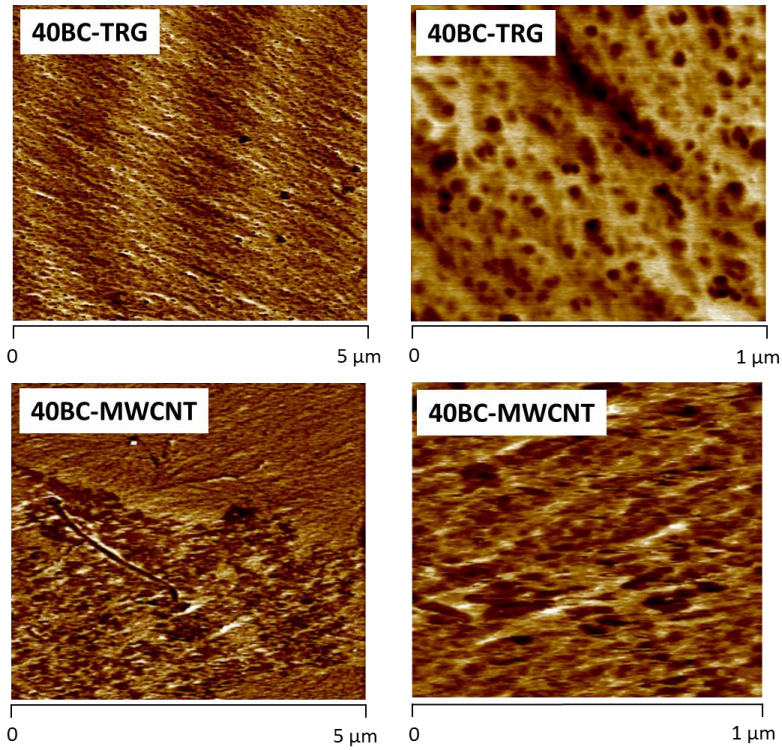

Figure VI.11: Tapping mode AFM images of 40BC-TRG and 40BC-MWCNT at 5x5 µm and 1x1 µm scales.

On the other hand, PEO-PPO-PEO BCs have also been employed to disentangle CNTs through non-covalent interactions between the blocks and the CNTs. This non-covalent functionalization is aimed to increase the stability of individual CNTs in organic solvents followed by evaporation and curing of the epoxy resin.[397, 398] A second approach to increase the dispersibility of CNTs using PEO-PPO-PEO is through wrapping processes.[396] However, the quantities of BC employed in these studies is not enough to generate a fully nanostructured system. In our study we employ larger quantities of BC which lead to the nanostructuration of the matrix and to the increase of the dispersibility of the nanoparticles.

The dispersion state of the nanoparticles was analyzed by SEM on cryofractured surfaces. The micrographs in Figure VI.12clearly show the different fracture mechanisms of the samples. For the neat epoxy resin, with neither BC nor nanofiller (Figure VI.12a), we can observe the classical brittle fracture with a flat surface and steps between cleavages on parallel planes. The addition of 40 wt. % of BC (Figure VI.12b) makes the fracture surface much rougher but it is still possible to observe some parallel

planes. Finally, the fracture for the 40 BC-TRG and 40BC-MWCNT (Figure VI.12c and d) show a much more ductile behavior without the previous evidences of brittle fractures. In both cases, TRG and MWCNTs are well dispersed and spread out through the epoxy matrix without forming agglomerates. In particular, the TRG can be found in stacks of a few graphene layers with a wrinkled geometry in a similar manner to previously reported observations.

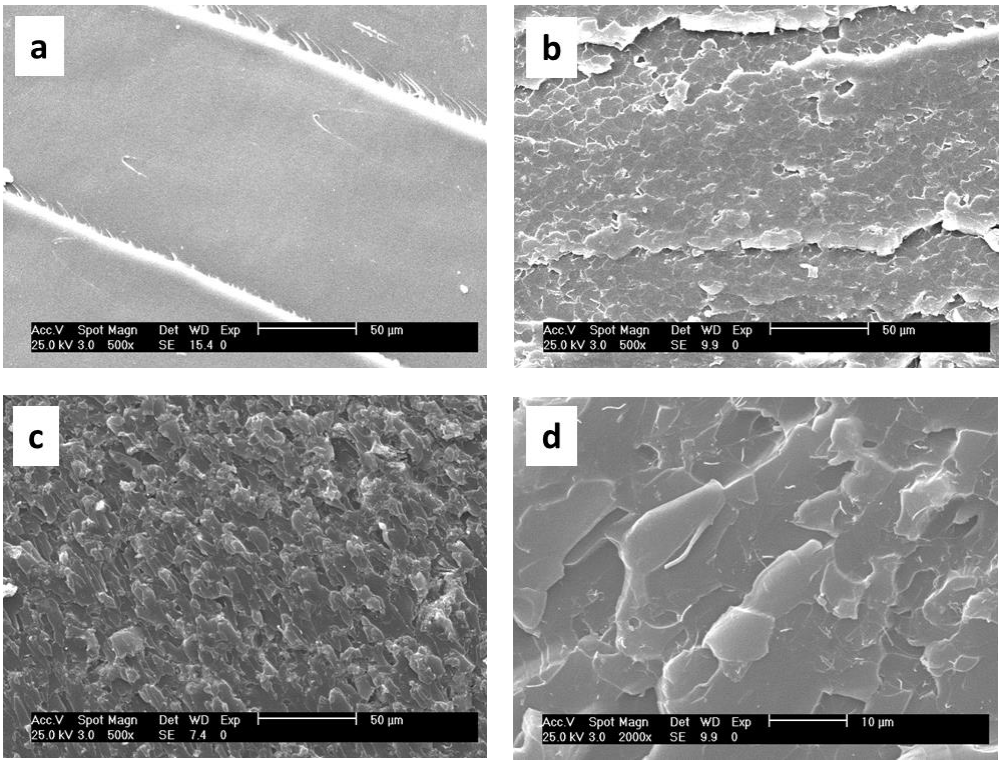

Figure VI.12: SEM images of a) neat epoxy resin, b) 40BC, c) 40BC-TRG and d) 40BC-MWCNT.

VI 6. TOUGHNESS

Mechanical properties of the cured mixtures were evaluated measuring the critical stress intensity factor (K_{IC}).

Figure VI.13 shows the positive effect of the BC and nanoparticles in the K_{IC}. The largest enhancement is obtained with the 40BC-TRG sample with an increment of

K_{IC} higher than 55 % compared to the neat epoxy resin (see values of K_{IC} in Table VI.2). TRG outperforms MWCNT due to the better adhesion of the graphene to the matrix produced by their surface functionalization, their high specific surface area and their wrinkle and planar geometry resulting in a better mechanical interlocking with the polymer chains and a more impeded crack propagation.[74, 373]

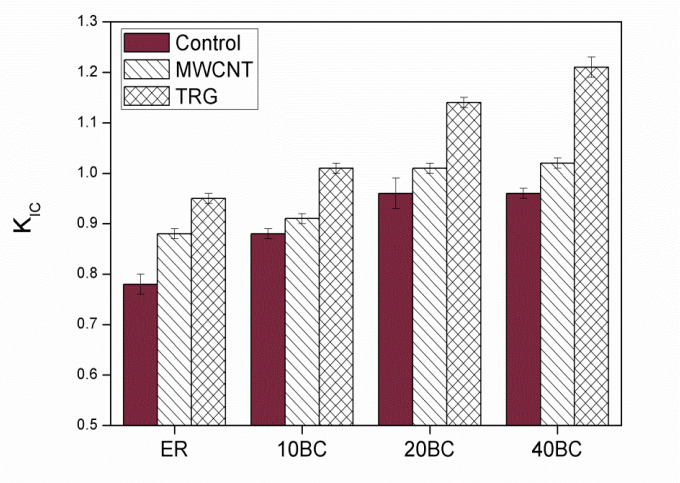

Figure VI.13: K_{IC} comparison.

Table VI.2: Toughness of the cured nanocomposites. K_{IC} (MPa $m^{1/2}$) values.

	Control	**TRG**	**MWCNT**
ER	0.78 ± 0.02	0.95 ± 0.01	0.88 ± 0.01
10BC	0.88 ± 0.01	1.01 ± 0.01	0.91 ± 0.01
20BC	0.96 ± 0.03	1.14 ± 0.01	1.01 ± 0.01
40BC	0.96 ± 0.01	1.21 ± 0.02	1.02 ± 0.01

When it comes to enhancing the toughness of epoxy resins using rigid particles, like TRG or MWCNTs, or a soft second phase, like a BC, there are several toughening mechanisms to take into account. Shear yielding is one of the most accepted mechanisms in polymers modified by a second phase. It involves the plastic deformation and cavitation of the particles and/or the matrix at the crack tip under the application of stresses.[399] Another toughening mechanism is the crack path deflection, in this case, the proposed role of the particles is to cause the crack to deviate from its plane. Such deviation results in an increased surface area reducing the mode I character of the opening of the crack.[400] The particle bridging mechanism supposes that the particles act as bridges compressing the crack path.[401] The microcracking mechanism supposes that the particles or the second phase generate microcracks increasing the toughness and originating tensile yielding and larger deformations.[402] Finally, in the crack pinning mechanism the rigid or soft particles behave as impenetrable objects that cause the crack to bow out, consuming extra energy to the crack propagation.[403] In the case of using nanoparticles as a toughening agent, particle pull-out should also be considered between the possible toughening mechanisms.[200]

However, none of the mechanisms explained above occur in an isolated way, more likely a combination of all of them may take place at the same time. For this reason, the integration of both toughening routes, the formation of a softer second phase and the addition of nanoparticles, would involve a larger number of toughening mechanisms.

VI 7. SUMMARY

Novel self-assembled nanocomposites based on blends of an epoxy resin and an amphiphilic triblock copolymer filled with carbon nanotubes and graphene were successfully prepared. A hierarchical nanostructure, with spherical PPO domains of 20-30 nm diameter homogeneously dispersed in the epoxy resin, was formed during curing reaction. A PEO-rich microphase was originated at a microscale for the blends above 20 wt. % of BC located at the interphase of PPO domains. The presence of the carbon nanoparticles appeared to inhibit this microphase separation, while no effect was

observed in either the size of the PPO nanodomains or their geometry. However, the carbon nanoparticles had a strong effect on the mechanical properties of the material. A synergic effect between the BC and the nanoparticles was observed, which gave rise to a significant increase of the toughness of the resin. In addition, the T_g of the resin was increased in more than 20 ºC upon the addition of TRG. TRG is the most effective property enhancer due to the better adhesion of the functionalized graphene layers with the matrix and their wrinkled and planar geometry.

Chapter VII. EPOXY NANOCOMPOSITE FOAMS

Part of the work described in this chapter has been patented:

- Spanish patent number P201430094 with the title: ***"Espumas rígidas termoestables conductoras"***.

VII 1. INTRODUCTION

This chapter comprises the development and characterization of electrically conductive epoxy nanocomposite foams. Conductive epoxy foams can be used to prevent electrostatic charge accumulation on electronic devices which are placed or wrapped in the foam. They can also be employed to increase the electrical conductivity or the electromagnetic interference (EMI) shielding of the sandwich structures employed with carbon fiber laminates.[404] Generally, the electromagnetic wave absorption effectiveness of materials depends on their dielectric properties (dielectric permittivity), magnetic properties, thickness and frequency range. The enhancement of these properties can be achieved by adding conductive fillers such as CNT, graphene, or metal particles.

The nanocomposite foams described in this chapter displayed electrical conductivities and permittivities five orders of magnitude higher than the unfilled epoxy foam. Besides, the excellent electrical conductivity of these foams is accompanied by slight increments on the thermal conductivity and in some cases improved mechanical properties.

The most common technique to prepare epoxy foams is through the combination of the epoxy formulation with low density glass microspheres. In our experiments, we used elastomeric microspheres which expand at the curing temperature. The use of these microspheres presents some advantages compared to the conventional glass microspheres:

- Lower contents of blowing agent are needed (7 wt. % against 50-60 wt. %).
- Elastomeric microspheres produce foams with lower density.
- Due to their flexibility, elastomeric microspheres do not break under the high pressures used during processing.
- They keep their elasticity before and after curing, reducing the generation of mechanical damage caused by thermal stresses.

On the other hand, low density polymer foams exhibit very poor flammability properties due to their cellular structure full of air, which leads to their rapid combustion. Usually, large amounts of flame retarding additives, like organohalogen or organophosphorus compounds, are used in the formulations to interfere with the condensed and gas phases during the combustion process. But these additives are closely linked to health and environmental issues. In our case, the addition of carbon nanoparticles increased the flammability resistance of the epoxy foams. Thereby, a reduction of the amount or elimination of flame retardants in the epoxy formulation could be considered.

VII 2. EXPERIMENTAL

Diglycidyl ether of bisphenol-A epoxy resin (product number: 405493), and diethylene triamine curing agent (D93856) used in this study were purchased from Sigma–Aldrich. Microspheres of Expancel (AzcoNovel 930 DU 120) were used as blowing agent.

First, the nanoparticles were dispersed using a three roll calender device (Figure VII.1) from EXAKT 80 E, EXAKT *Technologies, Inc.* following the three step protocol described in the Table VII.1.

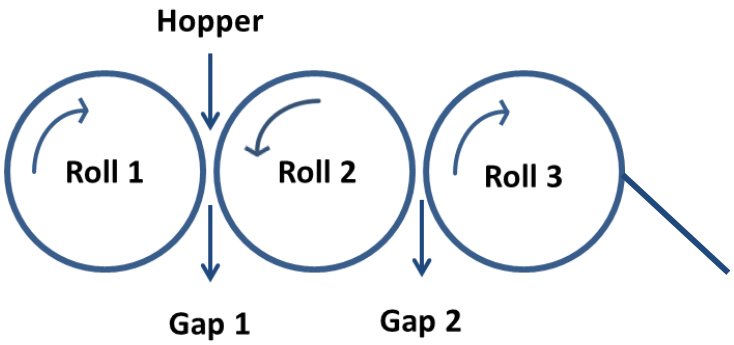

Figure VII.1: Scheme of the three roll calendar.

Table VII.1: Dispersing protocol.

	Gap 1 (µm)	Gap 2 (µm)	Speed (rpm)	Time (min)
Step 1	120	40	100	10
Step 2	60	20	80	10
Step 3	15	5	80	10

Then, the epoxy/nanofiller dispersion was degassed in a vacuum chamber until the complete removal of the air bubbles trapped in the resin. Epoxy/nanoparticle, the stoichiometric amount of hardener and a 7 wt. % of Expancel respect to the resin were mechanically stirred until a homogeneous blend was achieved. Then the mixture was poured inside a square metallic mold and placed in a hot press at 100 °C and 60 bars for 3 min and cooled down to room temperature. Finally, the foam was post-cured at 130 °C for 90 min. Varying the quantity of dispersion poured into the mold, it was possible to prepare samples with different densities. Foams with two different densities were produced, the low density set (LD) with a density around 250 kg/m^3 and the high density set (HD) with 800 kg/m^3 approximately.

The solid foamed squares were mechanized and 2 mm of solid skin was cut out from each side of the foam. The filler concentrations were selected according to the viscosity of the dispersion. In the case of MWCNTs, the maximum concentration was 0.5 wt. % while a 1.5 wt. % was introduced in the case of TRG. The whole experimental procedure is summarized in Figure VII.2.

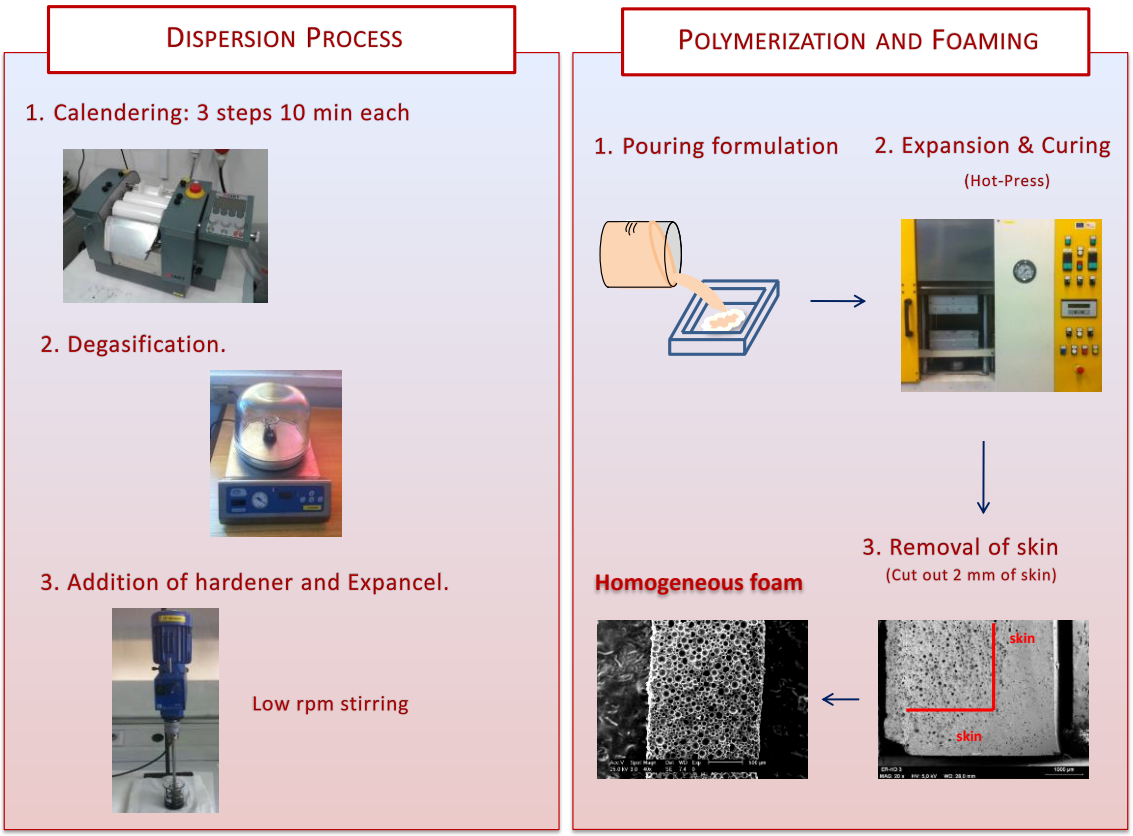

Figure VII.2: Experimental procedure of the foams preparation.

The density of a cubic sample was measured as the sample weight divided by its volume according to ASTM D 1622-03. The results were the average of at least three measurements.

The morphology of the foams and blowing agent were determined using scanning electron microscopy (SEM). The images were taken with a Philips XL30 ESEM at 25 kV. The samples were metallized with a 5 nm coating of gold/palladium.

The expansion of Expancel was analyzed using a Mettler Toledo822e DSC. Measurements from room temperature until 200 °C at a heating rate of 10 °C/min were carried out.

Thermal conductivity was measured by the Transient Plane Source (TPS) technique using a thermal conductivimeter model HDMD (hot-disk). TPS is a standard technique for thermal properties characterization of different materials (metals, ceramics, polymers, liquids, etc.). The basic principle of this method relies on a plane

element that acts both as temperature sensor and heat source. This TPS element is located between two samples with both sensor faces in contact with the two sample surfaces. Two samples of similar characteristics are required for this purpose.

Dynamic-mechanical tests were performed on a DMA-861e Mettler Toledo analyzer. Rectangular samples (45·7.5·2 mm) were tested in flexion mode from room temperature to 215 °C at 3 °C/min.

The limiting oxygen index (LOI) was measured according to ASTM Standard Method D2863-97 using a Metrotec Critical Oxygen Index (Mod. 1004050). This technique gives us information about the inflammability of the foams. It estimates the minimum concentration of oxygen in a nitrogen–oxygen mixture that will sustain combustion. Therefore, materials with LOI values higher than that of the usual percentage of oxygen in air (20 %) offer improved flammability properties.

Broadband dielectric spectroscopy was determined on an ALPHA high resolution dielectric analyzer (Novocontrol Technologies GmbH, Hundsangen, Germany) over a frequency range of 10^{-1}–10^{7} Hz at room temperature. The cured foams were held in the dielectric cell between two parallel gold-plated electrodes. The amplitude of the alternating electric current applied to the samples was 1 V.

VII 3. CHARACTERIZATION OF THE BLOWING AGENT AND DETERMINATION OF THE PROCESSING CONDITIONS

In order to obtain the final processing conditions described in the experimental section of this chapter, it was necessary to characterize first the blowing agent. The morphological characterization of the Expancel microspheres was carried out by SEM. Figure VII.3 shows the SEM image of the particles and their size distribution, with an average diameter around 30 μm.

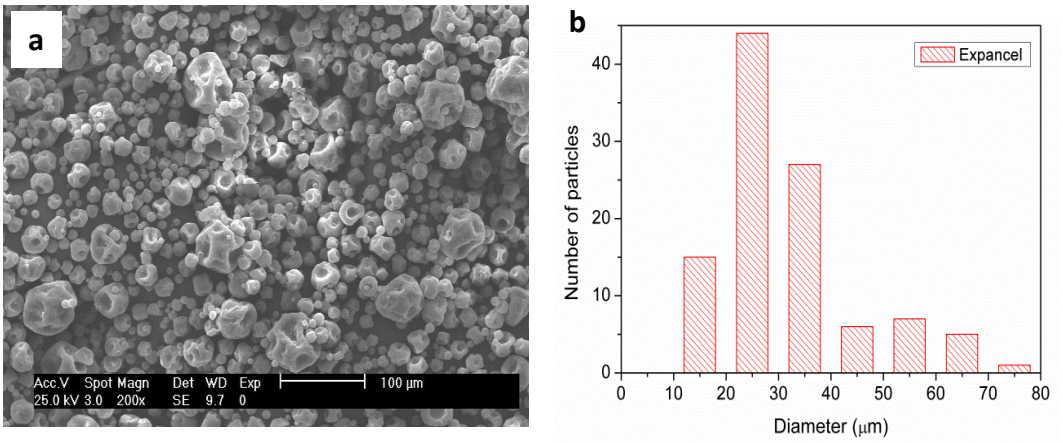

Figure VII.3: Morphological characterization of Expancel. a) SEM image and b) diameter distribution.

The material information provided by the manufacturer states an expanding temperature between 122 °C and 132 °C and a maximum temperature of use of 191 °C and 204 °C. In order to have a more precise range of temperatures, we performed a dynamic DSC. The thermogram (Figure VII.4) shows an endothermic process in a temperature range from 122 °C to 145 °C, corresponding to the expansion of the microspheres.

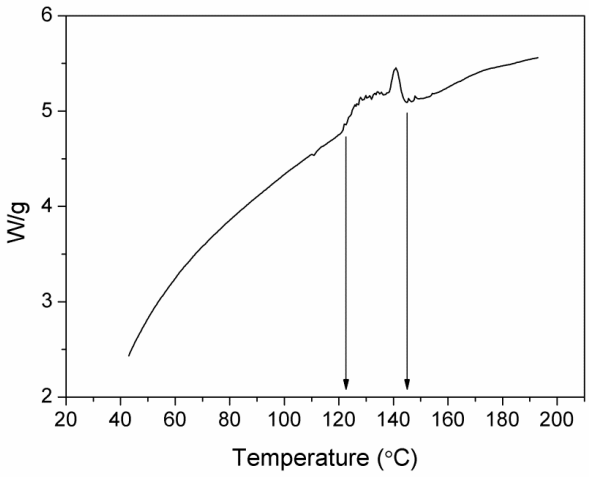

Figure VII.4: DSC of Expancel.

Curing conditions (temperature and time) must be selected in such way that the blowing process and the curing reaction occur at the same time. If the reaction is faster than the blowing process, the result will be a solid material with a high density. The first experiment was performed at 125 °C and after one minute all the epoxy resin degraded. This unexpected result was due to the fact that in the core of the mold, once the resin starts expanding, the temperatures were much higher than the initial temperature. The exothermal behavior of the curing reaction and the insulating character of the formed foam led to a quick degradation of the polymer. The second experiment was carried out at lower temperature (85 °C) and longer curing time (15 min). The result was a solid material with similar density to the epoxy resin without blowing agent (Figure VII.5a) indicating that the curing reaction finished before the expansion. Finally, intermediate temperatures and times were chosen, in particular 100 °C and 3 min led to a correct expansion and curing of the resin as can be observed in Figure VII.5b. These conditions were selected to prepare the rest of nanocomposite foams.

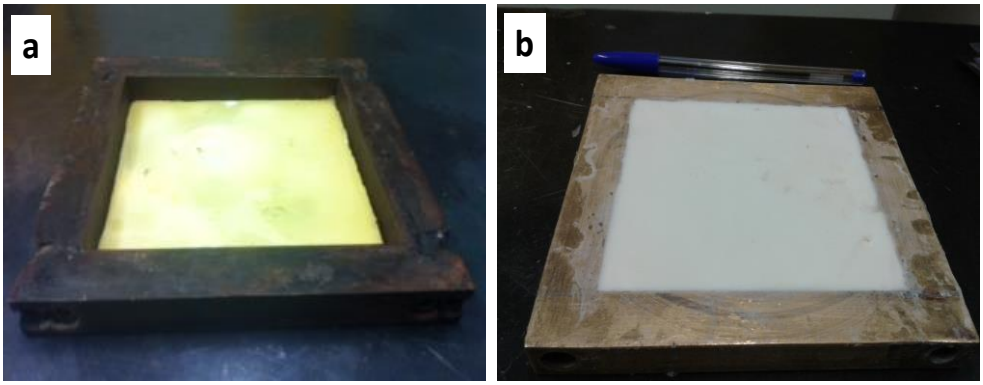

Figure VII.5: a) Premature curing without expansion (85 °C and 15 min) and b) full expanded epoxy foam (100 °C and 3 min).

VII 4. MORPHOLOGY

The cellular morphology of the epoxy foams will depend on the amount of Expancel microspheres introduced in the formulation and their final size. The cells generated by elastomeric microspheres are closed-cells with no interconnection or wall

ruptures. There will always be a cell wall, formed by the shell of the microsphere and the epoxy resin, separating the cells. In the case of nanocomposite foams, we start from a heterogeneous system containing the blowing agent, the polymer precursors and the CNPs. At the beginning of the blowing process we would have a homogeneous dispersion of the CNPs and Expancel within the liquid resin. Once we increase the temperature of the system, the microspheres start to expand, trapping the CNPs within the cell walls and the struts. This blowing process occurs simultaneously with the curing reaction. At the end of the foaming and curing processes, the CNPs would form a network throughout the sample. A schematic diagram of this process is depicted in Figure VII.6.

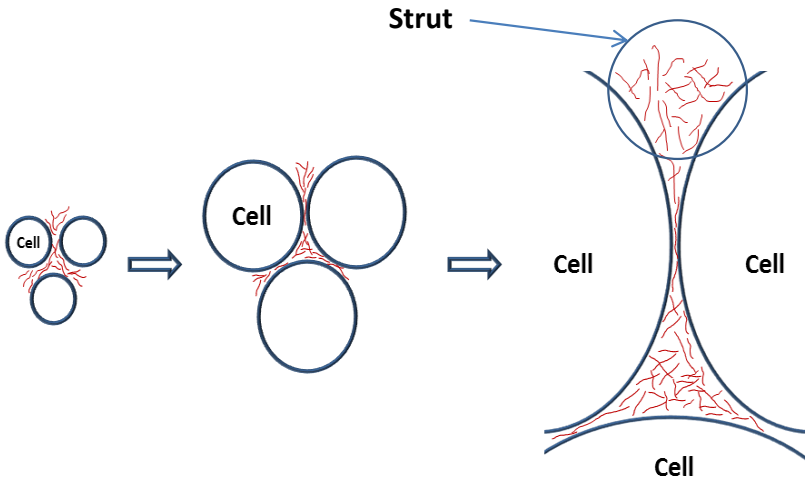

Figure VII.6: Schematic diagram of the changes on the cell structure in nanocomposite foams.

Figure VII.7 shows the cellular structure of the epoxy foams with low densities analyzed by SEM. It is possible to observe in the low magnification image (Figure VII.7a) that the ER-LD sample possesses a homogeneous distribution of the cells with an average size of 130 ± 29 µm and clear spherical shape (see Figure VII.7b, Figure VII.7d and values in Table VII.2) which is not affected by the addition of MWCNTs and TRG. In the case of the loaded foams, MWCNTs and TRG are well distributed throughout the struts and walls of the cells maintaining a percolated network within the

foamed matrix (Figure VII.7c and Figure VII.7d). The thickness of the cell walls is about 1-2 µm for all the samples.

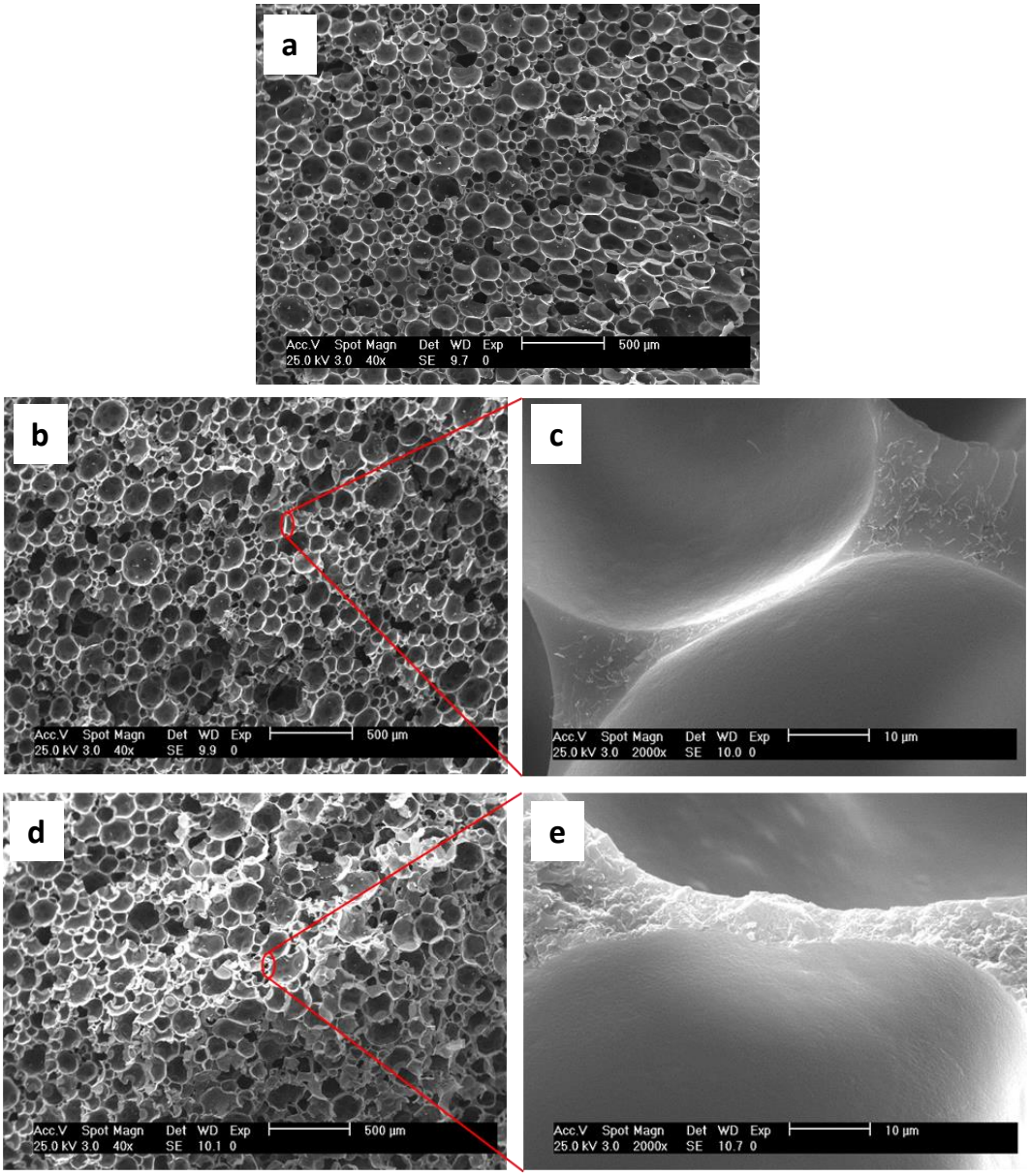

Figure VII.7: SEM images of the low density foams. a) pristine ER-LD, b) and c) 0.5 wt.% MWCNT-LD, d) and e) 1.5 wt.% TRG-LD.

Considering the initial value of the microspheres´ diameter before the expansion (30 µm) and the value of the cell size (taking 130 µm as reference), we obtain an expansion factor of approximately 4.3 for all the low density foams. This value is

slightly higher than the ones obtained by other authors using expandable microspheres in epoxy resins.[405] This expansion factor is related and agrees with the density reduction, from 1100 kg/m^3 to 250 kg/m^3.

Just by introducing a higher amount of formulation into the mold with the same amount of blowing agent, we were able to prepare foams with higher density. As in the case of the low density foams, the microspheres were homogeneously distributed before the expansion and resulted in an expansion factor around 1.5. Figure VII.8 shows the morphology of these foams, with cell sizes of around 56 ± 23 µm and wall thicknesses of 10-12 µm (Table VII.2). Individual MWCNTs and TRG were visible protruding from the polymer matrix and were uniformly distributed within both the struts and walls with no obvious aggregation (Figure VII.8c and Figure VII.8e).

Table VII.2: Cell size of the epoxy foams.

	Cell size (µm)
ER-LD	130 ± 29
0.25 wt. % MWCNT-LD	118 ± 41
0.5 wt. % MWCNT-LD	129 ± 36
1 wt. % TRG-LD	126 ± 35
1.5 wt. % TRG-LD	125 ± 31
ER-HD	58 ± 27
0.25 wt. % MWCNT-HD	53 ± 17
0.5 wt. % MWCNT-HD	55 ± 28
1 wt. % TRG-HD	56 ± 17
1.5 wt. % TRG-HD	57 ± 26

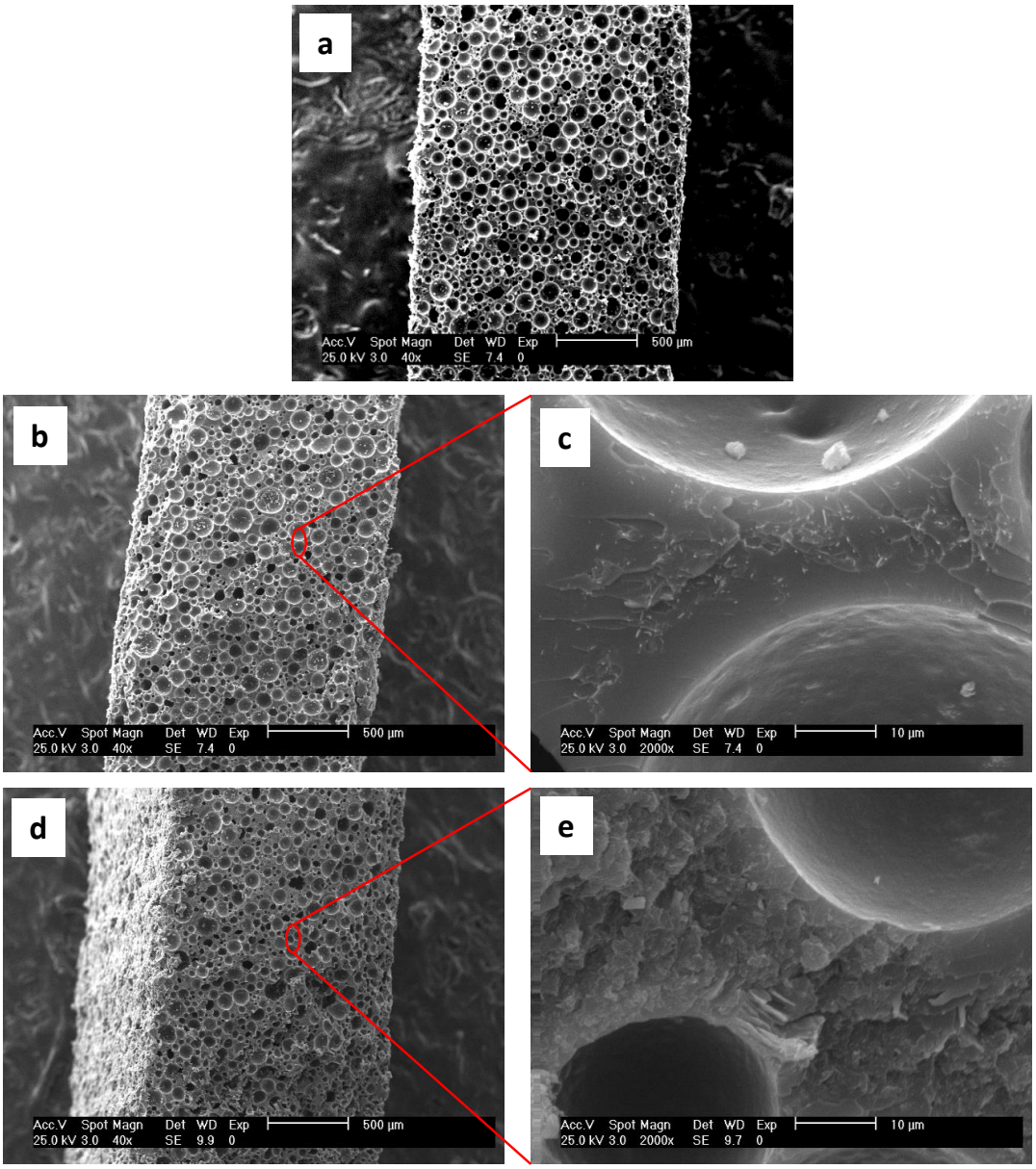

Figure VII.8: SEM images of the high density foams. a) pristine ER-HD, b) and c) 0.5 wt. % MWCNT-HD, d) and e) 1.5 wt. % TRG-HD.

VII 5. DYNAMIC MECHANICAL ANALYSIS

The mechanical properties of the epoxy foams were evaluated through their dynamic mechanical response. In order to compare the effect of the filler on the elastic modulus, we first analyze the dependence of the elastic modulus with the density to then, highlight the reinforcing effect of the CNPs. Thereby, small differences in the

density between samples will not have an impact on the evaluation of the reinforcing effect of the nanofiller. Figure VII.9 shows how the value of *E´* clearly increases with the density of the foam. The best fitting corresponds with a power law dependence with an exponent of 2.4.

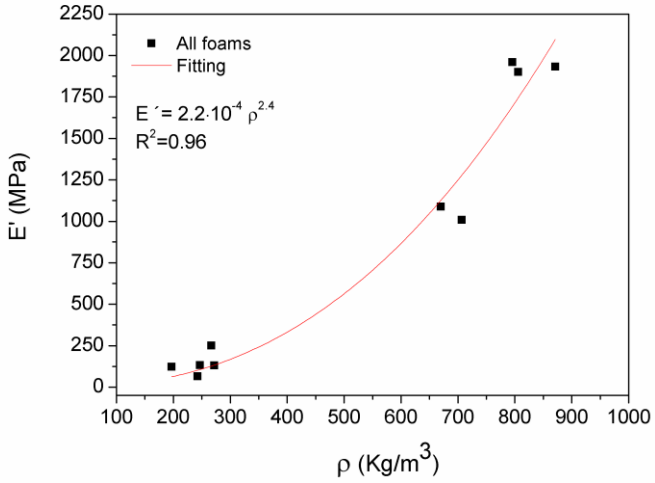

Figure VII.9: E´ vs ρ at room temperature.

Once the relationship between the modulus and the density is determined, it is possible to represent the specific elastic modulus ($E´/\rho^{2.4}$) as a function of the temperature (Figure VII.10). Analyzing the glass-rubber transition for both types of foams, we observe a decrease of the T_g with the density from around 131 °C for the low density foams to 115 °C for the high density foams. This difference on the T_g could be ascribed to a confinement effect of the polymer chains in the walls of the foams.[406] As previously demonstrated in Chapter IV of this thesis, MWCNTs and TRG usually constrain the chain mobility displacing the T_g towards higher temperatures. In the case of epoxy foams, the hindering effect of the nanoparticles on the chain mobility appears to be masked by the confinement of the epoxy chains when the density is reduced.

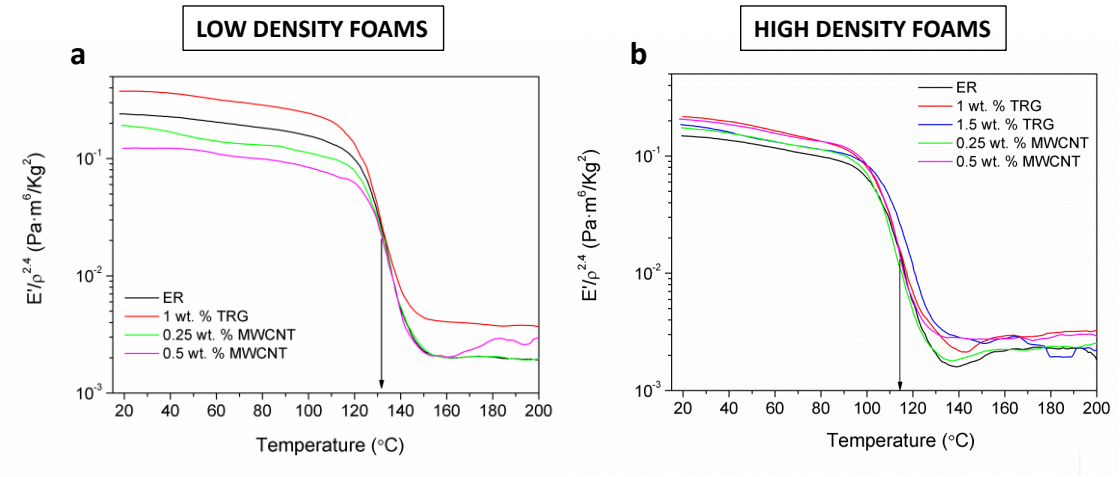

Figure VII.10: E´ vs temperature for a) low density and b) high density foams.

Low density foams filled with MWCNTs shows unexpected lower values of *E´* in the glassy state. While TRG shows enhanced mechanical properties in both regions of the chart, the glassy and rubbery states. The better performance of TRG is attributed to the improved interfacial interactions with the epoxy matrix as also observed in polyurethane foams[407] and other chapters of this thesis. Meanwhile, all the high density nanocomposite foams outperformed the mechanical response of the pristine epoxy foam. Therefore, the negative effect of MWCNTs in the low density foams must be related with the cellular structure of the foams, their thinner polymer walls and smaller struts may decrease the reinforcing effect of MWCNTs. The enhancements obtained with the high density foams are in the same range as the results published by other authors using epoxy resin, glass microballoons and CNTs,[195] graphene[408] or CNFs.[196, 198]

VII 6. FLAMMABILITY

Low density foams exhibit poor performance on combustion. Besides, polymer foams are used in a wide variety of structural applications, which should fulfil strict fire regulations under specific flame exposure and combustion conditions. Therefore, it is necessary to introduce large quantities of flame retardants in order to reduce their

flammability. Flame retarding additives interfere with the condensed and gas phases during all stages of the combustion process (heating, ignition, decomposition and flame spread) or on several of them simultaneously.[409] However, flame retarding additives are often associated with health and environmental issues, thus new approaches, like the use of nanoparticles, have been employed to improve the flame retardancy properties of polymer foams. CNTs and graphene have been proved to improve the flammability of polymer matrices like silicone,[410] polypropylene,[411] ethylene vinyl acetate,[412] epoxy resins,[255] among others. The proposed mechanism for this improvement is the formation of a protective flocculated layer covering the sample surface.[409]

Figure VII.11 shows three representative images at the initial stages of the LOI tests. The pristine epoxy resin developed a large flame after just few seconds of ignition at a 20.3 vol. % of oxygen as can be observed in Figure VII.11a. The filled foams exhibited improved flame propagation delay at that air composition, thus, a 21 vol. % of oxygen was employed. Figure VII.11b and Figure VII.11c shows the flames right after ignition for the 0.5 wt. % MWCNT-LD and 1.5 wt. % TRG-LD samples respectively. In both cases the flames developed by the nanocomposites foams are smaller than in the case of the neat epoxy resin even at a higher concentration of oxygen in air. In first instance, TRG seems to reduce more effectively the flammability of the foam. Nevertheless, at higher oxygen percentages TRG and MWCNT nanocompostie foams behaved very similarly, as evidenced by the final LOI values reported in Table VII.3.

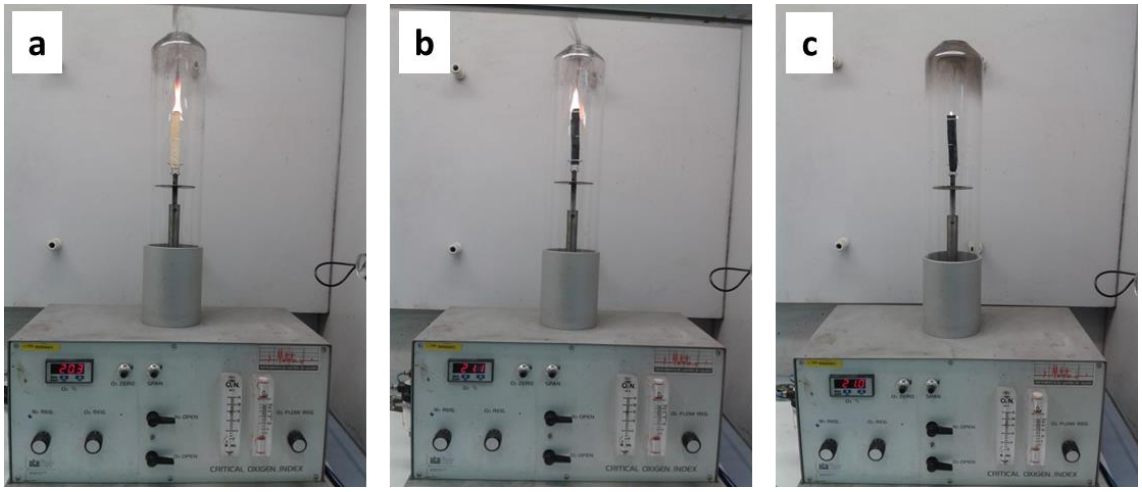

Figure VII.11: a) LOI test of ER-LD at 20.3 vol. % of oxygen, b) LOI test of 0.5 wt. % MWCNT-LD at 21.1 vol. % of oxygen and c) LOI test of 1.5 wt. % TRG at 21 vol. % of oxygen.

The improved flammability properties of the nanocomposite foams can be attributed to the presence of the CNP network on the cell wall. This network would protect the underlying layer of polymer retarding its combustion.[410]

Table VII.3: LOI values for the low density foams.

	LOI
ER	20.4 ± 0.3
0.25 wt. % MWCNT-LD	22.7 ± 0.1
0.5 wt. % MWCNT-LD	22.7 ± 0.1
1 wt. % TRG-LD	22.0 ± 0.2
1.5 wt. % TRG-LD	22.6 ± 0.5

VII 7. THERMAL CONDUCTIVITY

The cellular structure of polymer foams gives them very low thermal conductivity, which is a sought property for insulating applications. However, the addition of highly conductive CNPs could modify the insulating character of the foams by increasing their thermal conductivity (κ).

Figure VII.12 shows the variation of κ with the foam density. Low density foams exhibit very low values, around 0.05 W/m K which means a reduction of one order of magnitude compared to the solid resin (~ 0.3 W/m K). As in the case of the elastic modulus, the thermal conductivity varies with the density. In this case, there is a linear dependence with the density.

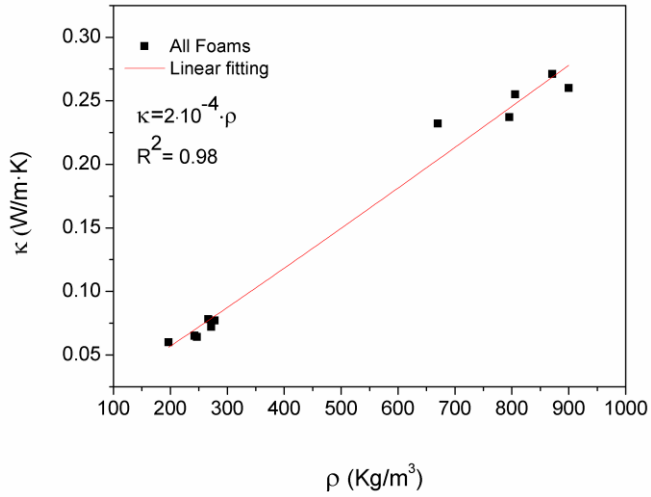

Figure VII.12: Variation of κ with the foam density.

It has been well established that the thermal conductivity generally decreases with cell size. On the other hand, the thermal conductivity increases with incorporation of nanofillers with superior thermal conductivity.[309, 407] As we could observe in the morphological analysis, the cell size of the foams is very similar among the samples with the same density. Therefore, the differences in the thermal conductivity of the nanocomposite foams with the same density should be ascribed to the effect of the nanofillers.

In order to eliminate the slight density differences within the low and high density set of samples, the specific value of the conductivity (κ/ρ) is represented in Figure VII.13. In both, low density and high density foams, the thermal conductivity of the nanocomposites foams is slightly higher than the neat epoxy resin. The addition of CNPs in the low density foams does not change the insulating behavior of the foam, as previously shown in Figure VII.12. Besides, the values of κ/ρ do not show a clear tendency with the amount of filler added into the foam. The increments in κ/ρ are more significant in the case of the high density foams, with a 20 % increase with the addition of 1.5 wt. % of TRG.

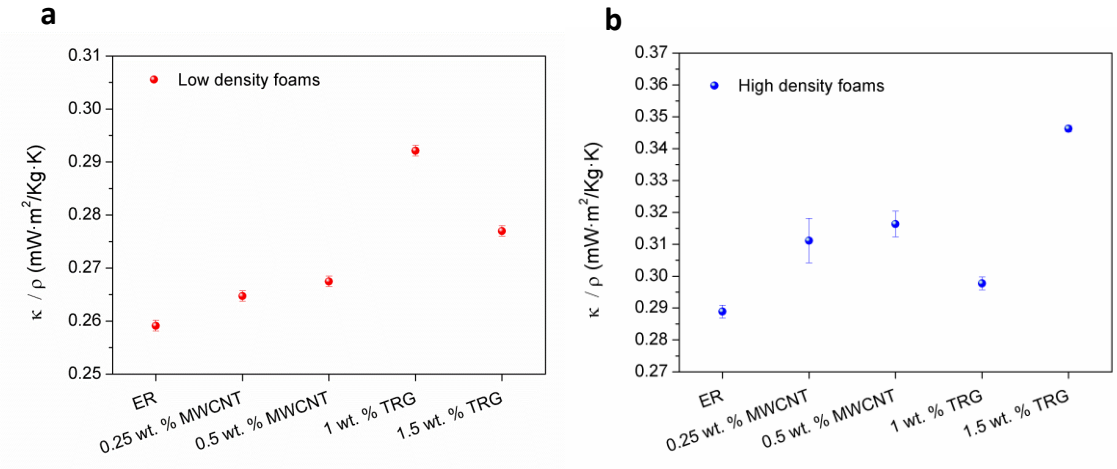

Figure VII.13: κ /ρ for a) low density foams and b) high density foams.

VII 8. ELECTRICAL PROPERTIES

Polymer foams are not usually chosen for their electrical properties which often play a secondary role in the final application of the foam. High electrical resistivity can be important for structural enclosures or insulating coatings. However, high resistivity is not always desired, certain degree of conductivity is sought to dissipate static electricity, for electrical screening or EMI shielding.[47, 404]

Figure VII.14a shows the electrical conductivity of the low density foams. The conductivity of the epoxy resin shows a linear dependency with the frequency, characteristic of an insulating material. This behavior is modified by the addition of the conductive nanofillers, where the conductivity shows a constant value at low frequencies. The significant increment on the electrical properties of the nanocomposite foams is attributed to the formation of a conductive filler network within the cell walls and struts. Both concentrations of TRG (1 wt. % and 1.5 wt. %) evidenced to be above the percolation threshold. The 0.5 wt. % of MWCNT sample shows the highest value of electrical conductivity, close to 10^{-5} S/cm. While the electrical response of the 0.25 wt. % MWCNT sample is insulating, overlapping the epoxy resin curve. High density foams give very similar results to the low density ones indicating that the effect of the density is small.

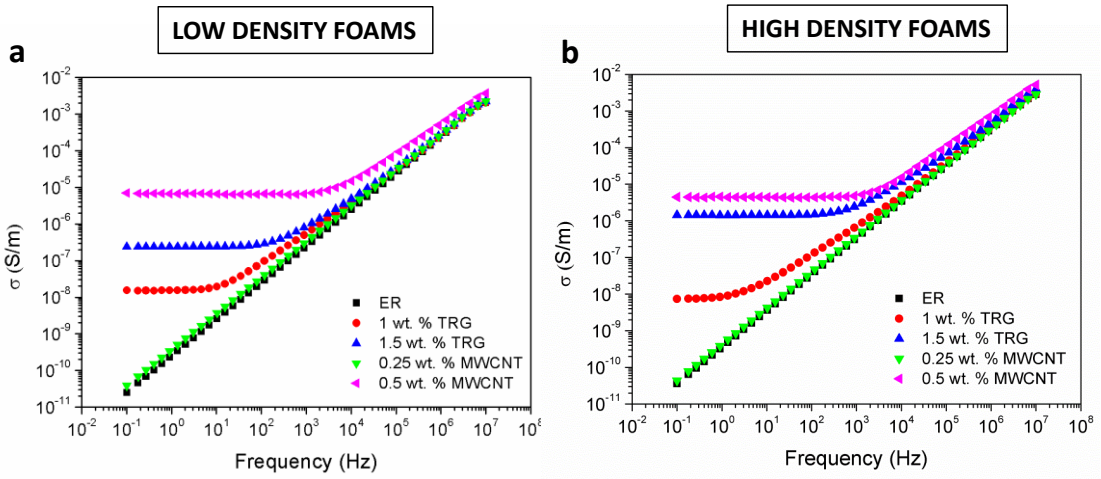

Figure VII.14: Electrical conductivity of the a) low density foams and b) high density foams.

According to the electromagnetic theory, the absorption of electromagnetic waves in a certain material depends on the polarization of the shielding material. The dielectric permittivity is a direct way to measure its polarizability. In other words, materials with high dielectric permittivity will be more efficient on EMI shielding. The permittivity of the foams is represented in Figure VII.15. As in the case of the electrical conductivity, all the systems with concentrations above the percolation threshold show

an important increase of the dielectric permittivity. Enhancements of six orders of magnitude are reached with 0.5 wt. % MWCNT.

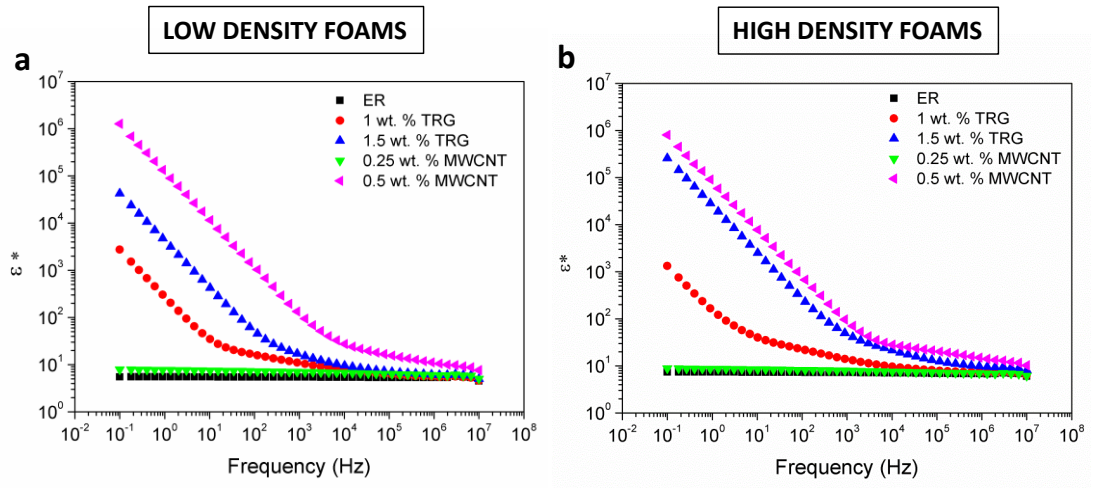

Figure VII.15: Permittivity of the a) low density foams and b) high density foams.

VII 9. SUMMARY

This chapter describes the experimental protocol and materials employed to produce low and high density epoxy foams (0.25 g/cm^3 and 0.8 g/cm^3 approximately) with enhanced electrical properties as their main feature. These rigid epoxy foams were produced using elastomeric microspheres as blowing agent and MWCNTs and TRG as conductive fillers.

The addition of 0.5 wt. % of MWCNTs produced enhancements of six orders of magnitude on the electrical conductivity and dielectric permittivity. The electrical conductivity was independent of the density of the foam, depending only on the generation of a percolated filler network in the cell walls and struts.

In addition to the electrical conductivity, the thermal conductivity was slightly increased by the nanoparticles in the low and high density foams. Nevertheless, the insulating behavior of the foams is maintained. The flammability of the low density

nanocomposite foams was also modified. In particular, the ease for ignition and the final LOI values improved respect to the pristine epoxy foam.

Dynamic mechanical analysis showed that the T_g of the low density foams was around 15 °C higher than in the high density foams. This result was attributed to the lower mobility of the polymer chains by confinement in the thinner cell walls and struts of the low density foams. This confinement effect on the T_g masked the influence of the nanoparticles on the T_g which remained invariable with the addition of the nanofillers. On the other hand, the elastic modulus was also improved in some of the systems studied. For the low density foams, the greatest enhancements were obtained for the samples with TRG. High density foams with MWCNTs and TRG exhibited improvements in the elastic modulus.

The development of electrical conductive epoxy foams through the experimental procedure explained in this chapter can find applications in different fields as shown in Figure VII.16. In the aeronautical sector, these foams could be applied in the sandwich structures of carbon fiber composites. The enhanced electrical conductivity would provide a higher electrostatic discharge after lightning strike. Conductive epoxy foams can also serve as EMI shielding barriers in electronics or in devices inside the aircrafts due to their light weight and high dielectric permittivity.

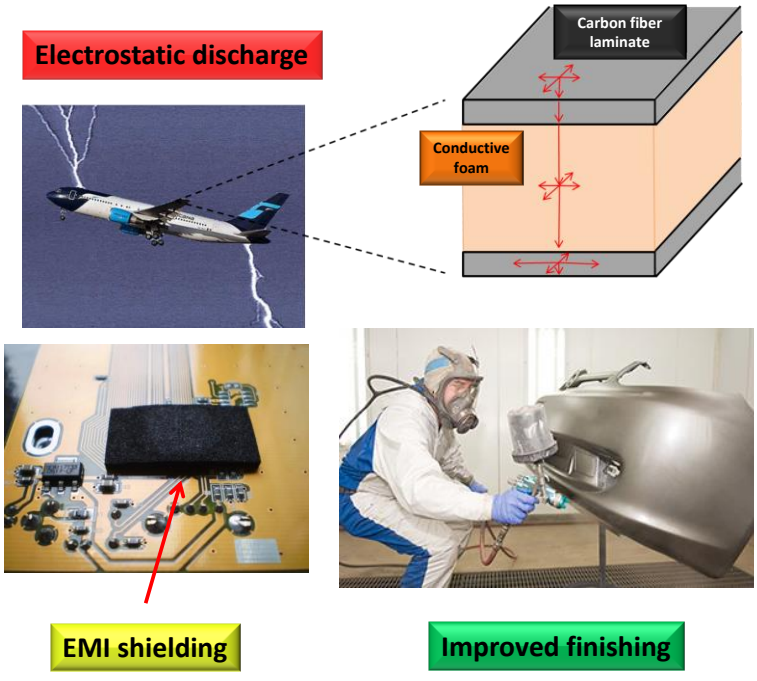

Figure VII.16: Application of conductive epoxy foams.

Chapter VIII. CONCLUSIONS

This thesis deals with the development of epoxy nanocomposites based on carbon nanostructures like MWCNTs and TRG. These CNPs were added into four different epoxy systems: thermally cured epoxy resins, UV cured epoxy coatings, nanostructured epoxy resin and low density epoxy foams. In the four cases, we analyzed and compared the effect of each type of nanofiller on the processing, cross-linking reaction morphology and final properties of the nanocomposites.

The following general conclusions can be extracted from this work:

- We studied the percolation network of MWCNT and TRG thermally cured epoxy nanocomposites through the rheology behavior of the dispersions. A lower rheological percolation threshold for MWCNTs was observed due to their rod-like geometry and a very high aspect ratio. MWCNTs changed the rheological behavior of the dispersion from a Newtonian fluid to a shear-thinning response while the planar structure and functional groups on the TRG did not to raise the viscosity of the dispersions even at high concentrations. This low viscosity plays a key role in their processing which allows us to introduce higher contents of TRG. The tensile tests performed on the thermally cured samples revealed notable enhancements in the elastic moduli and final strength of the composites, especially in the case of the nanocomposites containing TRG.

- Low field NMR experiments were demonstrated to be suitable to analyze the curing reaction, network structure and segmental dynamics of thermosetting polymers. The results related to the curing kinetics of the thermal curing reaction were compared and complemented with other traditional techniques. We observed an autocatalytic effect in the presence of the CNPs, reducing the induction and gel times, increasing the polymerization rate and decreasing the overall activation energy. The accelerating effect of the particles was attributed to the increment on the thermal conductivity of the dispersion, the presence of functional groups on the surface of the CNPs and their high SSA. It is worth noting that it was the first time that NMR approaches were used for this purpose.

- We employed an easy and direct method based on the hot wire technique to measure the thermal conductivity of epoxy nanofluids. We also studied the differences in heat conduction mechanisms using graphene sheets and different types of CNTs analyzing the role of surface functionalization and resistance to

heat flow at the interface in the thermal conductivity. The results showed that the layered structure of MWCNTs enables an efficient phonon transport through the inner layers, while o-MWCNTs and TRG have functional groups on their surface acting as scattering points for the phonon transport.

- A second epoxy system based on the UV curing technology was employed to develop multifunctional epoxy coatings containing different type of CNPs. The extents of reaction and polymerization rate were slightly delayed in the nanocomposites. A competition in light absorbance between the photoinitiator and the CNPs led to a reduction of the efficiency of the process. The dielectric properties of the photo-cured nanocomposites showed different percolation thresholds depending on the type of filler. The highest enhancement in electrical properties was achieved in the MWCNTs composites while in the sheet-like based nanocomposites were lower. These differences were attributed to the geometry of the filler, the filler dispersion and the more effective MWCNTs network to the electronic transport through overlapping of nanotubes. However, TRG had the best behavior in terms of mechanical performances showing an increase on the surface hardness with the TRG content and an increase of more than 20 °C in the T_g with the addition of 1 wt. % of TRG.

- Novel self-assembled nanocomposites based on blends of an epoxy resin and an amphiphilic block copolymer (PEO-PPO-PEO) filled with MWCNTs and TRG were successfully prepared. A synergic effect between the BC and the nanoparticles was observed, which gave rise to a significant increase of the toughness of the resin. In addition, the T_g of the resin was increased in more than 20 °C upon the addition of TRG.

- Finally, the fourth epoxy system evaluated, the epoxy foams, was produced using elastomeric microspheres as blowing agent and MWCNTs and TRG were employed mainly as conductive fillers. The addition of MWCNTs produced enhancements of five orders of magnitude on the electrical conductivity and dielectric permittivity. The electrical conductivity resulted to be independent of the density of the foam, depending only on the generation of a percolated filler network within the cell walls and struts. In addition, other physical properties

like the thermal conductivity and the elastic modulus were improved with the CNPs.

- A common denominator in all the systems studied was the fact that MWCNTs behaved better than TRG if transport properties are sought. The lower percolation threshold of this filler facilitated the transport of phonons and electrons increasing this way the thermal and electrical conductivities. On the other hand, the wrinkled planar geometry of TRG and its residual functional groups were not beneficial to enhance transport properties. However, these structural characteristics of TRG made its nanocomposites outperform MWCNTs due to a better crack interlocking and enhanced filler/matrix adhesion.

This thesis gathers a wide set of studies concerning different epoxy systems for the scientific understanding and industrial application of epoxy resin nanocomposites. The promising results reported herein represent an important contribution to the state of the art and opens new research lines to continue with the work performed in this PhD. Some recommendation to future works will be the use of the developed five-pulses sequence in NMR experiments to evaluate the effect of nanofillers on the microstructure and molecular hindering. The use of graphene produced through different methods (chemical reductions, type of graphite, thermal treatments) results in graphene sheets with different grades of crystallinity or geometries that can lead to significant differences in the final properties of the polymer nanocomposite.

ANNEX. Low field NMR for polymer networks

This annex aims to explain the principles and applications of NMR approaches for the characterization of cross-linked structures. Low field NMR techniques have been used to study the chain motion in systems like: entangled polymers, polymer melts, related mobile polymeric systems well above the glass transition and elastomers. We will focus on the application of NMR in elastomers due to the similarities with the epoxy resins from a structural point of view (both are cross-linked polymer networks).

The starting point for the understanding of the relationship between polymer chain dynamics and NMR-detected local order is the orientation dependence of the dipolar coupling. The angle α is the orientation of the internuclear axis with respect to the magnetic field or reference direction. α fluctuates rapidly with time evidencing the segmental dynamics as shown in Figure A..***1***.

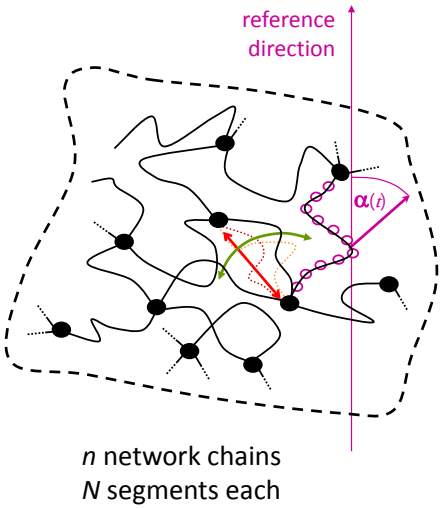

Figure A..1: Schematic representation of possible molecular conformations in a polymer network.

The time dependence $\alpha(t)$ can therefore monitor orientation fluctuations of the polymer backbone. Its dynamics could be described in terms of the classical theories of polymer dynamics and its spatio-temporal distribution can be quantified in terms of a uniaxial order parameter The characteristics of the uniaxial dynamics of $\alpha(t)$ is most conveniently described by the autocorrelation function $C_\alpha(t)$. This function basically gives the probability of finding a chain segment, that has been observed in a particular orientation $\alpha(t_a)$ at time t_a, again in the same orientation after certain time.

Figure A.2 shows the variation of C_α with time for polymer melts and networks. The first step corresponds to the sub-segmental motion of the molecules. The second decay is associated with Rouse-type chain motions, free and constrained Rouse motions. These types of dynamics are ultimately constrained by permanent cross-links, whereby a plateau arises as a feature for polymer networks. While for linear or end-tethered chains, reptation or free diffusion provides effective mechanisms for further loss of correlation. There are different models and approximations for C_α, many of them based on the Rouse/reptation or tube model[413] but a consensus has not been reached yet on its exact shape.

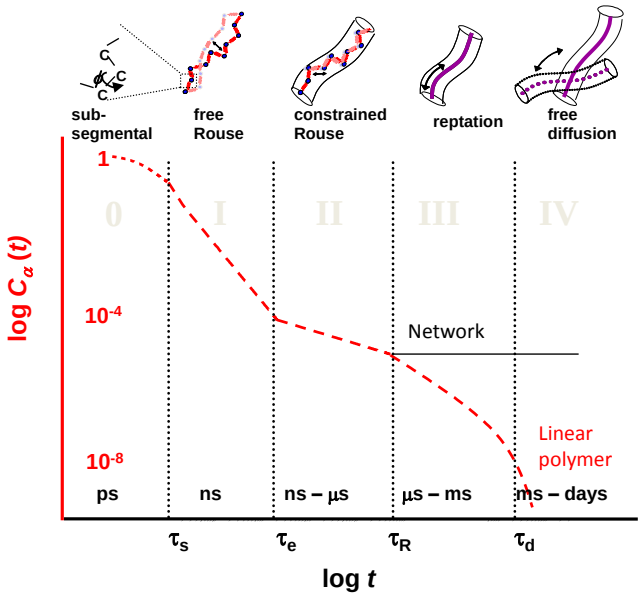

Figure A.2: Schematic representation of $C_\alpha(t)$ for entangled melt and polymer networks above T_g. Adapted with permission from.[334] Copyright (2011) American Chemical Society.

An important feature of the dynamics of cross-linked or entangled chains is the semi-local anisotropy. As commented before, fast motions such as Rouse modes are ultimately hindered by the presence of topological restrictions and long-lived orientation correlations are induced. Their magnitude is directly linked to microscopic parameters such as the cross-link density and the entanglement length. Consequently, knowledge about local order is highly relevant for the understanding of the connection

between the molecular structure and the final material's properties. In other words, the final result of an NMR experiment usually is the dipolar coupling constant (D_{res}) of the system. In polymer melts, due to the highly mobile molecules, the dipolar coupling among spins is zero (D_{res} = 0). However, the presence of constraint points, either physical (entanglements) or chemical (cross-linking points), hinders the molecular motion leading to a reduction of the molecular conformations. Such restrictions are the reason for permanent dipolar couplings ($D_{res} \neq 0$).

There are different experimental methods to obtain D_{res} by NMR.[333, 414-416] Among all of them, "*Double Quantum*" (DQ) NMR, also known as "*Multiple Quantum*" (MQ) NMR is one of the most versatile approaches to measure weak dipolar couplings. This technique is not only suitable to evaluate the structure of polymer networks, like defects of the network, cross-linking density and its distribution, but it also provides information about the dynamics of the polymer chains.[417]

In a MQ experiment, it is possible to obtain two qualitative different series of data: the double quantum intensity (I_{DQ}) which depends on the quantum coherence among spins and the reference intensity (I_{ref}). Both signals vary as a function of the DQ time (τ_{DQ}) as shown in Figure A.3.

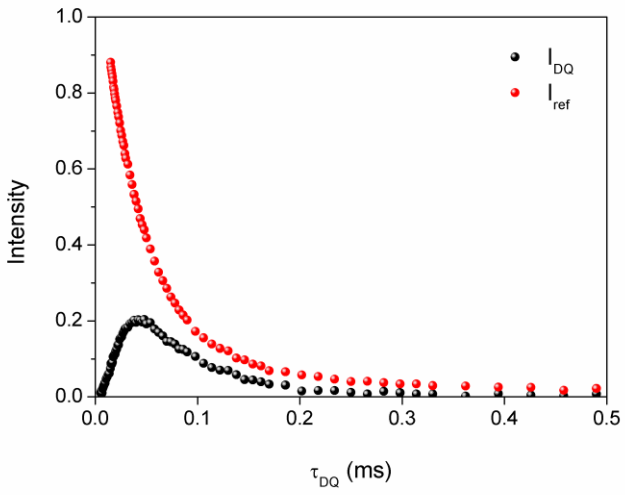

Figure A.3: Variation of I_{DQ} and I_{ref} with τ_{DQ}.

This way, I_{ref} provides information about the relaxation of the non-coupled segments (like defects of the network) and half of the coupled segments. I_{DQ} contains the information of the other half coupled segments. This means that we can study the structure of the polymer through the coupled segments and the molecular dynamics through the non-coupled segments.

Normalizing the intensities obtained in a MQ experiment it is possible to separate both contributions and analyze the structure of the network individually. I_{DQ} is normalized by the addition of $I_{DQ} + I_{ref} = I_{sDQ}$ which comprises the full magnetization of the sample subject to relaxation. The relaxation of the non-coupled segments or defects of the network follows an exponential dependence much slower than the segments that are included in the polymer network (Figure A.4) that fits Equation A.1.

$$I = B \cdot exp\left(\frac{\tau_{DQ}}{T_{def}}\right) \qquad \text{Equation A.1}$$

Where I is the intensity of the signal, B is the percentage of defects and T_{def} is the relaxation time of the defects.

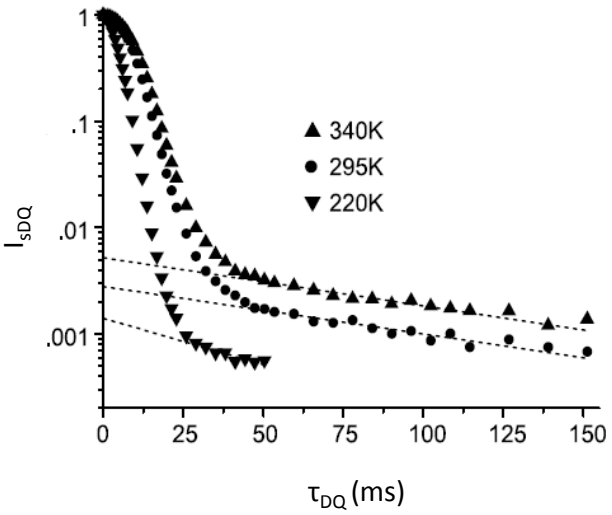

Figure A.4: Evolution of I_{sDQ} with τ_{DQ} of PDMS rubber. Adapted from,[333] copyright (2007) with permission from Elsevier.

To separate the structural information from the dynamics, it is necessary to eliminate the non-coupled fraction of segments related to the defects in the network, which is obtained with Equation A.1 obtaining the Equation A.2.

$$I_{sDQ} = I_{DQ} + I_{ref} - B \cdot exp\left(\frac{\tau_{DQ}}{T_{def}}\right) \qquad \text{Equation A. 2}$$

If now we normalize I_{DQ} with respect to I_{sDQ} we can obtain the corresponding normalized DQ intensity (I_{nDQ}), which depends exclusively on the structure of the network (Figure A.5). I_{nDQ} reaches a plateau at a value of 0.5 due to the fact that it only contains half of the coupled segments.

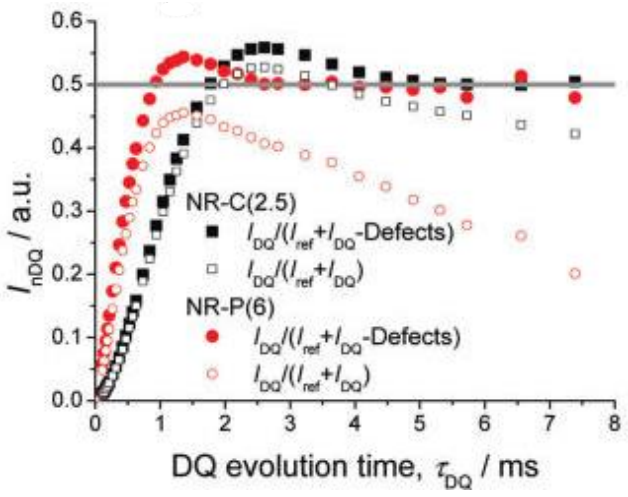

Figure A.5: Evolution of I_{nDQ}. Reprinted with permission from.[418] *Copyright (2010) American Chemical Society.*

The data treatment ends obtaining the value of D_{res}. In order to obtain a single value of D_{res}, the I_{nDQ} curves are fitted with buildup functions based on the static second-moment approximation (Equation A.3) or modifications of the model (depending on the polymer) like in the case of the Equation A.4.

$$I_{nDQ} = \frac{1}{2}\left(1 - exp\left[-\frac{2}{5}D_{res}^2\tau_{DQ}^2\right]\right)$$ Equation A. 3

$$I_{nDQ} = \frac{1}{2}\left(1 - \frac{exp\left(-\frac{2/5D_G^2 \cdot \tau_{DQ}^2}{1 + 4/5\sigma_G^2 \cdot \tau_{DQ}^2}\right)}{\sqrt{1 + 4/5D_G^2 \cdot \tau_{DQ}^2}}\right)$$ Equation A. 4

Where D_G and σ_G are the averaged D_{res} and its standard deviation, respectively. High values of D_{res} indicate that the polymer network possesses a high cross-linking density.

D_{res} is related to structural parameters through the Equation A.5, where S_b is the dynamic order parameter of the polymer back-bone, D_{stat} is the static limit dipolar coupling constant. The constant *k* describes the averaging due to very fast intra-segmental motions and it is particular for each polymer. As can be observed in the Equation A.5, S_b is related to the end-to-end vector *r* of the chain segment separating the constraints and to *N*, the number of statistical (Kuhn) segments between the constraints. It is not easy to obtain the value of *k*, complex simulations and calculations of the spin dynamics must be performed previously to the DQ experiment. Unfortunately, the value of *k* is only available for very few polymers, like natural rubber or polydimethylsiloxane.

$$S_b = k\frac{D_{res}}{D_{stat}} = \frac{3r^2}{5N}$$ Equation A.5

REFERENCES

1. May, C., *Epoxy Resins: Chemistry and Technology, Second Edition*. Taylor & Francis: New York, 1987.

2. Sedlácek, B.; Kahovec, J., *Crosslinked Epoxies*. Walter de Gruyter: New York, 1987.

3. Craver, C.; Carraher, C., *Applied Polymer Science 21st Century*. Elsevier: Oxford, 2000.

4. Gonzalez-Romero, V. M.; Casillas, N. Isothermal and Temperature Programmed Kinetic Studies of Thermosets. *Polymer Engineering and Science* **1989,** 29, (5), 295-301.

5. Lee, L. J.; Macosko, C. W. Heat Transfer in Polymer Reaction Molding. *International Journal of Heat and Mass Transfer* **1980,** 23, (11), 1479-1492.

6. Reboredo, M. M.; Vazquez, A. Curing of Thermosetting Polymers by an External Fluid. *Polymer Engineering & Science* **1995,** 35, (19), 1521-1526.

7. Charbonneaux, T. G.; Macosko, C. W. Modelling of Laminar Tube Flow of Thermosetting Polymers: Application of a Finite Element Method with Moving Grid. *Polymer Reaction Engineering* **1994,** 2, (4), 347-387.

8. Lo, Y.-W.; Reible, D. D.; Collier, J. R.; Chen, C.-H. Three-Dimensional Modeling of Reaction Injection Molding. Ii: Application. *Polymer Engineering & Science* **1994,** 34, (18), 1401-1405.

9. Borchardt, H. J.; Daniels, F. The Application of Differential Thermal Analysis to the Study of Reaction Kinetics. *Journal of the American Chemical Society* **1957,** 79, (1), 41-46.

10. Swarin, S.; Wims, A., A Method for Determining Reaction Kinetics by Differential Scanning Calorimetry. In *Analytical Calorimetry*, Porter, R.; Johnson, J., Eds. Springer US: 1977; pp 155-171.

11. Kenny, J. M.; Trivisano, A. Isothermal and Dynamic Reaction Kinetics of High Performance Epoxy Matrices. *Polymer Engineering & Science* **1991,** 31, (19), 1426-1433.

12. Kenny, J. M. Determination of Autocatalytic Kinetic Model Parameters Describing Thermoset Cure. *Journal of Applied Polymer Science* **1994,** 51, (4), 761-764.

13. Peyser, P.; Bascom, W. D. Kinetics of Epoxy Resin Polymerization Using Differential Scanning Calorimetry. *Journal of Applied Polymer Science* **1977,** 21, (9), 2359-2373.

14. Kamal, M. Thermoset Characterization for Moldability Analysis. *Polymer Engineering and Science* **1974,** 14, (3), 231-239.

15. Sourour, S.; Kamal, M. R. Kinetics and Thermal Characterization of Thermoset Cure. *Polymer Engineering and Science* **1973,** 13, (1), 59-64.

16. Katnam, K. B.; Stevenson, J. P. J.; Stanley, W. F.; Buggy, M.; Young, T. M. Tensile Strength of Two-Part Epoxy Paste Adhesives: Influence of Mixing Technique and Micro-Void Formation. *International Journal of Adhesion and Adhesives* **2011,** 31, (7), 666-673.

17. Zhang, K.; Gu, Y.; li, M.; Zhang, Z. Effect of Rapid Curing Process on the Properties of Carbon Fiber/Epoxy Composite Fabricated Using Vacuum Assisted Resin Infusion Molding. *Materials & Design* **2014,** 54, 624-631.

18. Decker, C., Photopolymerization and Ultraviolet Curing of Multifunctional Monomers. In *Materials Science and Technology*, Wiley-VCH Verlag GmbH & Co. KGaA: 2006.

19. Pappas, S. P., *Radiation Curing: Science and Technology*. New York, 1992.

20. Fouassier, J. P.; Rabek, J. F., *Radiation Curing in Polymer Science and Technology: Practical Aspects and Applications*. London, 1993.

21. Crivello, J. V. The Discovery and Development of Onium Salt Cationic Photoinitiators. *Journal of Polymer Science Part A: Polymer Chemistry* **1999,** 37, (23), 4241-4254.

22. Crivello, J. V.; Dietliker, K.; Bradley, G., *Photoinitiators for Free Radical Cationic & Anionic Photopolymerisation*. Wiley: 1999.

23. Sprenger, S. Epoxy Resins Modified with Elastomers and Surface-Modified Silica Nanoparticles. *Polymer* **2013,** 54, (18), 4790-4797.

24. Thomas, R.; Yumei, D.; Yuelong, H.; Le, Y.; Moldenaers, P.; Weimin, Y.; Czigany, T.; Thomas, S. Miscibility, Morphology, Thermal, and Mechanical Properties of a Dgeba Based Epoxy Resin Toughened with a Liquid Rubber. *Polymer* **2008,** 49, (1), 278-294.

25. Chaudhary, S.; Surekha, P.; Kumar, D.; Rajagopal, C.; Roy, P. K. Amine-Functionalized Poly(Styrene) Microspheres as Thermoplastic Toughener for Epoxy Resin. *Polymer Composites* **2014**.

26. Sangermano, M.; Messori, M.; Martin Gallego, M.; Rizza, G.; Voit, B.; Galleco, M. M. Scratch Resistant Tough Nanocomposite Epoxy Coatings Based on Hyperbranched Polyesters. *Polymer* **2009,** 50, (24), 5647-5652.

27. Johnsen, B. B.; Kinloch, A. J.; Mohammed, R. D.; Taylor, A. C.; Sprenger, S. Toughening Mechanisms of Nanoparticle-Modified Epoxy Polymers. *Polymer* **2007,** 48, (2), 530-541.

28. Jordan, J.; Jacob, K.; Tannenbaum, R.; Sharaf, M.; Jasiuk, I. Experimental Trends in Polymer Nanocomposites—a Review. *Materials Science and Engineering. A* **2005,** 393, (1-2), 1-11.

29. Bagheri, R.; Pearson, R. Role of Particle Cavitation in Rubber-Toughened Epoxies: 1. Microvoid Toughening. *Polymer* **1996,** 37, (20), 4529-4538.

30. Chandrasekaran, S.; Seidel, C.; Schulte, K. Preparation and Characterization of Graphite Nano-Platelet (Gnp)/Epoxy Nano-Composite: Mechanical, Electrical and Thermal Properties. *European Polymer Journal* **2013,** 49, (12), 3878-3888.

31. Pascault, J. P.; Williams, R. J. J., *Epoxy Polymers*. Wiley: 2009.

32. Bates, F. S.; Fredrickson, G. H. Block Copolymer Thermodynamics: Theory and Experiment. *Annual review of physical chemistry* **1990,** 41, 525-57.

33. Leibler, L. Theory of Microphase Separation in Block Copolymers. *Macromolecules* **1980,** 13, (6), 1602-1617.

34. Dean, J. M.; Lipic, P. M.; Grubbs, R. B.; Cook, R. F.; Bates, F. S. Micellar Structure and Mechanical Properties of Block Copolymer-Modified Epoxies. *Journal of Polymer Science. Part B, Polymer Physics* **2001,** 39, (23), 2996-3010.

35. Hillmyer, M.; Lipic, P.; Hajduk, D.; Almdal, K.; Bates, F. Self-Assembly and Polymerization of Epoxy Resin-Amphiphilic Block Copolymer Nanocomposites. *Journal of the American Chemical Society* **1997,** 119, (11), 2749-2750.

36. Lipic, P.; Bates, F.; Hillmyer, M. Nanostructured Thermosets from Self-Assembled Amphiphilic Block Copolymer/Epoxy Resin Mixtures. *Journal of the American Chemical Society* **1998,** 120, (35), 8963-8970.

37. Flory, P. J., *Principles of Polymer Chemistry*. Cornell University Press: 1953.

38. Yin, M.; Zheng, S. Ternary Thermosetting Blends of Epoxy Resin, Poly(Ethylene Oxide) and Poly(E-Caprolactone). *Macromolecular Chemistry and Physics* **2005,** 206, (9), 929-937.

39. Ni, Y.; Zheng, S. Influence of Intramolecular Specific Interactions on Phase Behavior of Epoxy Resin and Poly(E-Caprolactone) Blends Cured with Aromatic Amines. *Polymer* **2005,** 46, (15), 5828-5839.

40. Meng, F.; Zheng, S.; Zhang, W.; Li, H.; Liang, Q. Nanostructured Thermosetting Blends of Epoxy Resin and Amphiphilic Poly(E-Caprolactone)-Block-Polybutadiene-

Block-Poly(E-Caprolactone) Triblock Copolymer. *Macromolecules* **2006,** 39, (2), 711-719.

41. Meng, F.; Zheng, S.; Li, H.; Liang, Q.; Liu, T. Formation of Ordered Nanostructures in Epoxy Thermosets: A Mechanism of Reaction-Induced Microphase Separation. *Macromolecules* **2006,** 39, (15), 5072-5080.

42. Li, X.; Fu, W.; Wang, Y.; Chen, T.; Liu, X.; Lin, H.; Sun, P.; Jin, Q.; Ding, D. Solid-State Nmr Characterization of Unsaturated Polyester Thermoset Blends Containing Peo–Ppo–Peo Block Copolymers. *Polymer* **2008,** 49, (12), 2886-2897.

43. Fan, W.; Wang, L.; Zheng, S. Double Reaction-Induced Microphase Separation in Epoxy Resin Containing Polystyrene-Block-Poly(E-Caprolactone)-Block-Poly(N-Butyl Acrylate) Abc Triblock Copolymer. *Macromolecules* **2010,** 43, (24), 10600-10611.

44. Dean, J.; Grubbs, R.; Saad, W.; Cook, R.; Bates, F. Mechanical Properties of Block Copolymer Vesicle and Micelle Modified Epoxies. *Journal of Polymer Science. Part B, Polymer Physics* **2003,** 41, (20), 2444-2456.

45. Wagner, H. D. Nanocomposites: Paving the Way to Stronger Materials. *Nature Nanotechnology* **2007,** 2, (12), 742-744.

46. Klempner, D.; Sendijarevi′c, V.; Aseeva, R. M., *Handbook of Polymeric Foams and Foam Technology*. Hanser Publishers: 2004.

47. Gibson, L. J.; Ashby, M. F., *Cellular Solids: Structure and Properties*. Cambridge University Press: 1999.

48. John, B.; Reghunadhan Nair, C. P., 13-Syntactic Foams. In *Handbook of Thermoset Plastics* Dodiuk, H.; Goodman, S. H., Eds. William Andrew Publishing: Boston, 2014; pp 511-554.

49. Gupta, N.; Zeltmann, S.; Shunmugasamy, V.; Pinisetty, D. Applications of Polymer Matrix Syntactic Foams. *JOM* **2014,** 66, (2), 245-254.

50. Simpson, S. S.; Yeznach, A.; Barton, C. L., Bisphenol a-Epichlorohydrin Adduct; Anhydride Curing Agent. In Patent US4546118 A: 1985.

51. Celina, M. C., Process for Epoxy Foam Production. In Patent US8003730 B1: 2011.

52. Wade, R. C.; Letendre, C. Foaming Epoxy Resins and Pvc Plastisols with Sodium Borohydride Blowing Agent. *Journal of Cellular Plastics* **1980,** 16, (1), 32-35.

53. Diethelm, H., Hot-Foamable, Thermosetting Epoxy Resin Mixture. In Patent US4798848 A: 1989.

54. Kishima, N.; Matsumoto, A., Method of Producing Porous Material Having Open Pores. In Patent US4797425 A: 1989.

55. Fabrizio, Q.; Loredana, S.; Anna, S. E. Shape Memory Epoxy Foams for Space Applications. *Materials Letters* **2012,** 69, 20-23.

56. Quadrini, F.; Squeo, E. A. Solid-State Foaming of Epoxy Resin. *Journal of Cellular Plastics* **2008,** 44, (2), 161-173.

57. Squeo, E. A.; Quadrini, F. Shape Memory Epoxy Foams by Solid-State Foaming. *Smart Materials and Structures* **2010,** 19, (10).

58. Van Auken, R. L., Ski and Method of Making Same. In Patent US4065150 A: 1977.

59. Green, D. W.; Winandy, J. E.; Kretschmann, D. E., *Wood Handbook: Wood as an Engineering Material*. University Press of the Pacific: Madison, WI, 2000.

60. Guo, Q.; Liu, J.; Chen, L.; Wang, K. Nanostructures and Nanoporosity in Thermoset Epoxy Blends with an Amphiphilic Polyisoprene-Block-Poly(4-Vinyl Pyridine) Reactive Diblock Copolymer. *Polymer* **2008,** 49, (7), 1737-1742.

61. Ajayan, P. M.; Schadler, L. S.; Giannaris, C.; Rubio, A. Single-Walled Carbon Nanotube–Polymer Composites: Strength and Weakness. *Advanced Materials* **2000,** 12, (10), 750-753.

62. Puglia, D.; Valentini, L.; Kenny, J. M. Analysis of the Cure Reaction of Carbon Nanotubes/Epoxy Resin Composites through Thermal Analysis and Raman Spectroscopy. *Journal of Applied Polymer Science* **2003,** 88, (2), 452-458.

63. Puglia, D.; Valentini, L.; Armentano, I.; Kenny, J. M. Effects of Single-Walled Carbon Nanotube Incorporation on the Cure Reaction of Epoxy Resin and Its Detection by Raman Spectroscopy. *Diamond and Related Materials* **2003,** 12, (3–7), 827-832.

64. Montazeri, A.; Javadpour, J.; Khavandi, A.; Tcharkhtchi, A.; Mohajeri, A. Mechanical Properties of Multi-Walled Carbon Nanotube/Epoxy Composites. *Materials & Design* **2010,** 31, (9), 4202-4208.

65. Sandler, J.; Shaffer, M. S. P.; Prasse, T.; Bauhofer, W.; Schulte, K.; Windle, A. H. Development of a Dispersion Process for Carbon Nanotubes in an Epoxy Matrix and the Resulting Electrical Properties. *Polymer* **1999,** 40, (21), 5967-5971.

66. Zhu, J.; Peng, H.; Rodriguez-Macias, F.; Margrave, J. L.; Khabashesku, V. N.; Imam, A. M.; Lozano, K.; Barrera, E. V. Reinforcing Epoxy Polymer Composites through Covalent Integration of Functionalized Nanotubes. *Advanced Functional Materials* **2004,** 14, (7), 643-648.

67. Li, J.; Kim, J.-K.; Lung Sham, M. Conductive Graphite Nanoplatelet/Epoxy Nanocomposites: Effects of Exfoliation and Uv/Ozone Treatment of Graphite. *Scripta Materialia* **2005,** 53, (2), 235-240.

68. Miyagawa, H.; Drzal, L. T. Thermo-Physical and Impact Properties of Epoxy Nanocomposites Reinforced by Single-Wall Carbon Nanotubes. *Polymer* **2004,** 45, (15), 5163-5170.

69. Liang, J.; Wang, Y.; Huang, Y.; Ma, Y.; Liu, Z.; Cai, J.; Zhang, C.; Gao, H.; Chen, Y. Electromagnetic Interference Shielding of Graphene/Epoxy Composites. *Carbon* **2009,** 47, (3), 922-925.

70. Rafiee, M.; Yavari, F.; Rafiee, J.; Koratkar, N. Fullerene–Epoxy Nanocomposites-Enhanced Mechanical Properties at Low Nanofiller Loading. *J Nanopart Res* **2011,** 13, (2), 733-737.

71. Liao, Y.-H.; Marietta-Tondin, O.; Liang, Z.; Zhang, C.; Wang, B. Investigation of the Dispersion Process of Swnts/Sc-15 Epoxy Resin Nanocomposites. *Materials Science and Engineering: A* **2004,** 385, (1–2), 175-181.

72. Gong, X.; Liu, J.; Baskaran, S.; Voise, R. D.; Young, J. S. Surfactant-Assisted Processing of Carbon Nanotube/Polymer Composites. *Chemistry of Materials* **2000,** 12, (4), 1049-1052.

73. Lu, K. L.; Lago, R. M.; Chen, Y. K.; Green, M. L. H.; Harris, P. J. F.; Tsang, S. C. Mechanical Damage of Carbon Nanotubes by Ultrasound. *Carbon* **1996,** 34, (6), 814-816.

74. Rafiee, M. A.; Rafiee, J.; Wang, Z.; Song, H.; Yu, Z.-Z.; Koratkar, N. Enhanced Mechanical Properties of Nanocomposites at Low Graphene Content. *ACS Nano* **2009,** 3, (12), 3884-3890.

75. Yasmin, A.; Luo, J.-J.; Daniel, I. M. Processing of Expanded Graphite Reinforced Polymer Nanocomposites. *Composites Science and Technology* **2006,** 66, (9), 1182-1189.

76. Hernández-Pérez, A.; Avilés, F.; May-Pat, A.; Valadez-González, A.; Herrera-Franco, P. J.; Bartolo-Pérez, P. Effective Properties of Multiwalled Carbon Nanotube/Epoxy Composites Using Two Different Tubes. *Composites Science and Technology* **2008,** 68, (6), 1422-1431.

77. Thostenson, E. T.; Chou, T.-W. Processing-Structure-Multi-Functional Property Relationship in Carbon Nanotube/Epoxy Composites. *Carbon* **2006,** 44, (14), 3022-3029.

78. Gojny, F. H.; Wichmann, M. H. G.; Köpke, U.; Fiedler, B.; Schulte, K. Carbon Nanotube-Reinforced Epoxy-Composites: Enhanced Stiffness and Fracture Toughness

at Low Nanotube Content. *Composites Science and Technology* **2004,** 64, (15), 2363-2371.

79. Jimenez Suarez, A.; Campo, M.; Gaztelumendi, I.; Markaide, N.; Sanchez, M.; Ureña, A. The Influence of Mechanical Dispersion of Mwcnt in Epoxy Matrix by Calendering Method: Batch Method Versus Time Controlled. *Composites. Part B, Engineering* **2013,** 48, 88-94.

80. Jimenez Suarez, A.; Campo, M.; Sanchez, M.; Romon, C.; Ureña, A. Influence of the Functionalization of Carbon Nanotubes on Calendering Dispersion Effectiveness in a Low Viscosity Resin for Varim Processes. *Composites. Part B, Engineering* **2012,** 43, (8), 3482-3490.

81. Kovacs, J. Z.; Andresen, K.; Pauls, J. R.; Garcia, C. P.; Schossig, M.; Schulte, K.; Bauhofer, W. Analyzing the Quality of Carbon Nanotube Dispersions in Polymers Using Scanning Electron Microscopy. *Carbon* **2007,** 45, (6), 1279-1288.

82. Wichmann, M. H. G.; Sumfleth, J.; Fiedler, B.; Gojny, F. H.; Schulte, K. Multiwall Carbon Nanotube/Epoxy Composites Produced by a Masterbatch Process. *Mechanics of Composite Materials* **2006,** 42, (5), 395-406.

83. Chang, L.; Friedrich, K.; Ye, L.; Toro, P. Evaluation and Visualization of the Percolating Networks in Multi-Wall Carbon Nanotube/Epoxy Composites. *J Mater Sci* **2009,** 44, (15), 4003-4012.

84. Jimenez Suarez, A.; Campo, M.; Sánchez, M.; Romón, C.; Ureña, A. Dispersion of Carbon Nanofibres in a Low Viscosity Resin by Calendering Process to Manufacture Multiscale Composites by Varim. *Composites. Part B, Engineering* **2012,** 43, (8), 3104-3113.

85. Sanchez, M.; Rams, J.; Campo, M.; Jimenez Suarez, A.; Ureña, A. Characterization of Carbon Nanofiber/Epoxy Nanocomposites by the Nanoindentation Technique. *Composites. Part B, Engineering* **2011,** 42, (4), 638-644.

86. Inam, F.; Bhat, B. R.; Luhyna, N.; Vo, T. Comparison of Structural Health Assessment Capabilities in Epoxy – Carbon Black and Epoxy – Carbon Nanotube Nanocomposites. *Express Polymer Letters* **2013,** 8, (1), 55-61.

87. Chatterjee, S.; Wang, J. W.; Kuo, W. S.; Tai, N. H.; Salzmann, C.; Li, W. L.; Hollertz, R.; Nüesch, F. A.; Chu, B. T. T. Mechanical Reinforcement and Thermal Conductivity in Expanded Graphene Nanoplatelets Reinforced Epoxy Composites. *Chemical Physics Letters* **2012,** 531, 6-10.

88. Starkova, O.; Chandrasekaran, S.; Prado, L. A. S. A.; Tölle, F.; Mülhaupt, R.; Schulte, K. Hydrothermally Resistant Thermally Reduced Graphene Oxide and Multi-Wall Carbon Nanotube Based Epoxy Nanocomposites. *Polymer Degradation and Stability* **2013,** 98, (2), 519-526.

89. Chatterjee, S.; Nafezarefi, F.; Tai, N. H.; Schlagenhauf, L.; Nüesch, F. A.; Chu, B. T. T. Size and Synergy Effects of Nanofiller Hybrids Including Graphene Nanoplatelets and Carbon Nanotubes in Mechanical Properties of Epoxy Composites. *Carbon* **2012,** 50, (15), 5380-5386.

90. Prolongo, S. G.; Jimenez-Suarez, A.; Moriche, R.; Ureña, A. In Situ Processing of Epoxy Composites Reinforced with Graphene Nanoplatelets. *Composites Science and Technology* **2013,** 86, 185-191.

91. Valentini, L.; Puglia, D.; Carniato, F.; Boccaleri, E.; Marchese, L.; Kenny, J. M. Use of Plasma Fluorinated Single-Walled Carbon Nanotubes for the Preparation of Nanocomposites with Epoxy Matrix. *Composites Science and Technology* **2008,** 68, (3–4), 1008-1014.

92. Špitalský, Z.; Krontiras, C. A.; Georga, S. N.; Galiotis, C. Effect of Oxidation Treatment of Multiwalled Carbon Nanotubes on the Mechanical and Electrical Properties of Their Epoxy Composites. *Composites Part A: Applied Science and Manufacturing* **2009,** 40, (6–7), 778-783.

93. Zhu, J.; Kim, J.; Peng, H.; Margrave, J.; Khabashesku, V.; Barrera, E. Improving the Dispersion and Integration of Single-Walled Carbon Nanotubes in Epoxy Composites through Functionalization. *Nano Letters* **2003,** 3, (8), 1107-1113.

94. Sun, X.; Yu, A.; Ramesh, P.; Bekyarova, E.; Itkis, M. E.; Haddon, R. C. Oxidized Graphite Nanoplatelets as an Improved Filler for Thermally Conducting Epoxy-Matrix Composites. *Journal of Electronic Packaging* **2011,** 133, (2), 20905-20917.

95. Gojny, F. H.; Wichmann, M. H. G.; Fiedler, B.; Schulte, K. Influence of Different Carbon Nanotubes on the Mechanical Properties of Epoxy Matrix Composites - a Comparative Study. *Composites Science and Technology* **2005,** 65, 2300-2313.

96. Park, S.; Kim, D. Preparation and Physical Properties of an Epoxy Nanocomposite with Amine-Functionalized Graphenes. *Polymer Engineering and Science* **2014,** 54, (5), 985-991.

97. Fang, M.; Zhang, Z.; Li, J.; Zhang, H.; Lu, H.; Yang, Y. Constructing Hierarchically Structured Interphases for Strong and Tough Epoxy Nanocomposites by Amine-Rich Graphene Surfaces. *Journal of Materials Chemistry* **2010,** 20, (43), 9635-9643.

98. Martinez Rubi, Y.; Gonzalez-Dominguez, J. M.; Anson Casaos, A.; Kingston, C. T.; Daroszewska, M.; Barnes, M.; Hubert, P.; Cattin, C.; Martinez, M. T.; Simard, B. Tailored Swcnt Functionalization Optimized for Compatibility with Epoxy Matrices. *Nanotechnology* **2012,** 23, (28), 285701-285709.

99. Rosca, I. D.; Watari, F.; Uo, M.; Akasaka, T. Oxidation of Multiwalled Carbon Nanotubes by Nitric Acid. *Carbon* **2005,** 43, (15), 3124-3131.

100. Wan, Y.-J.; Tang, L.-C.; Yan, D.; Zhao, L.; Li, Y.-B.; Wu, L.-B.; Jiang, J.-X.; Lai, G.-Q. Improved Dispersion and Interface in the Graphene/Epoxy Composites Via a Facile Surfactant-Assisted Process. *Composites Science and Technology* **2013,** 82, 60-68.

101. Shahil, K. M. F.; Balandin, A. A. Graphene–Multilayer Graphene Nanocomposites as Highly Efficient Thermal Interface Materials. *Nano Letters* **2012,** 12, (2), 861-867.

102. Geng, Y.; Liu, M. Y.; Li, J.; Shi, X. M.; Kim, J. K. Effects of Surfactant Treatment on Mechanical and Electrical Properties of Cnt/Epoxy Nanocomposites. *Composites Part A: Applied Science and Manufacturing* **2008,** 39, (12), 1876-1883.

103. Cui, S.; Canet, R.; Derre, A.; Couzi, M.; Delhaes, P. Characterization of Multiwall Carbon Nanotubes and Influence of Surfactant in the Nanocomposite Processing. *Carbon* **2003,** 41, (4), 797-809.

104. Geng, Y.; Liu, M.; Li, J.; Shi, X.; Kim, J. Effects of Surfactant Treatment on Mechanical and Electrical Properties of Cnt/Epoxy Nanocomposites. *Composites. Part A, Applied science and manufacturing* **2008,** 39, (12), 1876-1883.

105. Dong, Y.; Wang, R.; Li, S.; Yang, H.; Du, M.; Fu, Y. Use of Tx100-Dangled Epoxy as a Reactive Noncovalent Dispersant of Vapor-Grown Carbon Nanofibers in an Aqueous Solution. *Journal of Colloid and Interface Science* **2013,** 391, 8-15.

106. Lan, L.; Zheng, Y. P.; Zhang, A. B.; Zhang, J. X.; Wang, N. Study of Ionic Solvent-Free Carbon Nanotube Nanofluids and Its Composites with Epoxy Matrix. *J Nanopart Res* **2012,** 14, (3), 753-763.

107. Ghorabi, S.; Rajabi, L.; Madaeni, S.; Zinadini, S.; Derakhshan, A. Effects of Three Surfactant Types of Anionic, Cationic and Non-Ionic on Tensile Properties and Fracture Surface Morphology of Epoxy/Mwcnt Nanocomposites. *Iranian Polymer Journal* **2012,** 21, (2), 121-130.

108. Ma, A. W. K.; Mackley, M.; Chinesta, F. The Microstructure and Rheology of Carbon Nanotube Suspensions. *International Journal of Material Forming* **2008,** 1, (2), 75-81.

109. Rahatekar, S. S.; Butler, S. A.; Elliott, J. A.; Windle, A. H.; Mackley, M. R. Optical Microstructure and Viscosity Enhancement for an Epoxy Resin Matrix Containing Multiwall Carbon Nanotubes. *Journal of Rheology* **2006,** 50, (5), 599-610.

110. Yokozeki, T.; Carolin Schulz, S.; Buschhorn, S. T.; Schulte, K. Investigation of Shear Thinning Behavior and Microstructures of Mwcnt/Epoxy and Cnf/Epoxy Suspensions under Steady Shear Conditions. *European Polymer Journal* **2012,** 48, (6), 1042-1049.

111. Godara, A.; Mezzo, L.; Luizi, F.; Warrier, A.; Lomov, S. V.; van Vuure, A. W.; Gorbatikh, L.; Moldenaers, P.; Verpoest, I. Influence of Carbon Nanotube Reinforcement on the Processing and the Mechanical Behaviour of Carbon Fiber/Epoxy Composites. *Carbon* **2009,** 47, (12), 2914-2923.

112. Chapartegui, M.; Markaide, N.; Florez, S.; Elizetxea, C.; Fernandez, M.; Santamaría, A. Specific Rheological and Electrical Features of Carbon Nanotube Dispersions in an Epoxy Matrix. *Composites Science and Technology* **2010,** 70, (5), 879-884.

113. Yokozeki, T.; Schulz, S.; Buschhorn, S.; Schulte, K.; Carolin Schulz, S. Investigation of Shear Thinning Behavior and Microstructures of Mwcnt/Epoxy and Cnf/Epoxy Suspensions under Steady Shear Conditions. *European Polymer Journal* **2012,** 48, (6), 1042-1049.

114. Ma, A. W. K.; Mackley, M.; Rahatekar, S.; Rahatekar, S. S. Experimental Observation on the Flow-Induced Assembly of Carbon Nanotube Suspensions to Form Helical Bands. *Rheologica Acta* **2007,** 46, (7), 979-987.

115. Sumfleth, J.; Prehn, K.; Wedekind, S.; Schulte, K. A Comparative Study of the Electrical and Mechanical Properties of Epoxy Nanocomposites Reinforced by Cvd- and Arc-Grown Multi-Wall Carbon Nanotubes. *Composites Science and Technology* **2010,** 70, (1), 173-180.

116. Song, Y. S.; Youn, J. R. Influence of Dispersion States of Carbon Nanotubes on Physical Properties of Epoxy Nanocomposites. *Carbon* **2005,** 43, (7), 1378-1385.

117. Zhu, J.; Wei, S.; Ryu, J.; Budhathoki, M.; Liang, G.; Guo, Z. In Situ Stabilized Carbon Nanofiber (Cnf) Reinforced Epoxy Nanocomposites. *Journal of Materials Chemistry* **2010,** 20, (23), 4937-4948.

118. Zhu, J.; Wei, S.; Yadav, A.; Guo, Z. Rheological Behaviors and Electrical Conductivity of Epoxy Resin Nanocomposites Suspended with in-Situ Stabilized Carbon Nanofibers. *Polymer* **2010,** 51, (12), 2643-2651.

119. Kim, J. A.; Seong, D. G.; Kang, T. J.; Youn, J. R. Effects of Surface Modification on Rheological and Mechanical Properties of Cnt/Epoxy Composites. *Carbon* **2006,** 44, (10), 1898-1905.

120. Abdalla, M.; Dean, D.; Adibempe, D.; Nyairo, E.; Robinson, P.; Thompson, G. The Effect of Interfacial Chemistry on Molecular Mobility and Morphology of Multiwalled Carbon Nanotubes Epoxy Nanocomposite. *Polymer* **2007,** 48, (19), 5662-5670.

121. Fan, Z.; Advani, S. Rheology of Multiwall Carbon Nanotube Suspensions. *Journal of Rheology* **2007,** 51, (4), 585-604.

122. Sydlik, S. A.; Lee, J.-H.; Walish, J. J.; Thomas, E. L.; Swager, T. M. Epoxy Functionalized Multi-Walled Carbon Nanotubes for Improved Adhesives. *Carbon* **2013,** 59, 109-120.

123. He, Z.; Zhang, X.; Chen, M.; Li, M.; Gu, Y.; Zhang, Z.; Li, Q. Effect of the Filler Structure of Carbon Nanomaterials on the Electrical, Thermal, and Rheological Properties of Epoxy Composites. *Journal of Applied Polymer Science* **2013,** 129, (6), 3366-3372.

124. Pötschke, P.; Abdel-Goad, M.; Pegel, S.; Jehnichen, D.; Mark, J. E.; Zhou, D.; Heinrich, G. Comparisons among Electrical and Rheological Properties of Melt-Mixed Composites Containing Various Carbon Nanostructures. *Journal of Macromolecular Science, Part A* **2009,** 47, (1), 12-19.

125. Gudarzi, M. M.; Sharif, F. Enhancement of Dispersion and Bonding of Graphene-Polymer through Wet Transfer of Functionalized Graphene Oxide. *Express Polymer Letters* **2012,** 6, (12), 1017-1031.

126. Sumfleth, J.; Buschhorn, S.; Schulte, K. Comparison of Rheological and Electrical Percolation Phenomena in Carbon Black and Carbon Nanotube Filled Epoxy Polymers. *J Mater Sci* **2011,** 46, (3), 659-669.

127. Yousefi, A.; Lafleur, P. G.; Gauvin, R. Kinetic Studies of Thermoset Cure Reactions: A Review. *Polymer Composites* **1997,** 18, (2), 157-168.

128. Zhou, T.; Wang, X.; Liu, X.; Xiong, D. Influence of Multi-Walled Carbon Nanotubes on the Cure Behavior of Epoxy-Imidazole System. *Carbon* **2009,** 47, (4), 1112-1118.

129. Tao, K.; Yang, S.; Grunlan, J. C.; Kim, Y.-S.; Dang, B.; Deng, Y.; Thomas, R. L.; Wilson, B. L.; Wei, X. Effects of Carbon Nanotube Fillers on the Curing Processes of

Epoxy Resin-Based Composites. *Journal of Applied Polymer Science* **2006,** 102, (6), 5248-5254.

130. Xie, H.; Liu, B.; Yuan, Z.; Shen, J.; Cheng, R. Cure Kinetics of Carbon Nanotube/Tetrafunctional Epoxy Nanocomposites by Isothermal Differential Scanning Calorimetry. *Journal of Polymer Science Part B: Polymer Physics* **2004,** 42, (20), 3701-3712.

131. Ventura, I.; Rahaman, A.; Lubineau, G. The Thermal Properties of a Carbon Nanotube-Enriched Epoxy: Thermal Conductivity, Curing, and Degradation Kinetics. *Journal of Applied Polymer Science* **2013,** 130, (4), 2722-2733.

132. Hongfeng, X.; Chengguo, L.; Zuanru, Y.; Hu, Y.; Zhiliu, W. Thermoanalytical Studies of High Performance Epoxy/Carbon Nanotube Composites. *Acta Polymerica Sinica* **2008**, (4), 332-336.

133. Jana, S.; Zhong, W.-H. Curing Characteristics of an Epoxy Resin in the Presence of Ball-Milled Graphite Particles. *J Mater Sci* **2009,** 44, (8), 1987-1997.

134. Baochun, G.; Jingjing, W.; Yanda, L.; Demin, J. Curing Behaviour of Epoxy Resin/Graphite Composites Containing Ionic Liquid. *Journal of Physics D: Applied Physics* **2009,** 42, (14), 145307-145317.

135. Qiu Shilong, S.; Yuting, W.; Chengshuang, W.; Zuanru, Y.; Yuan, Y. a.; Qiu, Y.; Wang, C.; Wang, Z.; Yuan, Y.; Huang, H.; Xie, R. Isothermal Curing Behaviors of Epoxy/Graphite Oxides Nanocomposites. *Acta Polymerica Sinica* **2012,** 012, (1), 25-32.

136. Qiu, S. L.; Wang, C. S.; Wang, Y. T.; Liu, C. G.; Chen, X. Y. Effects of Graphene Oxides on the Cure Behaviors of a Tetrafunctional Epoxy Resin. *Express Polymer Letters* **2011,** 5, (9), 809-818.

137. Xie, H.; Liu, B.; Sun, Q.; Yuan, Z.; Shen, J.; Cheng, R. Cure Kinetic Study of Carbon Nanofibers/Epoxy Composites by Isothermal Dsc. *Journal of Applied Polymer Science* **2005,** 96, (2), 329-335.

138. Seyhan, A. T.; Sun, Z.; Deitzel, J.; Tanoglu, M.; Heider, D. Cure Kinetics of Vapor Grown Carbon Nanofiber (Vgcnf) Modified Epoxy Resin Suspensions and Fracture Toughness of Their Resulting Nanocomposites. *Materials Chemistry and Physics* **2009,** 118, (1), 234-242.

139. Xie, H.; Liu, B.; Yang, H.; Wang, Z.; Shen, J.; Cheng, R. Thermal Characterization of Carbon-Nanofiber-Reinforced Tetraglycidyl-4,4′-Diaminodiphenylmethane/4,4′-Diaminodiphenylsulfone Epoxy Composites. *Journal of Applied Polymer Science* **2006,** 100, (1), 295-298.

140. Movva, S.; Ouyang, X.; Castro, J.; Lee, L. J. Carbon Nanofiber Paper and Its Effect on Cure Kinetics of Low Temperature Epoxy Resin. *Journal of Applied Polymer Science* **2012,** 125, (3), 2223-2230.

141. Chung, D. D. L.; Wu, J. Calorimetric Study of the Effect of Carbon Fillers on the Curing of Epoxy. *Carbon* **2004,** 42, (14), 3039-3042.

142. Abdalla, M.; Dean, D.; Robinson, P.; Nyairo, E. Cure Behavior of Epoxy/Mwcnt Nanocomposites: The Effect of Nanotube Surface Modification. *Polymer* **2008,** 49, (15), 3310-3317.

143. Zhou, T.; Wang, X.; Wang, T. Cure Reaction of Multi-Walled Carbon Nanotubes/Diglycidyl Ether of Bisphenol a/2-Ethyl-4-Methylimidazole (Mwcnts/Dgeba/Emi-2,4) Nanocomposites: Effect of Carboxylic Functionalization of Mwcnts. *Polymer International* **2009,** 58, (4), 445-452.

144. Zhou, T.; Wang, X.; Liu, X. H.; Lai, J. Z. Effect of Silane Treatment of Carboxylic-Functionalized Multi-Walled Carbon Nanotubes on the Thermal Properties of Epoxy Nanocomposites. *Express Polymer Letters* **2010,** 4, (4), 217-226.

145. Wang, Y. T.; Wang, C. S.; Yin, H. Y.; Wang, L. L.; Xie, H. F. Carboxyl-Terminated Butadiene-Acrylonitrile-Toughened Epoxy/Carboxyl-Modified Carbon Nanotube Nanocomposites: Thermal and Mechanical Properties. *Express Polymer Letters* **2012,** 6, (9), 719-728.

146. Valentini, L.; Armentano, I.; Puglia, D.; Kenny, J. M. Dynamics of Amine Functionalized Nanotubes/Epoxy Composites by Dielectric Relaxation Spectroscopy. *Carbon* **2004,** 42, (2), 323-329.

147. Cui, L.-J.; Wang, Y.-B.; Xiu, W.-J.; Wang, W.-Y.; Xu, L.-H.; Xu, X.-B.; Meng, Y.; Li, L.-Y.; Gao, J.; Chen, L.-T.; Geng, H.-Z. Effect of Functionalization of Multi-Walled Carbon Nanotube on the Curing Behavior and Mechanical Property of Multi-Walled Carbon Nanotube/Epoxy Composites. *Materials & Design* **2013,** 49, 279-284.

148. Ryu, S. H.; Sin, J. H.; Shanmugharaj, A. M. Study on the Effect of Hexamethylene Diamine Functionalized Graphene Oxide on the Curing Kinetics of Epoxy Nanocomposites. *European Polymer Journal* **2014,** 52, 88-97.

149. Schadler, L. S.; Giannaris, S. C.; Ajayan, P. M. Load Transfer in Carbon Nanotube Epoxy Composites. *Applied Physics Letters* **1998,** 73, (26), 3842-3844.

150. Allaoui, A.; Bai, S.; Cheng, H. M.; Bai, J. B. Mechanical and Electrical Properties of a Mwnt/Epoxy Composite. *Composites Science and Technology* **2002,** 62, (15), 1993-1998.

151. Jagtap, S. B.; Ratna, D. Preparation and Characterization of Rubbery Epoxy/Multiwall Carbon Nanotubes Composites Using Amino Acid Salt Assisted Dispersion Technique. *Express Polymer Letters* **2013,** 7, (4), 329-339.

152. Zhou, Y.; Pervin, F.; Lewis, L.; Jeelani, S. Experimental Study on the Thermal and Mechanical Properties of Multi-Walled Carbon Nanotube-Reinforced Epoxy. *Materials Science and Engineering: A* **2007,** 452–453, 657-664.

153. Choi, Y.-K.; Sugimoto, K.-i.; Song, S.-M.; Gotoh, Y.; Ohkoshi, Y.; Endo, M. Mechanical and Physical Properties of Epoxy Composites Reinforced by Vapor Grown Carbon Nanofibers. *Carbon* **2005,** 43, (10), 2199-2208.

154. Zhou, Y.; Pervin, F.; Rangari, V. K.; Jeelani, S. Fabrication and Evaluation of Carbon Nano Fiber Filled Carbon/Epoxy Composite. *Materials Science and Engineering: A* **2006,** 426, (1–2), 221-228.

155. Jimenez, G. A.; Jana, S. C. Oxidized Carbon Nanofiber/Polymer Composites Prepared by Chaotic Mixing. *Carbon* **2007,** 45, (10), 2079-2091.

156. Jana, S.; Zhong, W.-H.; Gan, Y. X. Characterization of the Flexural Behavior of a Reactive Graphitic Nanofibers Reinforced Epoxy Using a Non-Linear Damage Model. *Materials Science and Engineering: A* **2007,** 445–446, 106-112.

157. Rana, S.; Alagirusamy, R.; Joshi, M. Mechanical Behavior of Carbon Nanofibre-Reinforced Epoxy Composites. *Journal of Applied Polymer Science* **2010,** 118, (4), 2276-2283.

158. Rana, S.; Alagirusamy, R.; Joshi, M. Effect of Carbon Nanofiber Dispersion on the Tensile Properties of Epoxy Nanocomposites. *Journal of Composite Materials* **2011,** 45, (21), 2247-2256.

159. Chaos-Morán, R.; Salazar, A.; Ureña, A. Mechanical Analysis of Carbon Nanofiber/Epoxy Resin Composites. *Polymer Composites* **2011,** 32, (10), 1640-1651.

160. Ardanuy, M.; Rodríguez-Perez, M. A.; Algaba, I. Electrical Conductivity and Mechanical Properties of Vapor-Grown Carbon Nanofibers/Trifunctional Epoxy Composites Prepared by Direct Mixing. *Composites Part B: Engineering* **2011,** 42, (4), 675-681.

161. Shokrieh, M.; Esmkhani, M.; Vahedi, F.; Shahverdi, H. Improvement of Mechanical and Electrical Properties of Epoxy Resin with Carbon Nanofibers. *Iranian Polymer Journal* **2013,** 22, (10), 721-727.

162. Raza, M. A.; Westwood, A.; Stirling, C. Effect of Processing Technique on the Transport and Mechanical Properties of Vapour Grown Carbon Nanofibre/Rubbery Epoxy Composites for Electronic Packaging Applications. *Carbon* **2012,** 50, (1), 84-97.

163. Karippal, J.; Narasimha Murthy, H. N.; Rai, K. S.; Krishna, M.; Sreejith, M. Effect of Amine Functionalization of Cnf on Electrical, Thermal, and Mechanical Properties of Epoxy/Cnf Composites. *Polym. Bull.* **2010,** 65, (8), 849-861.

164. Richardson, M. C.; Park, E. S.; Kim, J. H.; Holmes, G. A. N-Pyrrolidine Functionalized C60-Fullerenes/Epoxy Nanocomposites. *Journal of Applied Polymer Science* **2010,** 117, (2), 1120-1126.

165. Bortz, D. R.; Heras, E. G.; Martin-Gullon, I. Impressive Fatigue Life and Fracture Toughness Improvements in Graphene Oxide/Epoxy Composites. *Macromolecules* **2011,** 45, (1), 238-245.

166. Liu, F.; Guo, K. Reinforcing Epoxy Resin through Covalent Integration of Functionalized Graphene Nanosheets. *Polymers for Advanced Technologies* **2014,** 25, (4), 418-423.

167. Ramos-Galicia, L.; Mendez, L. N.; Martinez-Hernandez, A. L.; Espindola-Gonzalez, A.; Galindo-Esquivel, I. R.; Fuentes-Ramirez, R.; Velasco-Santos, C. Improved Performance of an Epoxy Matrix as a Result of Combining Graphene Oxide and Reduced Graphene. *International Journal of Polymer Science* **2013**.

168. Wajid, A. S.; Ahmed, H. S. T.; Das, S.; Irin, F.; Jankowski, A. F.; Green, M. J. High-Performance Pristine Graphene/Epoxy Composites with Enhanced Mechanical and Electrical Properties. *Macromolecular Materials and Engineering* **2013,** 298, (3), 339-347.

169. Yi, X. F.; Mishra, A. K.; Kim, N. H.; Ku, B.-C.; Lee, J. H. Synergistic Effects of Oxidized Cnts and Reactive Oligomer on the Fracture Toughness and Mechanical Properties of Epoxy. *Composites Part A: Applied Science and Manufacturing* **2013,** 49, 58-67.

170. Tang, L.-c.; Zhang, H.; Han, J.-h.; Wu, X.-p.; Zhang, Z. Fracture Mechanisms of Epoxy Filled with Ozone Functionalized Multi-Wall Carbon Nanotubes. *Composites Science and Technology* **2011,** 72, (1), 7-13.

171. Wang, S.; Liang, Z. Y.; Liu, T.; Wang, B.; Zhang, C.; Wang, Z.; Liang, T.; Liu, B.; Wang, C. Effective Amino-Functionalization of Carbon Nanotubes for Reinforcing Epoxy Polymer Composites. *Nanotechnology* **2006,** 17, (6), 1551-1557.

172. Garg, P.; Singh, B.; Kumar, G.; Gupta, T.; Pandey, I.; Seth, R. K.; Tandon, R. P.; Mathur, R. Effect of Dispersion Conditions on the Mechanical Properties of Multi-Walled Carbon Nanotubes Based Epoxy Resin Composites. *Journal of Polymer Research* **2011,** 18, (6), 1397-1407.

173. Kathi, J.; Rhee, K.-Y.; Lee, J. Effect of Chemical Functionalization of Multi-Walled Carbon Nanotubes with 3-Aminopropyltriethoxysilane on Mechanical and Morphological Properties of Epoxy Nanocomposites. *Composites. Part A, Applied science and manufacturing* **2009,** 40, (6-7), 800-809.

174. Lee, J.-H.; Rhee, K.; Park, S. Silane Modification of Carbon Nanotubes and Its Effects on the Material Properties of Carbon/Cnt/Epoxy Three-Phase Composites. *Composites. Part A, Applied science and manufacturing* **2011,** 42, (5), 478-483.

175. Lee, J. H.; Rhee, K. Y.; Park, S. J. Effects of Silane Modification and Temperature on Tensile and Fractural Behaviors of Carbon Nanotube/Epoxy Nanocomposites. *Journal of Nanoscience and Nanotechnology* **2011,** 11, (1), 275-80.

176. Lu, Y.; Li, H.; Lin, M.; Ng, W.; Liu, H. Mechanical Properties of 3-Glycidoxypropyltrimethoxysilane Functionalized Multi-Walled Carbon Nanotubes/Epoxy Composites Cured by Electron Beam Irradiation. *Journal of Composite Materials* **2012,** 47, (14), 1685-1694.

177. Wan, Y.-J.; Tang, L.-C.; Gong, L.-X.; Yan, D.; Li, Y.-B.; Wu, L.-B.; Jiang, J.-X.; Lai, G.-Q. Grafting of Epoxy Chains onto Graphene Oxide for Epoxy Composites with Improved Mechanical and Thermal Properties. *Carbon* **2014,** 69, 467-480.

178. Miller, S. G.; Bauer, J. L.; Maryanski, M. J.; Heimann, P. J.; Barlow, J. P.; Gosau, J.-M.; Allred, R. E. Characterization of Epoxy Functionalized Graphite Nanoparticles and the Physical Properties of Epoxy Matrix Nanocomposites. *Composites Science and Technology* **2010,** 70, (7), 1120-1125.

179. Zaman, I.; Phan, T. T.; Kuan, H.-C.; Meng, Q.; Bao La, L. T.; Luong, L.; Youssf, O.; Ma, J. Epoxy/Graphene Platelets Nanocomposites with Two Levels of Interface Strength. *Polymer* **2011,** 52, (7), 1603-1611.

180. Liu, K.; Chen, S.; Luo, Y.; Jia, D.; Gao, H.; Hu, G.; Liu, L. Edge-Functionalized Graphene as Reinforcement of Epoxy-Based Conductive Composite for Electrical Interconnects. *Composites Science and Technology* **2013,** 88, 84-91.

181. Jiang, T.; Kuila, T.; Kim, N. H.; Ku, B.-C.; Lee, J. H. Enhanced Mechanical Properties of Silanized Silica Nanoparticle Attached Graphene Oxide/Epoxy Composites. *Composites Science and Technology* **2013,** 79, 115-125.

182. Naebe, M.; Wang, J.; Amini, A.; Khayyam, H.; Hameed, N.; Li, L.; Chen, Y.; Fox, B. Mechanical Property and Structure of Covalent Functionalised Graphene/Epoxy Nanocomposites. *Scientific Reports* **2014,** 4, 4375.

183. Yang, S.-Y.; Lin, W.-N.; Huang, Y.-L.; Tien, H.-W.; Wang, J.-Y.; Ma, C.-C. M.; Li, S.-M.; Wang, Y.-S. Synergetic Effects of Graphene Platelets and Carbon Nanotubes on the Mechanical and Thermal Properties of Epoxy Composites. *Carbon* **2011,** 49, (3), 793-803.

184. Li, Y.; Umer, R.; Isakovic, A.; Samad, Y.; Zheng, L.; Liao, K. Synergistic Toughening of Epoxy with Carbon Nanotubes and Graphene Oxide for Improved Long-Term Performance. *RSC Advances* **2013,** 3, (23), 8849-8856.

185. Li, W.; Dichiara, A.; Bai, J. Carbon Nanotube–Graphene Nanoplatelet Hybrids as High-Performance Multifunctional Reinforcements in Epoxy Composites. *Composites Science and Technology* **2013,** 74, 221-227.

186. Garmestani, H.; Al-Haik, M. S.; Dahmen, K.; Tannenbaum, R.; Li, D.; Sablin, S. S.; Hussaini, M. Y. Polymer-Mediated Alignment of Carbon Nanotubes under High Magnetic Fields. *Advanced Materials* **2003,** 15, (22), 1918-1921.

187. Martin, C. A.; Sandler, J. K. W.; Windle, A. H.; Schwarz, M. K.; Bauhofer, W.; Schulte, K.; Shaffer, M. S. P. Electric Field-Induced Aligned Multi-Wall Carbon Nanotube Networks in Epoxy Composites. *Polymer* **2005,** 46, (3), 877-886.

188. Khan, S. U.; Pothnis, J. R.; Kim, J.-K. Effects of Carbon Nanotube Alignment on Electrical and Mechanical Properties of Epoxy Nanocomposites. *Composites Part A: Applied Science and Manufacturing* **2013,** 49, 26-34.

189. Wang, Q.; Dai, J.; Li, W.; Wei, Z.; Jiang, J. The Effects of Cnt Alignment on Electrical Conductivity and Mechanical Properties of Swnt/Epoxy Nanocomposites. *Composites Science and Technology* **2008,** 68, (7–8), 1644-1648.

190. Camponeschi, E.; Vance, R.; Al-Haik, M.; Garmestani, H.; Tannenbaum, R. Properties of Carbon Nanotube–Polymer Composites Aligned in a Magnetic Field. *Carbon* **2007,** 45, (10), 2037-2046.

191. Prolongo, S. G.; Meliton, B. G.; Del Rosario, G.; Ureña, A. Simultaneous Dispersion and Alignment of Carbon Nanotubes in Epoxy Resin through Chronoamperometry. *Carbon* **2012,** 50, (15), 5489-5497.

192. Wang, Z.; Liang, Z.; Wang, B.; Zhang, C.; Kramer, L. Processing and Property Investigation of Single-Walled Carbon Nanotube (Swnt) Buckypaper/Epoxy Resin

Matrix Nanocomposites. *Composites Part A: Applied Science and Manufacturing* **2004,** 35, (10), 1225-1232.

193. García, E. J.; Hart, A. J.; Wardle, B. L.; Slocum, A. H. Fabrication and Nanocompression Testing of Aligned Carbon-Nanotube–Polymer Nanocomposites. *Advanced Materials* **2007,** 19, (16), 2151-2156.

194. Zegeye, E. F.; Woldesenbet, E. Processing and Mechanical Characterization of Carbon Nanotube Reinforced Syntactic Foams. *Journal of Reinforced Plastics and Composites* **2012,** 31, (15), 1045-1052.

195. Guzman, M. E.; Rodriguez, A. J.; Minaie, B.; Violette, M. Processing and Properties of Syntactic Foams Reinforced with Carbon Nanotubes. *Journal of Applied Polymer Science* **2012,** 124, (3), 2383-2394.

196. Dimchev, M.; Caeti, R.; Gupta, N. Effect of Carbon Nanofibers on Tensile and Compressive Characteristics of Hollow Particle Filled Composites. *Materials & Design* **2010,** 31, (3), 1332-1337.

197. Colloca, M.; Gupta, N.; Porfiri, M. Tensile Properties of Carbon Nanofiber Reinforced Multiscale Syntactic Foams. *Composites Part B: Engineering* **2013,** 44, (1), 584-591.

198. Poveda, R. L.; Dorogokupets, G.; Gupta, N. Carbon Nanofiber Reinforced Syntactic Foams: Degradation Mechanism for Long Term Moisture Exposure and Residual Compressive Properties. *Polymer Degradation and Stability* **2013,** 98, (10), 2041-2053.

199. Poveda, R.; Gupta, N. Carbon-Nanofiber-Reinforced Syntactic Foams: Compressive Properties and Strain Rate Sensitivity. *JOM* **2014,** 66, (1), 66-77.

200. Fiedler, B.; Gojny, F. H.; Wichmann, M. H. G.; Nolte, M. C. M.; Schulte, K. Fundamental Aspects of Nano-Reinforced Composites. *Composites Science and Technology* **2006,** 66, (16), 3115-3125.

201. Sun, L.; Warren, G. L.; O'Reilly, J. Y.; Everett, W. N.; Lee, S. M.; Davis, D.; Lagoudas, D.; Sue, H. J. Mechanical Properties of Surface-Functionalized Swcnt/Epoxy Composites. *Carbon* **2008,** 46, (2), 320-328.

202. Yu, N.; Zhang, Z. H.; He, S. Y. Fracture Toughness and Fatigue Life of Mwcnt/Epoxy Composites. *Materials Science and Engineering: A* **2008,** 494, (1–2), 380-384.

203. Bortz, D. R.; Merino, C.; Martin-Gullon, I. Carbon Nanofibers Enhance the Fracture Toughness and Fatigue Performance of a Structural Epoxy System. *Composites Science and Technology* **2011,** 71, (1), 31-38.

204. Miller, S.; Bauer, J.; Maryanski, M.; Heimann, P.; Barlow, J.; Gosau, J.-M.; Allred, R. Characterization of Epoxy Functionalized Graphite Nanoparticles and the Physical Properties of Epoxy Matrix Nanocomposites. *Composites Science and Technology* **2010,** 70, (7), 1120-1125.

205. Rafiee, M. A.; Rafiee, J.; Srivastava, I.; Wang, Z.; Song, H.; Yu, Z.-Z.; Koratkar, N. Fracture and Fatigue in Graphene Nanocomposites. *Small* **2010,** 6, (2), 179-183.

206. Tang, L.-C.; Wan, Y.-J.; Yan, D.; Pei, Y.-B.; Zhao, L.; Li, Y.-B.; Wu, L.-B.; Jiang, J.-X.; Lai, G.-Q. The Effect of Graphene Dispersion on the Mechanical Properties of Graphene/Epoxy Composites. *Carbon* **2013,** 60, 16-27.

207. Amaratunga, G. A. J.; Kymakis, E. Electrical Properties of Single-Wall Carbon Nanotube-Polymer Composite Films. *Journal of Applied Physics* **2006,** 99, (8), 084302.

208. Li, C.; Thostenson, E.; Chou, T.-W. Dominant Role of Tunneling Resistance in the Electrical Conductivity of Carbon Nanotube–Based Composites. *Applied Physics Letters* **2007,** 91, (22), 223114.

209. Sandler, J. K. W.; Kirk, J. E.; Kinloch, I. A.; Shaffer, M. S. P.; Windle, A. H. Ultra-Low Electrical Percolation Threshold in Carbon-Nanotube-Epoxy Composites. *Polymer* **2003,** 44, (19), 5893-5899.

210. Martin, C. A.; Sandler, J. K. W.; Shaffer, M. S. P.; Schwarz, M. K.; Bauhofer, W.; Schulte, K.; Windle, A. H. Formation of Percolating Networks in Multi-Wall Carbon-Nanotube–Epoxy Composites. *Composites Science and Technology* **2004,** 64, (15), 2309-2316.

211. Moisala, A.; Li, Q.; Kinloch, I. A.; Windle, A. H. Thermal and Electrical Conductivity of Single- and Multi-Walled Carbon Nanotube-Epoxy Composites. *Composites Science and Technology* **2006,** 66, (10), 1285-1288.

212. Bryning, M. B.; Islam, M. F.; Kikkawa, J. M.; Yodh, A. G. Very Low Conductivity Threshold in Bulk Isotropic Single-Walled Carbon Nanotube–Epoxy Composites. *Advanced Materials* **2005,** 17, (9), 1186-1191.

213. Kovacs, J. Z.; Velagala, B. S.; Schulte, K.; Bauhofer, W. Two Percolation Thresholds in Carbon Nanotube Epoxy Composites. *Composites Science and Technology* **2007,** 67, (5), 922-928.

214. Gojny, F. H.; Wichmann, M. H. G.; Fiedler, B.; Kinloch, I. A.; Bauhofer, W.; Windle, A. H.; Schulte, K. Evaluation and Identification of Electrical and Thermal Conduction Mechanisms in Carbon Nanotube/Epoxy Composites. *Polymer* **2006,** 47, (6), 2036-2045.

215. Kim, Y. J.; Shin, T. S.; Choi, H. D.; Kwon, J. H.; Chung, Y.-C.; Yoon, H. G. Electrical Conductivity of Chemically Modified Multiwalled Carbon Nanotube/Epoxy Composites. *Carbon* **2005,** 43, (1), 23-30.

216. Yu, A.; Itkis, M. E.; Bekyarova, E.; Haddon, R. C. Effect of Single-Walled Carbon Nanotube Purity on the Thermal Conductivity of Carbon Nanotube-Based Composites. *Applied Physics Letters* **2006,** 89, (13), 133102-133105.

217. Kim, B.; Lee, J.; Yu, I. Electrical Properties of Single-Wall Carbon Nanotube and Epoxy Composites. *Journal of Applied Physics* **2003,** 94, (10), 6724-6728.

218. Barrau, S.; Demont, P.; Maraval, C.; Bernes, A.; Lacabanne, C. Glass Transition Temperature Depression at the Percolation Threshold in Carbon Nanotube–Epoxy Resin and Polypyrrole–Epoxy Resin Composites. *Macromolecular Rapid Communications* **2005,** 26, (5), 390-394.

219. Brown, J. M.; Anderson, D. P.; Justice, R. S.; Lafdi, K.; Belfor, M.; Strong, K. L.; Schaefer, D. W. Hierarchical Morphology of Carbon Single-Walled Nanotubes During Sonication in an Aliphatic Diamine. *Polymer* **2005,** 46, (24), 10854-10865.

220. Li, J.; Ma, P. C.; Chow, W. S.; To, C. K.; Tang, B. Z.; Kim, J. K. Correlations between Percolation Threshold, Dispersion State, and Aspect Ratio of Carbon Nanotubes. *Advanced Functional Materials* **2007,** 17, (16), 3207-3215.

221. Du, F.; Guthy, C.; Kashiwagi, T.; Fischer, J. E.; Winey, K. I. An Infiltration Method for Preparing Single-Wall Nanotube/Epoxy Composites with Improved Thermal Conductivity. *Journal of Polymer Science Part B: Polymer Physics* **2006,** 44, (10), 1513-1519.

222. Barrau, S.; Demont, P.; Peigney, A.; Laurent, C.; Lacabanne, C. Dc and Ac Conductivity of Carbon Nanotubes−Polyepoxy Composites. *Macromolecules* **2003,** 36, (14), 5187-5194.

223. Liu, L.; Matitsine, S.; Gan, Y. B.; Chen, L. F.; Kong, L. B.; Rozanov, K. N. Frequency Dependence of Effective Permittivity of Carbon Nanotube Composites. *Journal of Applied Physics* **2007,** 101, (9), 94106-94113.

224. Yuen, S.-M.; Ma, C.-C. M.; Wu, H.-H.; Kuan, H.-C.; Chen, W.-J.; Liao, S.-H.; Hsu, C.-W.; Wu, H.-L. Preparation and Thermal, Electrical, and Morphological

Properties of Multiwalled Carbon Nanotubeand Epoxy Composites. *Journal of Applied Polymer Science* **2007,** 103, (2), 1272-1278.

225. Cardoso, P.; Silva, J.; Paiva, M. C.; Hattum, F.; Lanceros-Mendez, S. Comparative Analyses of the Electrical Properties and Dispersion Level of Vgcnf and Mwcnt: Epoxy Composites. *Journal of Polymer Science Part B: Polymer Physics* **2012,** 50, (17), 1253-1261.

226. Bal, S. Experimental Study of Mechanical and Electrical Properties of Carbon Nanofiber/Epoxy Composites. *Materials & Design* **2010,** 31, (5), 2406-2413.

227. Allaoui, A.; Hoa, S. V.; Pugh, M. D. The Electronic Transport Properties and Microstructure of Carbon Nanofiber/Epoxy Composites. *Composites Science and Technology* **2008,** 68, (2), 410-416.

228. El-Tantawy, F.; Kamada, K.; Ohnabe, H. In Situ Network Structure, Electrical and Thermal Properties of Conductive Epoxy Resin–Carbon Black Composites for Electrical Heater Applications. *Materials Letters* **2002,** 56, (1–2), 112-126.

229. Prasse, T.; Cavaillé, J.-Y.; Bauhofer, W. Electric Anisotropy of Carbon Nanofibre/Epoxy Resin Composites Due to Electric Field Induced Alignment. *Composites Science and Technology* **2003,** 63, (13), 1835-1841.

230. Ganguli, S.; Roy, A. K.; Anderson, D. P. Improved Thermal Conductivity for Chemically Functionalized Exfoliated Graphite/Epoxy Composites. *Carbon* **2008,** 46, (5), 806-817.

231. Monti, M.; Rallini, M.; Puglia, D.; Peponi, L.; Torre, L.; Kenny, J. M. Morphology and Electrical Properties of Graphene–Epoxy Nanocomposites Obtained by Different Solvent Assisted Processing Methods. *Composites Part A: Applied Science and Manufacturing* **2013,** 46, 166-172.

232. Biercuk, M. J.; Llaguno, M. C.; Radosavljevic, M.; Hyun, J. K.; Johnson, A. T.; Fischer, J. E. Carbon Nanotube Composites for Thermal Management. *Applied Physics Letters* **2002,** 80, (15), 2767-2769.

233. Choi, E. S.; Brooks, J. S.; Eaton, D. L.; Al-Haik, M. S.; Hussaini, M. Y.; Garmestani, H.; Li, D.; Dahmen, K. Enhancement of Thermal and Electrical Properties of Carbon Nanotube Polymer Composites by Magnetic Field Processing. *Journal of Applied Physics* **2003,** 94, (9), 6034-6039.

234. Yang, K.; Gu, M.; Guo, Y.; Pan, X.; Mu, G. Effects of Carbon Nanotube Functionalization on the Mechanical and Thermal Properties of Epoxy Composites. *Carbon* **2009,** 47, (7), 1723-1737.

235. Yu, A.; Ramesh, P.; Itkis, M. E.; Bekyarova, E.; Haddon, R. C. Graphite Nanoplatelet-Epoxy Composite Thermal Interface Materials. *The Journal of Physical Chemistry. C* **2007,** 111, (21), 7565-7569.

236. Bryning, M. B.; Milkie, D. E.; Islam, M. F.; Kikkawa, J. M.; Yodh, A. G. Thermal Conductivity and Interfacial Resistance in Single-Wall Carbon Nanotube Epoxy Composites. *Applied Physics Letters* **2005,** 87, (16), 161909.

237. Teng, C.-C.; Ma, C.-C. M.; Lu, C.-H.; Yang, S.-Y.; Lee, S.-H.; Hsiao, M.-C.; Yen, M.-Y.; Chiou, K.-C.; Lee, T.-M. Thermal Conductivity and Structure of Non-Covalent Functionalized Graphene/Epoxy Composites. *Carbon* **2011,** 49, (15), 5107-5116.

238. Song, S. H.; Park, K. H.; Kim, B. H.; Choi, Y. W.; Jun, G. H.; Lee, D. J.; Kong, B.-S.; Paik, K.-W.; Jeon, S. Enhanced Thermal Conductivity of Epoxy–Graphene Composites by Using Non-Oxidized Graphene Flakes with Non-Covalent Functionalization. *Advanced Materials* **2013,** 25, (5), 732-737.

239. Im, H.; Kim, J. Thermal Conductivity of a Graphene Oxide–Carbon Nanotube Hybrid/Epoxy Composite. *Carbon* **2012,** 50, (15), 5429-5440.

240. Yu, A.; Ramesh, P.; Sun, X.; Bekyarova, E.; Itkis, M. E.; Haddon, R. C. Enhanced Thermal Conductivity in a Hybrid Graphite Nanoplatelet – Carbon Nanotube Filler for Epoxy Composites. *Advanced Materials* **2008,** 20, (24), 4740-4744.

241. Shen, J.; Huang, W.; Wu, L.; Hu, Y.; Ye, M. Thermo-Physical Properties of Epoxy Nanocomposites Reinforced with Amino-Functionalized Multi-Walled Carbon Nanotubes. *Composites Part A: Applied Science and Manufacturing* **2007,** 38, (5), 1331-1336.

242. Shen, J.; Huang, W.; Wu, L.; Hu, Y.; Ye, M. The Reinforcement Role of Different Amino-Functionalized Multi-Walled Carbon Nanotubes in Epoxy Nanocomposites. *Composites Science and Technology* **2007,** 67, (15–16), 3041-3050.

243. Miyagawa, H.; Rich, M. J.; Drzal, L. T. Thermo-Physical Properties of Epoxy Nanocomposites Reinforced by Carbon Nanotubes and Vapor Grown Carbon Fibers. *Thermochimica Acta* **2006,** 442, (1–2), 67-73.

244. Ganguli, S.; Aglan, H.; Dean, D. Microstructural Origin of Strength and Toughness of Epoxy Nanocomposites. *Journal of Elastomers and Plastics* **2005,** 37, (1), 19-35.

245. Tseng, C.-H.; Wang, C.-C.; Chen, C.-Y. Functionalizing Carbon Nanotubes by Plasma Modification for the Preparation of Covalent-Integrated Epoxy Composites. *Chemistry of Materials* **2006,** 19, (2), 308-315.

246. Guadagno, L.; De Vivo, B.; Di Bartolomeo, A.; Lamberti, P.; Sorrentino, A.; Tucci, V.; Vertuccio, L.; Vittoria, V. Effect of Functionalization on the Thermo-Mechanical and Electrical Behavior of Multi-Wall Carbon Nanotube/Epoxy Composites. *Carbon* **2011,** 49, (6), 1919-1930.

247. Gojny, F. H.; Schulte, K. Functionalisation Effect on the Thermo-Mechanical Behaviour of Multi-Wall Carbon Nanotube/Epoxy-Composites. *Composites Science and Technology* **2004,** 64, (15), 2303-2308.

248. Wang, S.; Liang, Z.; Gonnet, P.; Liao, Y. H.; Wang, B.; Zhang, C. Effect of Nanotube Functionalization on the Coefficient of Thermal Expansion of Nanocomposites. *Advanced Functional Materials* **2007,** 17, (1), 87-92.

249. Moniruzzaman, M.; Du, F.; Romero, N.; Winey, K. I. Increased Flexural Modulus and Strength in Swnt/Epoxy Composites by a New Fabrication Method. *Polymer* **2006,** 47, (1), 293-298.

250. Ma, P. C.; Kim, J.-K.; Tang, B. Z. Effects of Silane Functionalization on the Properties of Carbon Nanotube/Epoxy Nanocomposites. *Composites Science and Technology* **2007,** 67, (14), 2965-2972.

251. Lau, K.-t.; Lu, M.; Chun-ki, L.; Cheung, H.-y.; Sheng, F.-L.; Li, H.-L. Thermal and Mechanical Properties of Single-Walled Carbon Nanotube Bundle-Reinforced Epoxy Nanocomposites: The Role of Solvent for Nanotube Dispersion. *Composites Science and Technology* **2005,** 65, (5), 719-725.

252. Shiu, S.-C.; Tsai, J.-L. Characterizing Thermal and Mechanical Properties of Graphene/Epoxy Nanocomposites. *Composites Part B: Engineering* **2014,** 56, 691-697.

253. Prolongo, S. G.; Jiménez-Suárez, A.; Moriche, R.; Ureña, A. Graphene Nanoplatelets Thickness and Lateral Size Influence on the Morphology and Behavior of Epoxy Composites. *European Polymer Journal* **2014,** 53, 292-301.

254. Guo, Y.; Bao, C.; Song, L.; Yuan, B.; Hu, Y. In Situ Polymerization of Graphene, Graphite Oxide, and Functionalized Graphite Oxide into Epoxy Resin and Comparison Study of on-the-Flame Behavior. *Industrial & Engineering Chemistry Research* **2011,** 50, (13), 7772-7783.

255. Wang, Z.; Wei, P.; Qian, Y.; Liu, J. The Synthesis of a Novel Graphene-Based Inorganic–Organic Hybrid Flame Retardant and Its Application in Epoxy Resin. *Composites Part B: Engineering* **2014,** 60, 341-349.

256. Harris, P. J. F., *Carbon Nanotube Science : Synthesis, Properties and Applications*. Cambridge University Press: Cambridge, UK; New York, 2009.

257. Cooper, C. A.; Young, R. J.; Halsall, M. Investigation into the Deformation of Carbon Nanotubes and Their Composites through the Use of Raman Spectroscopy. *Composites Part A: Applied Science and Manufacturing* **2001,** 32, (3–4), 401-411.

258. de Heer, W. A. Nanotubes and the Pursuit of Applications. *MRS Bulletin* **2004,** 29, (4), 281-285.

259. Cagin, T.; Gao, G.; Çagin, T.; Goddard, W. Energetics, Structure, Mechanical and Vibrational Properties of Single-Walled Carbon Nanotubes. *Nanotechnology* **1998,** 9, (3), 184-191.

260. Reilly, R. Carbon Nanotubes: Potential Benefits and Risks of Nanotechnology in Nuclear Medicine. *The Journal of Nuclear Medicine* **2007,** 48, (7), 1039-1042.

261. Popov, V. N. Carbon Nanotubes: Properties and Application. *Materials Science and Engineering: R: Reports* **2004,** 43, (3), 61-102.

262. Dresselhaus, S.; Dresselhaus, G.; Avouris, P., *Carbon Nanotubes: Synthesis, Structure, Properties, and Applications*. Springer: 2001.

263. Thostenson, E. T.; Ren, Z.; Chou, T.-W. Advances in the Science and Technology of Carbon Nanotubes and Their Composites: A Review. *Composites Science and Technology* **2001,** 61, (13), 1899-1912.

264. Dai, H. Carbon Nanotubes: Synthesis, Integration, and Properties. *Accounts of Chemical Research* **2002,** 35, (12), 1035-1044.

265. Kim, H.; Abdala, A. A.; Macosko, C. W. Graphene/Polymer Nanocomposites. *Macromolecules* **2010,** 43, (16), 6515-6530.

266. Verdejo, R.; Bernal, M. M.; Romasanta, L.; Lopez Manchado, M. Graphene Filled Polymer Nanocomposites. *Journal of Materials Chemistry* **2011,** 21, (10), 3301-3310.

267. Singh, V.; Joung, D.; Zhai, L.; Das, S.; Khondaker, S.; Seal, S. Graphene Based Materials: Past, Present and Future. *Progress in Materials Science* **2011,** 56, (8), 1178-1271.

268. Lee, C.; Wei, X.; Kysar, J.; Hone, J. Measurement of the Elastic Properties and Intrinsic Strength of Monolayer Graphene. *Science* **2008,** 321, (5887), 385-393.

269. Balandin, A.; Ghosh, S.; Bao, W.; Calizo, I.; Teweldebrhan, D.; Miao, F.; Lau, C. Superior Thermal Conductivity of Single-Layer Graphene. *Nano Letters* **2008,** 8, (3), 902-907.

270. Bunch, J. S.; Verbridge, S.; Alden, J.; van der Zande, A. M.; Parpia, J.; Craighead, H.; McEuen, P. Impermeable Atomic Membranes from Graphene Sheets. *Nano Letters* **2008,** 8, (8), 2458-2462.

271. Geim, A. K.; Novoselov, K. S. The Rise of Graphene. *Nature Materials* **2007,** 6, (3), 183-191.

272. Somani, P.; Somani, S.; Umeno, M. Planer Nano-Graphenes from Camphor by Cvd. *Chemical Physics Letters* **2006,** 430, (1-3), 56-59.

273. Reina, A.; Jia, X.; Ho, J.; Nezich, D.; Son, H.; Bulovic, V.; Dresselhaus, M.; Kong, J. Large Area, Few-Layer Graphene Films on Arbitrary Substrates by Chemical Vapor Deposition. *Nano Letters* **2009,** 9, (1), 30-35.

274. Novoselov, K. S.; Jiang, D.; Zhang, Y.; Geim, A. K.; Morozov, S. V.; Dubonos, S. V.; Grigorieva, I. V.; Firsov, A. A. Electric Field Effect in Atomically Thin Carbon Films. *Science* **2004,** 306, (5696), 666-669.

275. Berger, C.; Song, Z.; Li, X.; Wu, X.; Brown, N.; Naud, C. c.; Mayou, D.; Li, T.; Hass, J.; Marchenkov, A.; Conrad, E.; First, P.; de Heer, W. Electronic Confinement and Coherence in Patterned Epitaxial Graphene. *Science* **2006,** 312, (5777), 1191-6.

276. Jiao, L.; Zhang, L.; Wang, X.; Diankov, G.; Dai, H. Narrow Graphene Nanoribbons from Carbon Nanotubes. *Nature* **2009,** 458, (7240), 877-880.

277. Stankovich, S.; Dikin, D.; Piner, R.; Kohlhaas, K.; Kleinhammes, A.; Jia, Y.; Wu, Y.; Nguyen, S.; Ruoff, R. Synthesis of Graphene-Based Nanosheets Via Chemical Reduction of Exfoliated Graphite Oxide. *Carbon* **2007,** 45, (7), 1558-1565.

278. Tung, V.; Allen, M.; Yang, Y.; Kaner, R. High-Throughput Solution Processing of Large-Scale Graphene. *Nature Nanotechnology* **2009,** 4, (1), 25-29.

279. Park, S.; An, J.; Potts, J. R.; Velamakanni, A.; Murali, S.; Ruoff, R. S. Hydrazine-Reduction of Graphite- and Graphene Oxide. *Carbon* **2011,** 49, (9), 3019-3023.

280. Wang, G.; Shen, X.; Wang, B.; Yao, J.; Park, J. Synthesis and Characterisation of Hydrophilic and Organophilic Graphene Nanosheets. *Carbon* **2009,** 47, (5), 1359-1364.

281. Szabo, T.; Bourlinos, A.; Gournis, D.; Petridis, D.; Szabó, T.; Szeri, A.; Dékány, I. Graphite Oxide: Chemical Reduction to Graphite and Surface Modification with Primary Aliphatic Amines and Amino Acids. *Langmuir* **2003,** 19, (15), 6050-6055.

282. McAllister, M.; Li, J.-L.; Adamson, D.; Schniepp, H.; Abdala, A.; Liu, J.; Herrera Alonso, M.; Milius, D.; Car, R.; Aksay, I. Single Sheet Functionalized Graphene by Oxidation and Thermal Expansion of Graphite. *Chemistry of Materials* **2007,** 19, (18), 4396-4404.

283. Schniepp, H. C.; Li, J.-L.; McAllister, M. J.; Sai, H.; Herrera-Alonso, M.; Adamson, D. H.; Prud'homme, R. K.; Car, R.; Saville, D. A.; Aksay, I. A.

Functionalized Single Graphene Sheets Derived from Splitting Graphite Oxide. *The Journal of Physical Chemistry B* **2006,** 110, (17), 8535-8539.

284. Terrones, M.; Botello-Méndez, A. R.; Campos-Delgado, J.; López-Urías, F.; Vega-Cantú, Y. I.; Rodríguez-Macías, F. J.; Elías, A. L.; Muñoz-Sandoval, E.; Cano-Márquez, A. G.; Charlier, J.-C.; Terrones, H. Graphene and Graphite Nanoribbons: Morphology, Properties, Synthesis, Defects and Applications. *Nano Today* **2010,** 5, (4), 351-372.

285. Cao, A.; Ci, L.; Wu, G.; Wei, B.; Xu, C.; Liang, J.; Wu, D. An Effective Way to Lower Catalyst Content in Well-Aligned Carbon Nanotube Films. *Carbon* **2001,** 39, (1), 152-155.

286. Singh, C.; Shaffer, M. S. P.; Windle, A. H. Production of Controlled Architectures of Aligned Carbon Nanotubes by an Injection Chemical Vapour Deposition Method. *Carbon* **2003,** 41, (2), 359-368.

287. Hirsch, A.; Vostrowsky, O., Functionalization of Carbon Nanotubes. In *Functional Organic Materials*, Wiley-VCH Verlag GmbH & Co. KGaA: 2007.

288. Verdejo, R.; Lamoriniere, S.; Cottam, B.; Bismarck, A.; Shaffer, M. Removal of Oxidation Debris from Multi-Walled Carbon Nanotubes. *Chemical Communications* **2007,** 0, (5), 513-515.

289. Zhu, J.; Kim, J.; Peng, H.; Margrave, J. L.; Khabashesku, V. N.; Barrera, E. V. Improving the Dispersion and Integration of Single-Walled Carbon Nanotubes in Epoxy Composites through Functionalization. *Nano Letters* **2003,** 3, (8), 1107-1113.

290. Peng, H.; Alemany, L. B.; Margrave, J. L.; Khabashesku, V. N. Sidewall Carboxylic Acid Functionalization of Single-Walled Carbon Nanotubes. *Journal of the American Chemical Society* **2003,** 125, (49), 15174-15182.

291. Wu, Z.; Pittman Jr, C. U.; Gardner, S. D. Nitric Acid Oxidation of Carbon Fibers and the Effects of Subsequent Treatment in Refluxing Aqueous Naoh. *Carbon* **1995,** 33, (5), 597-605.

292. Dresselhaus, M. S.; Dresselhaus, G.; Saito, R.; Jorio, A. Raman Spectroscopy of Carbon Nanotubes. *Physics Reports* **2005,** 409, (2), 47-99.

293. Bandow, S.; Takizawa, M.; Hirahara, K.; Yudasaka, M.; Iijima, S. Raman Scattering Study of Double-Wall Carbon Nanotubes Derived from the Chains of Fullerenes in Single-Wall Carbon Nanotubes. *Chemical Physics Letters* **2001,** 337, (1–3), 48-54.

294. Ferrari, A. C. Raman Spectroscopy of Graphene and Graphite: Disorder, Electron–Phonon Coupling, Doping and Nonadiabatic Effects. *Solid State Communications* **2007,** 143, (1–2), 47-57.

295. Datsyuk, V.; Kalyva, M.; Papagelis, K.; Parthenios, J.; Tasis, D.; Siokou, A.; Kallitsis, I.; Galiotis, C. Chemical Oxidation of Multiwalled Carbon Nanotubes. *Carbon* **2008,** 46, (6), 833-840.

296. Stankovich, S.; Dikin, D. A.; Piner, R. D.; Kohlhaas, K. A.; Kleinhammes, A.; Jia, Y.; Wu, Y.; Nguyen, S. T.; Ruoff, R. S. Synthesis of Graphene-Based Nanosheets Via Chemical Reduction of Exfoliated Graphite Oxide. *Carbon* **2007,** 45, (7), 1558-1565.

297. Ago, H.; Kugler, T.; Cacialli, F.; Salaneck, W. R.; Shaffer, M. S. P.; Windle, A. H.; Friend, R. H. Work Functions and Surface Functional Groups of Multiwall Carbon Nanotubes. *The Journal of Physical Chemistry B* **1999,** 103, (38), 8116-8121.

298. Okpalugo, T. I. T.; Papakonstantinou, P.; Murphy, H.; McLaughlin, J.; Brown, N. M. D. High Resolution Xps Characterization of Chemical Functionalised Mwcnts and Swcnts. *Carbon* **2005,** 43, (1), 153-161.

299. Yang, D.; Velamakanni, A.; Bozoklu, G.; Park, S.; Stoller, M.; Piner, R. D.; Stankovich, S.; Jung, I.; Field, D. A.; Ventrice Jr, C. A.; Ruoff, R. S. Chemical Analysis of Graphene Oxide Films after Heat and Chemical Treatments by X-Ray Photoelectron and Micro-Raman Spectroscopy. *Carbon* **2009,** 47, (1), 145-152.

300. Wagner, C. D.; Davis, L. E.; Zeller, M. V.; Taylor, J. A.; Raymond, R. H.; Gale, L. H. Empirical Atomic Sensitivity Factors for Quantitative Analysis by Electron Spectroscopy for Chemical Analysis. *Surface and Interface Analysis* **1981,** 3, (5), 211-225.

301. Hunt, M. R. C.; Montalti, M.; Chao, Y.; Krishnamurthy, S.; Dhanak, V. R.; Šiller, L. Thermally Induced Decomposition of Single-Wall Carbon Nanotubes Adsorbed on H/Si(111). *Applied Physics Letters* **2002,** 81, (25), 4847-4849.

302. Bom, D.; Andrews, R.; Jacques, D.; Anthony, J.; Chen, B.; Meier, M. S.; Selegue, J. P. Thermogravimetric Analysis of the Oxidation of Multiwalled Carbon Nanotubes: Evidence for the Role of Defect Sites in Carbon Nanotube Chemistry. *Nano Letters* **2002,** 2, (6), 615-619.

303. Santangelo, S.; Messina, G.; Faggio, G.; Lanza, M.; Milone, C. Evaluation of Crystalline Perfection Degree of Multi-Walled Carbon Nanotubes: Correlations between Thermal Kinetic Analysis and Micro-Raman Spectroscopy. *Journal of Raman Spectroscopy* **2011,** 42, (4), 593-602.

304. Liu, J.; Rinzler, A. G.; Dai, H.; Hafner, J. H.; Bradley, R. K.; Boul, P. J.; Lu, A.; Iverson, T.; Shelimov, K.; Huffman, C. B.; Rodriguez-Macias, F.; Shon, Y.-S.; Lee, T. R.; Colbert, D. T.; Smalley, R. E. Fullerene Pipes. *Science* **1998,** 280, (5367), 1253-1256.

305. Thostenson, E.; Chou, T.-W. On the Elastic Properties of Carbon Nanotube-Based Composites: Modelling and Characterization. *Journal of Physics. D, Applied physics* **2003,** 36, (5), 573-582.

306. Peigney, A.; Laurent, C.; Flahaut, E.; Bacsa, R. R.; Rousset, A. Specific Surface Area of Carbon Nanotubes and Bundles of Carbon Nanotubes. *Carbon* **2001,** 39, (4), 507-514.

307. Brodie, B. C. On the Atomic Weight of Graphite. *Philosophical Transactions of the Royal Society of London* **1859,** 149, 249-259.

308. Dreyer, D.; Park, S.; Bielawski, C.; Ruoff, R. The Chemistry of Graphene Oxide. *Chemical Society Reviews* **2010,** 39, (1), 228-40.

309. Verdejo, R.; Barroso Bujans, F.; Rodriguez Perez, M.; de Saja, J.; Lopez Manchado, M. Functionalized Graphene Sheet Filled Silicone Foam Nanocomposites. *Journal of Materials Chemistry* **2008,** 18, (19), 2221-2226.

310. Misra, A.; Tyagi, P.; Singh, M. K.; Misra, D. S. Ftir Studies of Nitrogen Doped Carbon Nanotubes. *Diamond and Related Materials* **2006,** 15, (2-3), 385-388.

311. Stankovich, S.; Piner, R.; Nguyen, S.; Ruoff, R. Synthesis and Exfoliation of Isocyanate-Treated Graphene Oxide Nanoplatelets. *Carbon* **2006,** 44, (15), 3342-3347.

312. Lin, Y.; Jin, J.; Song, M. Preparation and Characterisation of Covalent Polymer Functionalized Graphene Oxide. *Journal of Materials Chemistry* **2011,** 21, (10), 3455-3461.

313. Rao, C. N. R.; Biswas, K.; Subrahmanyam, K. S.; Govindaraj, A. Graphene, the New Nanocarbon. *Journal of Materials Chemistry* **2009,** 19, (17), 2457-2469.

314. Akhavan, O. The Effect of Heat Treatment on Formation of Graphene Thin Films from Graphene Oxide Nanosheets. *Carbon* **2010,** 48, (2), 509-519.

315. Shen, J.; Hu, Y.; Shi, M.; Lu, X.; Qin, C.; Li, C.; Ye, M. Fast and Facile Preparation of Graphene Oxide and Reduced Graphene Oxide Nanoplatelets. *Chemistry of Materials* **2009,** 21, (15), 3514-3520.

316. Biedermann, L.; Bolen, M.; Capano, M.; Zemlyanov, D.; Reifenberger, R. Insights into Few-Layer Epitaxial Graphene Growth on 4h-Sic(0001) Substrates from Stm

Studies. *Physical Review. B, Condensed matter and materials physics* **2009,** 79, (12), 125411-125416.

317. Schulz, S. C.; Faiella, G.; Buschhorn, S. T.; Prado, L. A. S. A.; Giordano, M.; Schulte, K.; Bauhofer, W. Combined Electrical and Rheological Properties of Shear Induced Multiwall Carbon Nanotube Agglomerates in Epoxy Suspensions. *European Polymer Journal* **2011,** 47, (11), 2069-2077.

318. Schulz, S. C.; Schlutter, J.; Bauhofer, W. Influence of Initial High Shearing on Electrical and Rheological Properties and Formation of Percolating Agglomerates for Mwcnt/Epoxy Suspensions. *Macromolecular Materials and Engineering* **2010,** 295, (7), 613-617.

319. Bauhofer, W.; Schulz, S. C.; Eken, A. E.; Skipa, T.; Lellinger, D.; Alig, I.; Tozzi, E. J.; Klingenberg, D. J. Shear-Controlled Electrical Conductivity of Carbon Nanotubes Networks Suspended in Low and High Molecular Weight Liquids. *Polymer* **2010,** 51, (22), 5024-5027.

320. Xia, H.; Song, M. Preparation and Characterization of Polyurethane-Carbon Nanotube Composites. *Soft Matter* **2005,** 1, (5), 386-394.

321. Poetschke, P.; Abdel Goad, M.; Pegel, S.; Jehnichen, D.; Mark, J. Comparisons among Electrical and Rheological Properties of Melt-Mixed Composites Containing Various Carbon Nanostructures. *Journal of Macromolecular Science. Pure and Applied Chemistry* **2010,** 47, (1), 12-19.

322. Knauert, S. T.; Douglas, J. F.; Starr, F. W. The Effect of Nanoparticle Shape on Polymer-Nanocomposite Rheology and Tensile Strength. *Journal of Polymer Science Part B: Polymer Physics* **2007,** 45, (14), 1882-1897.

323. Alig, I.; Skipa, T.; Lellinger, D.; Pötschke, P. Destruction and Formation of a Carbon Nanotube Network in Polymer Melts: Rheology and Conductivity Spectroscopy. *Polymer* **2008,** 49, (16), 3524-3532.

324. Bernal, M. M.; Lopez-Manchado, M. A.; Verdejo, R. In Situ Foaming Evolution of Flexible Polyurethane Foam Nanocomposites. *Macromolecular Chemistry and Physics* **2011,** 212, (9), 971-979.

325. Tiwari, M.; Bazilevsky, A.; Yarin, A.; Megaridis, C. Elongational and Shear Rheology of Carbon Nanotube Suspensions. *Rheologica Acta* **2009,** 48, (6), 597-609.

326. Kinloch, I. A.; Roberts, S. A.; Windle, A. H. A Rheological Study of Concentrated Aqueous Nanotube Dispersions. *Polymer* **2002,** 43, (26), 7483-7491.

327. Kim, H.; Macosko, C. W. Processing-Property Relationships of Polycarbonate/Graphene Composites. *Polymer* **2009,** 50, (15), 3797-3809.

328. Fernandez, I.; Santamaría, A.; Muñoz, M. E.; Castell, P. A Rheological Analysis of Interactions in Phenoxy/Organoclay Nanocomposites. *European Polymer Journal* **2007,** 43, (8), 3171-3176.

329. Monti, M.; Puglia, D.; Natali, M.; Torre, L.; Kenny, J. Effect of Carbon Nanofibers on the Cure Kinetics of Unsaturated Polyester Resin: Thermal and Chemorheological Modelling. *Composites Science and Technology* **2011,** 71, (12), 1507-1516.

330. Raman, V.; Palmese, G. R.; Raman, G. Influence of Tetrahydrofuran on Epoxy−Amine Polymerization. *Macromolecules* **2005,** 38, (16), 6923-6930.

331. Stjohn, N. A.; St John, N.; George, G. Cure Kinetics and Mechanisms of a Tetraglycidyl-4,4′-Diaminodiphenylmethane/Diaminodiphenylsulphone Epoxy Resin Using near I.R. Spectroscopy. *Polymer* **1992,** 33, (13), 2679-2688.

332. Vyazovkin, S.; Sbirrazzuoli, N. Mechanism and Kinetics of Epoxy−Amine Cure Studied by Differential Scanning Calorimetry. *Macromolecules* **1996,** 29, (6), 1867-1873.

333. Saalwächter, K. Proton Multiple-Quantum Nmr for the Study of Chain Dynamics and Structural Constraints in Polymeric Soft Materials. *Progress in Nuclear Magnetic Resonance Spectroscopy* **2007,** 51, (1), 1-35.

334. Vaca Chávez, F.; Saalwächter, K. Time-Domain Nmr Observation of Entangled Polymer Dynamics: Universal Behavior of Flexible Homopolymers and Applicability of the Tube Model. *Macromolecules* **2011,** 44, (6), 1549-1559.

335. Vaca Chávez, F.; Saalwächter, K. Time-Domain Nmr Observation of Entangled Polymer Dynamics: Analytical Theory of Signal Functions. *Macromolecules* **2011,** 44, (6), 1560-1569.

336. Saalwächter, K.; Gottlieb, M.; Liu, R.; Oppermann, W.; Liu, W. Gelation as Studied by Proton Multiple-Quantum Nmr. *Macromolecules* **2007,** 40, (5), 1555-1561.

337. Che, J.; Toki, S.; Valentin, J. L.; Brasero, J.; Nimpaiboon, A.; Rong, L.; Hsiao, B. S. Chain Dynamics and Strain-Induced Crystallization of Pre- and Postvulcanized Natural Rubber Latex Using Proton Multiple Quantum Nmr and Uniaxial Deformation by in Situ Synchrotron X-Ray Diffraction. *Macromolecules* **2012,** 45, (16), 6491-6503.

338. Valentín, J. L.; Posadas, P.; Fernández-Torres, A.; Malmierca, M. A.; González, L.; Chassé, W.; Saalwächter, K. Inhomogeneities and Chain Dynamics in Diene

Rubbers Vulcanized with Different Cure Systems†. *Macromolecules* **2010,** 43, (9), 4210-4222.

339. Baum, J.; Pines, A. Nmr Studies of Clustering in Solids. *Journal of the American Chemical Society* **1986,** 108, (24), 7447-7454.

340. Saalwächter, K.; Ziegler, P.; Spyckerelle, O.; Haidar, B.; Vidal, A.; Sommer, J. U. 1h Multiple-Quantum Nuclear Magnetic Resonance Investigations of Molecular Order Distributions in Poly(Dimethylsiloxane) Networks: Evidence for a Linear Mixing Law in Bimodal Systems. *The Journal of Chemical Physics* **2003,** 119, (6), 3468-3482.

341. Valentin, J. L.; Mora Barrantes, I.; Carretero Gonzalez, J.; Lopez-Manchado, M. A.; Sotta, P.; Long, D. R.; Saalwächter, K. Novel Experimental Approach to Evaluate Filler−Elastomer Interactions. *Macromolecules* **2010,** 43, (1), 334-346.

342. Saalwächter, K. Microstructure and Molecular Dynamics of Elastomers as Studied by Advanced Low-Resolution Nuclear Magnetic Resonance Methods. *Rubber Chemistry and Technology* **2012,** 85, (3), 350-386.

343. Vieyres, A.; Pérez-Aparicio, R.; Albouy, P.-A.; Sanseau, O.; Saalwächter, K.; Long, D. R.; Sotta, P. Sulfur-Cured Natural Rubber Elastomer Networks: Correlating Cross-Link Density, Chain Orientation, and Mechanical Response by Combined Techniques. *Macromolecules* **2013,** 46, (3), 889-899.

344. Pérez-Aparicio, R.; Schiewek, M.; Valentín, J. L.; Schneider, H.; Long, D. R.; Saphiannikova, M.; Sotta, P.; Saalwächter, K.; Ott, M. Local Chain Deformation and Overstrain in Reinforced Elastomers: An Nmr Study. *Macromolecules* **2013,** 46, (14), 5549-5560.

345. Höpfner, J.; Guthausen, G.; Saalwächter, K.; Wilhelm, M. Network Structure and Inhomogeneities of Model and Commercial Polyelectrolyte Hydrogels as Investigated by Low-Field Proton Nmr Techniques. *Macromolecules* **2014,** 47, (13), 4251-4265.

346. Malmierca, M. A.; González-Jiménez, A.; Mora-Barrantes, I.; Posadas, P.; Rodríguez, A.; Ibarra, L.; Nogales, A.; Saalwächter, K.; Valentin, J. L. Characterization of Network Structure and Chain Dynamics of Elastomeric Ionomers by Means of 1h Low-Field Nmr. *Macromolecules* **2014,** 47, (16), 5655–5667.

347. Schneider, M.; Demco, D. E.; Blümich, B. 1h Nmr Imaging of Residual Dipolar Couplings in Cross-Linked Elastomers: Dipolar-Encoded Longitudinal Magnetization, Double-Quantum, and Triple-Quantum Filters. *Journal of Magnetic Resonance* **1999,** 140, (2), 432-441.

348. Fechete, R.; Blumich, B.; Demco, D. E.; BlÃ¼mich, B. Enhanced Sensitivity to Residual Dipolar Couplings of Elastomers by Higher-Order Multiple-Quantum Nmr. *Journal of Magnetic Resonance* **2004,** 169, (1), 19-26.

349. Voda, M. A.; Demco, D. E.; Perlo, J.; Orza, R. A.; Blümich, B. Multispin Moments Edited by Multiple-Quantum Nmr: Application to Elastomers. *Journal of Magnetic Resonance* **2005,** 172, (1), 98-109.

350. Schneider, M.; Blumich, B.; Demco, D. E.; BlÃ¼mich, B. 1h Nmr Imaging of Residual Dipolar Couplings in Cross-Linked Elastomers: Dipolar-Encoded Longitudinal Magnetization, Double-Quantum, and Triple-Quantum Filters. *Journal of Magnetic Resonance* **1999,** 140, (2), 432-441.

351. Perlo, J.; Blumich, B.; Voda, M. A.; Demco, D. E.; Orza, R. A.; BlÃ¼mich, B. Multispin Moments Edited by Multiple-Quantum Nmr: Application to Elastomers. *Journal of Magnetic Resonance* **2005,** 172, (1), 98-109.

352. Chassé, W.; Lang, M.; Sommer, J. U.; Saalwächter, K. Cross-Link Density Estimation of Pdms Networks with Precise Consideration of Networks Defects. *Macromolecules* **2011,** 45, (2), 899-912.

353. Valles, E. M.; Acosta, R.; Vega, D.; Villar, M.; Monti, G.; Vallés, E. Double Quantum Nmr Applied to Polymer Networks with Low Concentration of Pendant Chains. *Macromolecules* **2006,** 39, (14), 4788-4792.

354. Acosta, R.; Monti, G.; Villar, M.; Valles, E.; Vega, D.; Vallés, E. Transiently Trapped Entanglements in Model Polymer Networks. *Macromolecules* **2009,** 42, (13), 4674-4680.

355. Chasse, W.; Lopez Valentin, J.; Genesky, G.; Cohen, C.; Saalwächter, K. Precise Dipolar Coupling Constant Distribution Analysis in Proton Multiple-Quantum Nmr of Elastomers. *The Journal of Chemical Physics* **2011,** 134, (4), 044907.

356. Saalwächter, K. Detection of Heterogeneities in Dry and Swollen Polymer Networks by Proton Low-Field Nmr Spectroscopy. *Journal of the American Chemical Society* **2003,** 125, (48), 14684-14685.

357. Maeda, T.; Horie, C. Phonon Modes in Single-Wall Nanotubes with a Small Diameter. *Physica B: Condensed Matter* **1999,** 263–264, 479-481.

358. Popov, V. N. Theoretical Evidence for T1/2 Specific Heat Behavior in Carbon Nanotube Systems. *Carbon* **2004,** 42, (5–6), 991-995.

359. Qingwei, L.; Changhong, L.; Xueshen, W.; Shoushan, F. Measuring the Thermal Conductivity of Individual Carbon Nanotubes by the Raman Shift Method. *Nanotechnology* **2009,** 20, (14), 145702.

360. Mingo, N.; Broido, D. A. Carbon Nanotube Ballistic Thermal Conductance and Its Limits. *Physical Review Letters* **2005,** 95, (9), 096105.

361. Dresselhaus, M. S.; Dresselhaus, G.; Jorio, A.; Souza Filho, A. G.; Saito, R. Raman Spectroscopy on Isolated Single Wall Carbon Nanotubes. *Carbon* **2002,** 40, (12), 2043-2061.

362. Deng, F.; Zheng, Q.-S.; Wang, L.-F.; Nan, C.-W. Effects of Anisotropy, Aspect Ratio, and Nonstraightness of Carbon Nanotubes on Thermal Conductivity of Carbon Nanotube Composites. *Applied Physics Letters* **2007,** 90, (2), 021914.

363. Cagin, T.; Che, J.; Çagin, T.; Goddard, W. Thermal Conductivity of Carbon Nanotubes. *Nanotechnology* **2000,** 11, (2), 65-69.

364. Han, Z.; Fina, A. Thermal Conductivity of Carbon Nanotubes and Their Polymer Nanocomposites: A Review. *Progress in Polymer Science* **2011,** 36, (7), 914-944.

365. Kapitza, P. L. The Study of Heat Transfer in Helium Ii. *Journal of Physics* **1941,** 4, (1-6), 181-210.

366. Konatham, D.; Striolo, A. Thermal Boundary Resistance at the Graphene-Oil Interface. *Applied Physics Letters* **2009,** 95, (16), 163105.

367. Hamilton, R. L.; Crosser, O. K. Thermal Conductivity of Heterogeneous Two-Component Systems. *Industrial & Engineering Chemistry Fundamentals* **1962,** 1, (3), 187-191.

368. Choi, S. U. S.; Zhang, Z. G.; Yu, W.; Lockwood, F. E.; Grulke, E. A. Anomalous Thermal Conductivity Enhancement in Nanotube Suspensions. *Applied Physics Letters* **2001,** 79, (14), 2252-2254.

369. Vazquez Penas, J.; Peñas, J. R. V. z.; Khayet, M. Measurement of the Thermal Conductivity of Nanofluids by the Multicurrent Hot-Wire Method. *Journal of Applied Physics* **2008,** 104, (4), 044314.

370. Debelak, B.; Lafdi, K. Use of Exfoliated Graphite Filler to Enhance Polymer Physical Properties. *Carbon* **2007,** 45, (9), 1727-1734.

371. Huxtable, S. T.; Cahill, D. G.; Shenogin, S.; Xue, L.; Ozisik, R.; Barone, P.; Usrey, M.; Strano, M. S.; Siddons, G.; Shim, M.; Keblinski, P. Interfacial Heat Flow in Carbon Nanotube Suspensions. *Nat Mater* **2003,** 2, (11), 731-734.

372. Shenogin, S.; Xue, L.; Ozisik, R.; Keblinski, P.; Cahill, D. G. Role of Thermal Boundary Resistance on the Heat Flow in Carbon-Nanotube Composites. *Journal of Applied Physics* **2004,** 95, (12), 8136-8144.

373. RamanathanT; Abdala, A. A.; StankovichS; Dikin, D. A.; Herrera Alonso, M.; Piner, R. D.; Adamson, D. H.; Schniepp, H. C.; ChenX; Ruoff, R. S.; Nguyen, S. T.; Aksay, I. A.; Prud'Homme, R. K.; Brinson, L. C. Functionalized Graphene Sheets for Polymer Nanocomposites. *Nat Nano* **2008,** 3, (6), 327-331.

374. Leng, J.; Lau, A. K., *Multifunctional Polymer Nanocomposites*. Taylor & Francis: 2011.

375. Sangermano, M.; Pegel, S.; Poetschke, P.; Voit, B.; Pötschke, P. Antistatic Epoxy Coatings with Carbon Nanotubes Obtained by Cationic Photopolymerization. *Macromolecular Rapid Communications* **2008,** 29, (5), 396-400.

376. Hayward, D.; Pethrick, R.; Siriwittayakorn, T. Dielectric Studies of Heterogeneous Phase Polymer Systems: Poly(Ethylene Oxide) Inclusions in Polycarbonate - a Model System. *Macromolecules* **1992,** 25, (5), 1480-1486.

377. Bauhofer, W.; Kovacs, J. A Review and Analysis of Electrical Percolation in Carbon Nanotube Polymer Composites. *Composites Science and Technology* **2009,** 69, (10), 1486-1498.

378. Chen, G.-H.; Wu, D.-J.; Weng, W.-G.; Yan, W.-L. Preparation of Polymer/Graphite Conducting Nanocomposite by Intercalation Polymerization. *Journal of Applied Polymer Science* **2001,** 82, (10), 2506-2513.

379. Viculis, L.; Mack, J.; Kaner, R. A Chemical Route to Carbon Nanoscrolls. *Science* **2003,** 299, (5611), 1361-1361.

380. Du, J.; Zhao, L.; Zeng, Y.; Zhang, L.; Li, F.; Liu, P.; Liu, C. Comparison of Electrical Properties between Multi-Walled Carbon Nanotube and Graphene Nanosheet/High Density Polyethylene Composites with a Segregated Network Structure. *Carbon* **2011,** 49, (4), 1094-1100.

381. Wichmann, M. H. G.; Gojny, F.; Schulte, K.; Fiedler, B.; Kinloch, I.; Bauhofer, W.; Windle, A. Evaluation and Identification of Electrical and Thermal Conduction Mechanisms in Carbon Nanotube/Epoxy Composites. *Polymer* **2006,** 47, (6), 2036-2045.

382. Ocando, C.; Tercjak, A.; Dolores Martin, M.; Martín, M. D.; Ramos, J.; Campo, M.; Mondragon, I. Morphology Development in Thermosetting Mixtures through the Variation on Chemical Functionalization Degree of Poly(Styrene-B-Butadiene) Diblock

Copolymer Modifiers. Thermomechanical Properties. *Macromolecules* **2009,** 42, (16), 6215-6224.

383. Rebizant, V.; Abetz, V.; Court, F.; Leibler, L.; Abetz, F.; Tournilhac, F.; Court, L. Reactive Tetrablock Copolymers Containing Glycidyl Methacrylate. Synthesis and Morphology Control in Epoxy−Amine Networks. *Macromolecules* **2003,** 36, (26), 9889-9896.

384. Hameed, N.; Guo, Q.; Xu, Z.; Hanley, T.; Mai, Y.-W. Reactive Block Copolymer Modified Thermosets: Highly Ordered Nanostructures and Improved Properties. *Soft Matter* **2010,** 6, (24), 6119-6129.

385. Casaban, L.; Kirsten, M.; Pegel, S.; Carrasco, P. M.; García, I.; Stamm, M.; Kenny, J. M. Shear Induced Orientation of Phase Segregated Block Copolymer/Epoxy Blends. *European Polymer Journal* **2013,** 49, (10), 3359-3365.

386. Hu, D.; Xu, Z.; Zeng, K.; Zheng, S. From Self-Organized Novolac Resins to Ordered Nanoporous Carbons. *Macromolecules* **2010,** 43, (6), 2960-2969.

387. Mijovic, J.; Shen, M.; Sy, J.; Mondragon, I. Dynamics and Morphology in Nanostructured Thermoset Network/Block Copolymer Blends During Network Formation. *Macromolecules* **2000,** 33, (14), 5235-5244.

388. Guo, Q.; Thomann, R.; Gronski, W.; Thurn-Albrecht, T. Phase Behavior, Crystallization, and Hierarchical Nanostructures in Self-Organized Thermoset Blends of Epoxy Resin and Amphiphilic Poly(Ethylene Oxide)-Block-Poly(Propylene Oxide)-Block-Poly(Ethylene Oxide) Triblock Copolymers. *Macromolecules* **2002,** 35, (8), 3133-3144.

389. Larranaga, M.; Martin, M. D.; Gabilondo, N.; Kortaberria, G.; Corcuera, M. A.; Larrañaga, M.; Martín, M. D.; Riccardi, C. C.; Mondragon, I. Cure Kinetics of Epoxy Systems Modified with Block Copolymers. *Polymer International* **2004,** 53, (10), 1495-1502.

390. Larranaga, M.; Arruti, P.; Serrano, E.; Remiro, P. M.; Larrañaga, M.; Caba, K.; Riccardi, C. C.; Mondragon, I. Towards Microphase Separation in Epoxy Systems Containing Peo/Ppo/Peo Block Copolymers by Controlling Cure Conditions and Molar Ratios between Blocks. Part 2. Structural Characterization. *Colloid and Polymer Science* **2006,** 284, (12), 1419-1430.

391. Builes, D. H.; Hernández-Ortiz, J. P.; Corcuera, M. A.; Mondragon, I.; Tercjak, A. Effect of Poly(Ethylene Oxide) Homopolymer and Two Different Poly(Ethylene Oxide-B-Poly(Propylene Oxide)-B-Poly(Ethylene Oxide) Triblock Copolymers on

Morphological, Optical, and Mechanical Properties of Nanostructured Unsaturated Polyester. *ACS Applied Materials & Interfaces* **2013,** 6, (2), 1073-1081.

392. Chatterjee, T.; Yurekli, K.; Hadjiev, V. G.; Krishnamoorti, R. Single-Walled Carbon Nanotube Dispersions in Poly(Ethylene Oxide). *Advanced Functional Materials* **2005,** 15, (11), 1832-1838.

393. Martin-Gallego, M.; Bernal, M. M.; Hernandez, M.; Verdejo, R.; Lopez-Manchado, M. A. Comparison of Filler Percolation and Mechanical Properties in Graphene and Carbon Nanotubes Filled Epoxy Nanocomposites. *European Polymer Journal* **2013,** 49, (6), 1347-1353.

394. Trent, J. S.; Scheinbeim, J. I.; Couchman, P. R. Ruthenium Tetraoxide Staining of Polymers for Electron Microscopy. *Macromolecules* **1983,** 16, (4), 589-598.

395. Sun, P.; Dang, Q.; Li, B.; Chen, T.; Wang, Y.; Lin, H.; Jin, Q.; Ding, D.; Shi, A.-C. Mobility, Miscibility, and Microdomain Structure in Nanostructured Thermoset Blends of Epoxy Resin and Amphiphilic Poly(Ethylene Oxide)-Block-Poly(Propylene Oxide)-Block-Poly(Ethylene Oxide) Triblock Copolymers Characterized by Solid-State Nmr. *Macromolecules* **2005,** 38, (13), 5654-5667.

396. González-Domínguez, J. M.; Ansón-Casaos, A.; Díez-Pascual, A. M.; Ashrafi, B.; Naffakh, M.; Backman, D.; Stadler, H.; Johnston, A.; Gómez, M.; Martínez, M. T. Solvent-Free Preparation of High-Toughness Epoxy−Swnt Composite Materials. *ACS Applied Materials & Interfaces* **2011,** 3, (5), 1441-1450.

397. Moniruzzaman, M.; Winey, K. I. Polymer Nanocomposites Containing Carbon Nanotubes. *Macromolecules* **2006,** 39, (16), 5194-5205.

398. Grady, B. P. Recent Developments Concerning the Dispersion of Carbon Nanotubes in Polymers. *Macromolecular Rapid Communications* **2010,** 31, (3), 247-257.

399. Kinloch, A. J.; Shaw, S. J.; Tod, D. A.; Hunston, D. L. Deformation and Fracture Behaviour of a Rubber-Toughened Epoxy: 1. Microstructure and Fracture Studies. *Polymer* **1983,** 24, (10), 1341-1354.

400. Faber, K. T.; Evans, A. G. Crack Deflection Processes—I. Theory. *Acta Metallurgica* **1983,** 31, (4), 565-576.

401. Sigl, L. S.; Mataga, P. A.; Dalgleish, B. J.; McMeeking, R. M.; Evans, A. G. On the Toughness of Brittle Materials Reinforced with a Ductile Phase. *Acta Metallurgica* **1988,** 36, (4), 945-953.

402. Williams, S.; Beaumont, P. W. R.; Evans, A. G. On the Toughness of Particulate Filled Polymers. *J Mater Sci* **1985,** 20, (10), 3668-3674.

403. Pearson, R.; Yee, A. Toughening Mechanisms in Thermoplastic-Modified Epoxies: 1. Modification Using Poly(Phenylene Oxide). *Polymer* **1993,** 34, (17), 3658-3670.

404. Park, K.-Y.; Lee, S.-E.; Kim, C.-G.; Han, J.-H. Fabrication and Electromagnetic Characteristics of Electromagnetic Wave Absorbing Sandwich Structures. *Composites Science and Technology* **2006,** 66, (3–4), 576-584.

405. Wang, L.; Yang, X.; Zhang, J.; Zhang, C.; He, L. The Compressive Properties of Expandable Microspheres/Epoxy Foams. *Composites Part B: Engineering* **2014,** 56, 724-732.

406. Forrest, J. A.; DalnokiVeress, K.; Stevens, J. R.; Dutcher, J. R.; Dalnoki Veress, K. Effect of Free Surfaces on the Glass Transition Temperature of Thin Polymer Films. *Physical Review Letters* **1996,** 77, (10), 2002-2005.

407. Yan, D.; Xu, L.; Chen, C.; Tang, J.; Ji, X.; Li, Z. Enhanced Mechanical and Thermal Properties of Rigid Polyurethane Foam Composites Containing Graphene Nanosheets and Carbon Nanotubes. *Polymer International* **2012,** 61, (7), 1107-1114.

408. Zegeye, E.; Ghamsari, A. K.; Woldesenbet, E. Mechanical Properties of Graphene Platelets Reinforced Syntactic Foams. *Composites Part B: Engineering* **2014,** 60, 268-273.

409. Bourbigot, S.; Duquesne, S. Fire Retardant Polymers: Recent Developments and Opportunities. *Journal of Materials Chemistry* **2007,** 17, (22), 2283-2300.

410. Verdejo, R.; Barroso-Bujans, F.; Rodriguez-Perez, M. A.; Antonio de Saja, J.; Arroyo, M.; Lopez-Manchado, M. A. Carbon Nanotubes Provide Self-Extinguishing Grade to Silicone-Based Foams. *Journal of Materials Chemistry* **2008,** 18, (33), 3933-3939.

411. Kashiwagi, T.; Grulke, E.; Hilding, J.; Groth, K.; Harris, R.; Butler, K.; Shields, J.; Kharchenko, S.; Douglas, J. Thermal and Flammability Properties of Polypropylene/Carbon Nanotube Nanocomposites. *Polymer* **2004,** 45, (12), 4227-4239.

412. Peeterbroeck, S.; Laoutid, F.; Taulemesse, J. M.; Monteverde, F.; Lopez-Cuesta, J. M.; Nagy, J. B.; Alexandre, M.; Dubois, P. Mechanical Properties and Flame-Retardant Behavior of Ethylene Vinyl Acetate/High-Density Polyethylene Coated Carbon Nanotube Nanocomposites. *Advanced Functional Materials* **2007,** 17, (15), 2787-2791.

413. Doi, M.; Edwards, S. F., *The Theory of Polymer Dynamics*. Clarendon Press: 1988.

414. Litvinov, V. M. Epdm/Pp Thermoplastic Vulcanizates as Studied by Proton Nmr Relaxation: Phase Composition, Molecular Mobility, Network Structure in the Rubbery Phase, and Network Heterogeneity. *Macromolecules* **2006,** 39, (25), 8727-8741.

415. Callaghan, P. T.; Samulski, E. T. Molecular Ordering and the Direct Measurement of Weak Proton−Proton Dipolar Interactions in a Rubber Network. *Macromolecules* **1997,** 30, (1), 113-122.

416. Demco, D. E.; Hafner, S.; Fülber, C.; Graf, R.; Spiess, H. W. Two-Dimensional Proton Magnetization Exchange Nmr Spectroscopy in Cross-Linked Elastomers. *The Journal of Chemical Physics* **1996,** 105, (24), 11285-11296.

417. Graf, R.; Heuer, A.; Spiess, H. W. Chain-Order Effects in Polymer Melts Probed by Double-Quantum Nmr Spectroscopy. *Physical Review Letters* **1998,** 80, (26), 5738-5741.

418. Valentín, J. L.; Posadas, P.; Fernández-Torres, A.; Malmierca, M. A.; González, L.; Chassé, W.; Saalwächter, K. Inhomogeneities and Chain Dynamics in Diene Rubbers Vulcanized with Different Cure Systems. *Macromolecules* **2010,** 43, (9), 4210-4222.

LIST OF PUBLICATIONS AND PATENTS

The publications obtained from this thesis are:

- Mario Martin-Gallego, Raquel Verdejo, Mohamed Khayet, Jose Maria Ortiz de Zarate, Mohamed Essalhi and Miguel Angel Lopez-Manchado: *Thermal conductivity of carbon nanotubes and graphene in epoxy nanofluids and nanocomposites.* Nanoscale Research Letters 6 (2011), 610.
- Mario Martin-Gallego, Raquel Verdejo, Miguel Angel Lopez-Manchado, Marco Sangermano: *Epoxy-Graphene UV-cured nanocomposites.* Polymer 52 (2011), 4664.
- Mario Martin-Gallego, Marianella Hernández, Vicente Lorenzo, Raquel Verdejo, Miguel Angel Lopez-Manchado, Marco Sangermano: *Cationic photocured epoxy nanocomposites filled with different carbon fillers*. Polymer 53 (2012), 1831.
- Mario Martin-Gallego, Mar Bernal, Marianella Hernandez, Raquel Verdejo, Miguel Angel Lopez-Manchado: *Comparison of filler percolation and mechanical properties in graphene and carbon nanotubes filled epoxy nanocomposites.* European Polymer Journal 49 (2013), 1347.
- Mario Martin-Gallego, Raquel Verdejo, Adrian Gestos, Miguel Angel Lopez-Manchado, Qipeng Guo: *Morphology and mechanical properties of nanostructured thermoset/block copolymer blends with carbon nanoparticles.* Submitted to Composites Part A: Applied Science and Manufacturing.
- Mario Martín-Gallego, Juan Lopez Valentin, Raquel Verdejo, Miguel Angel Lopez-Manchado: *Epoxy resin curing reaction studied by proton double-quantum NMR.* Submitted to RSC Advances.

One patent has also resulted from the research of this thesis:

- Mario Martín Gallego, Raquel Verdejo, Miguel Angel Lopez-Manchado: *Espumas rígidas termoestables conductoras.* Spanish patent number P201430094.

Other publications derived from collaborations performed during the PhD:

- Mar Bernal, Mario Martin-Gallego, Laura J. Romasanta, Anne-Cecile Mortamet, Miguel Angel López-Manchado, Anthony J. Ryan, Raquel Verdejo: *Effect of hard segment content and carbon-based nanostructures on the kinetics of flexible polyurethane nanocomposite foams.* Polymer 53 (2012), 4025.
- Laura J Romasanta, Mario Martín-Gallego, Marianella Hernández, Miguel A. Lopez-Manchado, Raquel Verdejo: *La última frontera de los polímeros nanocompuestos: el grafeno.* Revista de plásticos modernos 676.
- Marianella Hernández, Laura J. Romasanta, Mario Martín Gallego, Raquel Verdejo, Miguel A. López-Manchado: *¿Cómo se mueven las cadenas elastoméricas en un nanocompuesto? Bondades de la Espectroscopia Dieléctrica.* Revista de plásticos modernos 680.
- Mar Bernal, Mario Martin-Gallego, Isabel Molenberg, Isabel Huynen, Miguel Angel Lopez-Manchado and Raquel Verdejo: *Influence of carbon nanoparticles on the polymerization and EMI shielding properties of PU nanocomposite foams.* RSC Advances 4 (2014), 7911.
- Luca Valentini, A. Bolognini, A. Alvino, Silvia Bittolo Bon, Mario Martin-Gallego, Miguel Angel Lopez-Manchado: *Pyroshock testing on graphene based EPDM nanocomposites.* Composites Part B 60 (2014), 479.
- Mario Martin-Gallego, Miguel Angel Lopez-Manchado, Paola Calza, Ignazio Roppolo, Marco Sangermano: *Gold-functionalized graphene as conductive filler in UV-curable epoxy resin.* Journal of Materials Science 50 (2015), 605.